Improved Probabilistic Representation of Facies through Developments in Geostatistical Practice

by

Saina Lajevardi

A thesis submitted in partial fulfillment of the requirements for the degree of

Doctor of Philosophy

in

Mining Engineering

Department of Civil and Environmental Engineering
University of Alberta

Abstract

Reservoir management requires high resolution numerical geologic models of facies and petrophysical properties. Facies are arguably the most important reservoir heterogeneity. Many geostatistical facies modeling techniques have been proposed during the years of heavily practiced geostatistics in reservoir assessment. Several aspects in current practices, outside the modeling technique itself, induce potential deficiencies in the representation of facies.

This thesis develops novel tools, techniques, and understanding that support geostatistical literature and improve reservoir modeling practice. Notable features of this thesis are (1) addressing information loss in facies upscaling process through a proposed measure which captures variability on non-major facies; (2) proposing a novel inverse modeling approach to estimate shale continuity in the form of a probability distribution function; (3) introducing stochastic regridding to correct the conventional approach of nearest neighbor assignment; (4) investigating the construction of high resolution models in MPS aspect; (5) enforcing the connectivity of disparate facies units such as levees by proposing an effective sequence of dilation-erosion approach while preserving the global proportions; and finally (6) proposing multiscale ranking that optimizes the selected realization performance over different recovery settings, and introducing realization clustering as an alternative to ranking when more than one factor is representative of the reservoir performance.

To the light of my life
my mom, Mitra...

Acknowledgements

My sincere gratitude goes to my supervisor, Professor Clayton Deutsch, for his guidance and extensive experience throughout this journey; without his mentorship, this thesis would have not been possible. Clayton's way of placing his students always just a little beyond our comfort zones has helped us mature in his CCG Group, both technically and professionally.

I would like to thank my colleagues and friends: Miguel, Diogo, Daniel, Flipe and Yevgeniy, for their time spent with me on geostatistical discussions and random chats, and for their sense of humor in passing through long working hours.

I am deeply grateful to my very good friend Tony, whose positive outlook always reminds me to stay energetic and hopeful during times of failure and frustration. I am also thankful to have my best friend in Edmonton, Maedeh R., whose beautiful spirit and wonderful personality have always made me feel happy and blessed. Our long time of running and working out together has always renewed my energy and helped me through the various challenges. My other friends, Mehdi K., Mahdi R. and Nima Y., have positively influenced my doctoral journey in one way or another. I would also like to thank my friend, Farzaneh M., for sharing her PhD experience with me.

I am deeply indebted to the unconditional love, support, and patience of my family: my beautiful mom Mitra, my brother Babak, my sisters Ajand and Parmida, and my brother-in-law Jeff. The company of Parmida and Jeff, the summer visits of my mother, and especially our nights of wings and kebabs have made my doctoral experience so much more joyful. Finally, I would like to mention Mahsa, my longest and everlasting friend, who is the loveliest person I have ever known.

Table of Contents

List of Figures

List of Tables

List of Abbreviations

Abbrv.	Definition	First Use
NTG	Net to gross	3
SAGD	Steam assisted gravity drainage	3
CSOR	Cumulative steam-oil ratio	4
3-D	Three dimensional	6
IHS	Inclined Heterolithic Stratification	9
SIS	Sequential indicator simulation	11
MPS	Multiple-point simulation	11
FMM	Facies mixing measure	19
SIHS	Sandy IHS	23
MIHS	Muddy IHS	23
Kh	Horizontal permeability	33
Kv	Vertical permeability	33
Keff	Effective permeability	33
MSE	Mean squared error	36
H:V	Horizontal to vertical anisotropy	47
CHV	Connected hydrocarbon volume	48
TSC	Total shale connectivity	50
cdf	Cumulative distribution function	57
SGS	Sequential Gaussian simulation	76
FOP	Frequency of patterns	90

Chapter 1

Introduction

The application of geostatistics to characterize petroleum reservoirs dates back to the pioneering work of Matheron (1962). Geostatistics constructs high resolution 3-D numerical geologic models of facies, porosity, permeability and other petrophysical properties to provide an understanding of the reservoir. Constructing such models is a challenging task due to complex geologic heterogeneity present in most reservoirs. Despite this heterogeneity, each reservoir is a deterministic phenomena; for the "true" distribution to be known, however, every single part of the reservoir should be examined (Haldorsen et al., 1988).

In any reservoir study, uncertainty exists due to limited sampling (Kupfersberger et al., 1998). The amount of data that can be practically collected from the reservoir is small relative to its size. The wells are widely spaced and represent the reservoir with a very small volume. The lack of data combined with geologic variability at different length scales and different degrees of precision (Deutsch and Hewett, 1996) lead to a partial understanding of the spatial distribution and a significant level of uncertainty in reservoir estimation. Thus, geostatistics utilizes stochastic techniques to quantify uncertainty. Stochastic simulation was developed and popularized in reservoir modeling because of its ability to characterize the heterogeneity and improve uncertainty assessment (Haldorsen et al., 1988; Haldorsen and Damsleth, 1990). This dates back to Matheron's prominent work on regionalized variables (Matheron, 1962, 1971). The Stochastic (probabilistic) approach aims at bridging the gap between sampled data and unsampled locations.

Accounting for uncertainty differentiates the probabilistic method from the conventional deterministic approach where only one numerical geologic model is used to represent the reservoir (Haldorsen and Damsleth, 1990; Hatløy, 1995; Srivastava,

1994). The importance of generating multiple realizations goes back to the underlying uncertainty and the fact that there exists many possible spatial distribution of reservoir properties that reproduce the data while leading to different reservoir responses (Srivastava, 1994; Deutsch and Srinivasan, 1996). The concept of generating stochastic realizations that permits transferring geological uncertainty through recovery performance predictions is well established (Haldorsen et al., 1988; Isaaks and Srivastava, 1988; Journel, 1989; Haldorsen and Damsleth, 1990; Journel and Alabert, 1990; Englund, 1993; Rossi et al., 1993).

The fundamentals of stochastic simulation within the random function framework can be found in excellent references including Journel and Huijbregts (1978); Luster (1985); Isaaks and Srivastava (1988); Isaaks (1990); Goovaerts (1997); Deutsch et al. (2002); Pyrcz and Deutsch (2014). Rossi et al. (1993) analogize the stochastic simulation to a jigsaw puzzle for which (i) the true/complete picture is not available; (ii) all pieces of the puzzle have the same shapes and sizes; and (iii) the number of pieces is theoretically infinity. The only known thing is the position of some of the pieces of the puzzle. Assuming that the known pieces can actually represent the final image, they permit inference of some characteristics, such as univariate statistics, or the greater likelihood for some specific pieces to be part of the final image.

Stochastic numerical geostatistical realizations are considered in the evaluation of resources and most importantly to study flow performances (Aziz, 1993). Understanding flow characteristics and properties around the wells is critical in decision making at different stages of petroleum exploration and production (Hove et al., 1992; Deutsch et al., 2002). These numerical models support a variety of decisions including the number and location of exploration wells, development sequencing, comparing production alternatives and profitability/investment assessment in general (Rose, 1987; Salomão and Grell, 2001). Decisions are often supported by processing multiple realizations through a flow simulator with the anticipated development strategy (Aziz and Settari, 1979; Deutsch et al., 2002). The uncertainty in flow performance which is characterized by different responses of multiple realizations (Deutsch et al., 2002) is considered in reservoir management by making decisions optimized over a set of choices. A comprehensive study of optimal decision making with reservoir uncertainty is available in Alshehri (2010).

The next section provides some background mainly on challenges specific to hor-

izontal wells recovery in heavy oil unconventional reservoirs. Although the following discussion is found to be the most relevant, the approaches and techniques addressed in this thesis are not limited to any specific reservoir type or geostatistical workflow.

1.1 Background

A large amount of heavy oil deposits have been discovered in Canada, Venezuela, California, and the North Slope of Alaska (Burton et al., 2005; Le Ravalec et al., 2009b). Bitumen is a low value product, and therefore its recovery in commercial operations requires the implementation of efficient processes (Edmunds, 1993). The main difference between bitumen and conventional oil is the mobility of the hydrocarbon. Conventional recovery techniques are not applicable to bitumen because of high viscosity. The McMurray Formation includes one of the biggest oil sands deposits in Western Canada, estimated to be about 170 billion barrels of oil (Labrecque et al., 2011). The McMurray consists of fluvial, estuarine and shoreface deposits with remnant shales and other geologic structures. The bitumen with high recovery potential is mainly located in thick high net to gross (NTG) ratio intervals (Ranger and Gingras, 2006). The minable area of Fort McMurray is at its north, along the Athabasca river valley (Wightman and Pemberton, 1997).

A significant number of oil sands deposits are deep underground so that surface mining methods would not be applicable for extracting oil (ERCB, 2013). Oil sands recovery techniques are developed so that bitumen movement is achieved through different means. As temperature has an extremely strong influence on bitumen viscosity (with the latter decreasing exponentially with the former), increasing the reservoir temperature is the principal means of recovering bitumen from the oil sands (Butler, 1991). The basis of most *in situ* oil sands recovery techniques is to achieve heating of the bitumen in the reservoir. Numerous technically and commercially successful production techniques have been developed during the past decades. These *in situ* techniques often utilize steam injection processes through vertical or horizontal wells such as Cyclic Steam Stimulation, Steam Drive (SD), Steam Stimulation, Pressure Cyclic Steam Drive, Horizontal Alternate Steam Drive and Steam Assisted Gravity Drainage (SAGD), amongst others (Wong et al., 1994; Hongfu et al., 2002; Butler and Yee, 2002).

SAGD is perhaps the most important recovery mechanism which is known to be cost effective for reservoirs containing immobile bitumen (Nzekwu, 1997). SAGD

was first introduced for bitumen recovery by Butler and his former colleagues at Imperial Oil in the late 1970s (Butler et al., 1981; Butler and Stephens, 1981). The success of SAGD was demonstrated at the Underground Test Facility (UTF) with Alberta oil sands (Edmunds et al., 1994; Komery et al., 1995). SAGD outperforms most *in situ* bitumen recovery techniques in terms of per-well production rates, reservoir recovery and lower steam-oil-ratio (SOR) (ERCB, 2013).

One main feature of the SAGD is the utilization of horizontal wells for increased contact with the reservoir; it involves drilling two parallel horizontal wells at the bottom of a thick sandstone reservoir: A production well and a steam injection well located 5 to 10 m above it (Butler, 1991, 1998). The idea is to heat the reservoir using the latent energy of injected steam until the viscosity of the bitumen decreases significantly and heavy oil is drained by gravity towards the production well. Steam, coming from the steam injection well, forms a vapor phase chamber that grows first vertically to the top of the reservoir and then laterally. The heated bitumen is captured and recovered by the production well as it drains downward due to gravity. However, the main mechanism in SAGD recovery is the steam chamber formation which must grow upwards in the reservoir.

Establishing communication between the production and injection well pairs is essential to SAGD initialization (Yang and Butler, 1992). It is important that steam breakthrough in one portion of the well does not unduly upset the pressure profile along the well. Steam trap control should be maintained and the steam chamber must spread uniformly along the well pair. The pressure difference should stay constant all along the horizontal wells. A non-uniform pressure difference would result in a non-uniform steam chamber at the top of the injector, which in turn may cause uneven bitumen flow in the production well. The injection rate must be controlled so that a rise in steam pressure does not lead to the loss of steam from the zone and distortion of the steam chamber.

Focusing on SAGD (currently the main practice in oilsand recovery in northern Alberta), two issues regarding horizontal well performance arise (1) the reservoir heterogeneity around the well pairs, and (2) the model resolution required for flow simulation forecasting. The first issue will be considered with respect to the small shales that could form local barriers that impede flow and the second issue will be discussed with regards to the appropriate model scale for flow forecasting.

1.1.1 Horizontal Wells and Stochastic Shales

Horizontal wells have proved to often be a better alternative than vertical wells in terms of enhancing oil recovery, economics, and production development for recovery of hydrocarbon reservoirs (Lien et al., 1992). It is also understood that shale barriers may significantly reduce horizontal well performance (Yang and Butler, 1992; Belgrave and Bora, 1996; Chen et al., 2008; Jimenez, 2008). The performance of horizontal wells decreases mainly due to the increase in tortuosity of flow paths (Belgrave and Bora, 1996); the impermeable flow units destabilize the rise of the steam chamber and have significant effects on well productivity, Cumulative Steam-Oil Ratio (CSOR) and oil recovery (Pooladi-Darvish and Mattar, 2002; Le Ravalec et al., 2009a).

The impact of shales is twofold. Firstly, shales are often saturated with water characterized by large specific heat. Consequently, some steam or extra heat is absorbed by the residual water inside the unproductive shale layers. The second and more important negative effect of shale layers is caused by the flow resistance of shales. For this reason, the characterization of thin shales is even more critical to SAGD recovery where its performance highly depends on the vertical permeability around the horizontal well pairs.

The effect of vertical permeability barriers have been accounted for in recovery evaluation through analytical or simulation approaches (Lien et al., 1992; Belgrave and Bora, 1996). In analytical studies of Giger et al. (1984); Joshi (1988), for example, the horizontal to vertical production rate is shown to be directly proportional to the vertical to horizontal permeability ratio. Or, Begg and Chang (1985) account for the shale barriers in the simulation by considering reduction in the vertical permeability. Lien et al. (1992) refers to Begg's techniques as an implicit characterization of impermeable barriers and compare its performance with Haldorsen's proposed technique in which the shale characterization is applied explicitly in simulations (Haldorsen, 1989). The latter shows a better match with the theoretical approach of Joshi (1988).

From a different perspective, shales as flow barriers are typically distributed with random geometric configurations. High resolution models in the region of recovery would be required to characterize the heterogeneity and capture the physics of the flow.

1.1.2 Horizontal Wells and High Resolution Models

Haldorsen and Damsleth (1993) discussed the challenges in reservoir modeling, arguing that if everything about a reservoir were known—including the architecture and properties, then what remained would be to (1) impose a sufficiently fine grid network to characterize the flow interactions, recovery process, and heterogeneities; and (2) optimize over many possibilities of reservoir distributions to select the optimal number of wells and their positions which requires extensive computational capacities. Despite the immense improvements in computational technology since more than twenty years ago when the paper was published, those challenges are yet to be met: The construction of geostatistical models are still constrained to grid cells or nodes of relatively coarse size to compromise between covering relatively large volumes of reservoir (physical) and the computational capacity.

Necessity to generate detailed models is especially prevailing to the SAGD scheme where the effect of small scale heterogeneity around the wells could be substantial. The most attractive approach that has been advocated and practiced so far is to construct the high spatial resolution models restricted to the area of interest conditioned to the initially generated coarse resolution model. This process is often known as model refinement or regridding since it is built on previously constructed models of coarse resolution and could consider a different grid alignment than the initial one. The initial model refers to a simulated 3-D model that is built at a unified intermediate scale.

The most prominent work on the generation of high resolution models from the coarse resolution ones is in global climate modeling (GCM). The developed techniques in climate forecasting provide models for regional domains with coarse grid cells of hundreds of kilometers (Jha et al., 2013) whereas the so called downscaled models are implemented to provide the local weather forecasting. The coarse resolution regional model is not capable of capturing variability in local areas. The downscaling methods are developed to capture small scale variability through integration of coarse resolution models and several local data sources that are not considered in simulating global models. Empirical techniques are then utilized to extrapolate spatial continuity to much higher resolution. Reference to large or small scale in GCM application mostly implies the model covering global or local regions.

The need for more detailed models is also considered in different fields at which

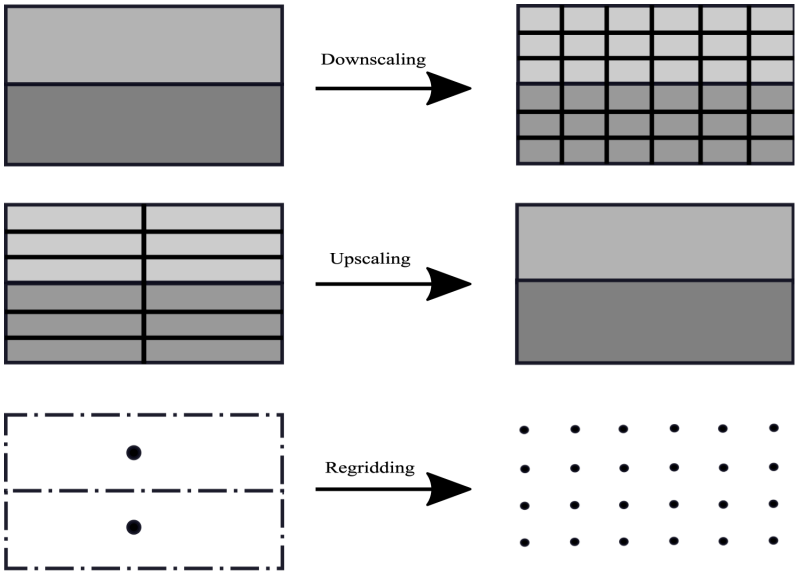

Figure 1.1: Illustration of downscaling, upscaling and regridding concepts. The sketch at the top depicts the downscaling concept. The one in the middle illustrates upscaling and the last one illustrates regridding in cell-based geostatistical simulation techniques. In the downscaling, the coarse scale grid cell (big rectangle) is divided into 18 small scale cells (small squares) painted the same color which could be considered as nearest neighbor approach. The upscaling is opposite: The 6 small scale rectangles are averaged to one big rectangle. In the regridding, one centroid is now represented by 12 centroids that are spaced regularly from each other.

the analysis are based on higher resolution images (i.e. super-resolution images) than the ones initially provided. In geostatistics, Hosseini et al. (2008) established an approach to characterize the uncertainty at small scale utilizing high resolution core photos. The high resolution core photos provide information at the scale of millimeters; the short scale variability is inferred from the resolution of the core photos. Statistical tools would then be deployed to extrapolate from data on coarse resolution models to fine resolution ones (Deutsch and Hewett, 1996; McLennan, 2005; McLennan and Deutsch, 2005a; Ren and Deutsch, 2005). In such techniques as well as those in GCM, one important element is the utilization of local data to extrapolate new information at the higher resolution. The problem addressed here is to generate high resolution models from coarse resolution ones with no access to small scale data. Thus, the high resolution model is constructed by regridding not downscaling.

It is important to note that the variable is defined at the grid nodes (centre of the grid cell) and not for the entire rectangular grid cell as shown in Figure 1.1. All proposed geostatistical frameworks in this thesis are presented and built on the Cartesian grid system. The properties are assigned to the centre point, but for

visualization and some numerical calculations, it is assumed that the grid node value defines the entire the entire grid cell. As can be observed in Figure 1.1, the upscaling is unique: The result of averaging is only one value. However, many different sets of small scale cell values could average into the value representing the coarse scale value. That is why going from coarser scale to finer scale is challenging and non-unique. The simple solution of assigning all small scale grid cells as coarse scale grid cell is practiced which does not accurately reflect the small scale heterogeneity. The same is true with the regridding sketched here. Defining data on the new grid points is challenging, especially when no reference regarding data at that resolution is available (i.e. regridding of geostatistical coarse scale models).

More Aspects

Thus far, the importance of improving facies representation is discussed through characterization of the shales and model regridding. The evaluation of reservoir connectivity, or more importantly, inter-well connectivity, is another important aspect which benefits largely from improvements in facies representation. Connectivities evaluated from 3-D models are not always representative, particularly if the stochastic simulation generates excessive broken or disconnected facies events inconsistent with the true geologic connectivity. The interest reader can consult recent studies of Li et al. (2009); Kaviani and Jensen (2010); Kaviani and Valkó (2010) for quantification of inter-well connectivity. In addition to the importance of correct assessment of connectivity, proper selection of realizations is also crucial for accurate performance forecasting. For clarity, the relevant literature on reservoir connectivity and realization selection will be left out at this point; it is more concise to discuss them in subsequent chapters where appropriate.

1.1.3 McMurray Formation

McMurray Formation is the host to the major Athabasca oilsands resources which is probably the single largest accumulation of hydrocarbons in the world (Demaison, 1977)—containing about 900 billion barrels of oil (Wightman and Pemberton, 1997). McMurray Formation was deposited in a north-south trending depression of Devonian limestone along the Athabasca River (Flach and Mossop, 1985). It rests directly on the Devonian evaporates and carbonates creating a sharp contact or unconformity. The three members of lower, middle and upper categorizes the

McMurray Formation informally (Carrigy, 1959), despite the fact that the fossil trace does not exactly support this generalization (Ranger et al., 2008). The overall changes in characteristics of the lithology from base to top of the formation—from fluvial to marine zone—support the division of the formation to three informal members. However, the Middle and Upper McMurray could also be regarded as one stratigraphic unit as proposed by Hein et al. (2000), since they have experienced the same depositional environments (Flach, 1984; Flach and Mossop, 1985; Wightman and Pemberton, 1997). The Lower McMurray (previously called Basal McMurray) units, in turn, are lithologically distinct and have different biostratigraphic ages (Hein et al., 2000).

The various depositional environments that results in heterogeneous geological features and rapid and abrupt changes of facies laterally and vertically, has made Athabasca lower Cretaceous sediments one of the most complex depositional system in Western Canada Basin (Ranger, 1994). It is mainly believed that the lower McMurray (Daphne Member) is dominated by fluvial origin, the middle McMurray (Steepbank Member) has estuarine origin, and the upper McMurray (Chard Member) includes marine environment. The thickness of McMurray Formation changes upto 110 m (Ranger and Gingras, 2003). The lower member of McMurray Formation found to be below 60 m, the middle member from 20 to 60 m, and upper member from above 20 m (Flach and Mossop, 1985).

The Middle McMurray contains stacked estuarine channel sands of 25—45 m thick known as large scale cross-stratified sand that are mainly put together with only bitumen. Cross-stratified sand bed sets have thickness of 0.5 m or more with strong tidal signatures (Ranger and Gingras, 2003). The petrophysical property of this part of deposit is exceptionally high with 33% to 35% porosity and 2—5 D permeability values (Cody et al., 2001). The thick reservoir sand interval in the Middle McMurray is overlain by sand to mud dominated Inclined Heterolithic Stratification, or IHS. The term IHS was first introduced by Thomas et al. (1987) to link the internal architecture description as opposed to the original term of *epsilon-cross-stratification* which communicates genetic bias. IHS describes three main characteristics of IHS set regarding: depositional dip, lithologically heterogeneous composition, and wide variety of thicknesses.

The main mechanism responsible for the formation of inclined strata sets is point bar lateral accretion within (20—45 m) meandering channel as also been recognized

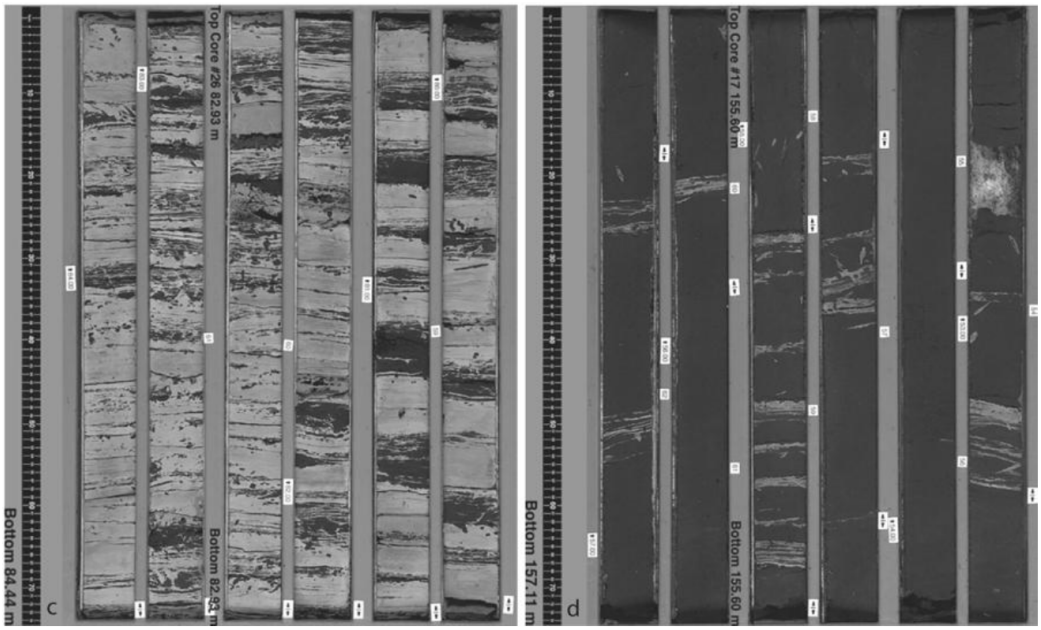

Figure 1.2: IHS core samples of McMurray Formation (taken from Lettley and Pemberton (2004)). The core sample on the left represents a muddy dominated IHS and the one on the right represents sandy dominated IHS.

in McMurray Formation (Mossop and Flach, 1983; Thomas et al., 1987). In fact, the dip direction of point bar IHS sequences is mainly angled to the direction of predominant flow (Thomas et al., 1987). In terms of McMurray Formation, the original dip of IHS sets varies within a range of 4 to 22° as originally reported by Mossop and Flach (1983). Upper McMurray Formation includes horizontal beds of sands and silts that are laid in sharp contrast to the IHS sequences of Middle McMurray (Ranger and Gingras, 2003).

The distribution and geometry of large-scale sandstone/mudstone IHS couplets in Lower Cretaceous McMurray Formation is believed to be responsible for the control over the oil migration pathways during genesis of Athabasca oilsands (Mossop and Flach, 1983). IHS can be lithologically classified into homogeneous "homolithic" or heterogeneous "heterolithic" units. As can be observed in Figure 1.2, IHS typically consists of interbedded sand and mud in varying amount. The feature of IHS in this deposit varies largely from containing mainly sand to being shale dominated. The lateral continuity of low permeability IHS beds depend on the presence/absence of erosional surfaces, and the size of the channels (Fustic et al., 2011).

The clean sand deposit which is free of IHS is the main target to SAGD and similarly, the sand dominated IHS deposit could be of recovery potential. The

mud dominated IHS with extensive lateral continuity could become problematic to the rise of SAGD steam chamber, or the heated oil flow. Mud dominated IHS (IHS silestone) from McMurray Formation are too thin to be identified by seismic imagining. They also cannot be correlated using delineation wells (Fustic, 2007). Thus, their characterization for reservoir modeling purposes are quite challenging.

Throughout the examples in this thesis, sand dominated IHS and mud dominated IHS are used frequently, either to represent permeable or impermeable facies, or to indicate reservoir or non-reservoir domain. Where appropriate the porosity and permeability values are considered distinctively for each one of these facies from sand the most permeable to shale the least permeable.

1.1.4 Facies and Facies Modeling

In reservoir studies, facies are the most important variable to define distinct reservoir quality. The variations in petrophysical properties, including porosity and permeability, within each facies is not as important as it is between the facies. Thus, facies in geostatistical reservoir modeling are considered as the foundation to support modeling other variables. Pyrcz (2004) defines a facies model as a generalized model that captures the essence of the depositional setting, lithofacies and architectures. The importance of facies modeling as a basis of geostatistical analysis, and the subsequent flow modeling, is well appreciated in reservoir management (Eidsvik, 2015; Pyrcz and Deutsch, 2014).

The meaning of facies has gone through changes in the past few decades. Today, facies are widely used and understood in their original context that was introduced by Glossy in 1838 (Cross and Homewood, 1997). The concept of facies, in the form used today, and its evolution is well documented by Dunbar and Rodgers (1957). According to Walker (1984), *facies* refers to rock units within stratigraphic layers that are separated by a sharp contact. The measurement within each unit is different from those above and below it. In early days, the classification was mostly descriptive. Thanks to the growth of sedimentary knowledge and increase in understanding of processes and environment, the term facies has also been used in a more genetic form, considering a body of rock through its formation. Reading (2001) provides a comprehensive description of the evolution of facies terminology and facies modeling. The key is to consider a limited number of categories with specific sedimentary or diagenetic properties that differentiates different geologic

units (Mikes and Geel, 2006); they are homogeneous units in which the relevant attributes are expected to behave similarly.

Despite different ways to define facies, and different factors to distinguish among them, facies in this thesis refer to categorical variables that define rock with distinct reservoir quality (Pyrcz and Deutsch, 2014). There has been much research devoted to improve facies representation and facies modeling in reservoir assessment due to the impact on all the subsequent modeling processes and reservoir evaluations. The information on facies modeling methods that follows is largely taken from the second edition of Geostatistical Reservoir Modeling by Pyrcz and Deutsch (2014). According to the facies discussion in this boos, the facies modeling techniques can be categorized into (i) variogram-based models; (ii) multiple-point-based models; (iii) object-based models; and (iv) process mimicking models. Among these, variogram-based models have popularity among practitioners because of their ability to reproduce local data, gain the required input statistics from well data (variograms), and construct reasonable geological variability (since relevant user-friendly tools are available) especially when no clear geometry is detectable from the reservoir. The variogram-based models include sequential indicator simulations (SIS), and truncated Gaussian simulation (TGS) techniques (Emery, 2007; Armstrong et al., 2003; Matheron et al., 1987). These technique are mostly appropriate when characterizing the geological features in the reservoir using two-point statistics is reasonable.

Multiple-point simulation (MPS) is mostly utilized when variogram-based simulation techniques are deemed inadequate to reproduce complex (geometrically structured) geological features. The MPS technique was introduced by Guardiano and Srivastava (1993) and developed for practical purposes by Strebelle (2000a). In MPS, statistical input regarding spatial heterogeneity of the reservoir is inferred from a training image that is a rasterized depiction of features that are expected in the geological model (Boisvert et al., 2007; Lyster, 2009; Boucher, 2009). The availability of a training image enables the inference of multi-point statistics as opposed to two-point statistics of variograms. That is why MPS techniques are especially appealing when the reservoir has nonlinear and complex features. The recent advancement in MPS is mostly directed towards handling nonstationarity in the reservoir modeling process (Chugunova and Hu, 2008; Straubhaar et al., 2010). Similar to variogram-based models, MPS are built on grid cells (cell-based models) and their implementation is sequential.

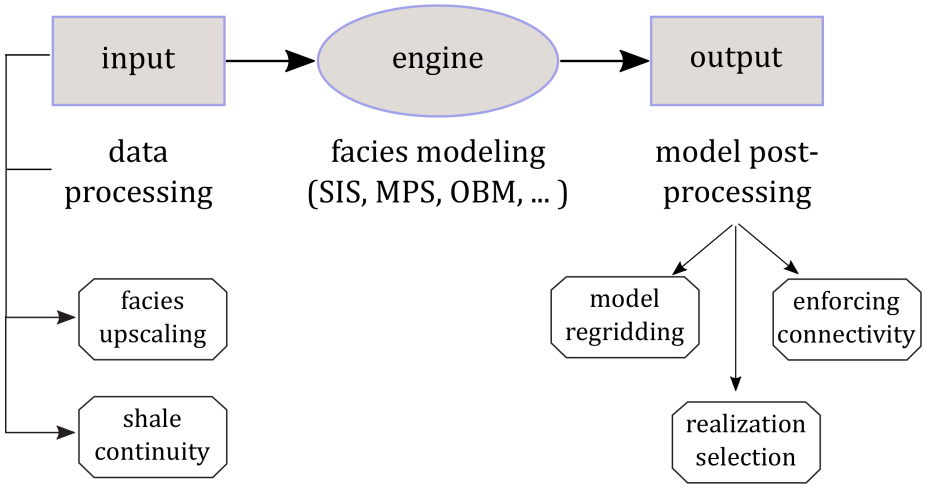

Figure 1.3: Demonstration of facies modeling techniques as the engine of facies characterization framework, in which the input are data prepared using pre-processing techniques, and the output are 3-D facies realizations that most probably need to go through post-processing techniques to get prepared to be considered in reservoir management. The aim of this thesis is to improve facies representation not through the engine, but through the side operations that their importance is often overlooked in geostatistical practices.

The main shortcoming of cell-based facies methods is the generation of unrealistic short scale variations (noise) that is undesired. This noise is partially controlled by image-cleaning techniques adopted as post-processing techniques. This is not an issue with object-based facies modeling technique. Object-based modeling is considered when there are distinctive geological units in the reservoir that can be characterized with geometric parametrization. In those reservoirs, the heterogeneity is only characterized when the reservoir elements are distinctively generated and placed all over the model. For example, fluvial reservoirs contains objects of channel, levee, splay that could only be modeled through hieratically object-based modeling. In fact, the desire to model the fluvial reservoirs in the Norwegian North Sea established the use of objects-based methods in reservoir modeling (Tyler et al., 1992; Clemensten et al., 1990; Stanley et al., 1990).

Process-mimicking facies modeling has been developed recently with the hope to integrate more geological concepts into geostatistical models. This technique is similar to object-based modeling technique, but is not widely-used due to difficulty in conditioning to well and seismic data especially if dense data are available. One example of its application is the Deepwater reservoir as implemented in Pyrcz et al. (2012).

If the central geostatistical framework could be reduced into three pieces shown

in Figure 1.3, the focus of this thesis is on the input and the output that will be discussed further in the next section.

1.2 Problem Setting

The main goal of this thesis is to improve facies representation in geostatistical practice. Note that facies representation differs from assigning the appropriate facies to the grid cells which is achieved by facies modeling. The aim of facies representation is to associate more information and/or geological realism to the facies model so that improved reservoir management decisions are ultimately made. Other than facies modeling techniques (the engine of this process), the input (pre-processing) and output (post-processing) of the system significantly contribute in the ultimate facies representation of the reservoir: There are several techniques available to prepare data for the modeling process, and several others to deal with the model after its construction. Their importance in the final outcome, however, has not been properly acknowledged: Many techniques are still practiced, despite their notable flaws. One aspect of this thesis is to raise selected overlooked issues that either appear prior to facies modeling or after the process, and establish approaches that can improve facies representation in the reservoir model.

This thesis encompasses six problems/techniques related to facies representation. The subjects are ordered according to the sequence of operations in a normal geostatistical workflow. Facies upscaling or blocking, therefore, comes first. Upscaling is an early step in any geostatistical modeling to unify the scales from all data to a target scale that should be considered in building the 3-D numerical models. Well log data comes at high resolution on order of 10 cm scale vertically. The vertical size represented in most geostatistical reservoir models is between 0.25 and 1 m; thus, unifying the data is achieved by pre-processing the well data to the chosen scale for reservoir modeling.

Averaging is considered to represent the upscaled intervals when the variable of interest is continuous; however, averaging cannot be applied to categorical variables such as facies. A reasonable solution to facies upscaling is to assign the upscaled interval with the majority facies. Although the majority could be the most effective facies in the upscaling interval in many cases, there will certainly be information loss. When the reservoir contains four or five main facies, there is always a good probability that the majority facies may have less than 50-60% proportion. De-

pending on how variable the interval is and how different the facies are (in terms of their petrophysical properties), the loss of information regarding non-major facies could be crucial. Although upscaling is a well-established process, the concern regarding loss of information in facies upscaling has hardly received any attention. This thesis identifies facies upscaling as one conventional operation in geostatistical pre-processing workflow and treats it to the level of detail that is appropriate to its importance.

The next challenge addressed is the shale characterization. The importance of shale characterization was discussed above. Only limited knowledge on the continuity of thin shales can be gained from well data. The presence of shales in the region of flow could be problematic; small shales that are laterally extensive can reduce recovery. Although this has sometimes been raised in the literature, it remains an important challenge in practice. Considering realistic lateral continuity of the shales is essential to accurate recovery assessment. Note that the study of this topic is mainly centred around variogram-based facies modeling techniques and is applied independently utilizing only well data.

Another consideration in the mis-representation of the thin remnant shales is the process of discretization and gridding. The facies units that are small relative to the scale of the grid cell are particularly prone to mis-representation. The gridding system and scale chosen to represent numerical models are fundamental elements in a geostatistical study. Selecting the "right" scale is a crucial task; the grid scale is selected accommodating for at least two factors simultaneously (a) sufficiently small to capture the heterogeneity; and (b) possibly large to cover the entire reservoir with the minimum number of grid blocks; the numerical storage and calculations of flow simulations are of computational concern even with the ongoing growth in computing capacity and resources.

Although the grid size is selected based on the purpose of the model, data spacing, variogram determinations, and depositional scale of events, it is largely constrained by computational capacity. This becomes more challenging when realizations are required at higher resolution than initially generated during the geostatistical workflow. One way around this is to limit the high resolution model to the area of interest. A common practice to model regridding is nearest neighbor assignment. The nearest neighbor approach can only replicate the same features to the new grid cells within the coarser grid cells. This is considered as poor practice since

nearest neighbor assignment is not capable of reproducing smaller scale geological heterogeneity and representing a realistic distribution of short scale variability.

The importance of generating high resolution models could also be recognized in appropriate characterization of the remnant shales. The coarse scale models are not adequate to properly characterize the small scale geologic features of the shales (as will be more discussed in Chapter 4; see Figure 4.2). The effect of misrepresentation of small scale features in the reservoir could be demonstrated in the vertical permeability which is a good flow performance metric especially in terms of SAGD recovery.

In terms of MPS, the deficiency of facies representation at smaller scale could also be due to the scale constraint of the training image. Training images should represent the correct scale of variability for the geological features that are being modeled. There are situations where a smaller scale than that of the training image is required. In variogram-based simulation techniques, the two-point statistics could be inferred at any scale smaller than the scale of measured data by extrapolating the variogram to smaller lag distances (see Figure 5.1 in Chapter 5). However, MPS techniques do not have such flexibility as the minimum scale at which the deposit can be modeled is the resolution of the training image. Therefore, to generate realizations at higher spatial resolution than that of the training image, the necessary spatial information could not be inferred directly from the corresponding training image. The investigation of this matter is one of the six main problems addressed in this thesis.

One other subject addressed in this thesis is the failure of simulation technique to preserve the connectivity of geologic units. The primary focus of most variogram-based stochastic simulation techniques is on honoring the small/large scale variability measured by the variogram; details of geologic realism may not be reproduced. The connectivity of net reservoir (mainly sand) is the potential environment for recovery. If different facies are coming in broken intervals rather than being fully distributed in the reservoir, the well placement and recovery evaluation will be faulted. Post-processing the generated realizations to impose the correct continuity could improve the facies representation and subsequent decision making process. Connecting the broken objects could be achieved using methodologies such as those in mathematical morphology.

Lastly, realization selection is often required prior to flow simulation and decision-

making. In practice, geostatistical modeling and post-processing techniques are constrained by computational limitations. The resolution and the number of realizations that can be generated and analyzed are limited. Flow simulation analysis of realizations is computationally expensive; it is intractable to process a large number of realizations in most reservoirs. Realization selection is the step to link the geostatistics to flow simulation process. Ranking selects those realizations that would span the uncertainty over a specific reservoir performance. Ranking could be improved in two aspects (1) consider multiple production volumes in ranking so that the selected realizations represent local regions as well as large scale regions; (2) consider grouping or clustering realizations when choosing arbitrary quantiles is not representative of the character of the realizations, or, more than one feature is required to asses the realizations performances.

Thesis statement: *In addition to facies modeling techniques, several other processes – whether as input or output – contribute to studying facies, which are the main representation of reservoir heterogeneity. This thesis focuses on the development/refinement of facies characterization to improve the probabilistic representation of reservoir heterogeneity.*

1.3 Thesis Outline and Approach

The second chapter addresses the information loss within facies upscaling and proposes a metric to account for the small scale information. The proposed metric associates the expected property (i.e. upscaled average porosity) of every facies to its proportion in the corresponding upscaling interval to quantify its potential influence on the final property of block interval. The deviation from expected property explains the type and amount of mixing. Factors like distance to dissimilar facies and contact are also considered. It is argued that preserving the information on non-major facies and accounting for them in estimation of petrophysical variables could potentially improve subsequent reservoir characterization and forecasting.

The third chapter discusses the importance of identifying and characterizing the stochastic shales in the reservoir, specifically in the region of recovery. A novel method to estimate the lateral continuity of such shales based on an inverse modeling approach is proposed; its framework is established independent of any gridding,

scaling, and/or resolution constraints. The estimation of the probability distribution of shale continuity relies on the data information gained from well pairs, the well spacing, and the overall well configuration in the reservoir. The knowledge of shale lateral extent provides additional information on reservoir connectivity assessment.

The fourth chapter addresses model regridding and proposes stochastic regridding to create appropriate small scale variability. While this chapter mainly discusses the proposed stochastic approach, it also compares it to the commonly practiced deterministic approach of assigning the finer grid cells with the closest coarse grid value. The latter, because of its nature, is unable to reproduce the spatial variability at smaller scale better than what the coarse scale already represents. The proposed methodology extracts the identified areas of interest, characterizes the local variability and simulates models at higher resolution conditioned to the coarse scale simulated model.

The fifth chapter studies the generation of high resolution models in the context of MPS. It discusses the challenges to infer multi-point statistics at smaller scale than that of the training image. As will be demonstrated in this chapter, investigating data interactions for different possible template configurations can be challenging since the number of patterns and within n-point arbitrary configurations increase exponentially. The chapter proposes to enhance the resolution of the training image and infer statistics at smaller scale, directly from the constructed high resolution training images. Interpolation tools and techniques are developed to extrapolate data from larger scale to grid points at smaller scale.

Chapter six raises the issue of realistic connectivity of facies events and proposes a technique based on two mathematical morphology of dilation and erosion, to enforce the realistic continuity on such disconnectivity. Developed methodology considers the disconnected intervals as individual objects and determines an object's maximum and minimum anisotropy for a controlled connecting approach. The proposed algorithm is established considering both 2-D and 3-D models that could be practiced as a post-processing technique. The professional interpretation regarding the unrealistic discontinuity should be made prior to applying the proposed tool.

Chapter seven addresses the limitations and shortcoming of ranking that has not been effectively discussed in literature in two parts (1) multiscale ranking is proposed as one way to improve ranking's limitations. Its idea is driven by the importance of local connectivity for recovery specifically in case of heterogeneous reservoirs.

Multiscale ranking scheme selects realizations considering different well placement and recovery scales, simultaneously; (2) clustering of realizations is considered as an alternative to ranking when a simple ranking process is not adequate. Unlike ranking, clustering uses an array of response variables to partitions realizations into groups that expect to perform similarly at the time of flow simulation.

This thesis closes with the conclusion chapter which summarizes the contributions of this thesis and suggest some research directions for future work. Finally, details on using model stochastic regridding program (Chapter 4) and enforcing connectivity programs (Chapter 5) are provided in Appendix A and B, respectively. These programs are developed in FORTRAN platform in GSLIB-like format.

Chapter 2

Measure of Facies Mixing

In geostatistics, upscaling is the process of increasing the support of information at the wells; going from data resolution to a larger target resolution of the model scale (Lake and Srinivasan, 2004). In facies upscaling, the upscaled interval is typically assigned based on the majority of the facies present in the corresponding interval. The process of assigning the majority facies results in a loss of information on the other facies in the interval (Pyrcz and Deutsch, 2014). This chapter addresses the information loss by retaining as much information as possible in the upscaling process and proposes a metric to account for small scale information that is lost during the process; such a metric is referred to as facies mixing measure (FMM). The first section introduces the problem and motivates the research. The second section introduces the FMM for evaluation of small scale information in facies mixing. The factors considered in this metric are studied in detail. The remainder of the chapter presents a workflow to account for facies mixing during subsequent geologic modeling of continuous variables.

2.1 Introduction

In reservoir modeling, different scales are considered for different purposes of geomodeling such as understanding the distribution of petrophysical properties, the geology of the reservoir and most importantly the flow behavior. The available data is often collected at a small scale e.g., 10 cm, which is not appropriate to be used in the construction of numerical models of the reservoir due to computational constraints (Pyrcz and Deutsch, 2014). The most common practice is to move from the measured data scale to a coarser scale closer to that of the ultimate flow simulation models; this is a process known as upscaling in the application of reservoir studies

(Christie, 1996; Li et al., 1995; Durlofsky et al., 1997; Boschan and Nœtinger, 2012; Durlofsky, 2005). In the upscaling process, the data at small scale are grouped into intervals of intermediate scales, e.g. 0.5 or 1 m, depending on the characteristics of the reservoir. The resulting upscaled intervals are represented with a set of attributes, including facies, porosity (ϕ), volume fraction of shale (Vsh), water saturation (Sw), and other properties of interest.

There are many publications devoted to the problem of upscaling. Many techniques have been developed to better identify the heterogeneity in the upscaling process, such as the ones proposed in Christie and Blunt (2001); Li et al. (1995); Lake and Srinivasan (2004); Durlofsky et al. (1997); Chu et al. (1998); Farmer (2002), amongst others. Most techniques focus on the flow properties such as permeability and the impact of upscaling on their behavior. A comprehensive review of the upscaling techniques which is basically a focus on the mathematical aspects is provided by Farmer (2002). Christie and Blunt (2001) also demonstrate a special comparative SPE project aimed at comparing upscaling methods. What is limited in this collection though, is the number of works that study facies and facies upscaling impact on the reservoir assessment; see for example Mikes and Geel (2006); Burns et al. (2010); Schaaf et al. (2002); Boschan and Nœtinger (2012). Although this chapter is not aimed at developing upscaling methods to examine flow behaviors, the idea of preserving information loss, in the context of facies upscaling, is believed to augment the representation of facies in reservoir modeling.

Regardless of the scale the model is prepared at, it is always advisable to understand the facies distribution in the reservoir: a suitable facies modeling technique should be applied first to obtain the stationary environments, and then properties are modeled within the relevant facies (Hatløy, 1995; Deutsch, 2006; Pyrcz and Deutsch, 2014; Eidsvik, 2015). Thus, this chapter is best described as a promising attempt in facies modeling improvements by retaining the information loss in the upscaling process and utilizing that information to better capture the facies distribution in the reservoir. Note that upscaling in this chapter is 1-D in contrast to the conventional reference to 3-D upscaling from fine scale models to coarser scale models.

2.2 Facies Upscaling

Facies upscaling may be achieved when defining a coarser interval containing multiple small scale intervals by the majority facies. The facies with the highest proportion is considered as the most representative of the corresponding upscaled interval. Upscaling could be thought of as a mixing process. In mixing, the varying quality of different small scale intervals influences the average quality of the entire interval. For instance, the quality of sand often diminishes in proximity to the lower quality facies (e.g. shale) while the quality of shale often increases in proximity to higher quality facies (e.g. sand). In terms of petrophysical properties (continuous variables) such as porosity and Vsh, the upscaled interval is assigned by the arithmetic average of these variables. As a result, the upscaled interval represents a mixture of properties of the high resolution data. When scaling up from the scale of data, the proportions of facies could be considered similar to upscaling of continuous variables. However, assigning facies to the upscaled intervals is far more appealing, as discussed in 1.1.4.

An indicator formalism is commonly adopted for categorical variables modeling, e.g. facies (Goovaerts, 1997). The main reason for indicator utilization is that the estimation of uncertainty can be achieved directly (Journel, 1983). If $\mathbf{u}_\alpha$ denotes a spatial location, and $i(\mathbf{u}_\alpha)$ indicates its corresponding categorical variable where there are K mutually exclusive categories, then:

$$i(\mathbf{u}_\alpha; k) = \begin{cases} 1, & \text{if facies } k \text{ prevails at location } \mathbf{u}_\alpha \\ 0, & \text{otherwise.} \end{cases}$$

Assuming well data consists of N varying lengths of data intervals, l, if upscaled to intervals of length L, containing N_L data, then the amount of facies k at spatial location $\mathbf{u}_{\beta,\alpha}, \alpha = 1, \ldots, N_L$, where β denotes the upscaled spatial location is as follows:

$$p_k(\mathbf{u}_\beta) = \frac{1}{N_L} \sum_{\alpha=1}^{N_L} i(\mathbf{u}_{\alpha,\beta}; k), \quad k = 1, \ldots, K$$

and

$$\sum_{k=1}^{K} p_k(\mathbf{u}_\beta) = 1$$

The spatial location, $\mathbf{u}_\beta$, is identified by the majority facies which is the argument of $\max\{p_k(\mathbf{u}_\beta)\}$. This process of assigning majority facies to the upscaled

interval results in information loss regarding the facies with non-majority proportions. Babak et al. (2013) quantifies the information loss in facies upscaling process by adopting the concept of entropy. Entropy is a well known measure of the information content introduced by Shannon (Shannon, 1948) and has been used accordingly by Babak et al. (2013). The proportions of different facies available in the corresponding upscaled intervals are considered to calculate the information loss as follows:

$$E(\mathbf{u}) = -\sum_{k=1}^{K} p_k(\mathbf{u}) \log p_k(\mathbf{u}) \tag{2.1}$$

in which the value zero for E denotes no information loss, and as E increases, so does the information loss. By convention, the base value of logarithmic term is 2, which refers to the binary variables in information theory where Shannon defined it originally. Similarly the logarithm base of 2 has been considered by Babak et al. (2013) for simplicity.

Entropy is a bounded value between zero, which indicates minimum entropy and no mixing, and a maximum value that varies depending on number of available facies in the upscaled interval. The maximum entropy occurs when there are equal facies proportions of $1/K$ for all facies in the interval. In terms of information, zero entropy indicates 100% certainty in the majority vote (the interval contains 100% of one facies); there is zero information loss regarding other facies. Whereas the maximum entropy indicates 100% uncertainty in the majority vote; no facies stands out to be assigned to the upscaled interval. For example, if the number of facies is five, then the entropy is at its maximum when the upscaling interval consists of all the five facies with an equal amount; the entropy is calculated to be $E_{\max} = -5\times[0.2\times\log(0.2)] = 2.32$. In the upscaling of five facies, any combination of different number of facies with different proportions has an information loss greater than 0 and less than 2.32. The higher the entropy, the more the information loss, that is, more mixing occurs during the upscaling process. The smaller the entropy, the less the uncertainty is. In the context of upscaling, smaller entropy means that the majority facies is strongly dominant within the upscaling interval.

Limitations of Entropy: Conditional Entropy

As shown in (2.1), entropy as a function of facies proportions would help only to identify the mixing intervals and quantify them. For instance, an interval containing

only sand results in the entropy value of 0 (= log(1)), and an interval containing only shale has also a zero entropy. However, apart from quantifying the amount of information loss, it is also important to retain information regarding the actual facies mixed which is a factor in the quality of upscaled interval. In the context of facies upscaling however, entropy fails to identify (1) what are the facies in the upscaling interval; and (2) what are the corresponding proportions.

Considering the two cases shown in Figure 2.1, sand as the majority facies occupies 40% of the interval, and the other 60% is filled with two other facies with equal proportions. Measuring entropy to be 1.571 for both cases, the interval on the left contains facies similar to the sand in terms of petrophysical properties, i.e., sandy IHS (SIHS), whereas the interval on the right contains facies somewhat different from the sand, i.e., mudstone (see subsection 1.1.3). This results in different properties of the two upscaled intervals which is not reflected on the entropy value. Note that throughout this thesis, five common facies in the McMurray formation, including, sand, breccia, sandy IHS (SIHS), muddy IHS (MIHS) and mudstone (with average porosities of 0.32, 0.25, 0.24, 0.16 and 0.05, respectively) are considered in different examples. IHS facies are common in the upper part of the McMurray Formation.

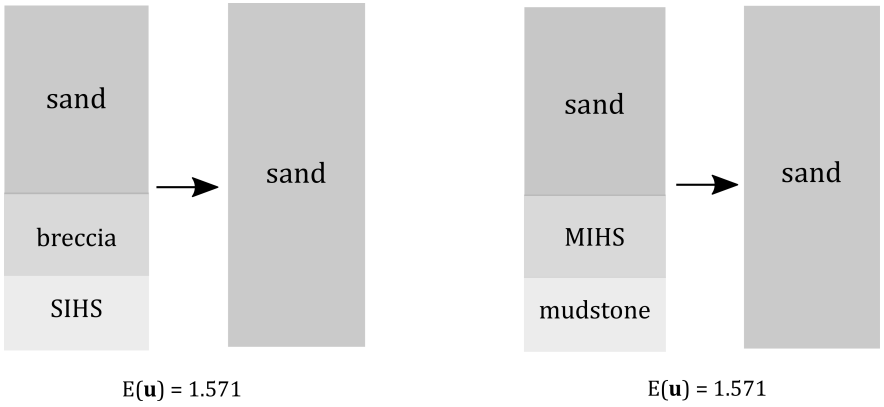

Figure 2.1: Illustration of the deficiency of entropy in identifying different mixing in the upscaling interval. The interval on the left hand side contains three facies of sand, breccia and SIHS with proportions of 40%, 30%, and 30%, respectively. The right interval, on the other hand, contains MIHS and mudstone instead of breccia and SIHS. In terms of petrophysical properties, the non-major facies in the left-hand side intervals are more similar to the major facies of sand than the ones on the right. Although the same entropy value for both intervals indicate similar mixing, the nature of these two mixing is different when the properties of upscaled interval is under investigation.

Babak et al. (2013) introduced the concept of conditional entropy, E_c, in order to make the entropy value more sensitive to the type of facies that are mixed

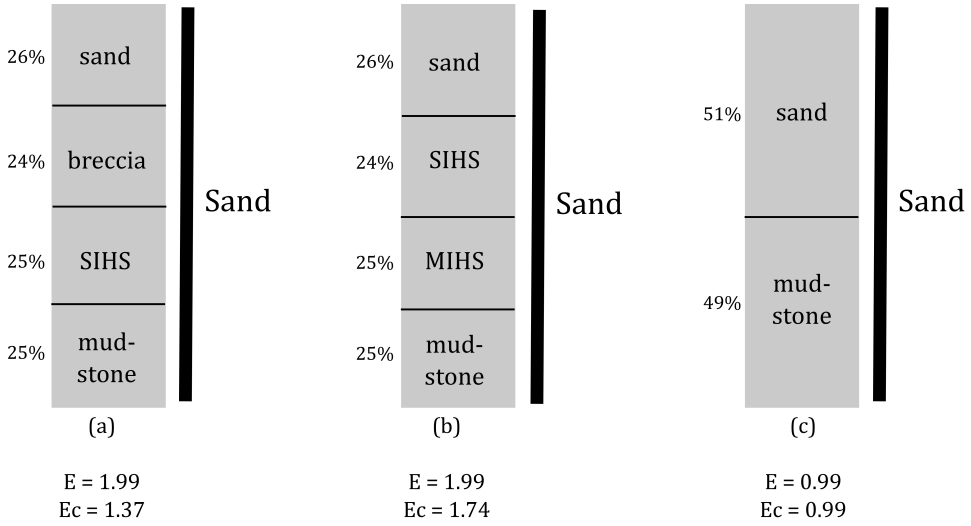

Figure 2.2: Three cases of facies mixing are shown. The similar proportions of different facies result in same entropy values for both cases in (a) and (b) while the type of mixed facies are not exactly similar. The difference in conditional entropy indicates that the mixing in case (a) is less sever.The example in (c) shows that although entropy is much smaller than the other two cases, the upscaled petrophysical property is expected to degrade more. Equal values for entropy and conditional entropy indicate that mixed facies have no similarity.

with the majority facies in the interval. Similarity between the mixed facies in the upscaled interval mitigates the effect of mixed facies on petrophysical attributes of the upscaled intervals. Thus, the similarity is utilized as a decreasing factor in the entropy value which is equivalent to less information loss. The difference between the conditional entropy and the entropy indicates if the mixed facies are similar to the majority facies.

Yet, the conditional entropy cannot describe the mixing in all its aspects. First of all, conditional entropy has no meaning in terms of petrophysical attributes. Second of all, conditional entropy cannot distinguish between the facies. In other words, the same value of entropy and/or conditional entropy could refer to different types of mixing in the interval. For example for the case of 60/40 of sand and shale, the entropy is about 0.97; this value stays the same if shale is the majority. The conditional entropy is also similar in both cases.

Figure 2.2 demonstrates examples of different facies with different forms of mixing. The entropy value for cases (a), and (b) are similar, even though the nature of mixing is different. Assuming the similarity factor of 0.5 between sand and breccia and 0.25 between sand and SIHS result in different conditional entropy values for both cases. The listed measurements show that there is 31% discrepancy between entropy and conditional entropy for case (a). This value is 13% for case (b) and

is zero for case (c). In this example, the conditional entropy helps to differentiate between the nature of mixing: mixing is most destructive for the upscaled interval of case (b), and least destructive for the case of (a). Moreover, the entropy value for case (c) is 0.99 which is about half the entropy for cases (a) and (b). It is however, easy to see that presence of 49% mud within the sand interval results in a more severe mixing in terms of influencing the petrophysical attributes compared to 25% mud in other two cases, while both entropy and conditional entropy are smaller for case (c).

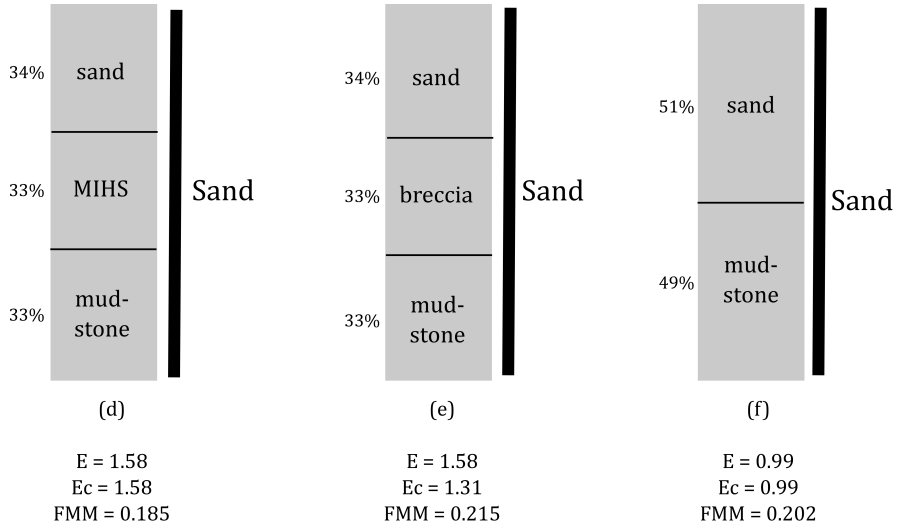

Figure 2.3: This example demonstrates the deficiency of conditional entropy in measuring the specific and direct influence of mixing types. Unlike the conditional entropy, FMM can address the mixing difference.

The next section introduces a new measure of facies mixing based on the discrepancy between the average porosity of the upscaled interval and the effective porosity of the corresponding facies to address the shortcomings of conditional entropy. The effectiveness of the proposed measure—facies mixing measure (FMM)—which will be discussed in detail momentarily, is demonstrated for three cases shown in Figure 2.3, where conditional entropy fails to differentiate between the mixing types. The values of entropy, conditional entropy and FMM are listed for the upscaled intervals. The conditional entropy is equal to the entropy value for cases (d) and (f). Because of the drop in conditional entropy for case (e), it can be inferred that mixing in this case is less severe; the facies are porosity-wise more similar to each other. However, the conditional entropy cannot help to differentiate between the other two cases. FMM is therefore proposed to address such cases; FMM value is

not the same for the three cases in Figure 2.3.

If the upscaled interval should mainly represent the average porosity of the majority facies, then the porosity of the interval should be close to the effective porosity of the majority facies. Considering this logic, the deviation from the effective porosity is an indication of the quality of mixing. For example, if the upscaled interval is assigned sand, and the upscaled porosity is smaller than the effective porosity of the sand in the dataset, say 0.32, it can be concluded that some mixing is involved (entropy is larger than zero). The FMM deviation from the effective porosity of sand is 43% for case (d), 35% for case (e), and 39% for case (f). Therefore, the mixing in case (d) is said the most severe, and case (e) the least severe.

2.3 Facies Mixing Measure

Facies mixing measure (FMM) is designed to quantify the loss of information during the facies upscaling process with respect to the amount and type of facies that are mixed. The FMM considers the details of mixing with special attention to the distance to the nearest dissimilar facies and its type. In a particular geologic setting, each facies, on average, is identified by a certain range of values of a petrophysical property. For example, porosity is typically within 0% to 40% and might be a reasonable measure of reservoir quality. Thus, porosity is selected in this work as the main factor to weigh the facies proportions in quantifying mixing. When mixing occurs, the property of the upscaled interval deviates from the expected property of the corresponding facies. The expected property is the property that a particular facies (in a dataset) behaves on average, and can be obtained by considering the average property of all upscaled intervals of the corresponding pure facies. The mixed upscaled intervals are likely to not behave sufficiently close to its expected property of the major facies. This deviation is normally positive for low quality facies like shale, and negative for high quality facies like sand. The quality of sand degrades when mixed with other facies and the opposite is true for shale.

The proposed measure integrates the expected porosity value of the available facies in the upscaled interval as well as their proportions, and compute FMM which

is a volume-based average measure and it follows:

$$\text{FMM}(\mathbf{u}) \;=\; \underbrace{p_k(\mathbf{u})\;\phi_k(d_{k,k'})}_{\text{major facies}} \;+\; \underbrace{\sum_{k=1}^{K-1} p_k(\mathbf{u})\;\phi_k}_{\text{non-major facies}} \tag{2.2}$$

where k denotes facies and $k^{'}$ refers to the nearest dissimilar facies to the major facies. In the proposed relation, expected porosity value of facies k, ϕ_k, could be persecuted as the weighting factor to the proportion of mixed facies. The average porosity, ϕ, is a function of distance, d, between upscaled facies to the nearest dissimilar facies (see Figure 2.4).

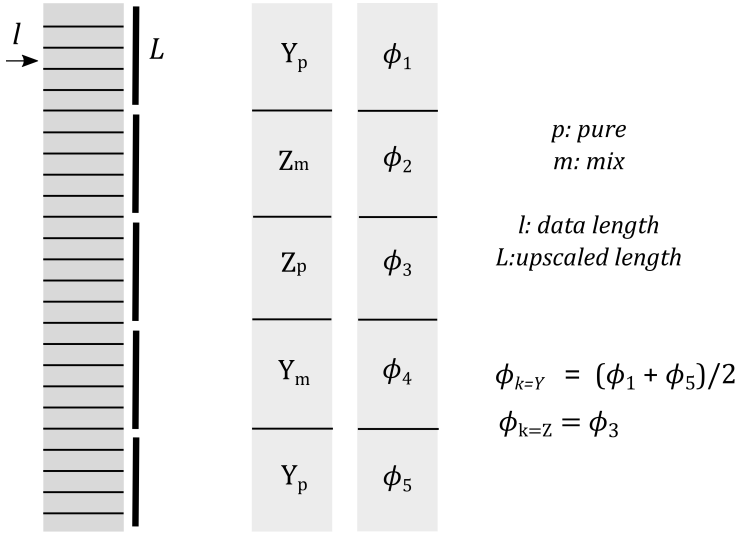

Figure 2.4: An illustration of what average porosity identifies different facies in FMM calculation. The weighting factor of average porosity for every assigned facies associated with the upscaled interval is evaluated from the intervals of pure facies. This is a simplified version FMM evaluation with no regard to the factor of distance.

The upscaled porosity is the arithmetic average of the data scale porosity, $\phi(\mathbf{u}_\beta) = \frac{1}{L}\sum_l \phi_l(\mathbf{u}_\alpha)$ (l refers to the small scale interval) which contains some information regarding the mixing in the upscaled interval. In the limits of 100% of facies k, the FMM value is $\phi_k(d_{k,k'})$ which is the mean porosity value for facies k at a certain distance from dissimilar facies. Therefore, the FMM value for pure upscaled intervals of facies k, is equivalent to the expected porosity. FMM as a measure of facies mixing in upscaling takes all these parameters into account to quantify the facies in relation to its average quality over all the reservoir (see Figure 2.5). A simplified version of (2.2), FMM $= \sum_k p_k\phi_k$, can be utilized when the effect of distance is negligible on the major facies in upscaled interval property. In principle, distance

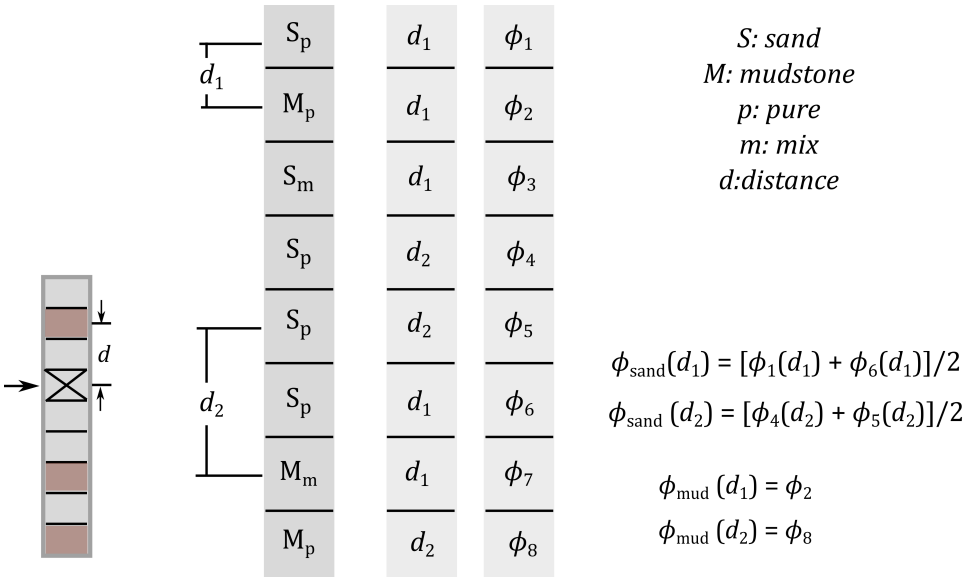

Figure 2.5: An illustration of how distance is integrated in the evaluation of average porosity which is eventually utilized in the calculation of FMM. Two facies of sand and mudstone are illustrated to be in contact within varying distances of 1 and 2 upscaled intervals. The distance therefore, is only considered to one other facies. Four different average porosity values are extracted: average porosity of sand at one-interval distance, average porosity of sand at two-interval distance, average porosity of mudstone at one-interval distance, and average porosity of shale at two-interval distance. Recall that distance is considered from the nearest dissimilar facies.

mainly matters to the facies with extreme petrophysical properties such as sand, in which the proximity to another facies like shale could highly degrade the expected quality of sand interval, or when a particular facies is present in form of large thicknesses, such as the case of IHS in the McMurray Formation in Northern Alberta as discussed in subsection 1.1.3.

As shown in Equation (2.2), the quality of the upscaled intervals not only depends on the amount and type of mixing but also on the distance from other facies and what facies are nearby. The larger the distance between facies, the quality of that interval is closer to the average quality of the corresponding facies (see Figure 2.5). To precisely integrate the property of majority facies into FMM, the expected porosity of majority facies is evaluated with respect to the distance from other facies, and contact to every other facies. This is established by defining the expected porosity for the majority facies, k, as a function of distance d to dissimilar facies, k'. Thus, in a dataset including five facies, four functions are defined to determine the expected porosity of facies, k, when in contact with dissimilar facies at any distance. In other words, the upscaled porosity as a function of distance in

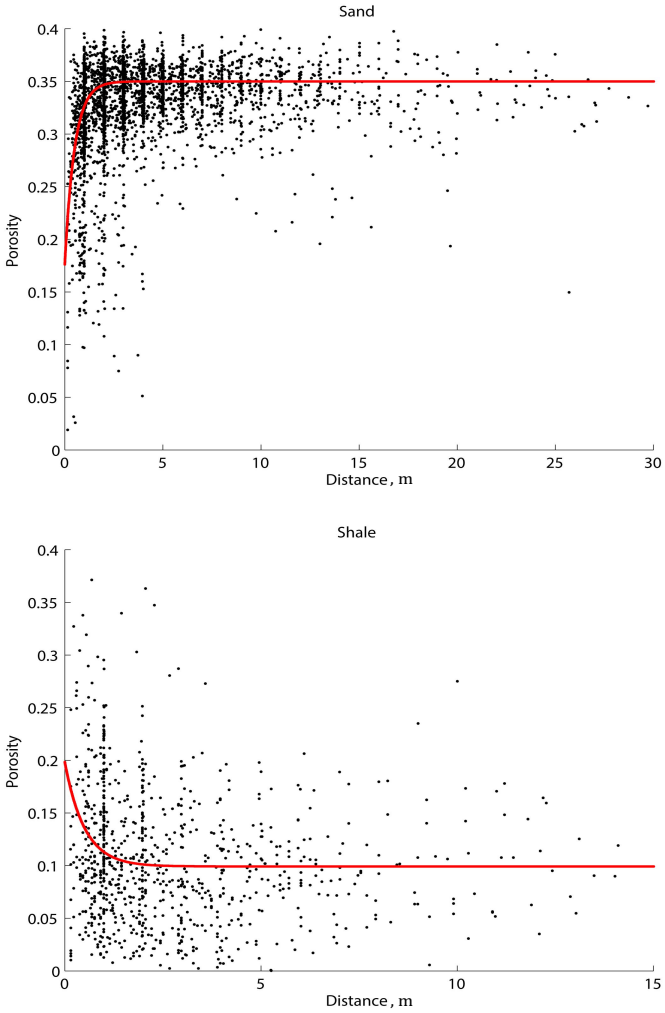

Figure 2.6: The average porosity of upscaled intervals are plotted against the distance for the case of sand (top) and shale (bottom). The quality of an upscaled interval of sand degrades the most in the direct contact with other facies ($d = 0$). It then, increases quickly and stabilizes after a few meters depending on the size of upscaled interval. A growing exponential curve, shown in red, approximates the behavior of the average porosity of sand intervals as a function of distance. The opposite is true for shale. The quality of upscaled shale interval is at its maximum in direct contact with the dissimilar facies. As the distance increases the quality of shale intervals drops quickly to its expected quality. A decaying exponential curve, shown in red, approximates the behavior of the average porosity of shale intervals as a function of distance. Note that as distance increases, the average porosity becomes insensitive to the distance.

proximity to shale is different than that of sand in proximity with SIHS.

In Figure 2.6, the upscaled porosity value for pure intervals of sand as a function of distance to the dissimilar facies of shale is shown in scatterplot at the top. As can be observed from the shape of the distribution, the influence of distance is at its maximum when the sand interval is in direct contact with shale, and the effect of distance diminishes as distance increases. A similar conclusion could be drawn

for the second scatterplot in which the average porosity of shale is at its maximum in direct proximity with sand. The effect of distance reduces as the dissimilar facies is further away. To utilize these distributions into FMM evaluation, curve fitting could be applied. Exponential functions are a good candidate to parameterize the average porosity when distance to dissimilar facies is a factor. As can be observed in Figure 2.6, a decaying exponential function for the case of sand and a growing exponential function for the case of shale can provide a good estimate of the behavior of average porosity of the upscaled intervals of sand and shales. To parameterize the functions, some approximations to the parameters of exponential distribution are proposed. The average porosity of sand as a function of distance can be approximated as follows:

$$\begin{aligned}\phi_{\text{sand}}(d_{\text{sand},k'}) &= g\ (1-\exp(-d_{\text{sand},k'}/a)) + c \\ a &\sim 1/\text{median}(d_{\text{sand},k'}) \\ c &\sim \text{median}(\phi_{\text{sand}}(d_{\text{sand},k'} \sim 0)) \\ g &\sim \text{median}(\phi_{\text{sand}}(d_{\text{sand},k'})) - c\end{aligned}$$

And the following approximation is used to fit the porosity for shale as a function of distance:

$$\begin{aligned}\phi_{\text{shale}}(d_{\text{shale},k'}) &= g\ (1+\exp(-d_{\text{shale},k'}/a)) + c \\ a &\sim 1/\text{median}(d_{\text{shale},k'}) \\ c &\sim \text{median}(\phi_{\text{shale}}(d_{\text{shale},k'} \sim 0)) \\ g &\sim \text{median}(\phi_{\text{shale}}(d_{\text{shale},k'})) - c\end{aligned}$$

The fitting curves in Figure 2.6 are evaluated applying the approximations above. The dissimilar facies, $k^{'}$, is shale for the case of sand at the top and is sand for the case of shale at the bottom.

FMM not only identifies the pure intervals from the mixed ones, but also differentiates between the pure intervals in terms of what facies contains the interval. In case of a pure upscaled interval, the entropy is always zero which says nothing about what facies has filled up the interval. FMM, however, distinguishes the pure interval from the mixed one as well as identifying its facies type. Figure 2.7 represents the FMM value and entropy of upscaled intervals of sand versus their corresponding porosity value. While entropy is 0 for any pure interval which is shown by the blue

horizontal line, FMM is changing between 0.32 and 0.37. The higher the average porosity (shown on the x-axis), the higher the FMM value is (shown on the right y-axis).

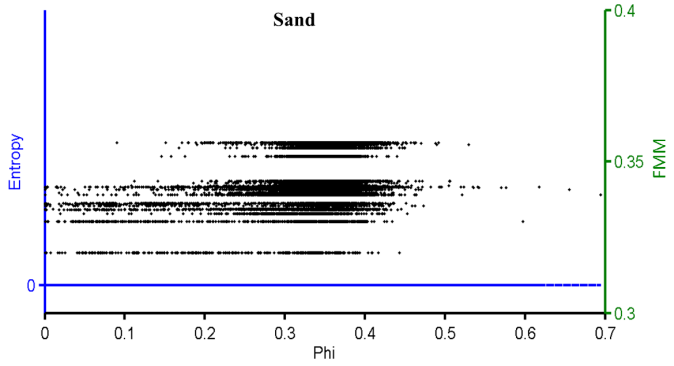

Figure 2.7: For all ranges of porosity representing the upscaled sand interval, the entropy for the pure interval is always zero. The FMM value however differs depending on the distance from the dissimilar facies.

Larger porosity values are mainly associated with higher FMM that would indicate the interval is further away from dissimilar facies. Recall that the quality of sand is lower when closer to other facies and it stabilizes at higher values as it gets away from other facies. Thus, it is reasonable to assume that the lower horizontal black lines which mostly associate with lower porosity values belong to the pure sand intervals in direct contact with shale intervals. It could also be concluded that the highest black horizontal line which is mostly associated with larger porosity values belong to sand intervals of large thickness with the closest dissimilar facies of SIHS, for example. The increasing trend of FMM in relation with the porosity could be of any combination with mixed facies and different distances. The number of such horizontal values depend on different combinations of distance and contact that occur in the well data for any specific upscaling size.

Differentiation between pure intervals when using FMM becomes important in the modeling process. Considering the facies mixing as the secondary variable, the entropy constant value of 0 for all pure intervals would not contribute into the modeling the same way that FMM does. FMM basically, identifies the quality of the interval using the porosity-type weighting factor, the distance, and the type of contact. For example, the continuous property associated with an upscaled interval of sand closer to shale would not be modeled the same as the one closer to breccia.

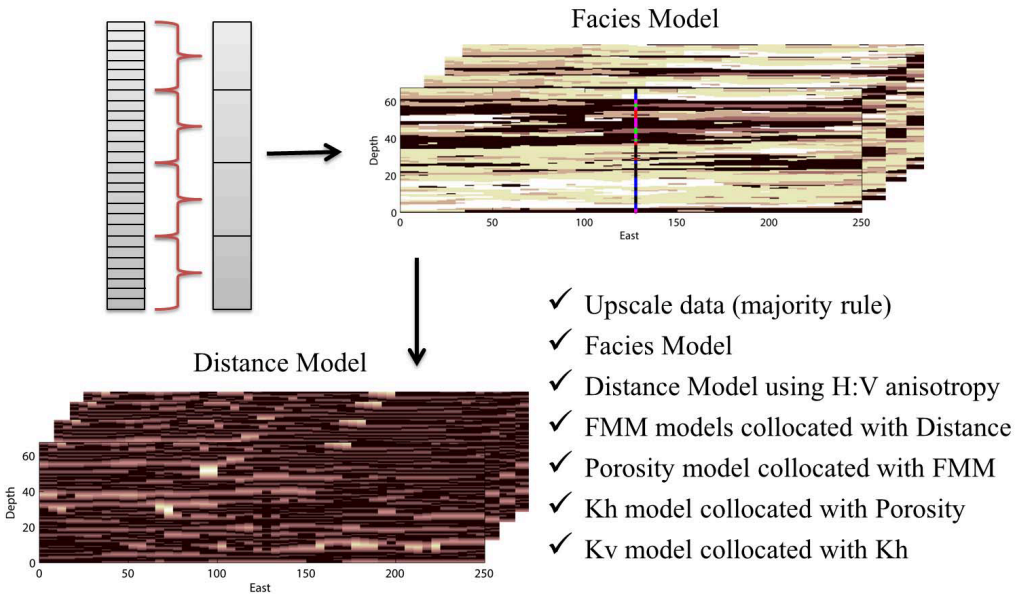

Figure 2.8: The proposed simulation workflow which utilizes FMM metric as a secondary variable to condition the geostatistical simulation workflow.

2.4 Proposed Modeling Workflow

FMM is proposed to account for facies mixing in reservoir modeling and integrate this information as a secondary variable to improve the property modeling process. The proposed modeling workflow that could account for the small scale variability which is lost during upscaling process is described as follows (also see Figure 2.8):

- Upscaling data (majority rule).
- Determining the corresponding variables such as porosity, volume shale fraction (Vsh) and FMM for the upscaled intervals.
- Processing 3-D facies modeling.
- Generating 3-D distance model corresponding to facies model using horizontal to vertical anisotropy.
- Generating FMM model by facies, considering 3-D distance model as exhaustive secondary data for collocated cokriging using proper correlation coefficient.
- Generating porosity model by facies, considering 3-D FMM model as exhaustive secondary data for collocated cokriging using the proper correlation coefficient.
- Generating horizontal permeability (Kh) model by facies, considering 3-D porosity model as exhaustive secondary data for collocated cokriging using the proper correlation coefficient.

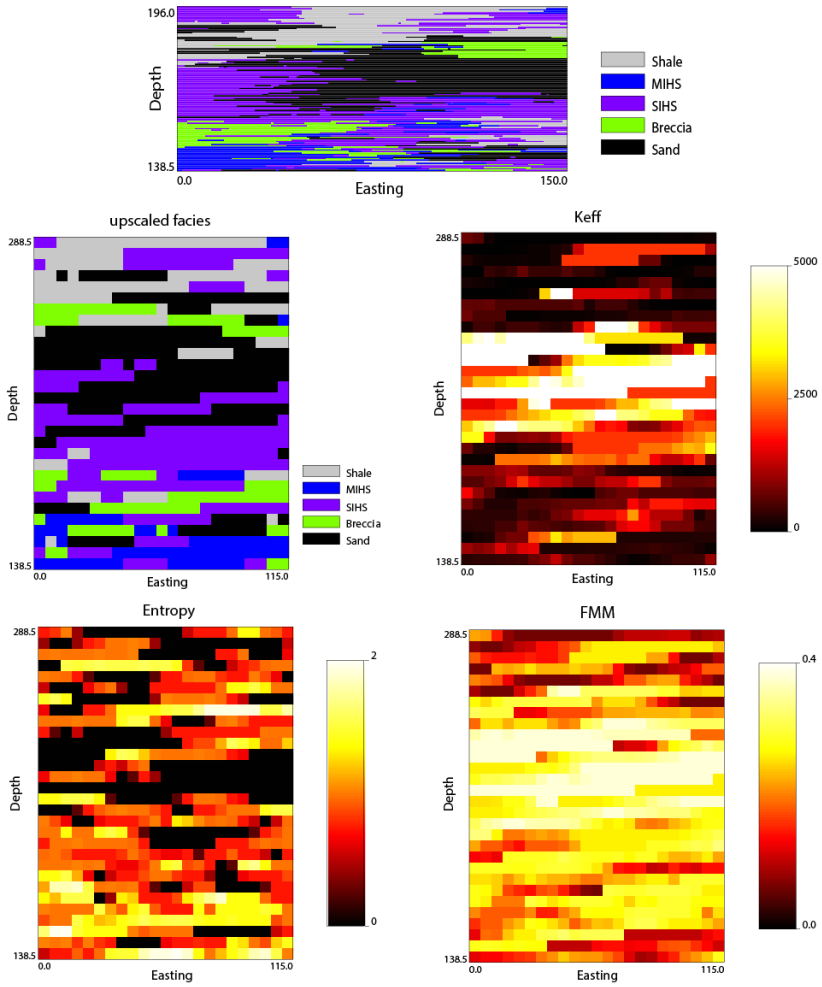

Figure 2.9: The high resolution facies model shown at the top is upscaled 5 times in both X and Z directions. The corresponding upscaled entropy, FMM and permeability maps are also present. All units are in meter.

- Generating vertical permeability (Kv) model by facies, considering 3-D Kh model as secondary data for collocated cokriging using the proper correlation coefficient.

The FMM variable is also readily adoptable into multivariate modeling framework. It can be considered as one of the many variables in the geostatistical multivariate modeling workflow proposed by Barnett (2015).

2.4.1 Synthetic Example

A 2-D example is designed at this point to demonstrate the improvement in modeling the reservoir property when facies mixing in the form of FMM, is considered. One well data from the Silver Willow project is considered to model a small 2-D reservoir around the well (Khan, 2014). The model has dimensions 150 m $\times$ 1 m $\times$ 115 m

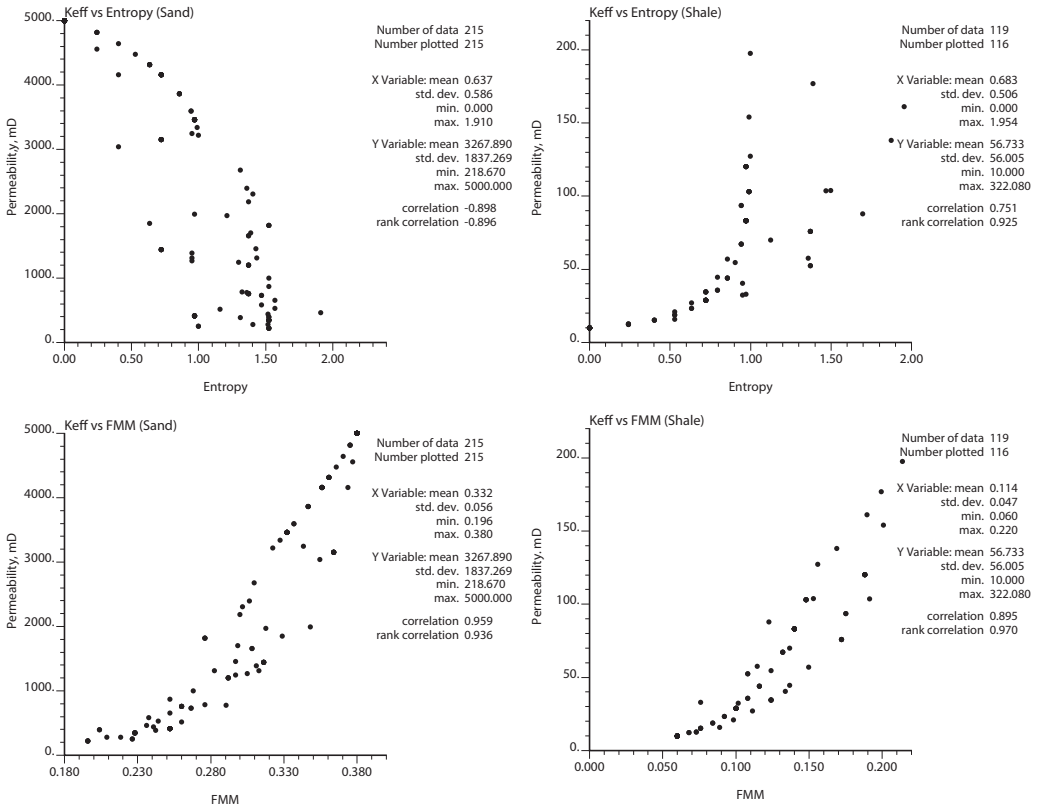

Figure 2.10: The relationships between Keff and entropy values for upscaled blocks (top), and relationships between Keff and FMM values for upscaled blocks (bottom). The scatterplots on the left represent the upscaled blocks assigned sand, and the ones on the right represent the upscaled blocks assigned shale.

which is generated using sequential indicator simulation (SIS) (Deutsch and Journel, 1998). The model is then upscaled 5 times to the dimension 30 m $\times$ 1 m $\times$ 23 m. In the upscaling process, for every interval, the corresponding entropy and FMM are evaluated using proportions of every facies in the corresponding interval and the mean porosity evaluated from data. As noted, the expected porosity for every facies is evaluated from pure upscaled intervals of well data. The effective permeability (Keff) map is the result of harmonic average of high resolution permeability map; a constant value for permeability is assigned to every facies of the high resolution map. The upscaled permeability map will be considered as the reference throughout this example. Figure 2.9 shows the upscaled facies map, the corresponding Keff map, the entropy map and the FMM map.

The idea is to estimate the permeability map for the upscaled model using FMM and entropy relation with Keff values. These relations would normally come from the well data. The relationship between entropy and Keff, and FMM and Keff should

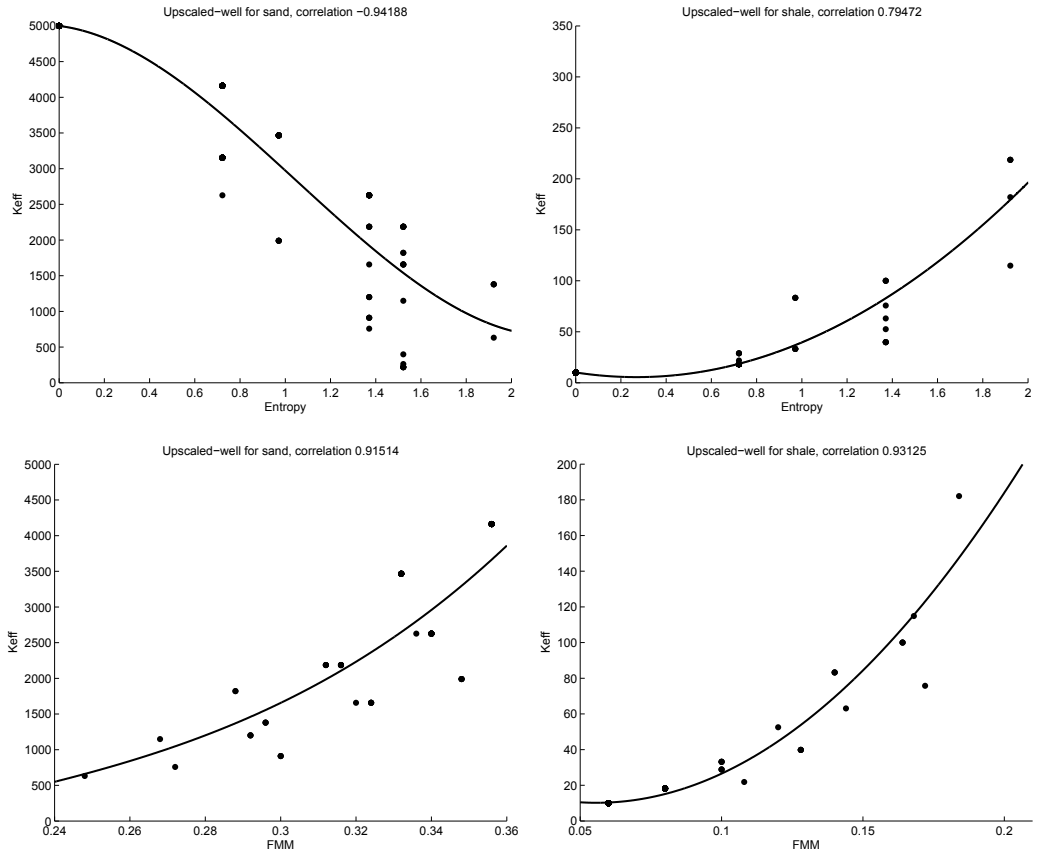

Figure 2.11: The upscaled well data is considered for the purpose of estimating Keff once considering Entropy (top), and once considering FMM (bottom).

be found through fitting the upscaled well data. Figure 2.10 shows the scatterplots of effective permeability versus (1) entropy, and (2) FMM for upscaled blocks of the map that are assigned sand or shale. Also, the scatterplots and fitting curves for well data are shown in Figure 2.11. Visually inspecting the fitting curves, the ones closely representing the scatterplots of upscaled maps shown in Figure 2.10 would do better in permeability estimation. This is true for FMM curves as they resemble the relationship for upscaled blocks relatively close. The fitting function that is specific to every facies provides a reference table that enables the assignment of Keff for the corresponding entropy or FMM value. The FMM and permeability relationships follow the fitting curves from the well data.

The Keff by Entropy and Keff by FMM maps in Figure 2.12 are the result of table reference assignment. The resulting permeability map by FMM which is on the right of Figure 2.12 shows more continuity compared to the one resulting from entropy assignment on the left. The reference values for Keff (true) versus the estimated ones for both cases of FMM and entropy are shown in scatterplots in

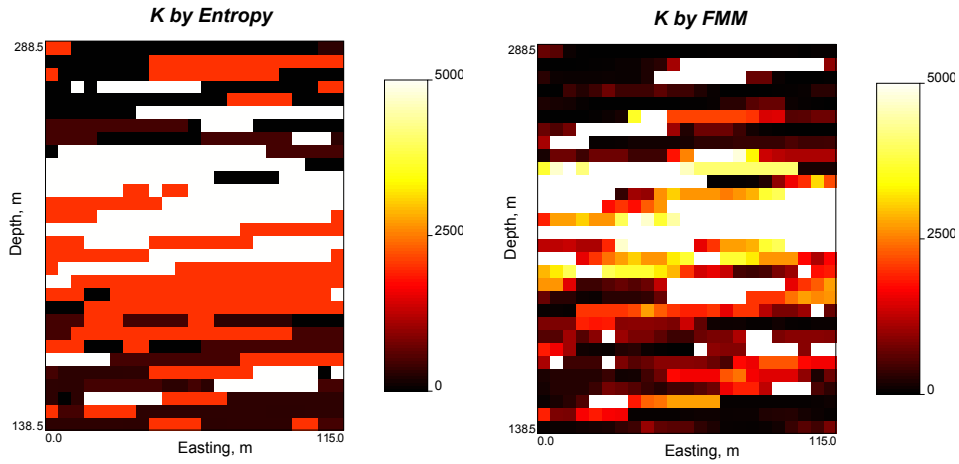

Figure 2.12: The effective permeability maps resulting from reference table assignment using FMM and entropy.

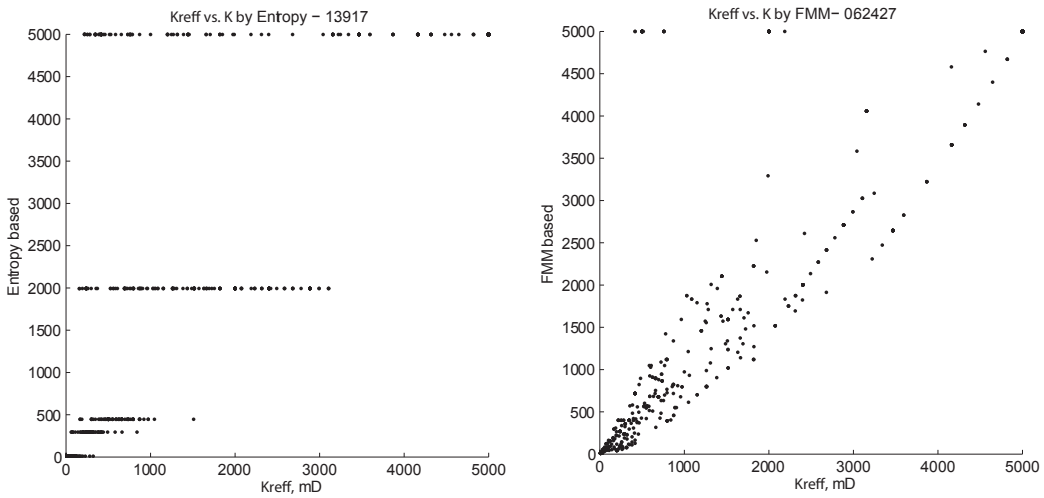

Figure 2.13: True (reference Keff) versus estimation of permeability based on entropy fitting function (left), and FMM fitting curve (right). The MAE quantifies the difference between estimates and true vales which is 1.39 for the case of entropy and 0.62 for FMM case. The mean squared error (MSE) percentage for the case of FMM is almost a quarter of the case of entropy which makes it a very strong candidate for conditioning.

Figure 2.13. For comparison purposes between the true and the estimate, the mean absolute error (MAE) is considered as follow:

$$\mathrm{MAE} = \frac{1}{n}\sum_{1}^{n}\left|\frac{\mathrm{Est}(n) - \mathrm{Tru}(n)}{\mathrm{Tru}(n)}\right|.$$

MAE, therefore, quantifies the difference between true values and their estimates. The MAE is 1.39 for the case of estimating permeabilities by entropy, and this value drops quickly to 0.62 for FMM case which is half of the estimated error for estimation by entropy. This example confirms the stability of FMM in the estimation of petrophysical or flow related variables when considering facies mixing into account.

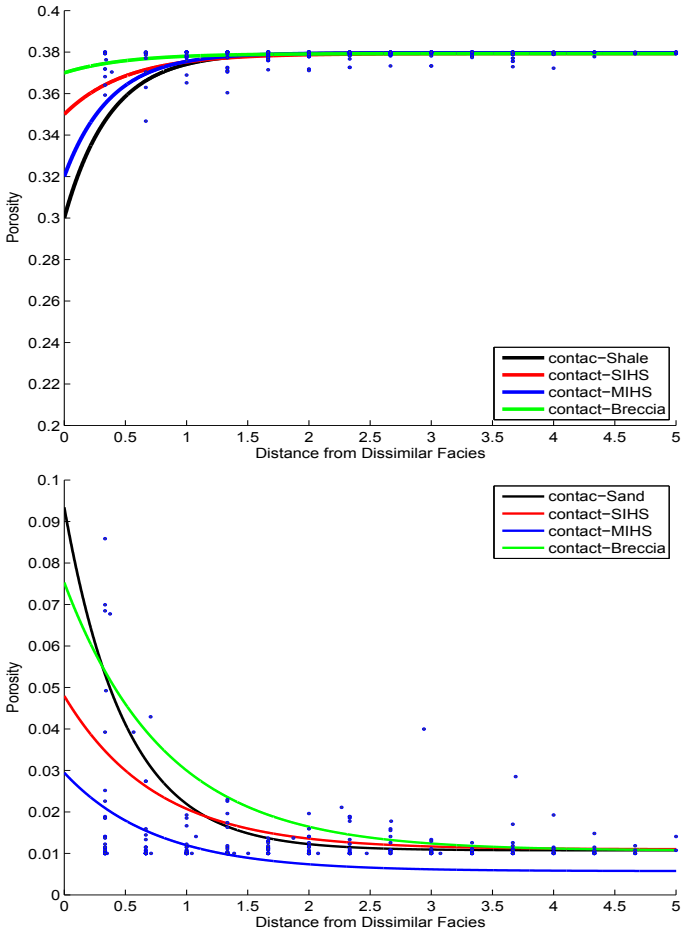

Figure 2.14: Evaluating the mean value of porosity for sand and shale in contact with other facies as a function of distance by adopting the fitting exponential curve.

In the following subsection, a case study is considered to evaluate FMM values for upscaled intervals and utilize them in modeling workflow. A cross validation technique is applied to compare the true values with the estimated ones.

2.4.2 Case Study

Twenty five Silver Willow well data with 0.25 m resolution are available for this study. Five facies of sand, breccia, SIHS, MIHS, and shale are identified in this dataset. The data is upscaled to an intermediate scale of 2 m for this example. The facies intervals are upscaled and FMM and entropy are calculated for every upscaled interval. In FMM evaluation, the relationship between the porosity and distance as a function of contact is being considered for non-mixed facies of sand and shale. Figure 2.14 represents the fitting functions for sand and shale that model the relationship of upscaled porosity and distance to other four dissimilar facies.

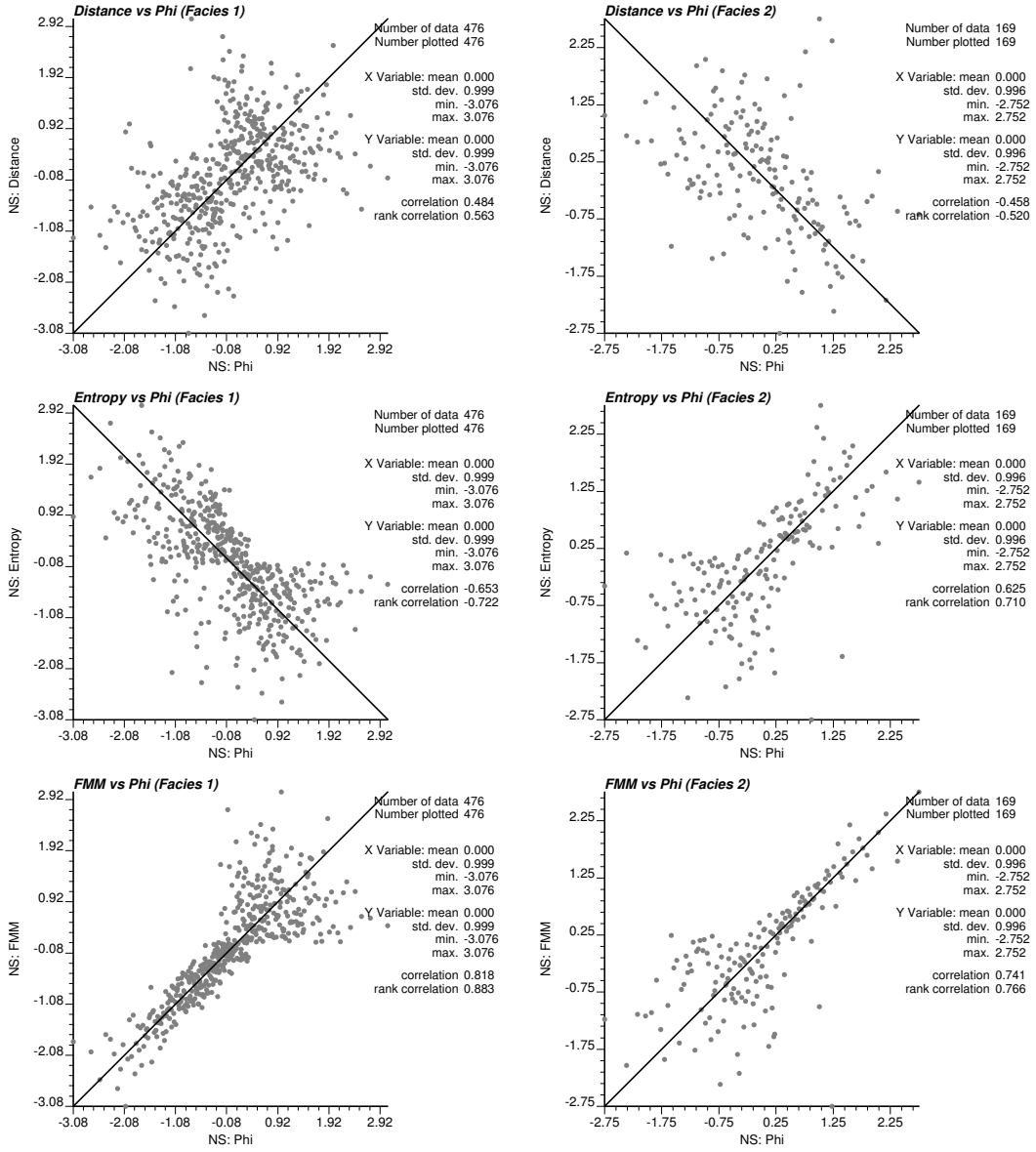

Figure 2.15: The data resolution is at 2 m interval. The relationships between normal score of porosity and normal score of distance (top), entropy (middle), and FMM (bottom). The scatterplots on the left represent the relationships for stationary domain of sand, and the ones on the right represent relationships for stationary domain of shale.

These fitting functions are considered in FMM evaluation of upscaled intervals as discussed earlier.

To demonstrate the effect of FMM (as a secondary variable) in reservoir modeling, cross validation is applied to compare the estimation with the true values. The two variables of distance and entropy are also considered as the secondary variable to model the upscaled porosity values. This is to compare the FMM performance in the estimation process. Figure 2.15 shows the relationship between porosity and

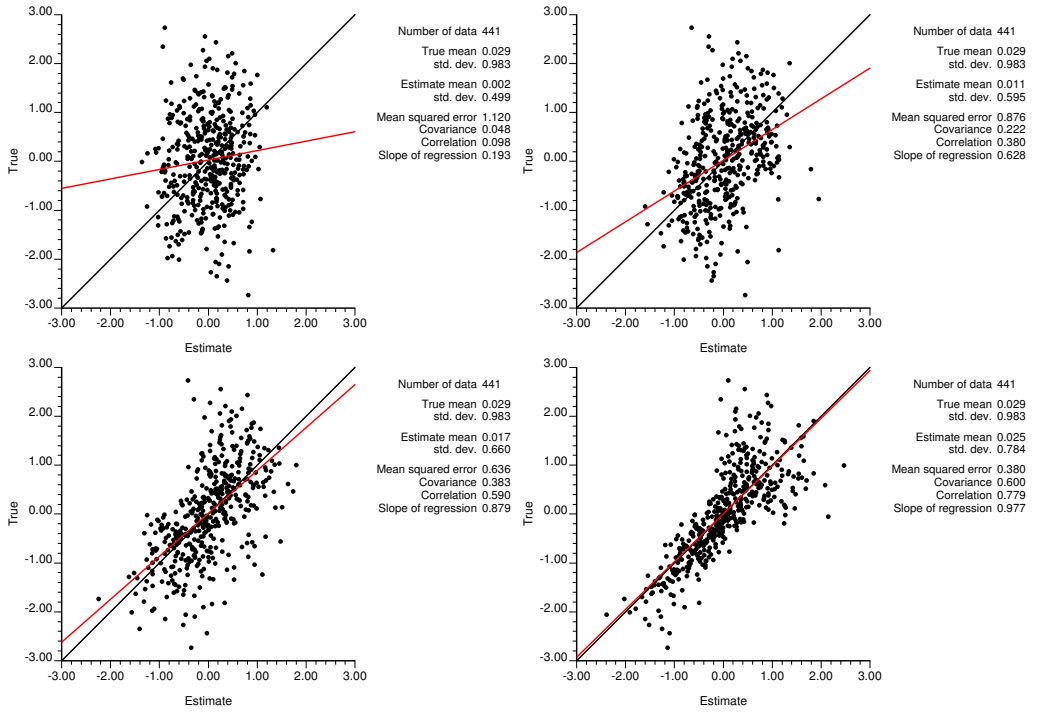

Figure 2.16: Porosity cross validation for 25 upscaled Silver Willow well data (sand): (1) simple kriging, MSE: 1.12 (2) collocated cokriging with distance, MSE: 0.87 (3) collocated cokriging with entropy, MSE: 0.63 (4) collocated cokriging with FMM, MSE: 0.38. There is a clear improvement when FMM is considered as collocated cokriging in the estimation of porosity.

distance (top), porosity and entropy (middle), and porosity and FMM (bottom), in the normal score domain. The cross validation study is applied by removing one well at every iteration and trying to estimate based on the other well data information. In the first trial, the estimates are evaluated using simple kriging. The simple kriging is applied to estimate the porosity value for the data of the removed well. The cross validation plot with the corresponding data statistics are shown in Figure 2.16 at the top. The cases of collocated cokriging with distance, entropy, and FMM are also shown in the same figure for 441 data.

The same cross validation scatterplots are shown for shale in Figure 2.17. There are 92 upscaled intervals that are assigned shale. The MSE improves gradually from the case of estimation with no secondary variables to the case with FMM collocation cokriging. The cross validation is quite poor for the simple kriging case with MSE of 1.08. When distance is considered as collocated variable, the MSE improves to 0.83. In another case, entropy is considered for collocation cokriging by which MSE improves to 0.64. This value even drops further to 0.4, when FMM is considered as the secondary variable for collocated cokriging estimation. The statistics of cross

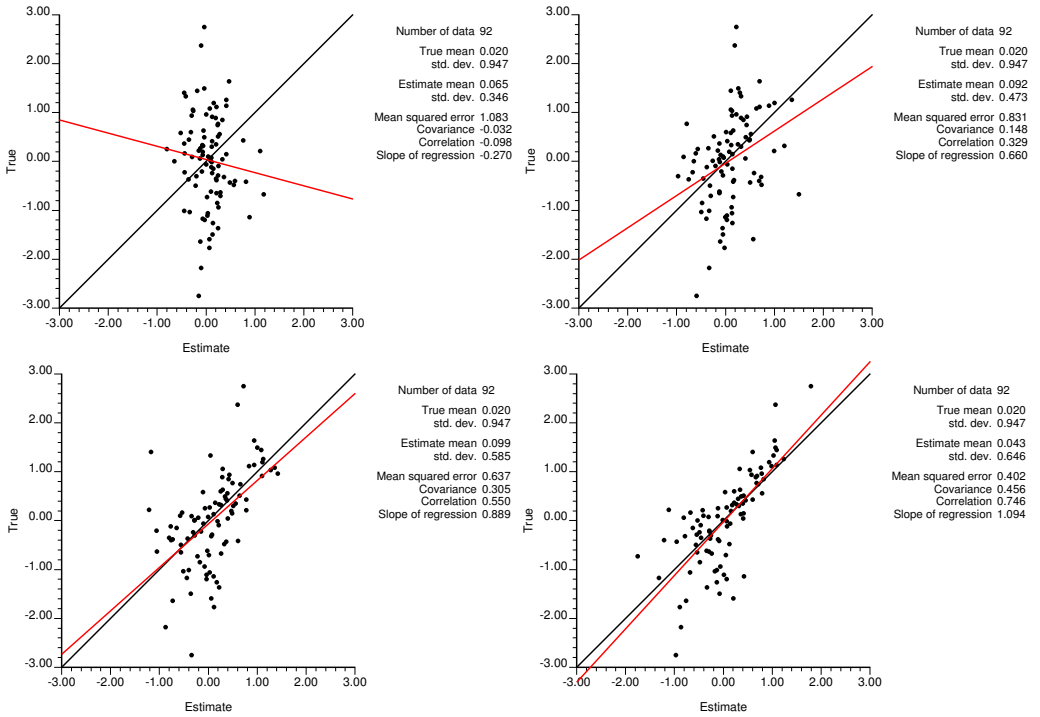

Figure 2.17: Porosity cross validation for 25 upscaled Silver Willow well data (shale): (1) simple kriging, MSE: 1.08 (2) collocated cokriging with distance, MSE: 0.83 (3) collocated cokriging with entropy, MSE: 0.63 (4) collocated cokriging with FMM, MSE: 0.4. There is a clear improvement when FMM is considered as collocated cokriging in the estimation of porosity.

validation study for sand are summarized in Table 2.1.

Table 2.1: Summary statistics for sand cross validation of porosity with different cases shown, in Figure 2.16.

	Simple Kriging	CCK-distance	CCK-entropy	CCK-FMM
MSE	1.12	0.87	0.63	0.38
Correlation	0.1	0.38	0.59	0.78
Covariance	0.05	0.22	0.38	0.6

The same study is repeated with the type of estimation from simple kriging to collocated kriging using exhaustive secondary variables. The second cross validation plot is generated when estimating using the distance as secondary variable with correlation coefficient of 48% which is calculated from data. The MSE improves from about value 1.12 to 0.87. In the second plot the same process is applied with entropy as the secondary variable. The correlation coefficient between the porosity values and entropy for upscaled intervals is -65%. The cross validation results, shown in third plot, indicate an improvement comparing with distance collocation.

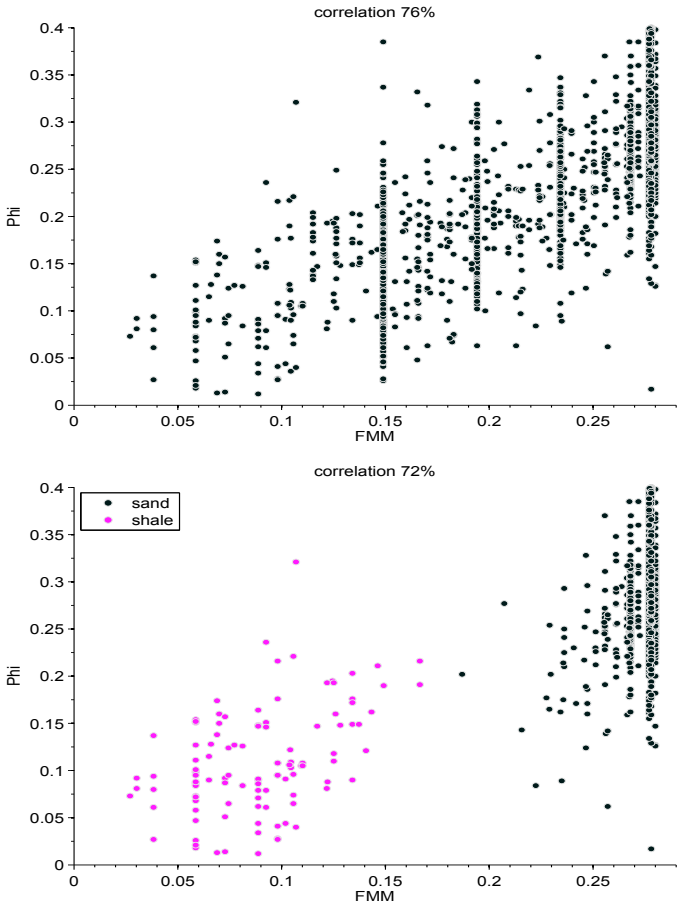

Figure 2.18: The scatterplot at the top shows upscaled porosity values versus the calculated FMM. There is 76% correlations between porosity and FMM. The presence of vertical lines in the scatterplot indicates pure upscaled intervals. The second scatterplot shows only those upscaled intervals that are assigned sand (in black) and shale (in pink). A clear trend could be observed for FMM with the increase of porosity.

The MSE has dropped to 0.63. In the last trial, shown in the last plot, FMM is considered as the exhaustive secondary variable for collocated cokriging estimation of well data. The correlation coefficient between the porosity values and FMM is 82%. As shown in the cross validation plot, the estimation has been improved significantly and the mean squared error value has dropped to almost half, 0.38.

CCG Micromodeling Data

This subsection presents another dataset. In this dataset, the correlations between different variables are smaller than the previous case. Figure 2.18 shows the scatterplot of porosity versus FMM (top) for all upscaled data with 76% correlation. The vertical dots in this scatterplot represent the pure interval where the resulting FMM is only the average porosity of corresponding facies ($1 \times \phi_k$). The second

scatterplot includes the upscaled intervals that are assigned sand or shale. There are more vertical lines of similar FMM values and different porosity for the case of sand, and a few for shale. This is because the average porosity in case of sand and shale differs for different combinations of contact and distance.

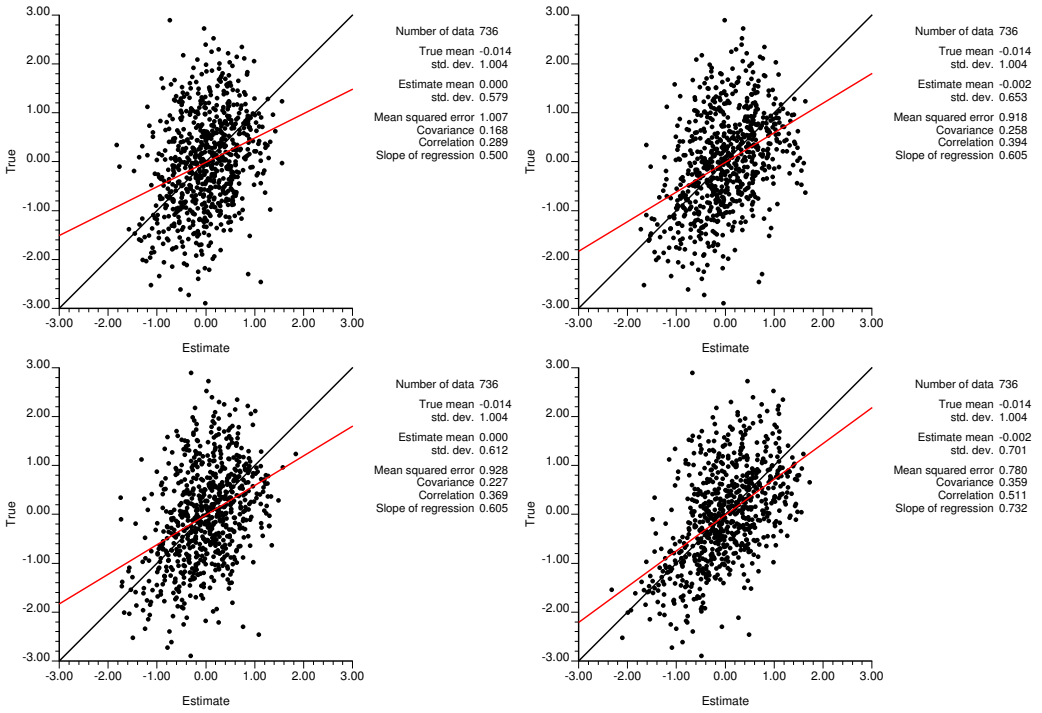

Figure 2.19: Porosity cross validation for CCG micromodeling data (sand): (1) simple kriging, MSE: 1.0 (2) collocated cokriging with distance, MSE: 0.91 (3) collocated cokriging with entropy, MSE:0.93 (4) collocated cokriging with FMM, MSE: 0.78.

Similar to the previous example, three secondary variables of (1) distance (2) entropy and (3) FMM are considered in the estimation of porosity. Provided there are enough data, cross validation is a reliable technique to compare the estimated values with the true in all estimation cases. Using the common simple kriging approach to estimate porosity results in the largest mean squared error. A significant improvement can be observed in the estimation of porosity when FMM is used for collocated cokriging in comparison to distance and entropy. One well is removed at every estimation, and associated porosity for upscaled intervals of the removed well are estimated every time. The mean squared error for this estimation is minimum (= 0.78) when FMM is considered as the collocated variable. Figure 2.19 illustrates the estimated porosity versus the true values considering simple kriging (top-left), collocated with distance (top-right), collocated with entropy (bottom-left), and col-

located with FMM (bottom-right). There is a clear improvement in the estimation of porosity when FMM is considered as the secondary variable.

2.5 Chapter Summary

The motivation for this chapter is mitigating the amount of information loss in facies upscaling. Although the well data upscaling process is an important step in reservoir modeling, it also results in a loss of small scale information due to averaging. There is no doubt that what really limits the reservoir models is the physical constraints in data collection. Retaining information loss through upscaling process is addressed in this chapter by introducing FMM which results in a solid improvement to the work done previously by Babak et al. (2013). They propose conditional entropy to account for the mixing in the upscaling process. Entropy can only quantifies the amount of mixing. It does not explain the type of mixing or identify the facies involved. Conditional entropy was proposed to provide information regarding the mixing intensity by similarity measure. Depending on how similar the facies in upscaling intervals are, the amount of entropy would be reduced to a smaller value. This is consistent with a smaller value of entropy representing less mixing. Conditional entropy, however, has some shortcomings which is discussed in detail. Thus, FMM is proposed to address the entropy's limitations and provide the reservoir modeling with valuable small scale information.

FMM is a volume-based average metric. The value of FMM is an explicit accounting for mixing, and for the proximity of the interval to other facies. FMM is defined to distinguish between pure and mixed intervals, and differentiate between facies. In other words, FMM can be seen as a porosity type measure with specific ranges for every facies, and specific values within the ranges for pure and mixed intervals associated with each facies. Then, the reservoir modeling workflow considers FMM as an intermediate (secondary) variable that informs the petrophysical properties to be modeled with precise evaluation of amount of mixing, proximity to other facies and the type of facies they are in contact with. FMM is required to be calculated at the upscaling process and treated as a pseudo-petrophysical attribute that corresponds to upscaling data interval. Using two different dataset, the cross validation results confirm the improvements in porosity estimation.

Chapter 3

Lateral Continuity of Stochastic Shales

Characterizing small shale local barriers in reservoirs is important for recovery forecasting, particularly for heavy oil reservoirs. High NTG ratio reservoirs such as the bitumen deposits in the McMurray formation contain small shale intervals that impede local flow of steam and bitumen. The information collected from vertical delineation wells provides only limited knowledge on the horizontal extent and connectivity of these intervals. The main challenge is that such flow barriers are not correlated between relatively widely spaced delineation wells; the shales are laterally discontinuous. Even if such shale barriers are detected by the delineation wells, their lateral continuity cannot be easily ascertained. This chapter proposes a novel methodology based on an inverse modeling scheme to estimate the lateral extent of thin shale barriers. The chapter begins with some background and motivation on thin shale studies, and continues with the principles and methodology with supporting examples; the required mathematics will also be developed.

3.1 Introduction

Shale, in the context of relatively high NTG ratio sandstone reservoirs, was aptly described by Haldorsen and Lake (1984). Shale includes shale lamina, shale streaks, shale drapes, and massive shales. Shales are indurated sedimentary rocks with finely laminated structures that are related to the orientation of micaceous clay mineral constituents. Each type of shale has a different length scale as discussed by Larue and Hovadik (2006); Hovadik and Larue (2007); Larue and Hovadik (2008); Marren et al. (2006); Michel et al. (2010).

Small discontinuous shale intervals that are uncorrelated between well data, are referred to as *stochastic shales* in the literature (Haldorsen and Lake, 1984). Stochastic shales could be reasonably considered as remnant objects that are distributed with various lateral continuities in the reservoir (Pyrcz and Deutsch, 2014). This is in contrast to *deterministic shales* that can be correlated between well data; see sketch in Figure 3.1.

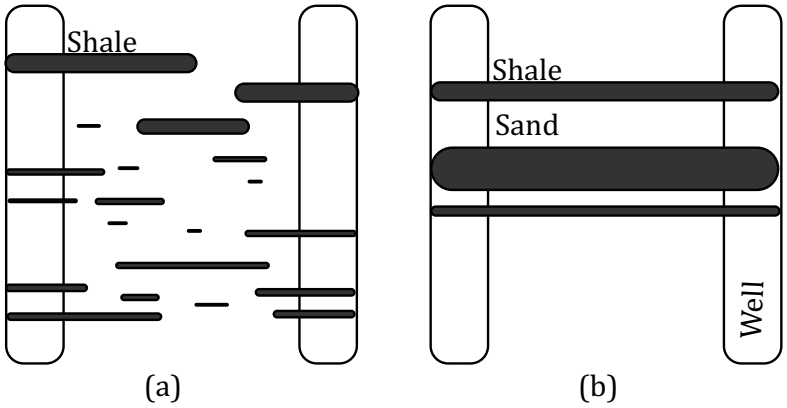

Figure 3.1: Sketch of a cross section showing (a) stochastic shales; (b) deterministic shales (after Haldorsen and Lake (1984)).

The characteristics of shale intervals are a strong function of their depositional environment. Over the past few decades, a significant amount of stratigraphic literature on the nature and character of mud beds in fluvial and tidal settings has been published (Henriquez et al., 1990; Galloway and Hobday, 1996; Miall, 1996; Dalrymple and Choi, 2007; Ichaso and Dalrymple, 2009; Johnson and Dashtgard, 2012). A detailed description of the shale barrier characteristics associated with different depositional environments can be found in Richardson et al. (1978). The detailed geometry and structure of remnant shales in dominantly sandy sediments, however, is not well documented which motivates studies such as this one.

Haldorsen and Lake (1984) note that the information regarding shale distribution can be gained (1) empirically from an observed sand/shale sequence; or (2) statistically from outcrops of similar depositional environments. Zeito (1965) provides tabulated statistics on the proportions of shales and their lateral continuity for different outcrops. In this table, the outcrops are identified with their lengths and thicknesses within the channel, deltaic and marine environments. Similarities between the geometry, frequency, and lithology of shales in reservoirs largely depend on the environment of depositional rocks. This is supported by Zeito (1965);

Verrien et al. (1967); Sneider et al. (1978); Richardson et al. (1978); Pryor and Fulton (1978). Extensive studies on different distributions and continuity of sandstone reservoirs provide many conceptual models for these purposes (Le Blanc, 1977).

Stochastic shales generation has been a common approach to account for discontinuous shales. The distributions of discontinuous shales can be hardly characterized in geologic models of reservoirs. Although the distribution of shale barriers is mainly determined by the geology of the reservoir, such flow barriers could not typically be correlated from the drilled data. Assuming rectangular, square, and ellipsoidal shapes for the barriers, and randomly placing them in the recovery region, has proved to reasonably approximate the shale distributions and their influence on performance (Haldorsen, 1989; Belgrave and Bora, 1996).

The statistical method of Begg and Chang (1985) accounts for the effect of shale barriers in the simulation process by considering reduction in the vertical permeability. Lien et al. (1992) refer to Begg's method as an implicit characterization of impermeable barriers and compare its performance with the technique proposed by Haldorsen (1989) in which the shale characterization is applied explicitly in simulations. The latter shows a better match with the theoretical approach of Joshi (1988). The study carried out by Belgrave and Bora (1996) also shows the strong influence of the shale size on the productivity of the horizontal wells, and how the size of horizontal wells relative to the size of shales influences the recovery performance. Lien et al. (1992) show that shale density around the horizontal well pairs is an important factor in adversely affecting the recovery performance of the horizontal wells.

Shale does not always form a barrier. Depending on the nature of the shale, its continuity, its relative distribution and/or position relative to the production well, the fluids may bypass the shale within the time frame of the process and make the effect of the shale negligible (Sharma et al., 2002). In most cases, the use of the word "barrier" implies a significant influence on fluid flow. For example, in the following statement, the shales are referred to as barriers that adversely affect the SAGD recovery project: The Peace River oilsand deposit, located in central Alberta, contains relatively large amount of marine shale in the form of discontinuous and continuous barriers (Webb et al., 2005).

Most of the bituminous reservoirs of the McMurray formation in Alberta occur in sequences of channel sands cutting through previously deposited marine sediments

(Pooladi-Darvish and Mattar, 2002). The channel sands are generally characterized by high porosity and permeability with seldom inter-bedded shale barriers or baffles. These shales, if present in the recovery region, create tortuous flow or may even prevent flow depending on their distribution (Haldorsen and Lake, 1984). In the case of SAGD, which is an important recovery technique in oilsand deposits of Northern Alberta, the adverse effect of the continuity of shales between the injector and producer is well documented (Peaceman, 1993).

SAGD relies on the vertical expansion of a steam chamber. Shale would alter steam rise and could even prevent the steam chamber from expanding vertically with significant effects on well productivity, cumulative steam-oil ratio (CSOR) and oil recovery (Pooladi-Darvish and Mattar, 2002; Le Ravalec et al., 2009a). The findings and analysis of Christina Lake SAGD project by Zhang et al. (2007) demonstrate the strong influence of shale barriers on the steam chamber growth in the near-well region. Numerical analysis by Chen et al. (2008) also shows the nonuniform distribution of the steam rise and oil drainage in different regions of the reservoir as a result of the heterogeneity.

The presence of shale barriers results in permeability anisotropy which was not initially considered in Butler's SAGD theory (Butler and Stephens, 1981). Analyzing and modeling the effect of permeability anisotropy on the distortion of steam chamber has attracted numerous studies in the past few decades, including: Kamath et al. (1993); Sharma et al. (2002); McLennan and Deutsch (2006); Chen et al. (2008); Azom and Srinivasan (2011); Azom (2013). Although this chapter is not directly concerned with the details of modeling such effects, developing methods to estimate the lateral extents of shales will substantially help with similar analysis—(Lajevardi et al., 2015) proposes another approach to estimate lateral continuity of shales.

An example is shown at this point to demonstrate the effect of shale barriers on the recovery of horizontal wells. The vertical permeability is determined for models of different sizes and different shale lateral extents. The size of the model is considered to reasonably indicate a window for recovery. As the model size increases with constant shale sizes, the effective vertical permeability increases. Whereas, for a given model size with the given shale proportion, as the shale continuity increases, the effective vertical permeability decreases. In other words, it becomes more difficult for the fluid to find vertical pathways with larger shale barriers in the reservoir. Figure 3.2 illustrates the changes in effective vertical permeability with respect to

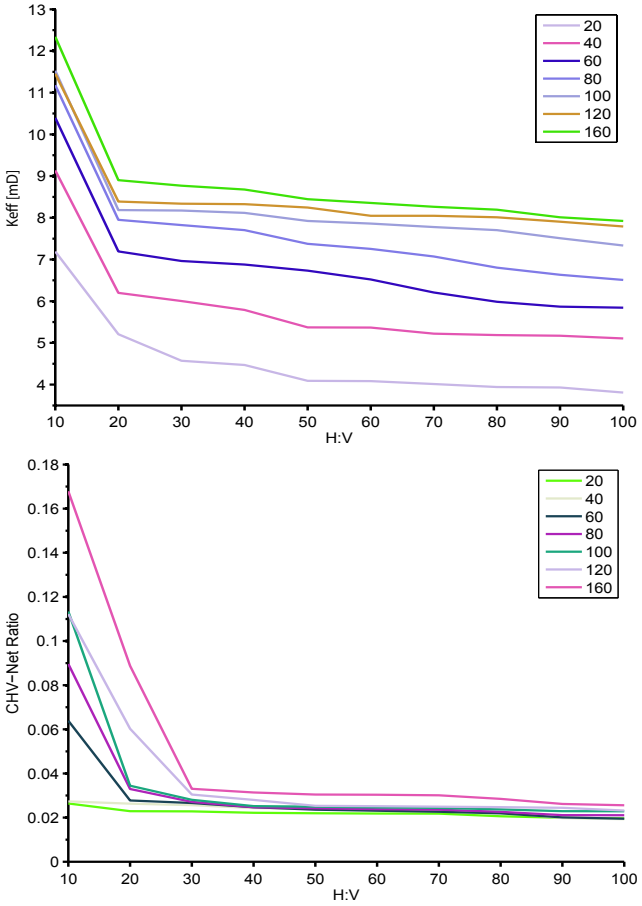

Figure 3.2: The effective vertical permeability versus the shales horizontal to vertical (H:V) ratio for the model sizes changing from 20 to 160 m is shown at the top. The plot at the bottom is the illustration of the same concept but a different metric which is the ratio of CHV over the total amount of net reservoir. The CHV-net ratio drops quickly for smaller H:V ratio of the shale barriers.

the shale anisotropy ratio for seven different models where the size is changed from 20 to 140 m with intervals of 20 m. An object based modeling technique, specifically `ELLIPSIM` program from GSLIB by Deutsch and Journel (1998) is used to generate the models with the ellipsoid-like shales in this example.

The same behavior can be observed when connected hydrocarbon volume (CHV) is considered as the reservoir response (Fenik et al., 2009b). CHV basically measures the amount of net reservoir that can be potentially produced. Figure 3.2 shows the increase of CHV for model sizes changing from 20 to 160 m. Also, for a given model size, as the barrier lateral continuity increases, the CHV decreases. Note that the NTG ratio is the same for all the models. The challenge is to infer the horizontal extent of the shale barriers so that their influence can be predicted and managed.

3.2 Proposed Methodology

The proposed methodology to estimate the lateral continuity of shales in this chapter is based on an inverse modeling approach. The inverse modeling approach proposes a framework to incorporate the information from well data, well placement, and well spacing to reach an educated estimate for the shale continuity. This approach is basically a function of well configuration in the area which mimics the reservoir with close NTG ratio. This might imply that geology is overlooked in this approach. Of course, geological understanding provides context and critical supporting information. For example, in the lower McMurray formations the shales are believed to be 5 to 100 m in lateral extent.

If a close pair of vertical delineation wells both intersect a shale barrier, the shale length could be assumed larger than the spacing of the well pair. The same analogy is at the heart of the proposed methodology in this chapter. The shale intervals detected from data are paired up between nearby wells and the possibility of their connection is investigated. Yet, it is difficult to confidently pair up shale intervals from sparse wells and assign them as connected; there is a possibility that two different shales appear connected, but are not. That is why the definition of connection here is only "apparent," that is, the shale intervals appear to be connected. The lateral continuity of shales is then represented by a distribution that is a function of the number of apparent connected shale intervals by performing a Monte Carlo simulation study, as will be described shortly. Performing the simulation would allow a probabilistic assessment of how many apparently connected shales could be actually connected.

The scheme of this approach can be broken up into three main steps of measuring the apparent total shale connectivity (TSC) for (1) real data (2) simulated data and (3) random data. The connected shale intervals of the random data help validate the measurements from the real data and simulation case contains actual information. Also, the comparison provided by connected shales of simulated data and the real case provides quantified knowledge on the possible shale continuities that could result in TSC measured from the real data which is referred to as observed TSC throughout this chapter. In fact, the term "inverse" refers to the process in which the corresponding shale continuity is inferred from TSC intersection measured from well data.

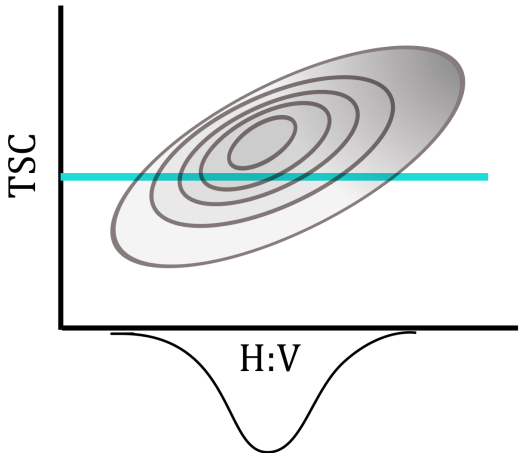

Figure 3.3: The schematic representation of inverse modeling approach: the x-axis represents the H:V ratio of the shales for scenarios generated. The y-axis represents TSC variable where the solid blue line indicates the observed TSC and the cloud indicates measured TSC of the simulated scenarios.

Figure 3.3 summarizes the proposed framework in form of a scatterplot. The clouds represent the connected shales for simulated scenarios and the area where the measured connected shales of the real wells matches the ones from simulated realizations provide information on the shale lateral extent. Thus, establishing the proper simulation scenarios is important. The idea is to simulate many realizations with specified shale continuity of specified amount of shales. The realizations should be generated mimicking the reservoir properties to the extent known by the geologic understanding and data analysis. The key is to keep all known parameters such as the NTG ratio, well configuration, and size of the area of study consistent within the framework. Incorporating the geological understanding of the area is an important factor: the correct NTG imposes the direct relation between the number of shale objects of certain anisotropy.

Note that shale continuity and H:V anisotropy ratio of shale might be used interchangeably in this chapter. Also, it is worth mentioning that the initial choice on the fixed shale continuities in the simulation scenarios comes from a geological understanding of the reservoir. The knowledge on the characteristics of the reservoir provides an *a priori* distribution of the shale lateral continuity as a reference for the fixed continuity scenarios.

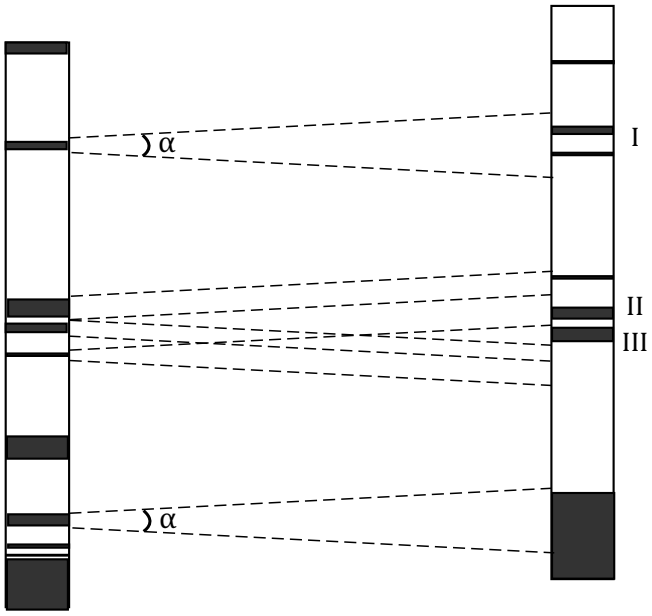

Figure 3.4: A schematic depiction of identifying the connected shale intervals of adjacent wells. Assuming α is the angle of apparatus, the roman numbers of I, II and III count the potential connected shale intervals. The first α represents a case where two shales from nearby wells are candidate for connectivity. The second α represents a case where a shale with large thickness is in the line of sight of a very small shale interval. Although aspect ratio is almost non-uniform all throughout the shale continuity but too much tortuosity is also not expected unless backed up with geological evidence.

3.2.1 Calculating Total Shale Connectivity

Total shale connectivity or TSC is a primary factor in the inverse modeling approach proposed in this chapter. The TSC measures the number of connected shale intervals that can be observed from the specific well configuration. An algorithm is designed to calculate the amount of apparent connected shale intervals from the well data, that is, to determine if two shale intervals seen by a close pair of vertical wells could be one shale barrier.

Important parameters in TSC calculations include (a) the size (thickness) of the shale intervals and (b) their presence in nearby wells along the direction of stratigraphic correlation. Figure 3.4 demonstrates some different situations for shale intervals seen by nearby wells. As can be seen from Figure 3.4, among all these shale intervals captured by the well pairs, only three pairs meet the criteria to have an apparent connection. For example, if there is another shale interval in the adjacent well in which it is placed at the other shale's line of sight within 5° deviation and its size is within 40% of the size of the other shale interval, the two will be considered as connected. In this analysis, shale intervals of any thickness cannot be considered

as stochastic thin shales; a detected 10 m shale interval cannot be a small barrier in reservoir but is probably part of the non-reservoir region, that is, a mud plug formed by an abandoned channel. A maximum thickness of 3 m could probably be a reasonable assumption for small shale intervals. Note that these numbers are not definite and could change depending on the knowledge of the reservoir. One could also examine a well pair from a place where its geology is known and decide on these parameters by observing how the shales seem to be extending over the area. Adjusting the required parameters and analyzing the results relative to what is known and what is expected are also recommended.

A similar procedure to identify the connected shales should be carried out for all the well pairs since the final TSC value is total connected shale over all the well pairs. TSC fraction is used to report the amount of connected shale intervals instead of the TSC number. The TSC fraction is defined by the TSC value over the number of "qualified" shale intervals to be connected. For example, the three shale intervals in the middle of schematic in Figure 3.4 are qualified for connection. However, the choice of parameters only accepts 2 out of 3 pairs as having apparent connections. The TSC fraction is therefore 2/3. Note that any reference to TSC from here on would imply the fraction of total number of connected shales to the potential intervals.

Another important point in calculating the connected shale intervals is seeing the nearby shale from both wells. Note that in Figure 3.4 the connection is seen from the well on the left to the well on the right. The shales connection could be also seen from the other well. The connections identified when seen from both sides are considered in the measure of total connected shales unless some anisotropic geologic information lead to a precise decision on the direction that connection should be examined.

It is essential to consider the exact same parameters when calculating the TSC for simulated realizations as from the original well data. Therefore, for any given H:V scenario, a corresponding TSC fraction represents the probability of connected shales. Note that when the two shale intervals are marked as connected, the corresponding continuity of the connected shale is inferred from the spacing between the well pairs. Thus, the final shale continuity would be represented by a distribution spreading over the possibilities of H:V ratio concentrating around the point of intersection.

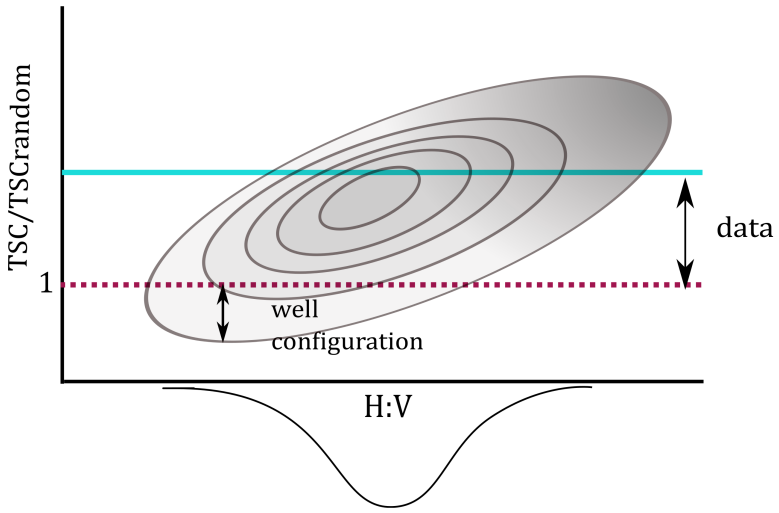

Figure 3.5: A schematic representation of the scatterplot of TSC relative to TSC random versus the H:V ratio of simulated shales. The solid green line represents the relative observed TSC, and the dashed red line represents the relative random TSC which is indeed 1. The well configuration influences the amount of cloud under the random TSC.

Random TSC

Among all parameters contributing to TSC analysis, well spacing is one main variable and stays fixed throughout the analysis. For example, if two shale intervals are said to be apparently connected between nearby wells, the spacing between the wells is an important constraint on the understanding of the lateral extent of the shale. Two questions arise while relating TSC to the well spacing (1) does observed TSC suggest a value smaller than what could be observed randomly? (2) does the observed TSC suggest too small well spacing relative to shale continuity?—The first question refers to inadequate data. However, the second question relates to what happens if the wells are too close relative to the shale continuity; this may confound the number of connected shales, that is, many will appear connected.

To study these questions further, the meaning of random TSC should first be clarified in this context. The remainder of this subsection discusses how to evaluate the corresponding random TSC for a particular configuration of wells and to calibrate it to different shale sizes. The observed TSC can only be meaningful relative to the random TSC with everything but the lateral extent fixed. The random TSC for every case is evaluated by covering the non-net reservoir with random shale continuity and using the same well configuration as what is studied. Note that selecting the range of shale continuity for the random case could come from the *a priori* distribution of shale lateral extents that is typically gained from a geological

perspective. Thus, the random TSC is not unique: Firstly, it is evaluated relative to the well configuration and other simulation factors. Secondly, it depends on all the factors discussed in TSC measurement.

The amount of information gained regarding the shale continuity depends on how the cloud of simulated TSC, the observed TSC, and the random TSC are placed relative to each other. Figure 3.5 is a schematic view of these parameters. The larger the gap between the observed TSC and random TSC, the more informative is the data, and the more reliable is the estimation of shale continuity. The cloud below the random TSC is directly related to the well configuration. More well pairs and/or closer wells relative to shale continuity would result in a decrease of the area below the random TSC.

3.2.2 Sensitivity Analysis

Since the quantification of shale continuity is a direct result of well spacing, some comparison could be discussed. The TSC accounts for the shale intervals that seem to be connected to the one at the right size and elevation, being observed at the adjacent well. The continuity of the connected shale intervals can then be determined based on the spacing between the adjacent wells. Adding more wells in the area results in capturing more shale intervals and possibly higher number of connection (larger TSC). The rate of the increase in TSC depends on the well distribution covering the area of interest, as well as the shale distribution. More wells provide more information which results in the growth of TSC.

The TSC algorithm with fixed parameters is applied to the simulated realizations to count the shale intervals appeared to be connected. On average, the counted connected shales observed by adjacent wells increase with the increase of the shale continuity relative to its vertical thickness.

The other factor, well spacing, determines the number of shale connections that could be captured. These factors are all relative. Closer well spacing does not necessarily result in TSC growth, but depends on the shale continuity, too. For example, if the shale intervals in the area are less than 30 m long and the wells are spaced more than 60 m from each other, no true shale connection is captured. But if the wells are 20 m apart, then the possibility of more shale intervals being identified is higher. The influence of the number of wells and the well spacing are dependent; the interdependence between the two factors in addition to the shale

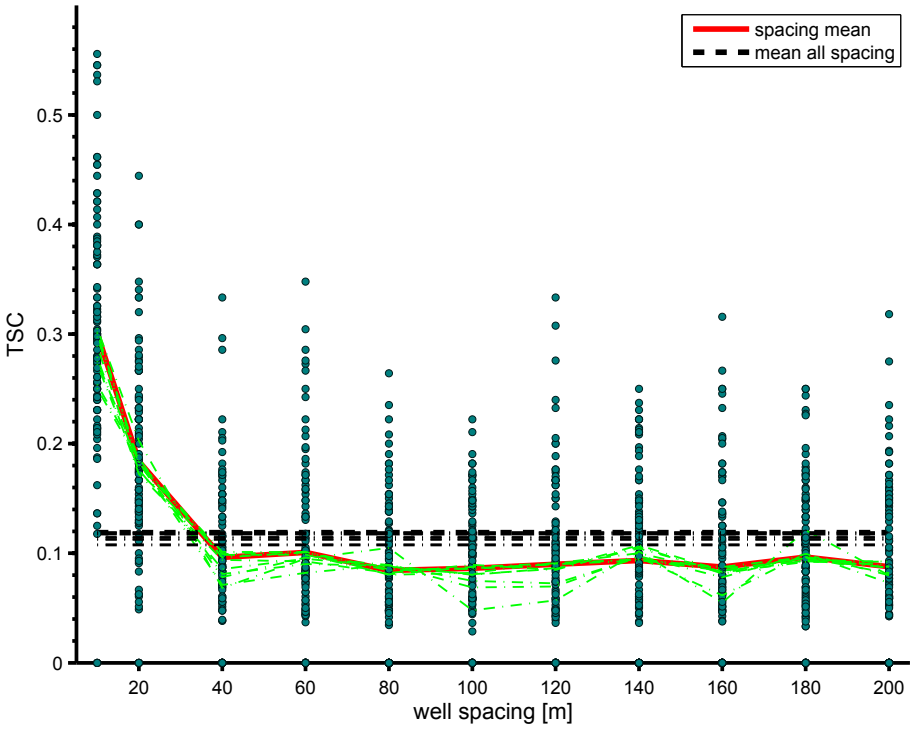

Figure 3.6: Changes in TSC for the increase in the number of wells and/or well spacing. For specific well spacing shown on the x-axis, the TSC is calculated for many realizations. A systematic drop of TSC can be observed as the well spacing grows larger. Note that 10 well pairs are available in every scenario. The red line connects the mean TSC for every scenario, and the dashed green lines is the mean for TSC values when the number of well pairs is growing larger from 2 to 10 well pairs. The black line represents the mean TSC when 10 well pairs are available and every well pair has a different spacing.

continuity makes the parametrization of their correlation challenging. What could be said is that TSC increases in the presence of more number of wells, with the proper spacing relative to the shale continuity. Figure 3.6 illustrates these factors in a TSC versus well spacing plot. Recall that such interdependency is established by the Monte Carlo simulation in the proposed inverse modeling approach.

An example is designed to discuss the implementation details in terms of main TSC evaluation and simulating and calculating the random TSC as well as discussing the relationship between the shale continuity and well spacing. A synthetic reservoir volume with dimensions of 1100 m $\times$ 2200 m $\times$ 60 m and 94% NTG is generated for this example. Wells are drilled at 9 regular spacings of 100 m, 500 m, and 900 m along easting, and 200 m, 1000 m, and 1800 m along northing. Then the well pairs are placed at certain spacing to the east of all the 9 wells, with well spacing of 30, 60, 80, 100, 120 and 140 m. The model is filled with isotropic shales of the same continuity which occupies 6% of the volume. The lateral continuity of shales are

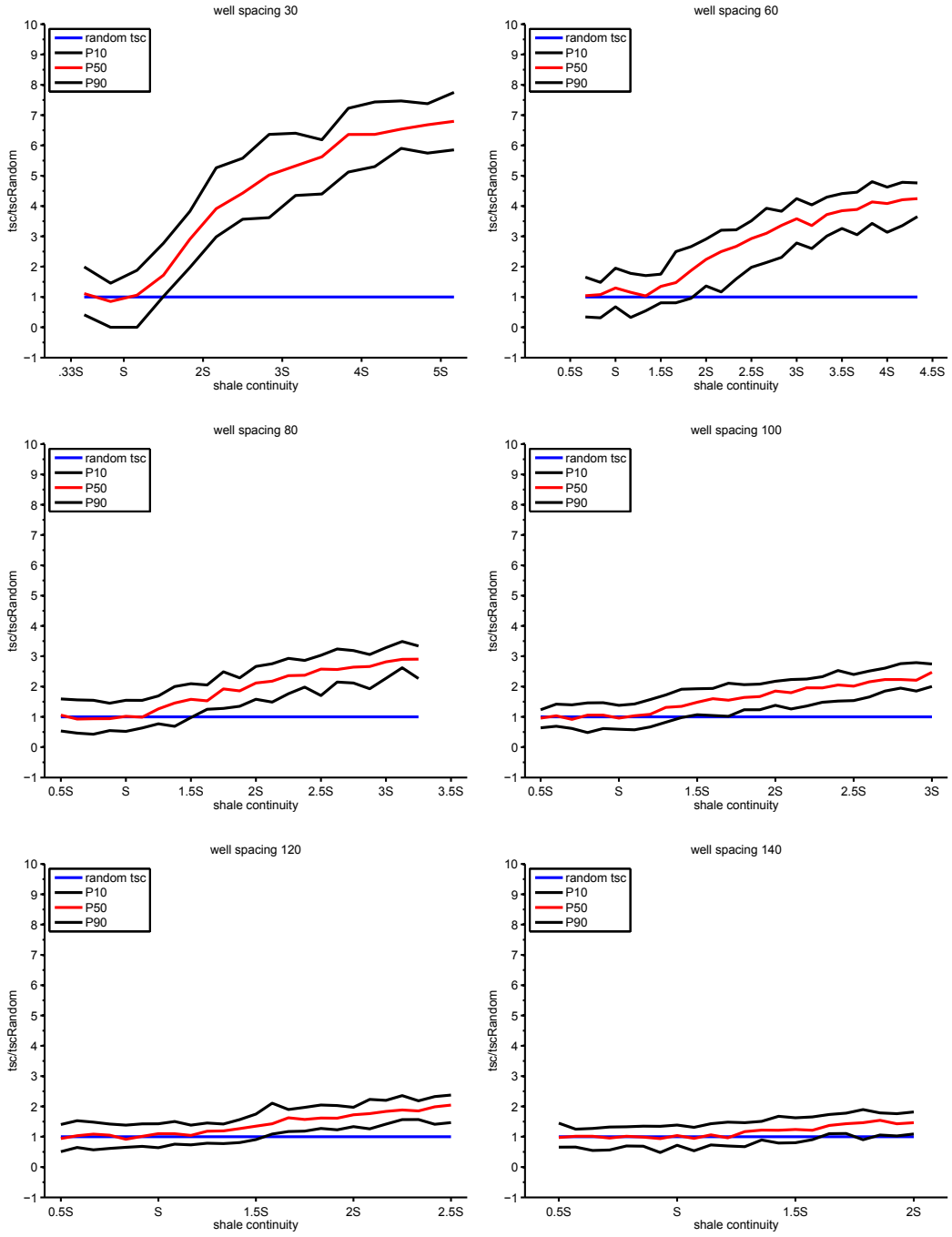

Figure 3.7: The scatterplot of TSC versus the shale continuity for well spacing of 100, 120, 140, and 160 m. As can be observed the area of the cloud above random TSC decreases as the well spacing increases.

changed from 10 to 400 m. The main idea is to have a large range of shale continuity which covers from half the well spacing to about 4 times the well spacing. As the well spacing increases, relative TSC seems to flatten off and become closer to the relative TSC of 1 since less information regarding shale continuity can be collected.

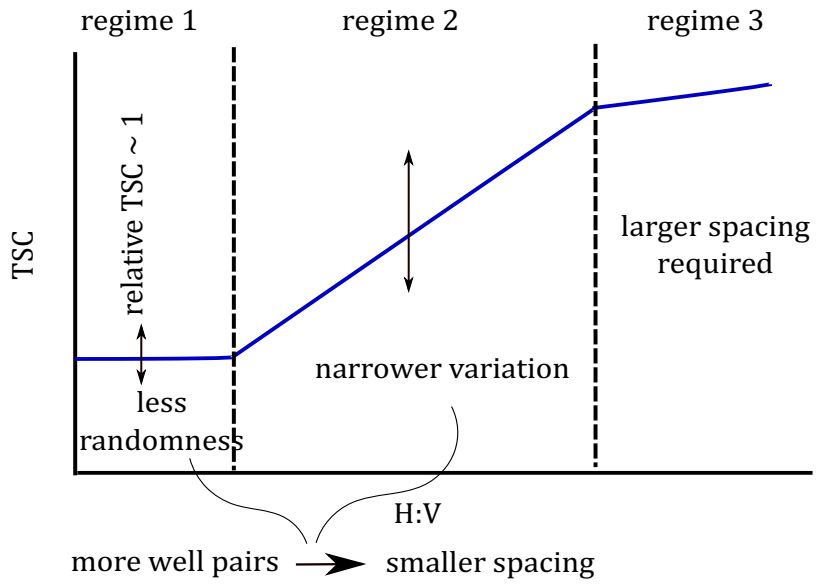

Figure 3.8: The three regimes defined considering the interdependency between shale continuity and well spacing.

The scatterplots of relative TSC (fraction of TSC over the random TSC) versus shale continuity for well pairs of constant spacing are shown in Figures 3.7. The P10, P50, and P90 are shown instead of the entire cloud of TSC values. The area of the cloud under the value 1 (where TSC equals the random TSC) increases as well spacing increases. Looking at these plots, the following regimes could be defined as (a) shale continuity is smaller than well spacing ($H < 1S$), then the observed TSC would be very close to random TSC; (b) shale continuity is between the well spacing and 3 times larger than well spacing ($1S \leqslant H \leqslant 3S$), then the observed TSC is reliable and inference of shale continuity is more precise; (c) shale continuity is significantly larger than the well spacing, by more than 3 times larger ($H > 3S$), then the results are not representative and those wells spaced further apart should be selected for the shale continuity inference (see Figure 3.8).

3.3 Formulation of Inverse Stochastic Approach

This section discusses the approach to estimate the distribution of the shale lateral continuity from observed TSC. The inverse modeling approach determines the probability for every simulated H:V ratio to contribute to the estimation of the probability distribution function of the shale continuity. The probability distribution of shale continuity given TSC is proposed to be inferred inversely from the intersection of the observed TSC with the cumulative distribution function (cdf) of simulated

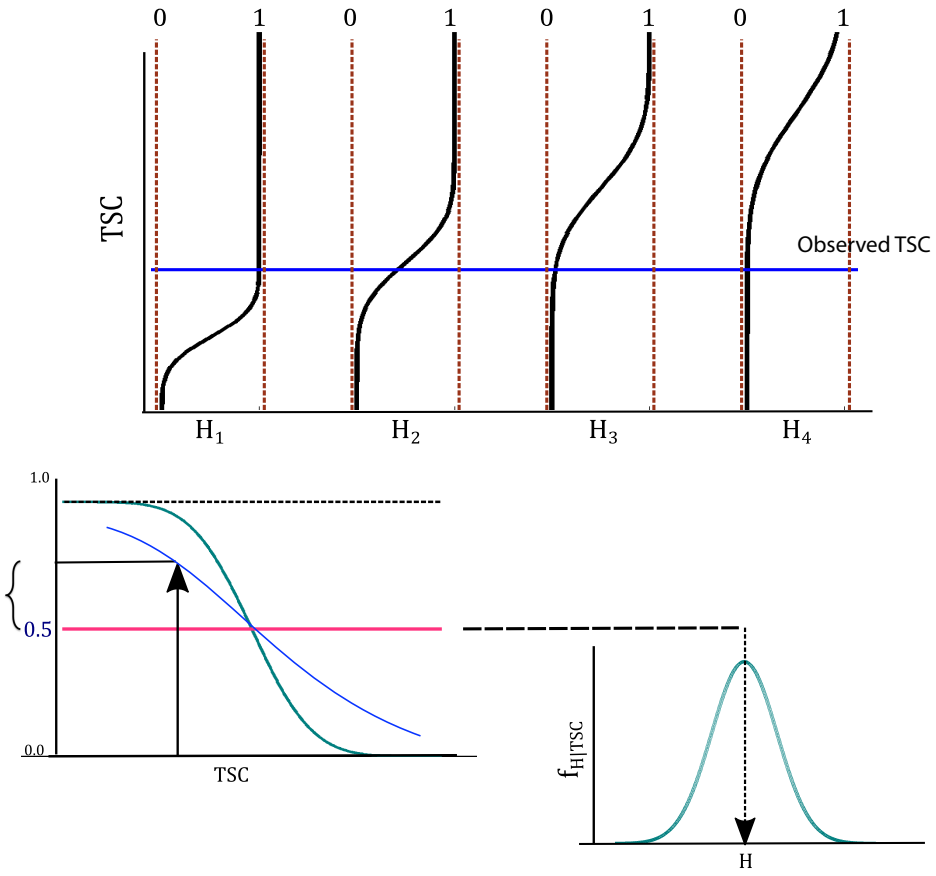

Figure 3.9: Estimating the probability distribution of lateral continuity of shale barriers from cdf of TSC for different H:V anisotropy ratios. The cumulative distribution function of TSC is determined for every H value. This is depicted in the top plot where F_{TSC} are shown for some shale continuity of H_1, H_2, H_3 and H_4. The solid blue line represents the observed TSC which intersects with all these cdfs at some points. This intersection is considered as the probability value for the corresponding H once forming the probability distribution of shale continuity. This probability value is evaluated by comparing the intersection point on the cdf with the 0.5 value. Thus, the mode of the a posteriori distribution is where the observed TSC intersects the cdf at the value of 0.5.

TSC for every H:V ratio. This information is contributed into the shale continuity by the following proportionality

$$f^*{}_{H|TSC}(h) \;\propto\; (0.5 - |0.5 - F_{TSC|H=h}(TSC_{\text{obs}})|) \tag{3.1}$$

which basically forms the probability distribution function of H given TSC. In other words, if the intersection point of TSC_{obs} and H distribution is considered to be the mode of the probability distribution function of H—TSC, then deviation from 0.5 on the cdf of TSC—H, is the amount of contribution of that corresponding H value in $f^*_{H|TSC=TSC_{\text{obs}}}(h)$; see Figure 3.9. This value is still altered with the weighting factor of $f_H(h)$, as will be described momentarily.

The inference of shale continuity from observed and simulated TSC is now described. Considering both shale continuity, H, and TSC, the following relation of conditional cdf holds true:

$$F_{H|TSC}(h)\ F_{TSC}(tsc)\ =\ F_H(h)\ F_{TSC|H}(tsc) \tag{3.2}$$

Recall that H is considered instead of H:V ratio to simplify the written formulas.

In (3.2), $F_{H|TSC}(h)$ is being calculated, and $F_{TSC|H}(tsc)$ is measured from the simulation of the particular shale continuity with fixed NTG and well configuration. Taking the derivative of both sides of (3.2) with respect to the variable H, the following will result:

$$\begin{aligned} \frac{d}{dh}[F_{H|TSC}(h)]\ F_{TSC}(tsc)\ &=\ \frac{d}{dh}[F_H(h)]\ F_{TSC|H}(tsc) \\ f_{H|TSC}(h)\ &=\ \frac{f_H(h)}{F_{TSC}(tsc)}\ F_{TSC|H}(tsc) \end{aligned} \tag{3.3}$$

The relationship in (3.3) could be interpreted as the probability distribution function (pdf) of shale continuity for a given TSC is proportional to the conditional cdf of TSC given shale continuity and the weighting factor of marginal distribution of shale continuity. Thus, the approximation shown in (3.1) shows the following proportionality exists:

$$f_{H|TSC=\mathrm{TSC_{obs}}}(h)\ \propto\ f_H(h) \times F_{TSC|H}(\mathrm{TSC_{obs}}).$$

For the case where there is no real *a priori* knowledge on the distribution of H, considering uniform distribution is reasonable which results in:

$$f_{H|TSC=\mathrm{TSC_{obs}}}(h)\ \propto\ F_{TSC|H}(\mathrm{TSC_{obs}}).$$

One way to validate the proposed approximation is to design an example with Gaussian assumption where the conditional distributions can be determined with an exact mean and a variance. Thus, the exact probability density function of the conditional distribution could be compared with the estimated pdf when derived from Relation 3.3. If TSC and H are denoted by variables Y and X, respectively, for a given Y in a joint Gaussian distribution, the probability distribution function of X, $f_{X|Y}(x)$, can be written as a Gaussian distribution with the mean, m_c, and standard deviation, σ_c, where

$$m_c = m_x + \rho\ \sigma_x\ \frac{y_0 - m_y}{\sigma_y},$$

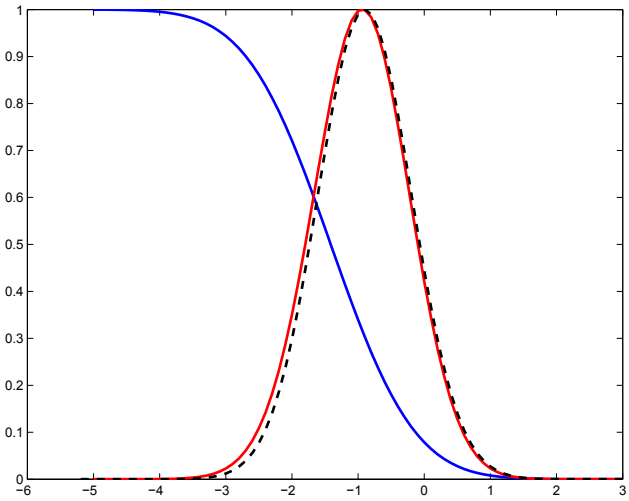

Figure 3.10: The illustration of the exact conditional Gaussian distribution, $f_{X|Y}(x)$, and the approximated one, $f^*_{X|Y}(x)$, from the cdf approach of (3.1) which is evaluated for the Gaussian example. There is a clear match between the two conditional pdfs when the Gaussian marginal distribution of $f_X(x)$ is also applied as the weighting factor to the cdf approximation when $y_0 = -1.0$.

and

$$\sigma_c{}^2 = \sigma_x{}^2 \ (1 - \rho^2).$$

Now, considering the proportionality in (3.3), the approximation of probability distribution of $X|Y$, is as follows:

$$f^*_{X|Y=y_0}(x) \propto F_{Y|X=x}(y) \times f_X(x)$$

where

$$F_{Y|X=x}(y) \ \sim N(m_c, \sigma_c),$$

and

$$m_c = m_y + \rho\sigma_y \frac{x - m_x}{\sigma_x},$$

and

$$\sigma_c{}^2 = \sigma_y{}^2(1 - \rho^2).$$

Without loss of generality, m_X and m_Y are assumed to be 0, and σ_X and σ_Y are assumed to be 1. Also, the correlation factor of $\rho = \sqrt{0.5}$ is considered for the joint distribution of f_{XY}. The point of $y_0 = -1.0$ is the at which the conditional probability is of interest. As can be observed in Figure 3.10, the approximated distribution of X given Y, $f^*_{X|Y=y_0}(x)$ closely follows the exact distribution, $f_{X|Y=y_0}(x)$.

3.4 Case Study

This section implements the inverse modeling approach to an area covered with 8 wells of varying spacing shown on the top left of Figure 3.11. The TSC is determined for 5 well pairs with specific parameters of 4° line of sight and 20% size deviation of the shale intervals between the two adjacent wells. Note that as discussed earlier, the parameters for TSC evaluation should be adjusted based on geological understanding or knowledge of wells configuration. Also, for this case, the shale intervals of less than 3 m thickness are considered in TSC evaluation. The study requires generating many realizations with shales having different H:V ratio with the same NTG as the study area which is about 92%. The realizations are generated for H:V ratio changing within the range of 10—300 with intervals of 10. For every H:V ratio, 40 realizations are generated covering the same region as the study region. The available well data is approximately 60 m thick over an area 1400 m along east and 2400 m along north. The TSC algorithm with the same parameters is applied to every realization of every H:V ratio. Note that the selection of H:V ratio is not arbitrary: it is originated from the geological understanding of the area, data and well configuration. When the observed TSC reaches some conclusive information with regards to the simulated shales and the wells configuration (correlating the shale intervals), the validation of this inverse modeling approach is confirmed.

A grid-free scheme is implemented to ease computational cost of the shale generation, well drilling, and TSC evaluation to avoid dealing with large 3-D volumes which for this study would be at least 1200 ($= 40 \times 30$) models. The idea is to evaluate the number of objects (e.g. ellipsoids), in order to cover the non-net reservoir, i.e. 8%. Then those amount of objects are randomly placed in the region of study. Depending on what shale continuity is applied, the volume of the shale is considered to be equivalent to the volume of an ellipsoid with circular plan view. Then, to calculate the number of objects required to cover the non-net reservoir is straightforward: it is determined by dividing the non-net reservoir volume by the volume of the shale (ellipsoid). Note that since objects are randomly placed in the model, there is a probability that the shales will overlap. However, since the volume of non-net reservoir is small relative to the net reservoir, accounting for a very small percentage overlap is neglected.

After the shales are placed in the model with the proper geometry and coor-

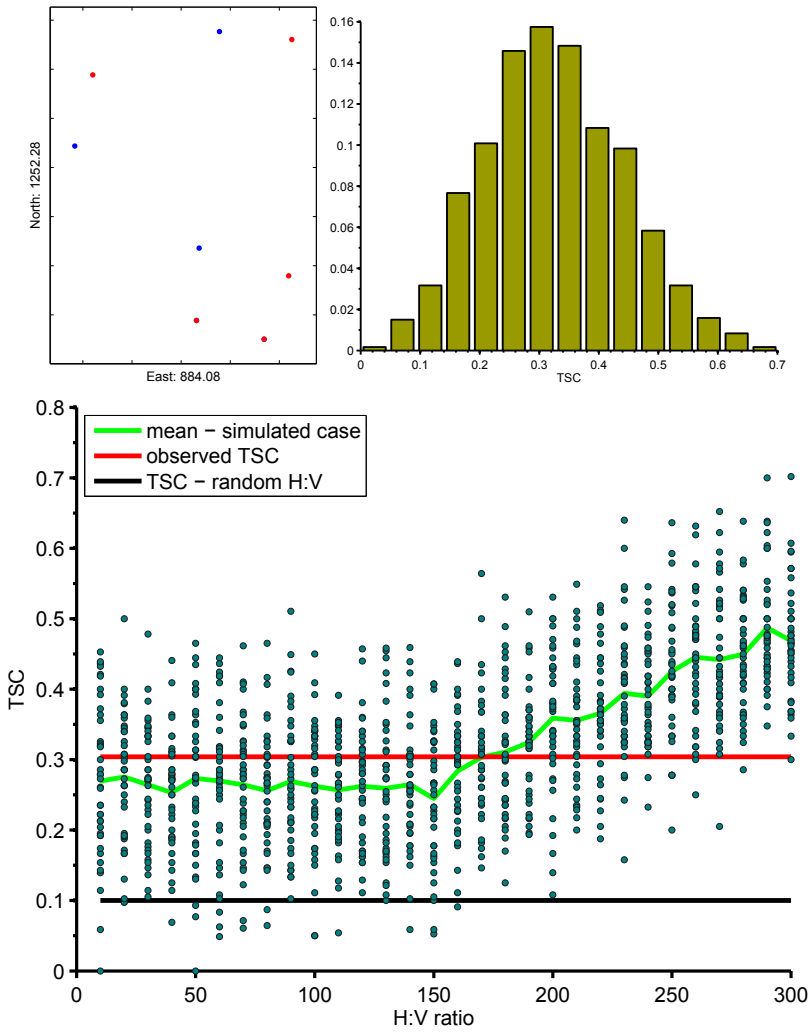

Figure 3.11: Map of the well configuration for the case study for the case study (top left corner). TSC is determined for cases of H:V ratio changing from 10 to 300 m. There are 40 realizations simulated using object based modeling technique for every case of H:V ratio (shales are modeled as ellipsoids shown in Figure 3.8). The specific well configurations must remain unchanged for inference from inverse approach study. The observed TSC calculated from the real data, shown in solid red, is about 0.304 (number of connected shales over the number of potential intervals for connection). The TSC distribution generated from 1200 realizations is also shown. The same well configuration captures TSC of about 0.1 (shown in solid black), if the non-net reservoir is covered with random shales of different continuity and locations.

dinates, the overlap between the shales and wells are studied. Any overlap is the detection of a shale interval. Depending on how the shales are distributed, the thickness of the shale interval varies. For example, if a few shale intervals are stacked on top of each other, then the shale thickness appears large. Note that the simulations in this approach are performed unconditionally since conditional object based modeling algorithms are non-standard and not available to this study.

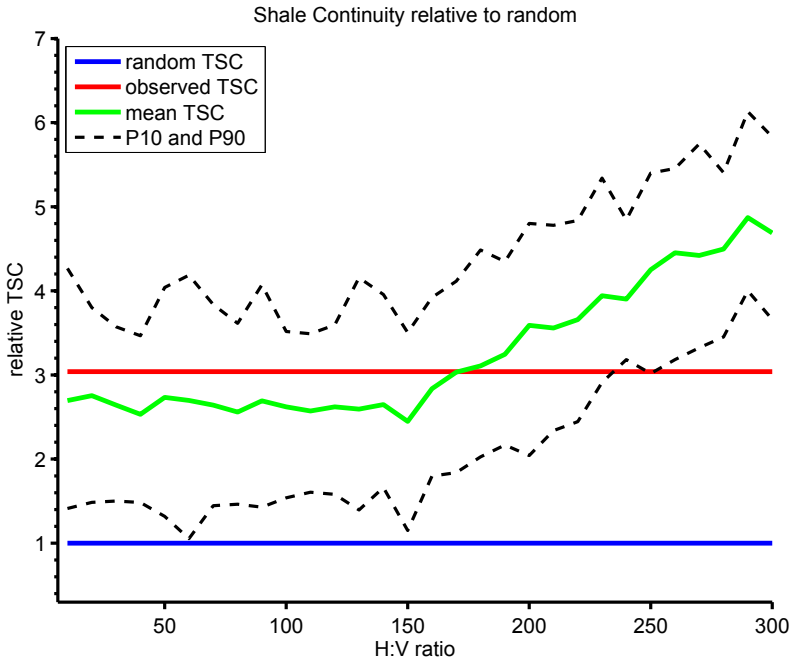

Figure 3.12: Relative TSC which is the ratio of TSC over the random TSC is calculated for the realizations in Figure 3.11. The mean TSC for every case of specific H:V ratio is shown in solid green and the P10 and P90 quantiles are shown in dashed black. As can be seen the P10 quantile is above the value 1 which represents the relative random TSC. This basically means that 90% of the time the evaluated TSC for the proposed scenarios are higher than random TSC. This could be considered as an insurance to the inference of probability distribution of shale continuity.

The advantage of this grid-free scheme over the simulation of grid cells is that it is not actually required to place the objects within the volume and store them. Once the centres of objects are randomly assigned in the area, the surrounding occupied grid cells could be identified with simple geometry. The well locations are also known from the well configuration, therefore, the portions of shales that intersect with the wells could be readily determined and the TSC evaluation could proceed with wells' intervals of shale and sand.

Figure 3.11 shows the scatterplot of TSC values for the range of simulated shale continuity. The mean of TSC for all 40 realizations is shown with the solid green in the plot. The mean value for TSC of different scenarios grows larger with an increase in H:V ratio as expected; as the lateral continuity of shale increases, the chances for a shale interval to be identified as connected to another shale interval also increases. Also, the solid black line in this figure represents the random TSC which is determined from the average TSC over many realizations with random shale continuity in the same reservoir model and well configuration.

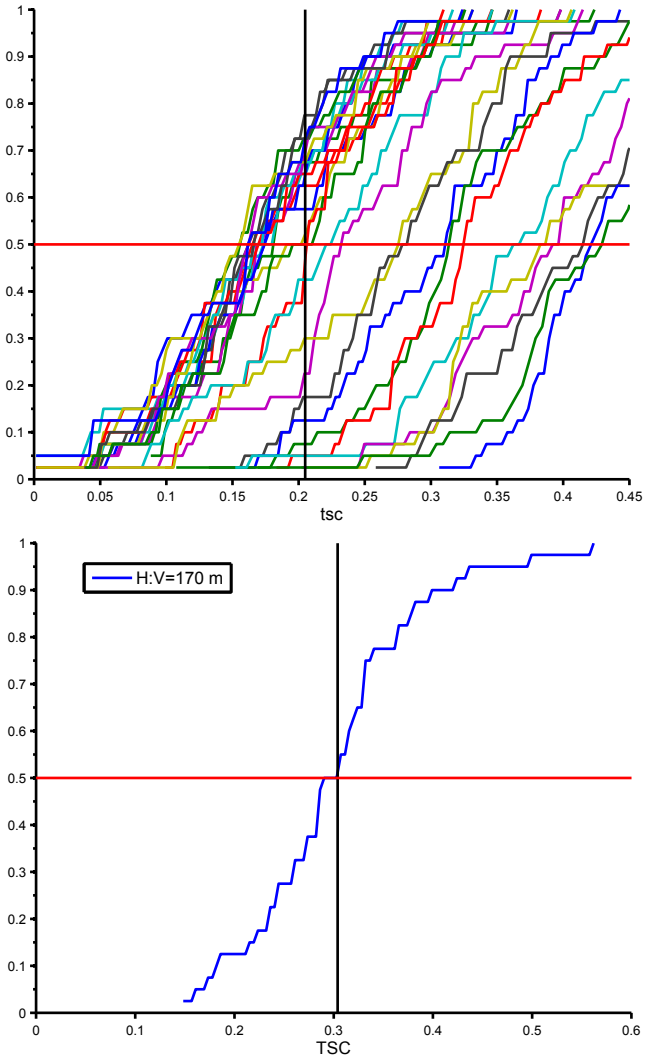

Figure 3.13: The modeled distribution of TSC for every case of H:V ratio. In this study, kernel estimation is used to model the distribution non-perimetrically. The vertical black line indicates the observed TSC which is shown in red in Figure 3.14. The observed TSC line intersects the probability distributions at different values. The second plot shows the TSC probability that intersects with the observed TSC which occurs for the H:V ratio of 170 m. This is also considered as the mode of the a posteriori distribution of the shale continuity distribution.

The results show that the 5 well pairs over the study area with specific well spacing and locations detect 0.304 of shale intervals to be connected. In Figure 3.11, it can be observed that the gap between 0 and random TSC is almost empty. The random TSC which has been calculated from random shale continuity realizations is very close to 0.1 as well. This value is almost 33% of the observed TSC. This confirms that the observed TSC is reliable and has information regarding the shale continuity. In other words, if the observed TSC was just random, it should have stayed around 0.1. Interestingly, most realizations in all different H:V ratio cases have their TSC

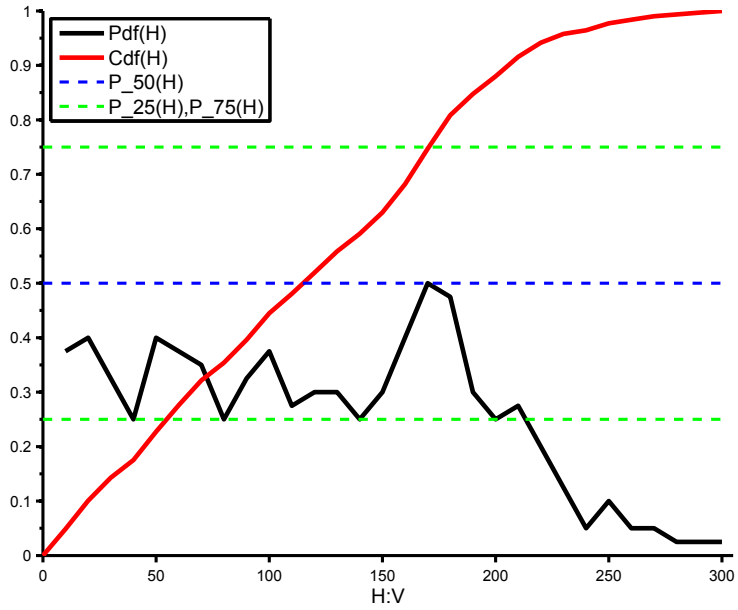

Figure 3.14: The empirical estimation of the horizontal continuity of the shale barriers is mostly distributed around 30 to 220 m. The empirical cdf of shales continuity distribution is plotted in red. The P50 is about 115 m, while there is also 50% probability for the shale to have an areal continuity between 50 to 160 m. It can be concluded that the shales in the study region most probably have an H:V anisotropy ratio of 115.

larger than the TSC value of the random case. Looking at the Figure 3.12 where the y-axis represents the relative TSC (fraction of TSC over random TSC), 90% of the TSC of simulated scenarios are above the minimum threshold which is indicated in solid blue.

As the scattered points in the same figure represents, there is a TSC distribution for every case of H:V ratio. The observed TSC intersects with these distribution at a different point; see Figure 3.13. For some of the distributions, the intersection happens at higher end of the probability distribution and for some it happens at the lower tail. The CDF of TSC for shale anisotropy of 170 m intersects with observed TSC at 0.5 value. Thus, applying the proposed inverse modeling approach, this H:V ratio represents the mode of the a posteriori distribution of shale continuity as shown in solid black in Figure 3.14. The solid red is the cumulative distribution function of the inferred probability distribution of the shale continuity. The median of this distribution is around H:V ratio of 100 m and the P25 and P75 of the estimation are changing between 50 m to 150 m. Thus, it could be concluded that in this reservoir, based on the data and well configuration, the shales mostly have 100 m of shale continuity if the thickness is 1, and this value could vary from 50 to 150 m.

The agreement between the expected shale continuity (imposed in generating the shales) and the conclusions that are drawn from TSC evaluation support the validity of the proposed inverse modeling methodology.

3.5 Chapter Summary

Uncertainty in reservoir characterization comes from the lack of knowledge of reservoir geometry, property distribution, fluid flow and response to external stimuli. In this chapter, the lateral continuity of thin stochastic shales is addressed. An inverse modeling approach is proposed to quantify the lateral continuity of shale barriers in the regions with high NTG. The basis of this approach is on measuring the shale intervals seen by well pairs that appear to be connected within the constraints of some defined parameters such as the line of sight, and difference in the size of the shale intervals. This measurement is called TSC and once calculated for well data would be considered as the reference point for the inverse modeling approach. The basis of inverse modeling approach is to infer the shale continuity from the TSC measured for cases of simulated realizations with shales of certain continuity to cover the study area. The shale continuity simulated in the realizations is changing for a range of values that best represents the characteristics of the reservoir (a priori distribution of shale continuity based on geologic understanding of the reservoir). The intersection of observed TSC and simulated TSC would be considered to infer the probability distribution of shale continuity.

Monte Carlo simulation permits incorporating all the factors in an inverse inference process. The well configuration is one main factor in this whole analysis which is also the important parameter in TSC evaluation. The comparison of evaluated TSC for a random case mimicking the reservoir, the real case, and many simulated realizations for fixed shale continuity provide understandings on shale continuity distribution which is discussed in this chapter. Considering the proposed methodology to predict the lateral continuity of shales in reservoir with presence of facies trend has the potential for the future direction. Although the proposed inverse modeling approach is sensitive to the number of wells, well spacing, and well configuration, it is considered as a consistent analysis since all parameters, measurements and comparisons are specific to the study region and well configuration.

Chapter 4

Stochastic Model Regridding

Regridding geological models to a higher resolution for flow simulation is an important problem in geostatistical modeling. For practical reasons, over a large area, models can only be built at a relatively coarse resolution. Subsequently, the resolution of specified regions of interest must be increased before upscaling for flow modeling. It is standard practice to implement nearest neighbor interpolation to increase the resolution of models. Despite its wide use, nearest neighbor introduces spatial continuity artifacts that are often unrealistic. This chapter proposes a stochastic model regridding approach along with implementation of the automated program to generate high resolution realizations conditioned to coarse resolution models. The advantage of this workflow is discussed in a comparison to conventional nearest neighbor regridding. The chapter closes with a case study and related conclusions.

4.1 Introduction

In petroleum application, different types of reservoir evaluations and applications require models with different levels of detail and precision (Aziz, 1993; Durlofsky, 2003; Manchuk, 2010; Pyrcz and Deutsch, 2014). While a coarse resolution model might be adequate to serve purposes such as volumetric characterization of the reservoir, it might not be capable of providing suitable input to capture physics of flow near the well region. Models of higher resolutions may be required for detailed flow analysis and subsequent optimal well placement (Hewett, 1993; Norrena and Deutsch, 2002; McLennan and Deutsch, 2005b; Pyrcz and Deutsch, 2014). Detailed analysis is accomplished by implementing a regridding scheme which can introduce appropriate small scale heterogeneity. The ability to vary the resolution of numerical models to meet specific conditions for reservoir characterization is a longstanding problem

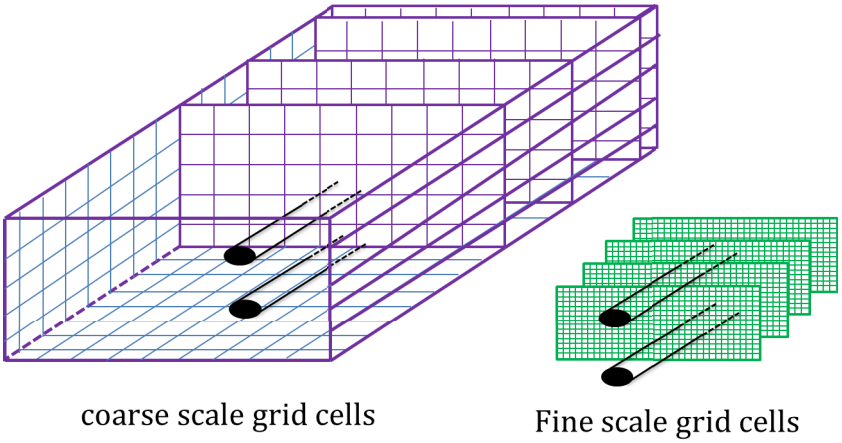

Figure 4.1: Schematic representations of the coarse resolution grid configuration for generating geostatistical realizations of the reservoir along with a horizontal well pair (left), and the high resolution grid configuration to be considered for flow simulation (right).

(Pyrcz and Deutsch, 2014). As mentioned in Chapter 1, many factors contribute to model grid selection including, the underlying reservoir geology, scale and amount of data available, types of fluid present in the reservoir, location and types of wells, development plans, objective of the simulation study, desired numerical accuracy, and available computer resources (Aziz, 1993). Yet, it is important to recognize the need for the proper resolution of the model for different regions and applications to avoid over/under representation of geological features.

In the SAGD recovery scheme, flow performance is mainly determined based on the connectivity of net reservoir near the horizontal well pairs. Small scale heterogeneities in between the wells, such as shales (as discussed in the previous chapter), disrupt the connectivity of net reservoir; this can lead to serious difficulties in accurate reservoir prediction (Nzekwu, 1997). This suggests the need for a thorough study of flow around the well pairs (Ding, 2004) which requires high resolution realizations to represent the reservoir at finer scale than what it is typically modeled; see Figure 4.1. Ding (2004) discusses the impact of different resolution models when studying well performances. Understanding the flow behavior is even more crucial when the reservoir is highly heterogeneous and coupled with non-linearity of the fluid-flow processes (Deutsch, 1987; Nœtinger and Zargar, 2004; Nœtinger et al., 2005). The flow velocity is higher near the wells and slower away from wells. Thus, it is reasonable to facilitate the numerical models with higher resolution to solve for flow equations involving more information. The precise flow analysis in heterogeneous reservoirs has been tackled by different approaches in literature. For example,

Ding (1996) and Durlofsky et al. (2000) addressed this problem by refining the near-well grid cells so that the problem of flow is reduced into homogenous permeability variations between refined cells.

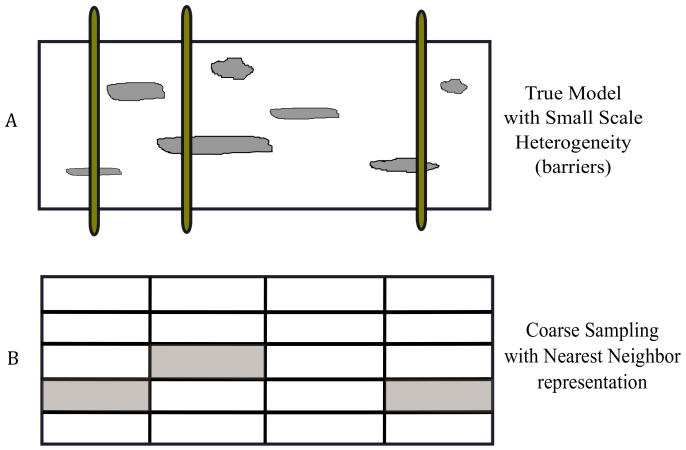

Figure 4.2: Illustration of the grid cell assignment based on well data. Model A represents the true reservoir with small shales distributed randomly. The three wells shown in A, sample three of the present shales. In model B, data samples are assigned to coarse grid cells. The shale on the left is overestimated to the coarse grid cell and the shale on the right is almost overestimated but mainly mis-located in the grid model. As a result, the effective vertical permeability is evaluated to be smaller than the true model in A.

The amount of grid cells to characterize the reservoir geology in numerical models are typically in the order of millions (Durlofsky, 2003). The amount of grid cells that could be handled in different modeling software packages has increased almost linearly with time (Durlofsky, 2005) thanks to the rapid advancement in computing technology. Also, parallel processing has augmented the capacity of handling models with larger number of grid cells. Despite computing advancements, generation of higher resolution models is still constrained by the amount of grid cells.

Depending on the grid size and its relative scale to the size of geological features, the gridding limits the features that can be represented, see Figure 4.2. Any mis-representation at this level could be transferred into finer scale model when a higher resolution is required. For instance, a shale continuity of 25 m is overestimated when generating a coarse scale model of 50 m by 50 m cell size. This model, if regridded to 25 m by 25 m grid cells, would not correctly locate the shale to **one** grid block. Using a nearest neighbor approach, the shale would be represented by at least four grid cells of 25 m areal size.

The nearest neighbor interpolation is especially inadequate when the small scale variability is high. Nearest neighbor is of earliest interpolation methods in which

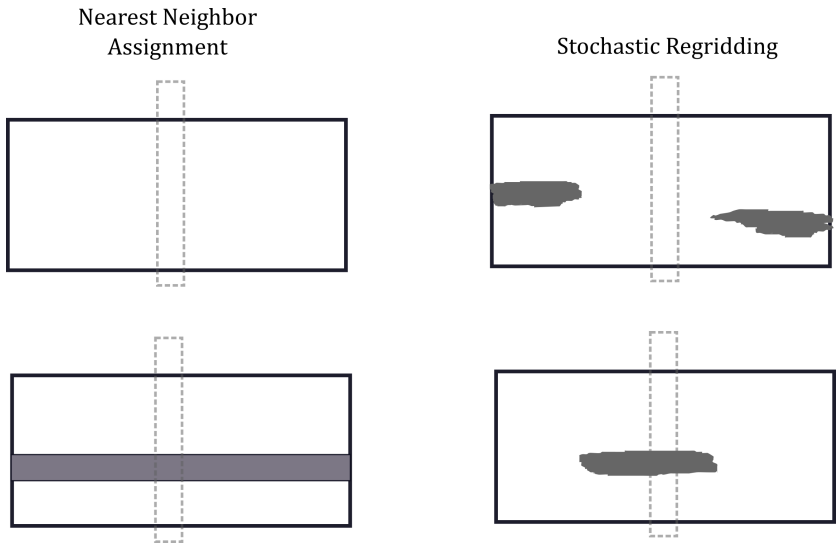

Figure 4.3: Two scenarios demonstrate the difference between nearest neighbor assignment and stochastic regridding approach when generating high resolution models conditioned to coarse resolution one. Using nearest neighbor, the effective vertical permeability could be estimated too large or too small relative to the true distribution due to improper shale distribution.

every new grid location is deterministically defined by assigning the nearest coarse grid value to the finer grid points (Gonzalez et al., 2009). This understates the spatial variability that is expected at smaller scales (Pyrcz and Deutsch, 2014) that could also introduce bias in the flow analysis of the reservoir. Figure 4.3 demonstrates the possible bias in two scenarios (1) the shale is not detected by the coarse resolution model at the top; (2) the shale is detected by the coarse resolution model at the bottom. In the first scenario, using nearest neighbor interpolation, no shale is assigned to the grid cells around the well, thus, the upscaled vertical permeability will be overestimated. The stochastic regridding however, generates some shale variability which reduces the vertical permeability. The second scenario illustrates the opposite in which the shale is detected by the coarse resolution model. When characterizing the new grid nodes, the shale is inevitably enlarged applying nearest neighbor. The upscaled vertical permeability could drop to a very low value due to the generated shale barriers. The stochastic regridding shown on the right, depicts more realistic distributions of shale.

Grid Cell

Gridding is, of course, not part of nature; no reservoir or geologic feature comes inherently gridded. Gridding, however, is a convenient way to represent geologic heterogeneity of reservoirs and solve flow equations (Aziz, 1993). Defining reservoir

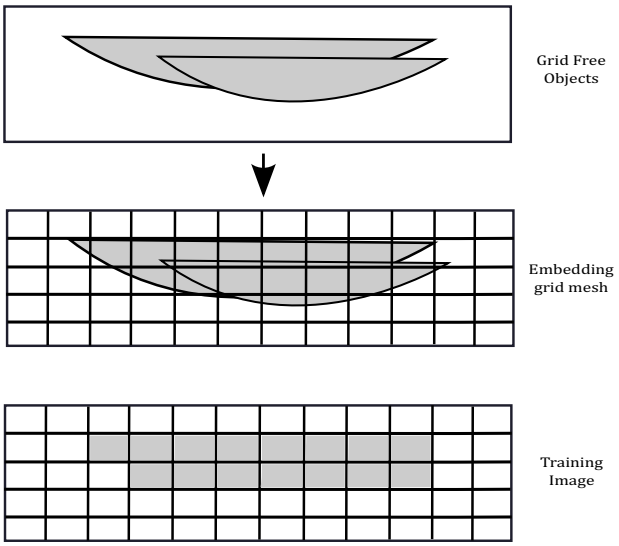

Figure 4.4: The 2-D schematic view of imposed grid system on geological models which results in inevitable deformation of objects.

models using a gridding system is equivalent to populating the spaced points with some representative properties. The grid points at the scale of the well data are typically considered to be placed at the centre of the grid's geometric shape (i.e. a rectangular parallelepiped), and the space between two grid points is the size of the grid cell. This space could be filled with points and assigned with corresponding values of interest. Although regular Cartesian grid cells are not necessarily computationally efficient, they are widely utilized in geostatistical practice and software. As explained by Pyrcz (2004), the inefficiency of the regular grid system is due to the constant level of discritization which may be different along every direction but is same everywhere in that direction. This implies that the same amount of precision to characterize the homogeneous and heterogeneous parts of the reservoir is a waste of computational capacity. A number of suggestions on model cell size selection has been discussed in (Pyrcz and Deutsch, 2014), under *Gridding for Geologic Modeling* subsection, in Chapter 3.

In addition to computational inefficiency, the grid system is a source of misrepresentation: constraining the geology into grid cells and deforming geological features into irregular shapes. For example, at facies transitions, the boundaries may be enlarged or reduced to fit with the geometric form of the regular grid shapes as can be observed in Figure 4.4. In general, as shown in Figure 4.5, the gridded distribution is different than realistic shapes encountered in the reservoir.

The following section discusses the proposed stochastic regridding approach and

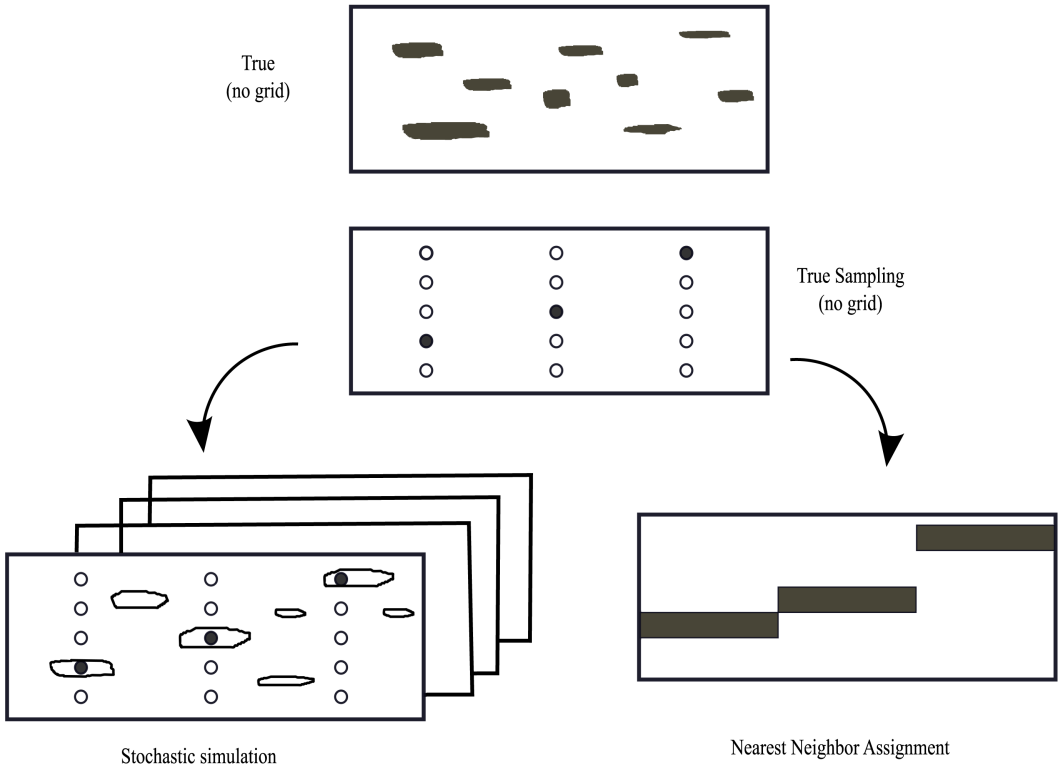

Figure 4.5: The 2-D schematic view of moving from true geology to representing the samples on models with grid system.

its implementation details to characterize small scale variabilities in high resolution models.

4.2 Methodology

The regridding process includes extracting coarse resolution information from a region of interest and characterizing the corresponding geology at a finer grid resolution. The approach presented in this chapter is to apply stochastic simulation to generate high resolution realizations conditioned to the coarse resolution simulated values. This method consists of implementing stochastic simulation, where the geologic characteristics at the new grid locations are determined via a stochastic process that accounts for the spatial structure of the geologic setting (Lajevardi and Deutsch, 2015). Thus, the simulation approach has the advantage of generating a set of realizations that accounts for uncertainty by imposing the expected variability at the small scale.

Stochastic regridding could easily become a professional and computational demanding approach as it involves constructing high resolution models of many vari-

ables. For example, in reservoir studies, a typical dataset contains facies, a primary variable (e.g. porosity or Vsh) and a secondary variable (e.g. seismic data) which are available at a coarser grid resolution (about 100 realizations). Therefore, the stochastic regridding process would require the calculation of the variogram for each variable (facies, porosity, and other variables such as directional permeability and residual saturations), and then simulation which is conditioned to coarse resolution model should be applied separately within each facies to satisfy the assumption of stationarity (Pyrcz and Deutsch, 2014). In some cases, the secondary variable might also need to be modeled at higher resolution to be considered in collocation of the primary variable when simulating the high resolution model. Often, geostatistical practitioners avoid sensitivity analysis and local studies of the reservoir due to lack of automated tools available and time constraints. Developing a stochastic regridding workflow that automatically extracts the relevant information in the area of interest and applies the sequence of the simulation processes would be professionally and computationally beneficial to reservoir characterization.

The fundamentals of stochastic regridding workflow could be summarized by (1) model extraction within the region of interest (2) local variogram determination to capture local variability, and (3) generation of 3-D model at small scale grid cells; data defined on the centroid of the coarse resolution grid cells are considered as conditioning data (McLennan, 2005).

As mentioned, in geostatistical modeling every grid cell is defined at a point rather than over an entire interval or block. In the regridding approach, the new simulated values define the corresponding properties for the grid nodes placed at higher resolution. This is more important when the initial grid system has large spacing in any of the three directions. Although, in general, the overall continuity and structure of the region should have been well captured by the initial simulation, the locally varying structure in a local part of the region will be influenced by local conditioning and stochastic variations. The stochastic regridding process is driven by the initial coarse resolution model through data conditioning. Determining the horizontal variograms of each facies is fundamental to understanding the spatial correlation of the geological structure of the reservoir. Types of facies present in the model, their spatial continuity, statistical inferences, the variables of study, and the volume of interest should be established before the regridding process starts.

One main feature that has been considered in the automation of the regridding

process is its ability to prepare such statistical information and subsequent variography determination with a limited amount of professional input. After extracting the volume of interest and acquiring the data statistics regarding the facies, their proportions, other variables of interest, and the horizontal and vertical variograms are determined for the subsequent simulation process. The local variogram is calculated for a number of directions so that the anisotropy of each facies is captured. This step could be omitted if global variograms are considered.

4.2.1 Stochastic Regridding Program

The regridding process has been automated and developed in scripting and custom programs. The process includes the extraction of specified regions of interest, definition of corresponding local variograms, and implementation of sequential Gaussian simulation (SGS) and/or SIS to characterize continuous and/or categorical variables, respectively. In each specified region, the local variography can be defined by either implementing automatic fitting algorithms or assigning the global variography initially used to build the coarse scale model. All inputs and outputs of this process are implemented in a Cartesian restored geological coordinate system. The data from the coarse scale model is assigned to the centre point of every grid cell. The refined grid size is specified by the user and the entire process of regridding is applied to each realization within each sub area under consideration.

To generate a high resolution model, the area of interest should first be identified using an origin, the length of the region of interest in all directions, and the rotation angle from the x-axis. The details of implementation and utilization of the proposed stochastic regridding approach are fully described in Appendix A. Regridding is applied on every coarse resolution realization one at a time. The realizations that are considered for regridding could be selected by the user. For example, if the user would like to have high resolution realizations for only P10, P50, and P90 selected realizations of the model, the user could execute the program only for those realizations. The resulting high resolution realizations are then created in a separate directory with specific names. Generating multiple regridded realizations from multiple coarse resolution realizations is considered as good practice since it enables the user to understand and exploit the variability of uncertainty of the high resolution realizations within and between the original coarse resolution realizations. The local coordinate system for simulation may be rotated with respect to the initial

reservoir model (see Figure 4.6).

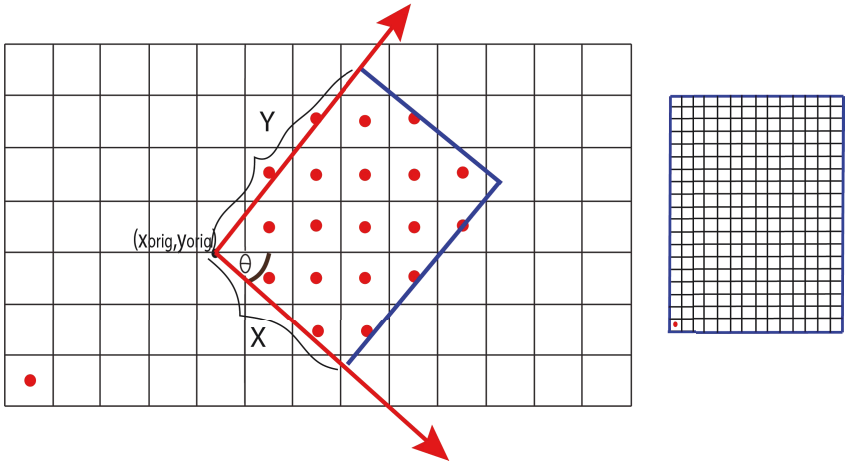

Figure 4.6: Schematic representation of the Cartesian grid for simulation and data extraction. The blue boundary represents the limits of the area of interest. The red dots represent the coarse scale nodes extracted. The angle θ is the horizontal rotation of the region studied.

After the region of interest and all its specifications have been determined, the procedure for re-simulation must be established. This decision is based on the combination of categorical and continuous variables to be processed. For the case of categorical data, the data statistics of the facies within the volume of interest must be determined. The facies proportions in the area of interest should be considered for the regridding process. In presence of continuous variables only, the entire domain of interest is assumed stationary following conventional geostatistical assumptions.

At this point, the continuity of the data variables must be determined. The variogram for every variable within each stationary facies domain is automatically calculated for a number of directions. Normally, the Z direction is orthogonal to the stratigraphic correlation and that direction is computed separately. Then, anisotropy in the horizontal X-Y plane can be determined by pre-specified directions or calculating the variogram in a number of directions with varying azimuth. There is always a chance that one category has a shortage of pairs for the variogram to be determined reliably. One option is to combine the data from different facies together. Such considerations are embedded in the program.

Note that to determine the variogram of continuous variables, the input data needs to be in normal score units since they will be used in simulation. In general, it is strongly recommended to fix the nugget effect to zero and consider two structures. It is very common to observe variograms with such variograms of different ranges

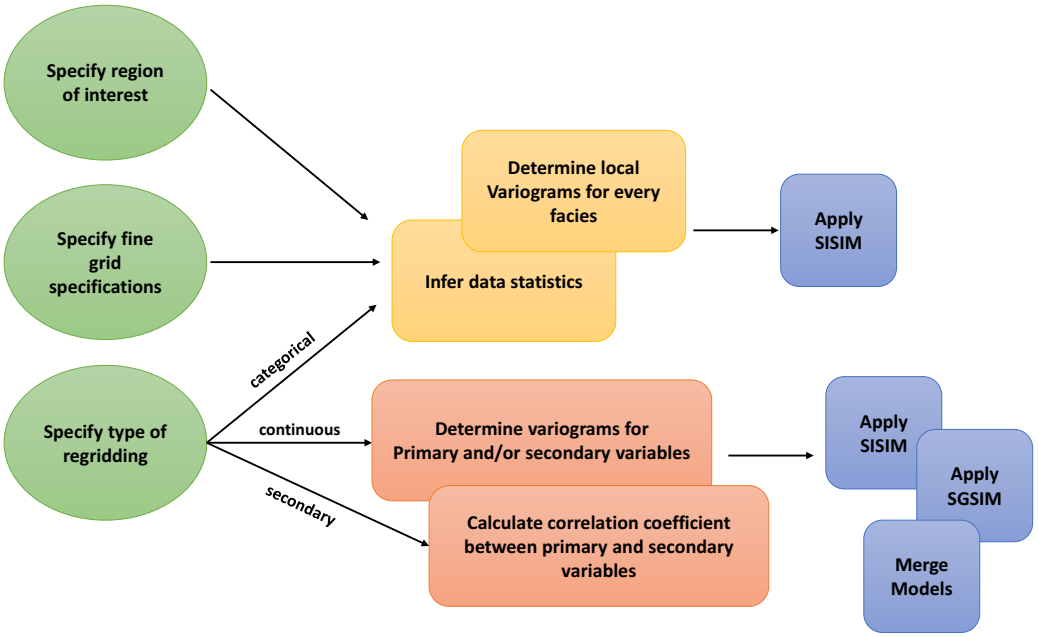

Figure 4.7: Flowchart of the stochastic regridding process.

and structures. Considering only one structure may compromise the fit for the short scale lags, which is critical for the correct short scale variability. Local variography determination is placed within the process, however, checking for the variogram outside the regridding process is always recommended.

The simulation is implemented on the new grid specification based on the dimensions of the region of interest and the resolution of the re-simulation. The parameters for simulating the regridded realizations are selected automatically although some checking is warranted. The number of facies, the facies codes, and their proportions are all extracted from the simulated values at the region of interest. The maximum search radii could be reliably kept to 4 times the original coarse grid size. Throughout the regridding process, strong conditioning from the coarse scale model permits this screening approach. Regardless of the variogram range, the closer grid nodes will get the main influence and more distant data will receive much smaller weights or even negative weights. In the presence of secondary variables, collocated cokriging could be implemented. The correlation coefficient of the primary and secondary variables is evaluated by the program for the collocated simulation.

Sequential Gaussian Simulation (SGS) is considered to stochastically regrid continuous variable at the area of interest. In SGS, the lower and upper tails of each variable distribution are required to be known. The maximum and minimum data

associated with every variable could be used in simulation. Of course, there is a small probability of even lower or greater values, but the dense conditioning due to the coarsely gridded model reduces the impact of this decision. The separate realizations of variables corresponding to different facies are then merged to fill the entire domain. The final merged models at this point are the ones which will be transferred to the specific directory of high resolution realizations. Figure 4.7 summarizes the stochastic regridding workflow which is considered in the process of automation.

Example

A data file contains 40 realizations with 100 grid nodes in the X direction, 130 grid nodes in the Y direction, and 1 in the Z direction. The cell size is 24.0 m by 24.0 m in the horizontal plane and 1.0 m in the vertical direction. The regridding is applied on the area of interest which is at (20, 20) of the original domain with the rotation angle of 10° and 240 m along the X direction and 480 m along the Y direction. The regridding process generates the models with 24×24 times higher resolution than that of the coarse resolution model (i.e. cell grid size has reduced from 24.0 m to 1.0 m).

The simulation in the regridding process exploits the spatial variability by generating multiple realizations of facies conditioned to the coarse resolution facies and the indicator variograms. The variograms for all three categories are modeled with two spherical structures and zero nugget. Figure 4.8 shows two realizations that are the result of regridding process.

The amount of variability in the simulated high resolution realizations conditioned to one coarse resolution model depends on the additional resolution to the coarse resolution model and variogram model which impose the spatial continuity. Applying the stochastic regridding conditioned to multiple coarse resolution realizations, and subsequently simulating high resolution realizations for every coarse resolution model result in generation of a large number of high resolution realizations characterizing the local spatial distribution. This large number of realizations is later considered to characterize the reservoir uncertainty and improve decision making regarding well placement and recovery evaluation.

Figure 4.9 shows high resolution realizations conditioned to a number of realizations from a set of simulated coarse resolution models. It can be observed that when the extracted area of interest is small relative to the size of the entire domain

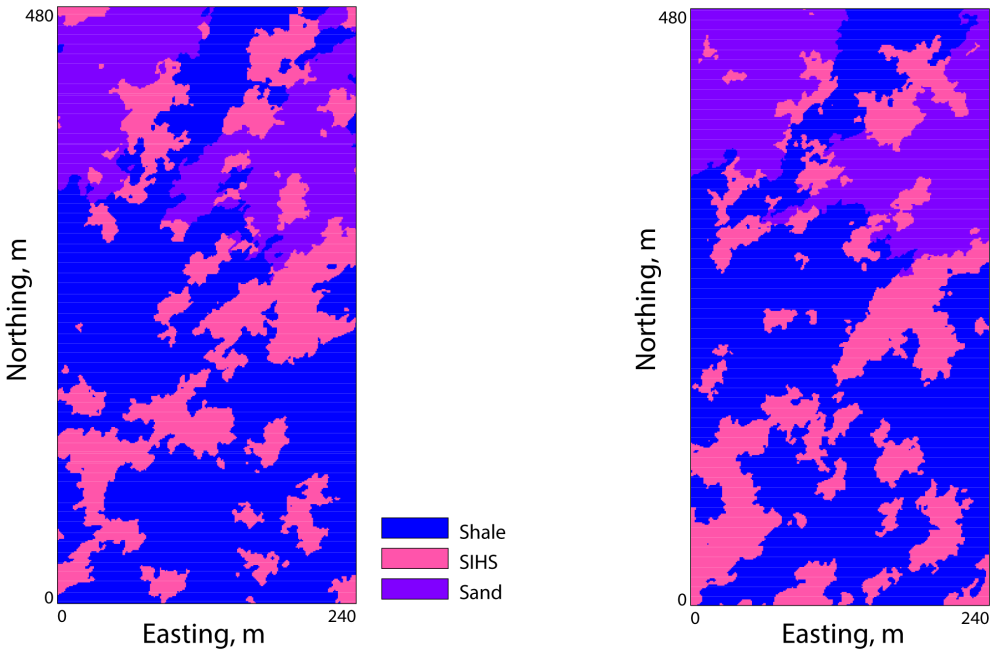

Figure 4.8: Regridded realizations of facies for the region of interest with the specifications mentioned in the Example section.

(i.e. less than one third of the entire domain), the local variogram is more directionally anisotropic which results in more variation among re-simulated realizations. However, when the extracted area of interest is relatively large (i.e. more than half the entire domain), the local variogram resembles the global variogram very closely. This can also be seen in Figure 4.10 where two regridded realizations conditioned to two different coarse resolution realizations have very similar spatial distributions although the variogram has been determined locally.

4.2.2 Analysis of Variance for Realizations

A large number of realizations could be generated to reproduce the local data and geological features yet present different possible spatial distributions. The realizations typically consider relatively widely spaced grid nodes. So far, the proposed stochastic approach to generate high resolution realizations over a region of interest is discussed. This is achieved by applying the regridding scheme which has been automated, implemented and discussed in detail.

This section discusses the variability between realizations utilizing a transfer function for performance quantification of multiple but equiprobable realizations. CHV is a highly correlated metric to some recovery performance parameters (especially in terms of SAGD recovery); such as cumulative oil production rate, and/or

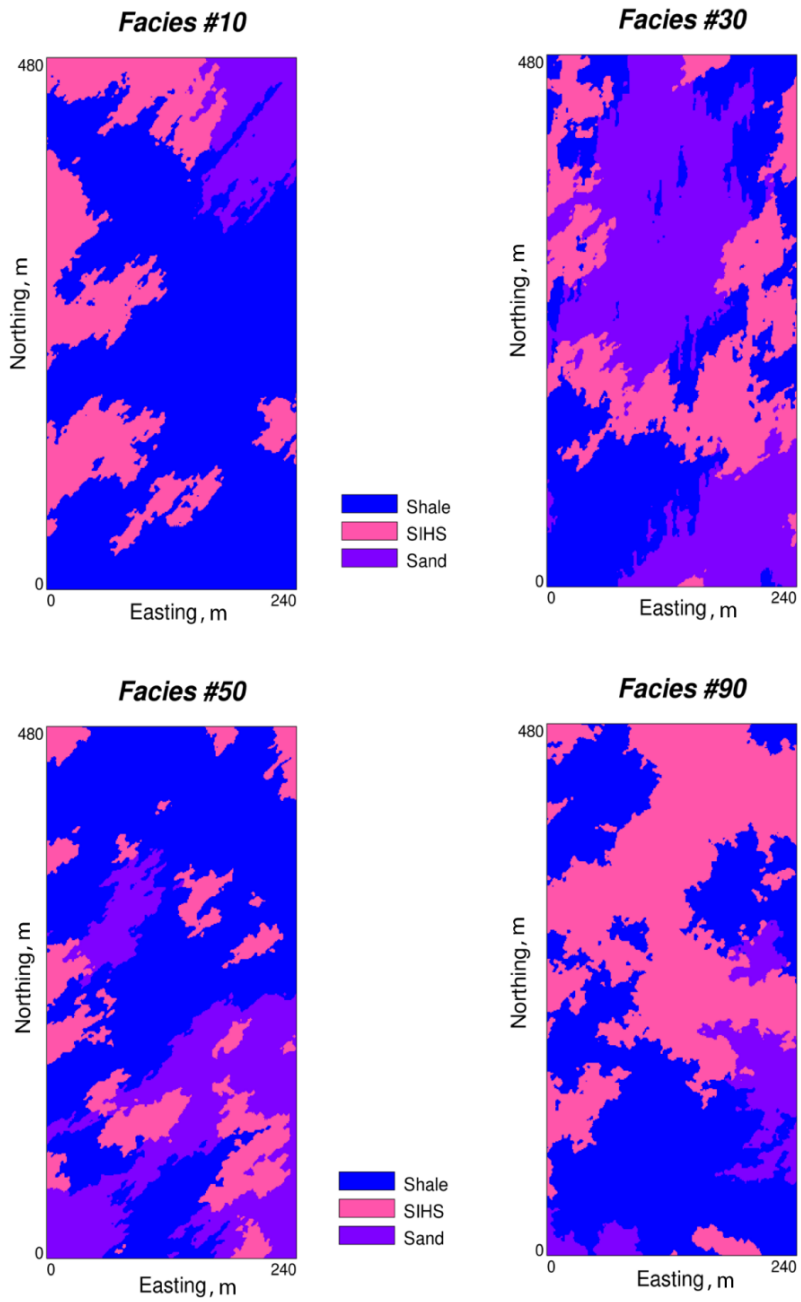

Figure 4.9: Illustration of realizations at high resolution extracted from 100 realizations at coarse grid size. Local variography and strong conditioning result in different spatial distribution.

CSOR (Fenik et al., 2009a). The CHV metric measures the connectivity considering net reservoir distribution with a local recovery window around the SAGD injector and producer well pairs. Here, the net reservoir refers to high permeability facies such as sand and/or SIHS (see the discussion on McMurray facies associations in subsection 1.1.3). For this example, the CHV is determined considering the recov-

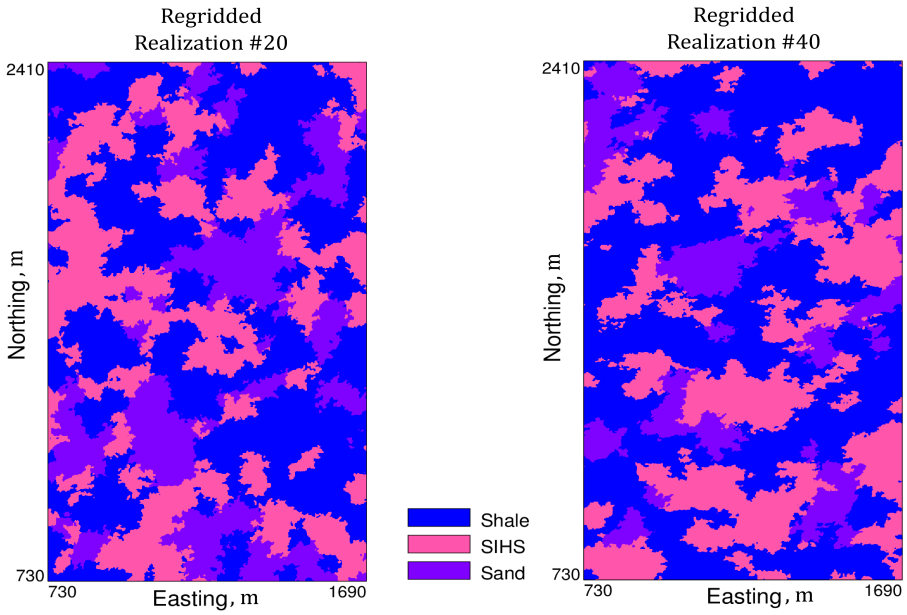

Figure 4.10: Illustration of two resulting realizations of re-simulation with resolution of 12 times higher. Since the area of interest is not much smaller than the entire domain, the local variogram does not change direction too quickly unlike the realizations in Figure4.9.

ery window around a hypothetical well pair near the middle of the region of interest in which the regridding process has been applied. The variability in CHV measurements represents the spatial variability explained by the regridded realizations. An LxM matrix with entries of CHV values, represents the spatial variability of regridded realizations both globally (column-wise) and locally (row-wise). The variability column-wise depends on the spatial variability of the domain and ergodic fluctuations.

Here, in the regridding process, L realizations, simulated at coarse resolution grid cell are selected and regridded. For every coarse resolution realization, M realizations are simulated to model the spatial distribution at high resolution. The M regridded realizations corresponding to every coarse resolution realization honor the same dense conditioning data while addressing uncertainty associated with local variability. This confirms that re-simulated realizations at finer grid cells originating from different L realizations would represent sufficient variability despite the strong conditioning. Nevertheless, given the small area, these local fluctuations reasonably represent the local uncertainty.

Considering M columns of regridded realizations conditioned to L rows of coarse resolution realization, every coarse resolution realization determines the spatial dis-

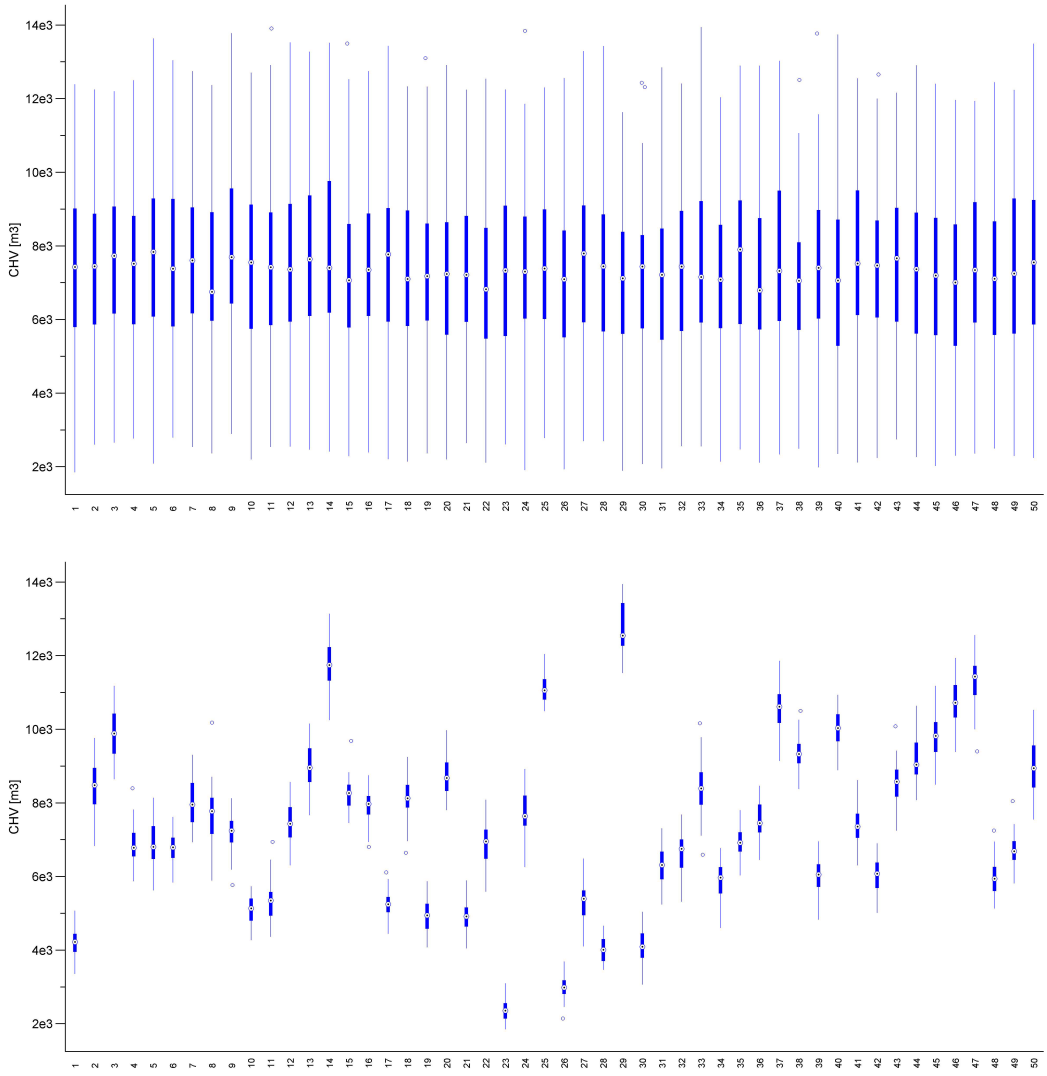

Figure 4.11: Illustration of dispersion of CHV values along the columns (top) and rows (bottom). Realizations along the columns replicate the ergodicity of simulation while the realizations along the rows replicate the features of deposit of the corresponding coarse scale realizations.

tribution and set the main features at its corresponding row (M realizations). In other words, realizations at every column, L, model global spatial distribution while the realizations row-wise display local variability. For example, if the 10th coarse resolution realization ($l = 10$) has high permeability in the area of interest, the high permeability features will be replicated along the rows when regridding is carried out. As can be observed from the top plot in Figure 4.11, the variability between the columns are very similar which is the result of ergodicity. The bottom plot in Figure 4.11 illustrates the variability within and among the rows. As expected, the variability shown is different for every row as it represents the local variability and

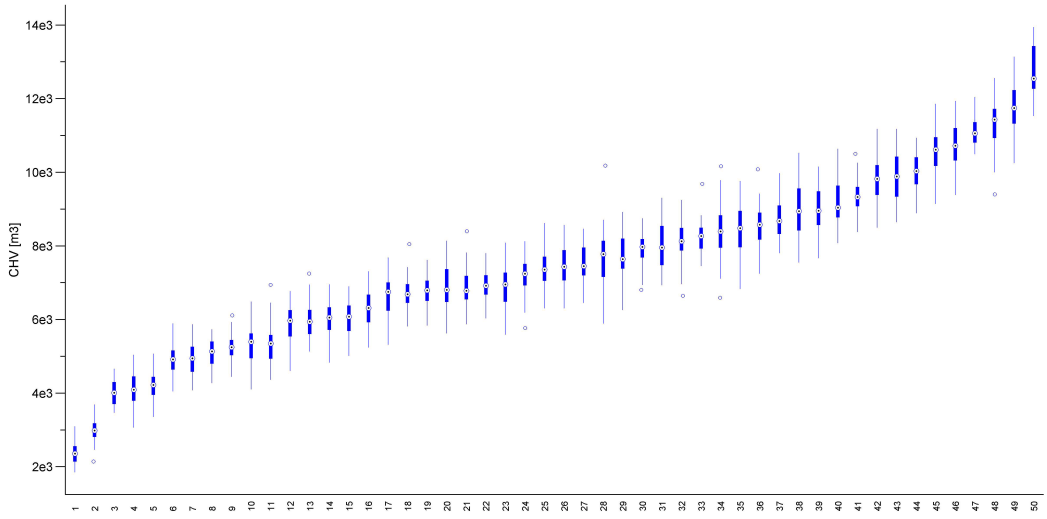

Figure 4.12: The boxplot illustrates the ranked realization based on locally re-simulated CHV values (see Figure 4.11).

features of deposit represented by its corresponding coarse resolution realization.

In the example shown in Figure 4.11, 50 realizations containing three facies ($L = 50$) are considered at coarse resolution with grid specifications of 100×100×2 and cell size of 24 m in X-Y plane and 1 m in vertical direction. The area of interest that should be extracted is 40 m in X and 20 m in the Y direction, with a rotation angle of 10° clockwise from the x-axis and the length of 720 m along the x-axis and 120 m along the y-axis. The length of the extracted area of 30 and 50 in X and Y respectively. The re-simulation is applied to the area of interest to regrid the realization to 12 times higher resolution (new cell size would be 2 m) in 50 new realizations (M =50). For CHV determination, a hypothetical well-pair is horizontally placed at the middle of regridded realization; the local window of recovery around the well-pair is almost the entire area in the regridded realization. Figure 4.11 show the variability in CHV measurements when regridded realizations are locally conditioned. The variability shown through the re-simulation of coarse resolution realizations can be utilized in further analysis such as ranking for post-processing purposes. Figure 4.12 illustrates the ranked realizations based on the CHV values determined for high resolution re-simulated realizations using the regridding scheme. The following section shows a case study comparing the stochastic regridding scheme proposed in this chapter with the conventional approach of nearest neighbor.

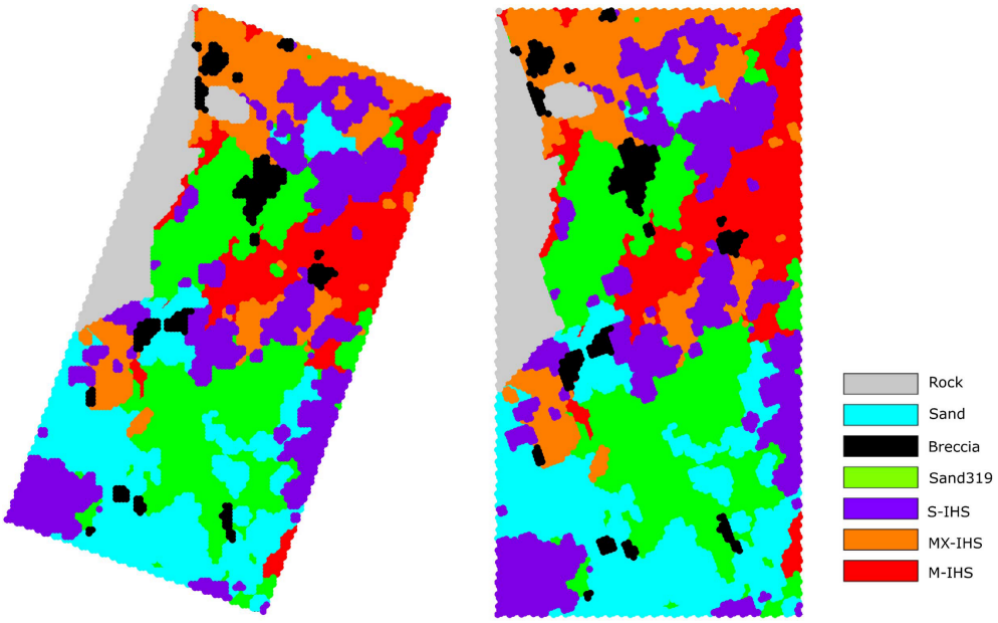

Figure 4.13: Illustration of an arbitrary slice extracted from coarse resolution model to be considered for regridding process.

4.3 Case Study

The main purpose of this section is to demonstrate how the regridding approach affects the evaluation of the flow within the region of interest. After generating high resolution models using stochastic regridding and nearest neighbor, the performance of the regridded models are evaluated in terms of flow by calculating the vertical permeability which is an essential factor in recovery performance in SAGD productions (Deutsch, 2010).

The available model for this study is the P50 coarse resolution realization as part of a model of the middle McMurray Formation. The size of the model including the null part is 8.46 km East, 11.64 km North, and 55.5 m vertically in the form of $423\times582\times111$ grid cells with cell size of 20 m $\times$ 20 m $\times$ 0.5 m. The reservoir contains six different facies: sand, breccia, sand-319, SIHS, mixed IHS, MIHS. Typically, IHS facies containing less than 30% shale is considered recoverable, and MIHS and mud are expected to be less permeable in terms of flow, as also discussed in 1.1.3. In this case study, these two facies are considered as the non-net reservoir in the model.

Figure 4.13 shows a slice of the region of interest which has been extracted with a rotation angle of 20° clockwise from the x-axis. The origin of the extracted part is selected to be (30, 40) grid cells from the origin on X-Y plane of the coarse

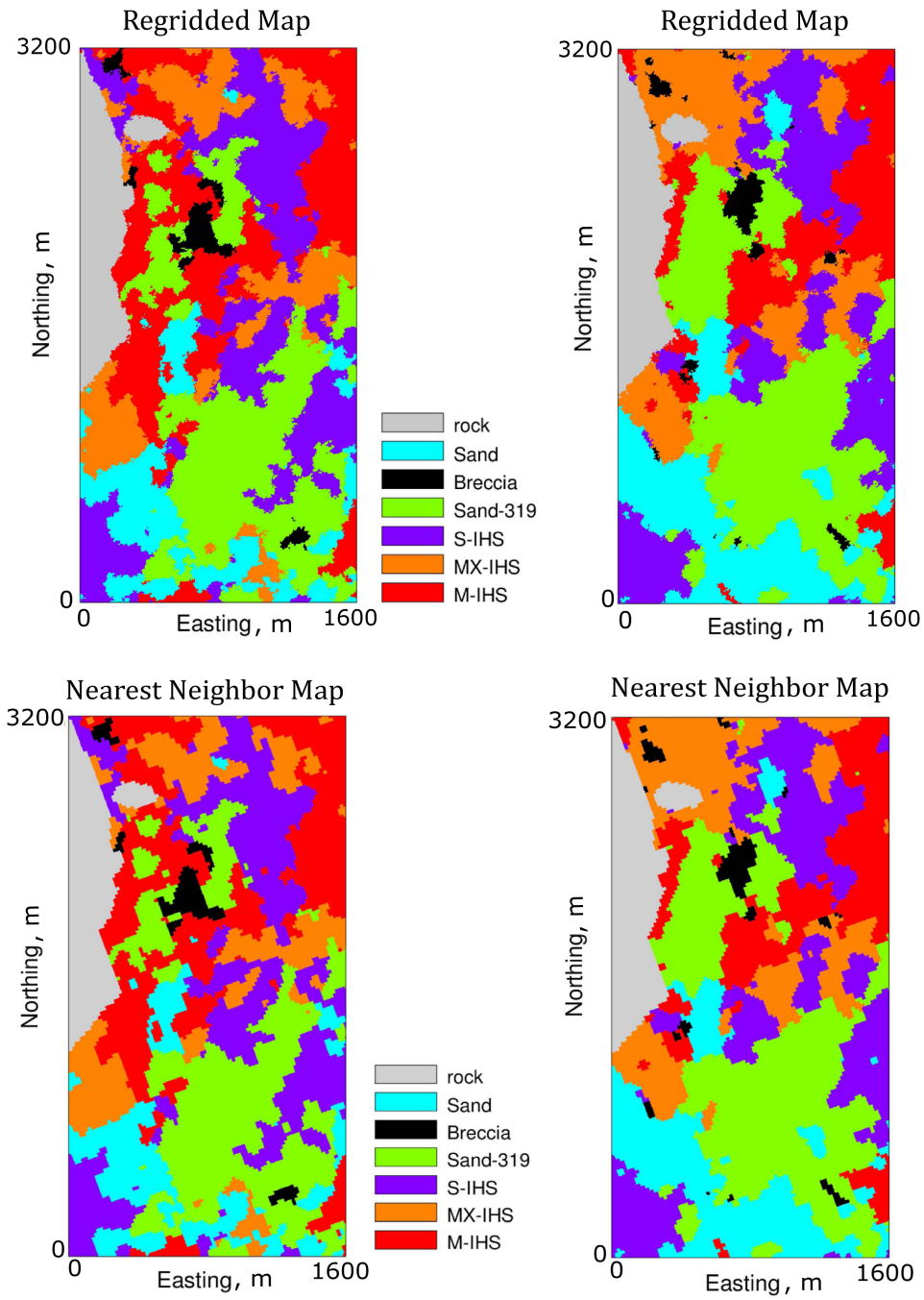

Figure 4.14: Illustration of two arbitrary slices from regridding an area of interest of the case study model. The maps at the top are generated models using the automated stochastic regridding and the ones at the bottoms are generated models using nearest neighbor interpolation.

resolution model. The extracted region is 1600 m long in X direction, 3200 m long in Y direction, and 10 m long in Z direction. This region contains about 60% of less permeable facies, with low permeability values. In this case study, facies have been modeled to construct the high resolution models at 10 times of the original scale.

Therefore, the regridded model is built at scale of 2 m × 2 m × 0.5 m, relative to the cell size of 20 m × 20 m × 0.5 m of the coarse scale model. The regridding is applied to the horizontal plane since the model has high resolution in vertical direction because of the excessive data availability from the well log data, which is almost always the case in practice. Two slices of the simulated high resolution models from the case study are shown in Figure 4.14. The surface grid of the top are generated using automatic stochastic regridding approach, and the surface grids of the bottom are the results of nearest neighbor interpolation.

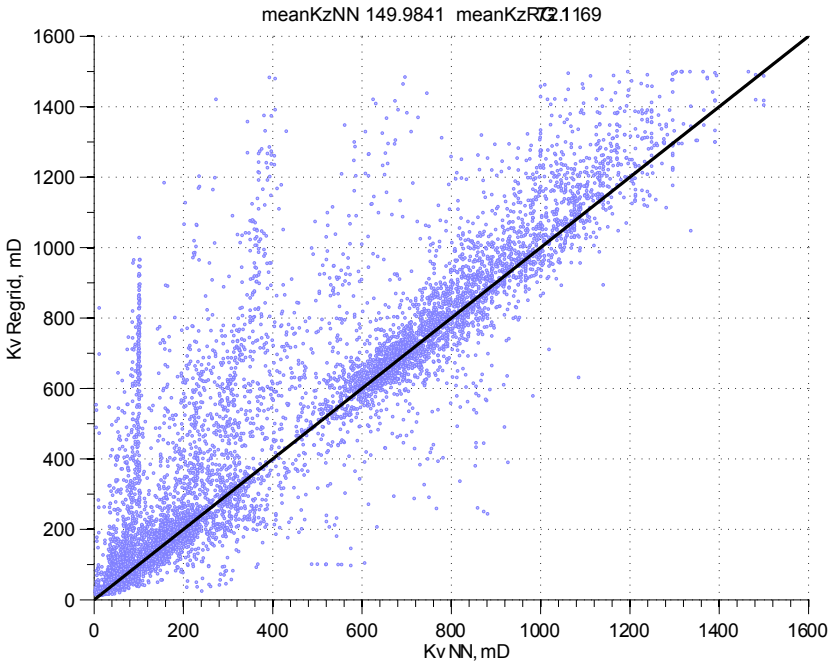

Figure 4.15: Scatter plot of effective vertical permeability of stochastic regridding approach versus nearest neighbor approach.

To compare the high resolution realizations resulting from stochastic regridding proposed in this chapter, and the conventional approach of nearest neighbor interpolation, flow performances could be considered. This is in addition to the visual evaluation of the bulky edges at the facies boundaries and the generation of unrealistic continuity that result from nearest neighbor interpolation. The distribution of facies in the region of study influences flow in the volume. Such unrealistic continuity especially in terms of non-net reservoir or impermeable rock types could adversely affect the evaluation of flow performance. The nearest neighbor approach could create blockage to the flow because of the exaggeration of continuity in lateral direction that could make it difficult for the flow to find its way up; the evaluated

flow would be less realistic and underestimated. The implementation of stochastic regridding introduces the required variability and realistic continuity: The flow paths created this way are more realistic and reliable for decision making.

The flow performance is evaluated in terms of vertical permeability (Kv) because of its role in the recovery performance of SAGD (Deutsch, 2010). Kv is highly influenced by the flow path and the distribution of non-net reservoir. A pressure solver is utilized to calculate Kv for the upscaled grid blocks at the region of interest. Figure 4.15 compares the performance of high resolution models by the scatterplots of Kv for the upscaled blocks of stochastic approach versus those of nearest neighbor approach. Kv is changing from 0 to 1500 mD as shown in the scatterplot. The 45° line is also shown to ease the comparison. For many blocks of low or medium Kv from nearest neighbor approach, there are high values of Kv from regridding approach. Figure 4.16 isolates (a) medium Kv blocks of nearest neighbor approach and the corresponding Kv for stochastic approach, and (b) the Kv values for upscaled blocks of regridding approach with their corresponding Kv from nearest neighbor approach. As can be seen, for the moderate values of Kv for nearest neighbor approach which is changing from 130 mD to 650 mD, the corresponding stochastic regridding blocks have Kv values changing up to 1400 mD and for most blocks the Kv for regridding block is larger. However for case (b) the corresponding nearest neighbor blocks of moderate Kv are smaller than that of regridding approach. The continuity of the impermeable facies seems to be larger in terms of nearest neighbor which results in poor vertical permeability for many blocks relative to stochastic approach.

The regridding is not a downscaling problem, but an increase in resolution and small scale information. New information is required to be added to the model in order to represent smaller scale variability compared to the *a priori* model. The conventional method of nearest neighbor does not add any new information when representing smaller scale. It only replicates the old information representing the coarse resolution model. Although nearest neighbor is an easy technique but it is not the solution to the recovery of small scale information. However, the stochastic regridding approach imposes new information to the finer scale grid cells which describes the small scale variability based on local variography and coarse resolution data. Therefore, it is reasonable to conclude that for the specified region (e.g. SAGD local recovery region) of the case study, the continuity of the small scale variability

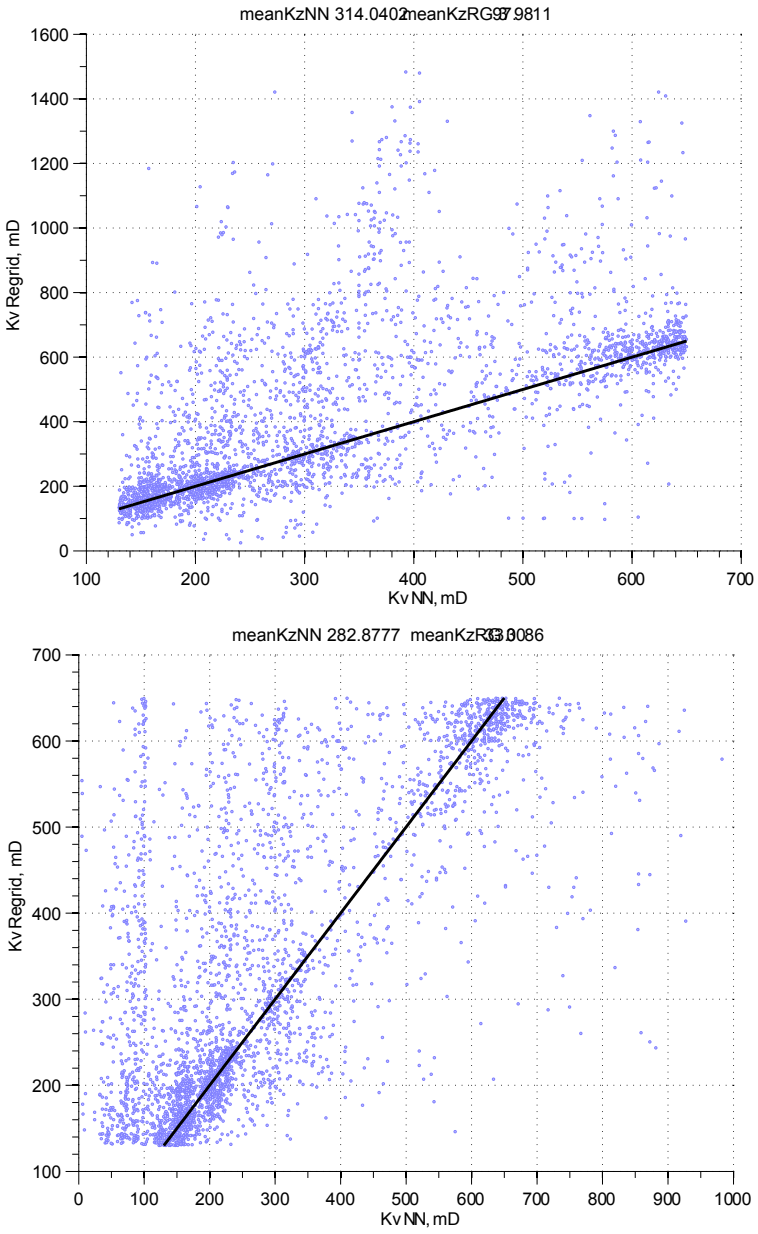

Figure 4.16: The Kv performance is compared for two approaches of nearest neighbor and stochastic regridding. For the moderate Kv of nearest neighbor changing from 130 to 650 mD, the corresponding stochastic regridded blocks are changing from 40 to 1500 mD. For moderate Kv values of stochastic regridding approach, the corresponding nearest neighbor Kv results are lower. In other words, the nearest neighbor interpolation is overestimating the continuity of impermeable facies in this case.

is overestimated laterally for the case of nearest neighbor approach compared to stochastic regridding.

4.4 Chapter Summary

A workflow has been developed to automatically regrid portions of coarse resolution realizations to higher resolutions. The proposed process is an automatic stochastic regridding approach based on simulation. The simulation is conditioned to the initial coarse resolution model. The value of stochastic regridding is discussed through a comparison to the nearest neighbor interpolation that is commonly implemented in most petroleum software packages. It is shown that the nearest neighbor interpolation is not the best approach when small scale variability is high. The advantage of stochastic approach is in the improvement in the realistic spatial variability features of small scale geologic heterogeneity. The importance of building high resolution models are discussed for a case study in the McMurray formation, through the evaluation of vertical permeability. An advantage of the stochastic regridding approach over the nearest neighbor technique can be observed in vertical permeability that is underestimated in the latter case. Moreover, the stochastic approach results in a set of realizations that characterizes a more realistic variability through a response distribution while the nearest neighbor approach is deterministic and can only generate one model.

Overall, stochastic regridding is a better alternative because it introduces new information in the new fine scale grid cells thus, it is more realistic; the realistic variability in the stochastic regridding approach provides improved characterization of flow parameters. The evaluation of Kv for both cases of stochastic regridding and nearest neighbor in case study confirms that realistic distribution of reservoir at finer scale could make a difference in understanding the flow behavior around the well.

Chapter 5

MPS Aspects of Model Resolution Enhancement

Current MPS implementations generate geostatistical models at the scale of the training image; there is an assumption that the categories are exclusive at smaller scales. This is a potential limitation that is discussed through "model resolution enhancement" in this work. The goal is to generate high resolution models with MPS to characterize the geologic features at a higher resolution than that of the available training image. This chapter addresses model resolution enhancement in the context of MPS by studying the scale-dependence of spatial structure in MPS based models. The first approach investigates through the manipulation of MPS probabilities. A number of challenges in characterizing smaller scale variability using high-order statistics are documented. The chapter concludes by advocating the direct rescaling of the training image to generate models at higher resolution.

5.1 Introduction

In MPS, the relationship between categories at different locations is provided through high-order statistics inferred from a training image that represents the type of structural characteristics that are expected in the geological setting of the deposit. The training image must be representative of the geology under study in terms of its complexity and scale. As discussed in the previous chapter, numerical models at higher resolution are often required as the study progresses; precise assessment of connectivity for instance may warrant models at higher resolution (Larue and Hovadik, 2006; Hovadik and Larue, 2007). A training image, however, is often available only at a fixed scale.

Extrapolation of spatial statistics to different scales than that of the conditioning data has been considered in many conventional geostatistical technique. In terms of simulation, data reconciliation at different scales is often addressed through simulation at the point scale of the data then averaging to larger scales (Frykman and Deutsch, 1999). Variogram extrapolation from the smallest lag distance to the nugget effect, permits specifying statistics at a higher resolution than data spacing (Kupfersberger et al., 1998; Frykman and Deutsch, 1999) (see Figure 5.1). MPS techniques, however, do not have this flexibility as the minimum scale at which the deposit can be modeled is the resolution of the training image.

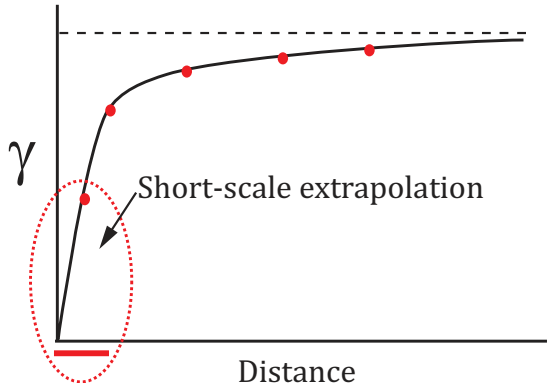

Figure 5.1: A schematic of extrapolating variogram to smaller scale, with the intention of modeling short scale variability. The distanced red dots represent experimental variogram values at a specific distance. The red horizontal line underneath the distance axis shows that the extrapolation of first experimental variogram value to zero value permits the variogram determination for distances smaller than the average data spacing.

The spatial high-order statistics in MPS simulations are captured through occurrences of patterns of n-point (limited to four, six and nine in this chapter) template configurations. The number of patterns for a template configuration is K^N, where K is the number of facies and N is the number of locations. For example, five rock types (K=5), and six locations ($N = 6$) will result in 15625 ($= 5^6$) possible configurations. The possibility that all these combinations are found in a training image is low.

Similar to the variogram that determines the variability of two-point data statistics as a function of lag distance, the increase or decrease of the frequency of occurrence of high-order patterns also represents the variability in terms of lag distance. Some patterns are expected to be more common at a particular scale, while some others would appear infrequently. If one pattern occurs more, the remaining patterns of the same configuration must occur less.

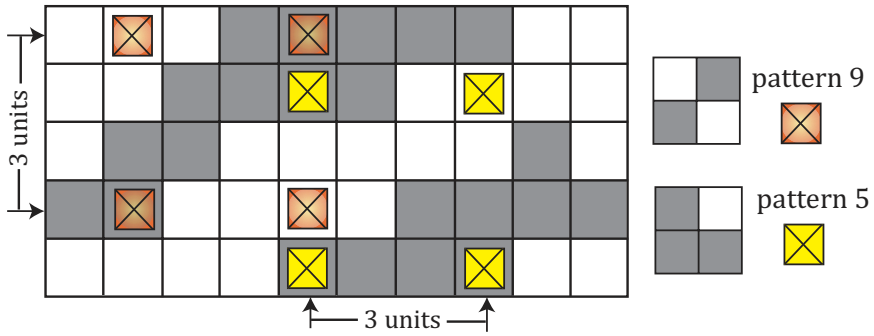

Figure 5.2: Example on pattern extraction in training image in terms of lag distance. The two patterns on the right are extracted on the map with 3 units distance lag shown in yellow and orange.

The key concept developed here is to predict the frequency of patterns (FOP) at smaller scales by extrapolating the FOP plot to shorter lag distances as done for the variogram. The variations in FOP depend on the training image, the continuity, and the scale of the structures. Patterns that appear more frequently at a zero lag distance represent the structuredness of the training image. With the increase of lag distance, patterns become more random. Thus, the proposed FOP plot is expected to reveal the structuredness (as opposed to the randomness) of patterns in the model. This is analogous to nature where the geological features are often highly structured at small scale and become less predictable at large scale.

Figure 5.2 illustrates two examples of pattern extraction for lag distances of 3 units and two patterns that are identified according to indexing shown in Figure 5.3. In the image depicted in Figure 5.2, 14 patterns of 3 units lag could be extracted $(= (10-3) \times (5-3))$. The patterns with high frequency represents some essential structure of the training image. As the lag distance between points on the pattern increases, the structure likely diminishes and patterns become more random.

5.1.1 Quantification of Structuredness/Randomness

The frequency or proportion of patterns can be understood as the ratio of occurrence of a specific pattern to the total number of patterns of the same configuration. This ratio depends on the global proportion of facies (categories); the continuity and spatial structure of the model interacts with the global proportions. For instance, if there is more black than white, the frequency of patterns that contain more black will be larger than those that have more white. Standardized or SFOP is defined to present the occurrence of pattern independent of the univariate proportions of

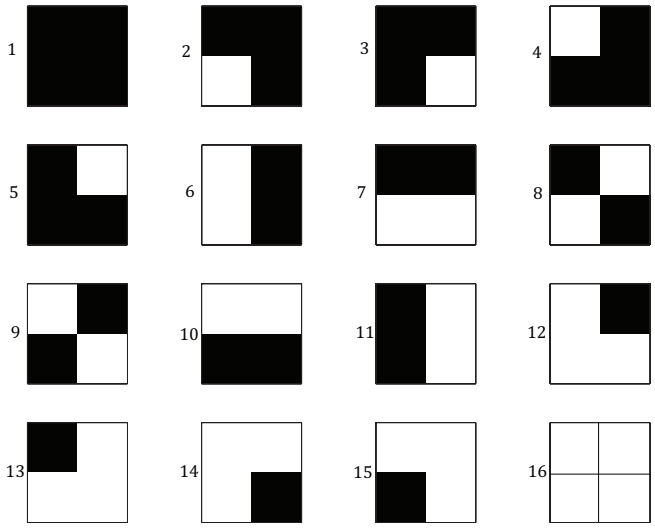

Figure 5.3: Template configuration for 2×2 binary patterns. Any reference to a 2×2 template configuration in this chapter refers to this image.

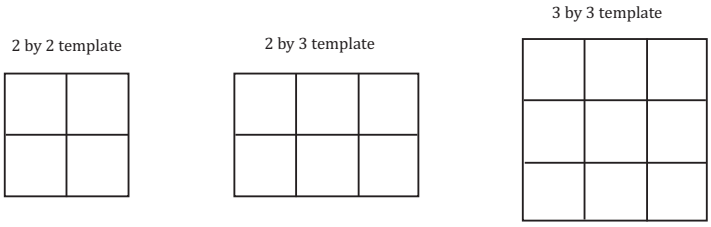

Figure 5.4: Three templates of 2×2, 2×3 and 3×3 are applied for FOP determinations.

categories. The ratio is scaled by $\prod \mathrm{P}_i$, where i indicates a location in the pattern, varying between 1 and N, and P represents the global proportion of the specific category. This product can be redefined as the proportion of a specific pattern if the image was random. The inverse of $\prod \mathrm{P}_i$ could also be interpreted as the maximum occurrence of a particular pattern since the value 1 in the numerator could indicate the case that a pattern has occurred 100% in the map. Therefore, it is reasonable to redefine the independent FOP as a factor of its maximum possible occurrence. If Prp stands for proportion and rnd for random, the following describes the presented logic in the so called SFOP definition:

$$\begin{aligned} &\mathrm{FOP} = \mathrm{Prp}_{\mathrm{pattern}}, \\ &\mathrm{Prp}_{\mathrm{rnd}} = \prod \mathrm{P}_i, \quad i \in \text{locations} \\ &\mathrm{FOP}_{\max} = 1/\mathrm{Prp}_{\mathrm{rnd}} \\ &\mathrm{SFOP} = \mathrm{FOP} \times \mathrm{FOP}_{\max}. \end{aligned} \tag{5.1}$$

Table 5.1: Frequency of occurrence for binary pattern in 2×2 configuration for a map consists of 60% black and 40% white.

pattern	Prp_{rnd}	Total FOP
1	0.1296	0.1296
2–5	0.0864	0.3456
6–11	0.0576	0.3456
12–15	0.0384	0.1536
16	0.0256	0.0256

Prp_{rnd} for every pattern converges to $1/K^N$ if the global proportions are equal for all facies and the map is random. The lower limit of SFOP is 0 which occurs when the frequency of a specific pattern is 0, and the upper limit is FOP_{max}, when the frequency of a specific pattern is 1.

An example is shown to demonstrate how global proportions of categories directly influence the probability of occurrence of specific patterns. Figure 5.5 illustrates the probability of occurrence, FOP_{max}, for all 16 patterns in 5 groups for the binary template of 2×2 configuration for a noisy map consisting 60% black and 40% white. The 16 patterns are grouped into 5 categories based on the number of locations devoted to each of the binary facies; see Table 5.1. The grouping is justified as the probability of every pattern is evaluated based on facies proportions (P_b and P_w); neighboring is not considered. For the considered map, the patterns 2, 3, 4 and 5 in Figure 5.3 (3 blacks and 1 white) have the maximum occurrence of $(0.6^3 \times 0.4^1 = 0.0864)$ which is greater than the FOP_{max} of the same patterns if the global proportions for black and white were 50/50 (=0.0625), as expected. It can also be observed from Table 5.1, that the chances for patterns containing 1 black and three white is less than half the probability of occurrence for patterns with 3 black and 1 white, although the global proportion of black is only 1.5 times that of white. This confirms that the global proportions impact the occurrence of patterns.

5.1.2 Odds Ratios for FOP Evaluations

Odds ratios are another representation of association. The interpretation of probabilities of events relative to other events in the form of odds ratios are quite popular in statistics and medical literature. Odds ratios are mainly used when the study

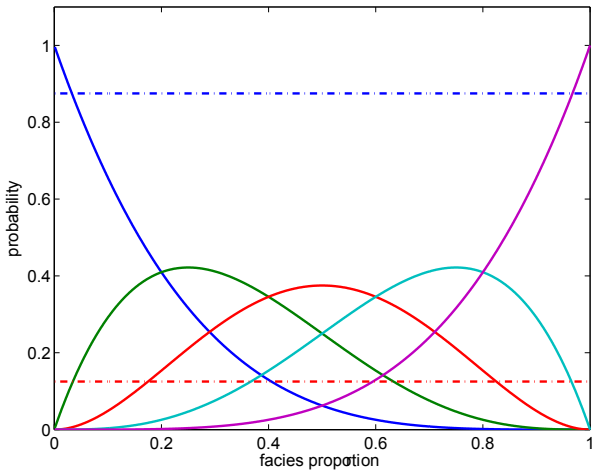

Figure 5.5: Illustration of probability of occurrence of patterns in binary 2×2 configuration in 5 groups of Table 5.1. The curves of blue, green, orange, cyan and purple represent the indexed patterns indicated in every row in Table 5.1, respectively. Assuming pattern 1 and 16 to be the ordered ones and the rest to be non-ordered, the maximum of non-ordered would be 0.875 shown as dashed blue line. Similarly, considering patterns 8 and 9 to be the least structured as opposed to the rest, the maximum of these two occurring would not go more than 0.125 shown in dashed red line.

is designed in the form of case-control. To analyze the frequency of patterns independent of the global proportions of category, the model with random occurrence of patterns with same proportions could be selected as the control case (Grimes and Schulz, 2008). The odds of occurrence of a specific pattern relative to its associated control model could be used to discuss structuredness in MPS models. Therefore, the Odds-FOP is the ratio describing the odds that pattern n occurs relative to the rest of the patterns in the template, which is the probability of the occurrence of pattern n to the probability of occurrence of all other patterns. For example, for a total number of templates in a map (M), and m number of occurrence for pattern n, the odds of pattern n is evaluated as the proportion of $m/(M-m)$. In other words, Odds-FOP explains the probability of pattern n occurs to the probability that it does not occur (Bland and Altman, 2000). Also, the odds of occurrence of every pattern in a model of study relative to its occurrence in its corresponding random model (baseline model) could be expressed in the odds ratio:

$$\begin{aligned}
&\text{odds_FOP} = \text{FOP}/(1-\text{FOP}),\\
&\text{odds_Prp}_{\text{rnd}} = \text{Prp}_{\text{rnd}}/(1-\text{Prp}_{\text{rnd}})\\
&\text{odds_ratio} = \text{odds_Prp}/\text{odds_Prp}_{\text{rnd}},\\
&\text{odds_ratio} = \frac{\text{SFOP}(\text{FOP}_{\max}-\text{SFOP})}{\text{FOP}_{\max}-\text{SFOP}}
\end{aligned} \tag{5.2}$$

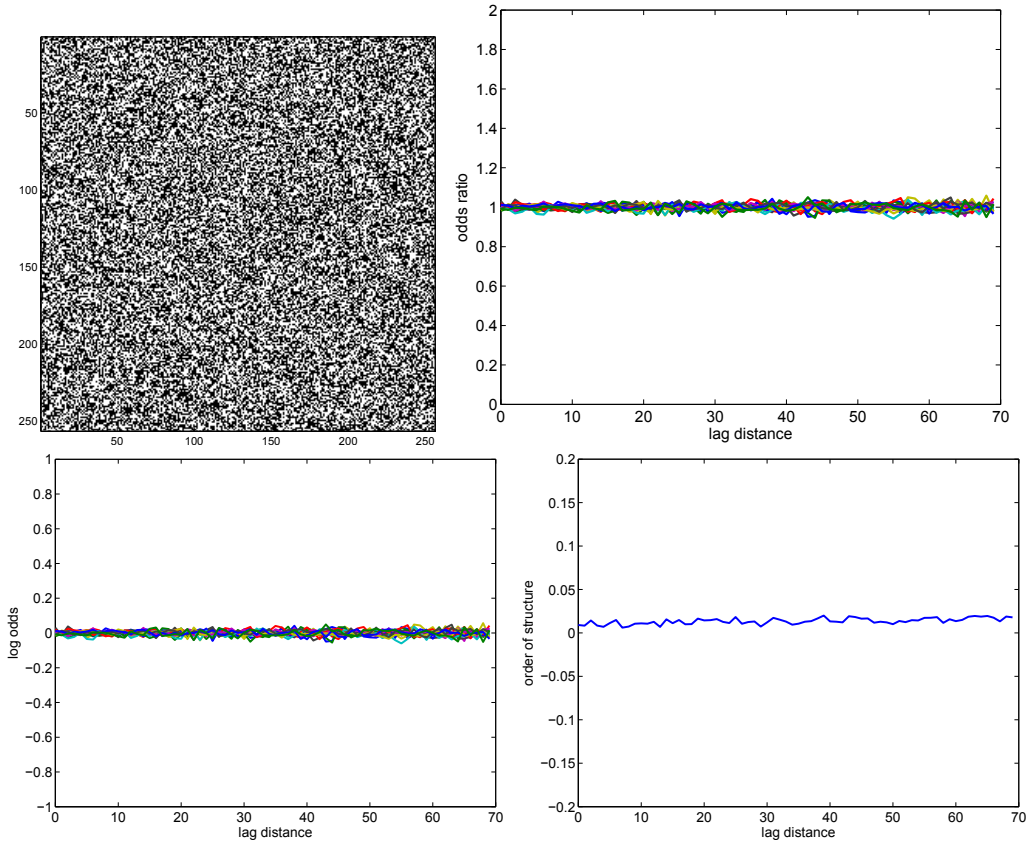

Figure 5.6: A binary training image is shown on the top-left representing a random map with equal proportions of black and white. This leads to equal FOP of 1/16 for all 2×2 patterns. The plots for odds ratio (=1) and log odds (=0) have been represented. The order of structure is very small value at all lag distances.

This ratio has a lower bound of 0 indicating no occurrence of a specific pattern and has no upper bound. For 100% FOP, the odds ratio is undefined since SFOP reaches $\mathrm{FOP}_{\max}$. Also, The odds ratio is 1 when FOP is equivalent to $\mathrm{Prp}_{\mathrm{rnd}}$. Thus, the value 1 for odds ratio could be expresses as the case of independency.

In two-point statistics, the assumption of stationarity provides a standardization of the variogram. The sill is the maximum data variance for a stationary model. A similar concept could be applied to the multiple-point (MP) statistics. As discussed above, 1 is the reference value for the random case. Thus, in the context of occurrence of patterns, the SFOP or odds ratio of every pattern converges to a value of 1 at a very large lag distance, since the model commonly loses its structure when the lag distances increase (see Figure 5.6). Therefore, it is reasonable to interpret any deviation from the baseline (=1) to be an indication of some form of continuity or structuredness as opposed to randomness, as defined below.

A relation that represents structuredness in MPS, "Order of Structure", is introduced at this point. The order of structure is the result of adding up absolute values of all deviations from the reference value of 1 at every lag distance. In the random case, odds-ratio for patterns are very close to 1. This summarizes the FOP behavior for all patterns in a covariance type plot which is more illustrative than following K^N (e.g. 16) lines on one graph.

$$\text{Order of Structure} \equiv \frac{\sum_{k=1}^{K^N} \mid \text{odds\_ratio} - 1 \mid}{K^N}. \tag{5.3}$$

Examples

Six binary maps of different structure and continuity are considered to examine and understand the FOP introduced in this section (see Figure 5.7). The maps are roughly ordered from the most structured to least. The behavior of 16 patterns in Figure 5.3 are studied as a function of lag distance. The 2×3 and 3×3 configurations are also considered in this section, but the results are only documented in summary to avoid plotting a very large number of curves on one graph (i.e. 2^6=64, or 2^9=512). Figure 5.8 represents the FOP of all 16 patterns as a function of lag distance ranging from 0 to 150. Figure 5.9 represents the odds proportions in the standard mode defined in Equation (5.1). For the six images, two patterns of 1 and 16 have their odds proportions decreasing as the lag distance increases. These two patterns represent the structuredness in the maps. For larger lag distances, all 16 patterns appear to converge at some point. The natural logarithm of odds ratio are more interpretable as discussed above. The logarithm of odds ratio is shown in Figure 5.10. The logarithm is often used to exaggerate the values larger than the reference value. As can be seen, the logarithm of patterns is between -4 and 4 where 0 is the reference value. The values are constrained by a maximum of 4 and minimum of -4.

An interesting observation is that the two patterns of 1 and 16 switch position in Figures 5.9 and 5.10 compared to Figure 5.8. The one having the maximum odds for FOP has its maximum occurrence because of the larger proportion of corresponding category. Also, the first map with the black circle has the most structuredness; some patterns have zero probabilities throughout the range of lag distance. A few patterns have very small occurrences and start at later lags. The same is true for the second image. As can be seen in Figure 5.10, the odds ratio of frequency of patterns 8 and 9 is very small until lag distance of about 40. Figure 5.11 illustrates the order of

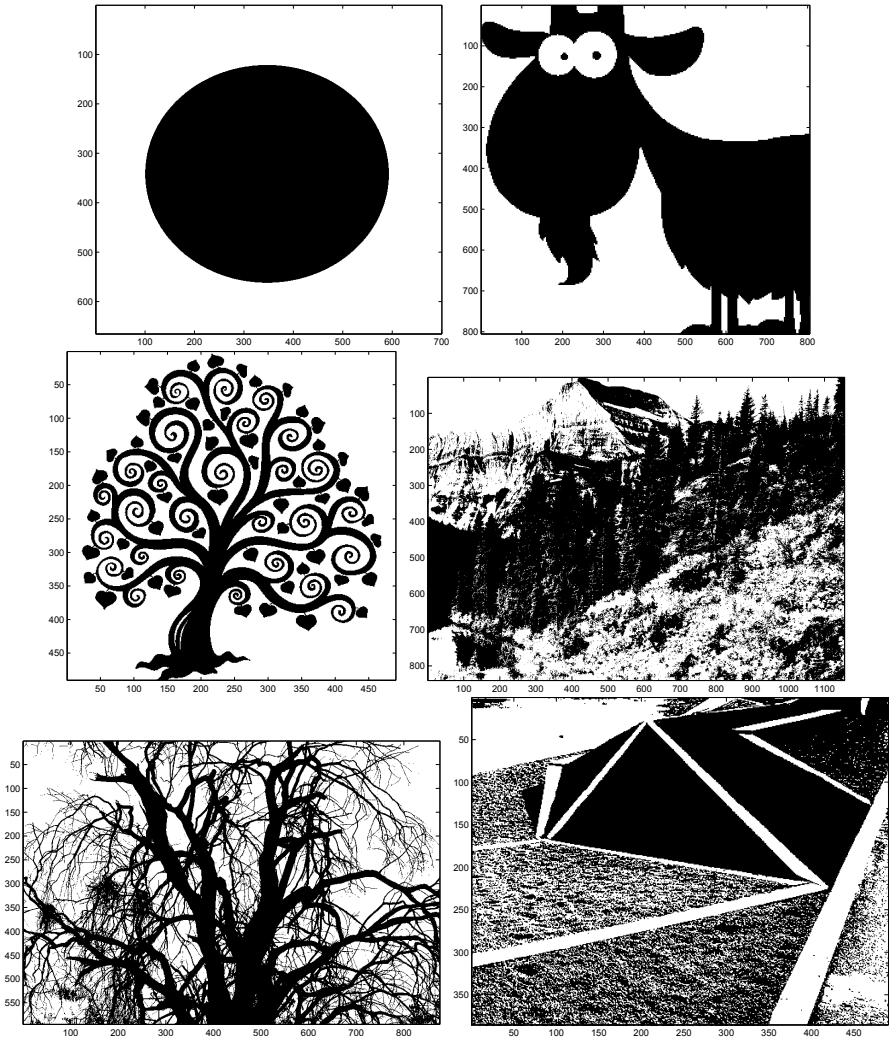

Figure 5.7: The maps are listed from left to right and up to bottom from 1 to 6 (ima, e,d,b,a,c). The results and analysis on every training image have listed in the same order in the following figures.

structure for patterns of 2×2 configuration. At 0 lag distance, the deviation from 1 is at its maximum and the order of structure drops as the lag distance increases. The minimum value for order of structure is 0 at very large lag distances and represents randomness in the map. A variogram plot represents the nugget effect, variogram range and how the variability increases with the lag distance. Similarly, the order of structure can point out similar concepts in multiple-point data interactions. The structure factor starts at a value greater than 0 at zero lag distance and falls as the lag distance increases. The slope of the decay represents how quickly the order of structure is decreasing within the model A zero structure factor suggests noise. For example, in Figure 5.11, the structure factor for the 4th map stabilizes at some

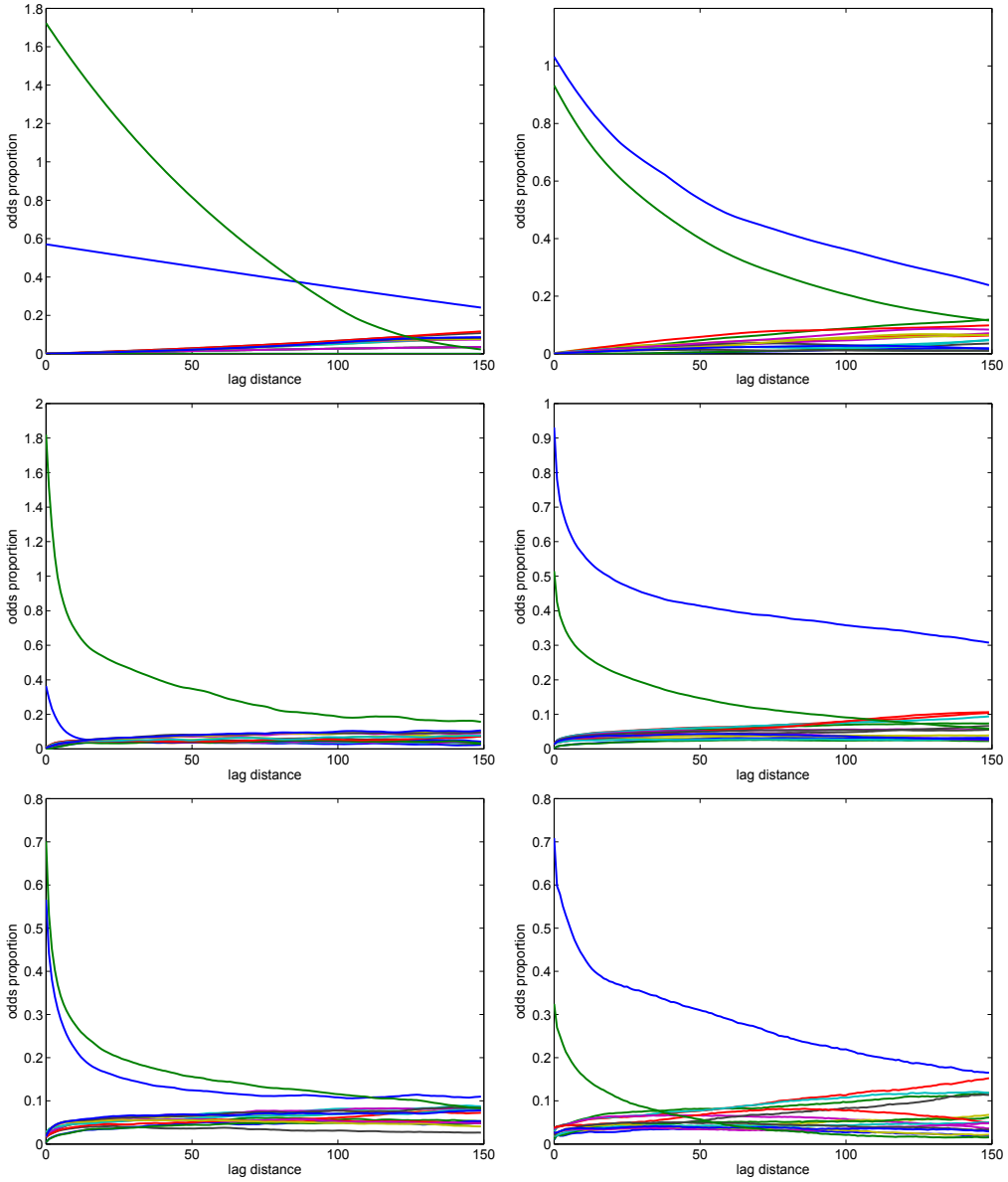

Figure 5.8: The occurrence of all 16 patterns of 2×2 configuration are plotted as a function of lag distance. The dominant patterns of 1 and 16 at zero lag distances are shown in blue and violet; these two patterns are the most structured as they are at their maximum at lag 0. The other three lines represent group patterns of (1) one white, three black (2) two white, two black (3) one black, three whites. These 14 patterns represent non-structured (noise) in the map. The proportion increase with the lag distance as the continuity of the structure discontinues with the continuity of spatial structure.

point and falls very slowly with lag distance. This indicates that the corresponding map has large scale structure. The steep fall of the structure factor suggests small scale structure. For example, the maximum structure factor at zero lag distance for the first tree is at least four times of that of the second tree. This could be the result of short scale features repeating over the model.

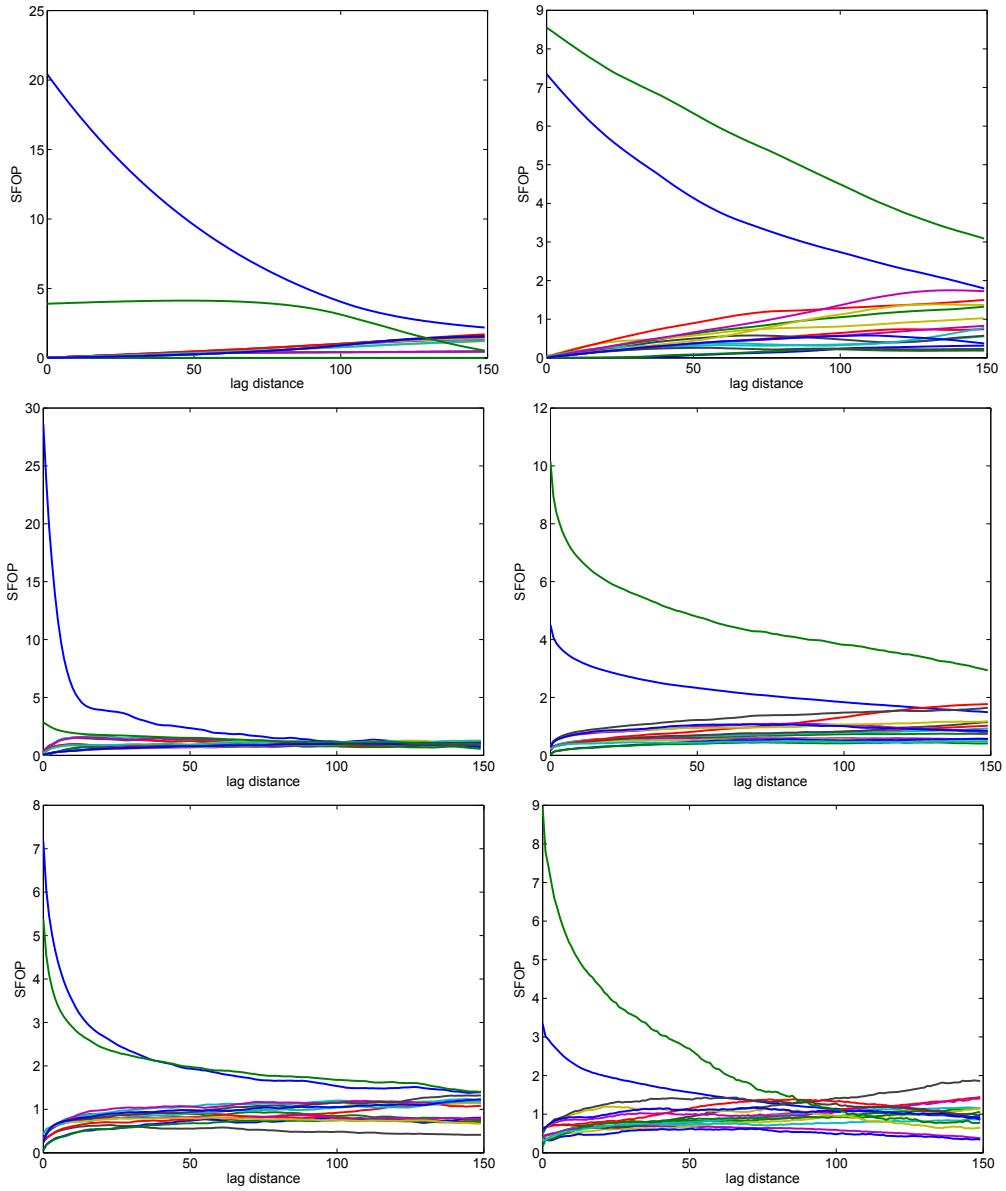

Figure 5.9: The standardize frequency of every pattern are shown for the six images. SFOP has been determined as shown in (5.1). The two patterns of maximum occurrence or the more structured ones which are shown in blue and green revert position compares to odds proportions of patterns plot. The standardization of the odds proportions account for the available data and probability of occurrence.

Figure 5.12 illustrates the order of structure for the same templates for all 6 training images in one plot. The figure at the top is for 2×2 patterns, the one in the middle illustrates the order of structure for 2×3 configurations and finally the one at the bottom corresponds to 3×3 templates. It can be observed that the more structured images start at higher order of structure and decline slowly. Therefore, higher data interactions deal with larger deviation from the baseline. The maximum

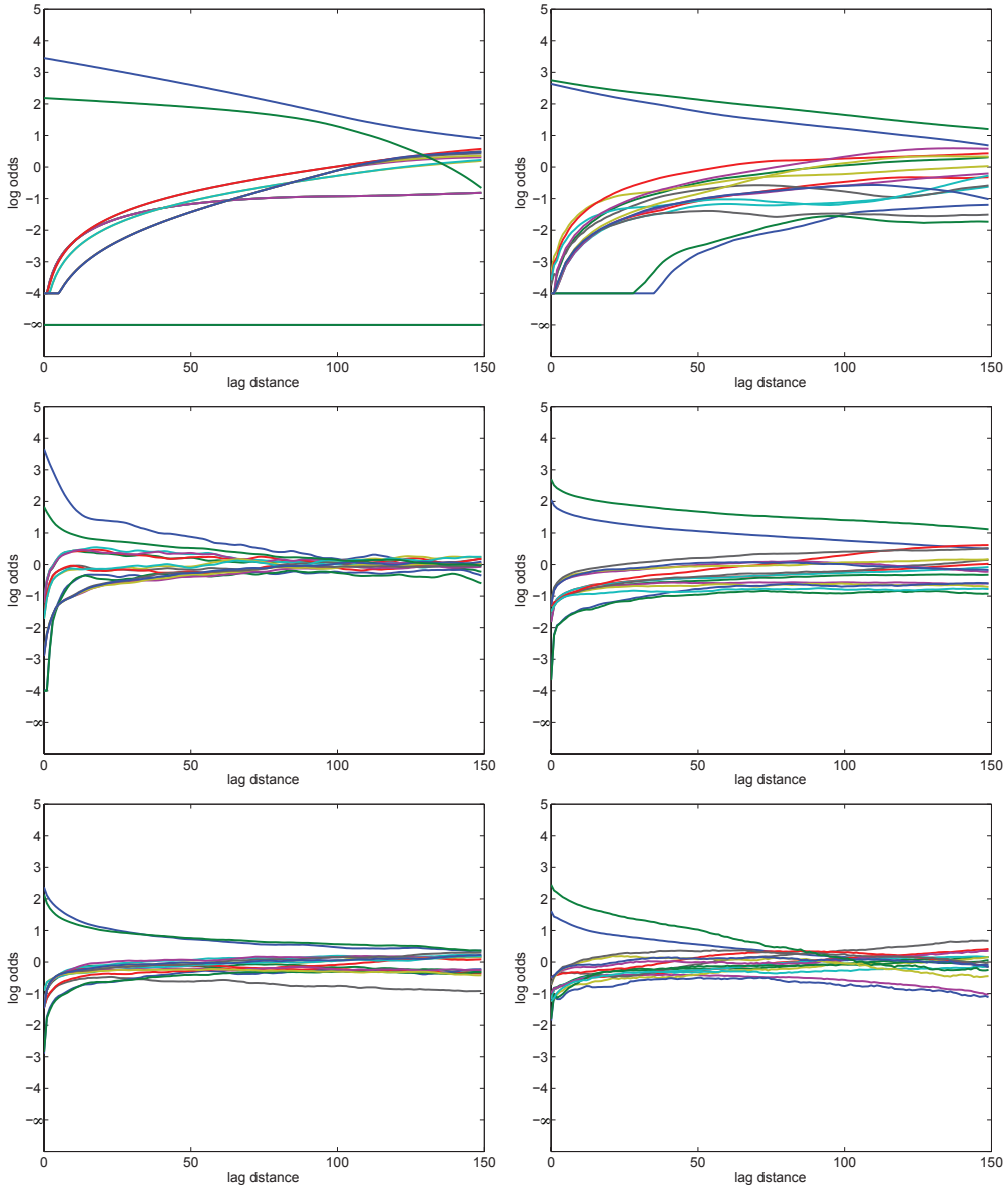

Figure 5.10: The log of odds ratio for 16 patterns of 2×2 configuration are shown for the six images. The lag distance starts at 0 and goes for a range of 150. All log ratios are constrained to the range of -4 and 4. Occurrence of real zero is represented by -∞ in the plot and any log odds less than -4 or greater than 4 would be represented as the minimum of -4 or maximum of 4.

also increases as the number of locations in the template increases. However, it seems that the increase is stable for all the images. For example, the red curve in three plots of Figure 5.12 belongs to the third image representing a tree which has the largest order of structure at zero lag in all three pattern extraction. This is not shown for template configuration of 3×3 as the maximum value is very large. Another observation is that the order of structure for the template configuration of

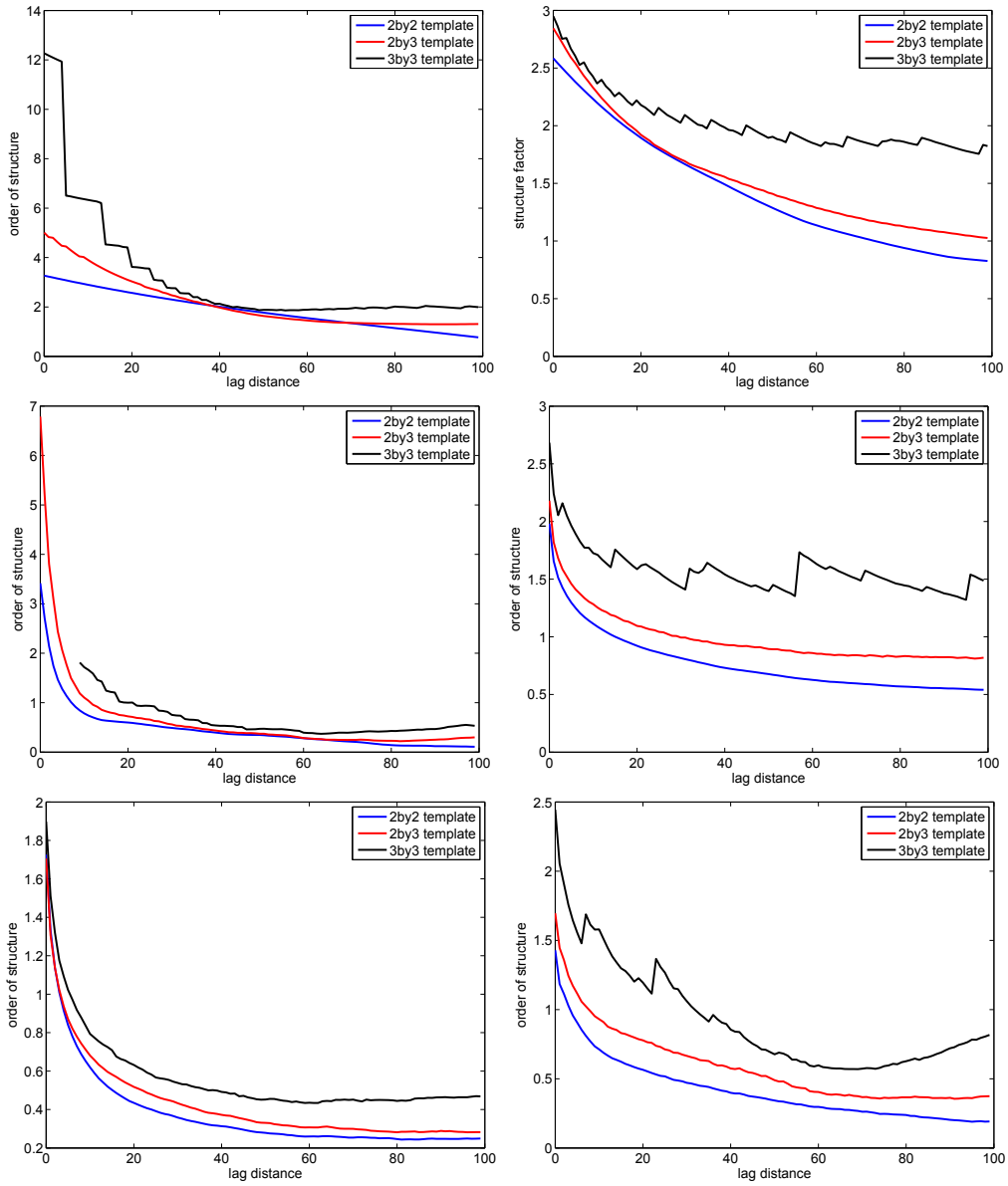

Figure 5.11: An analogy to the standardized variogram plot that represents the spatial continuity within 0 and 1. The FOP ratio in y-axis are determined by calculating the ratio of non-ordered structure as a function of all patterns FOP. The jump from zero is analogous to nugget effect in variogram plot. The first two maps are the least noisy and have nugget effect of almost zero value.

3×3 is not as smooth. The overall behavior of the order of structure however is very similar in all three pattern configurations; it starts at higher values and falls slowly as the lag distance increases.

Figure 5.13 illustrates the estimation for FOP values at scale 0 based on the information regarding FOP at scales 1 and 2. This is analogous to extrapolation at smaller scales with variograms. This estimation is calculated from two points, that

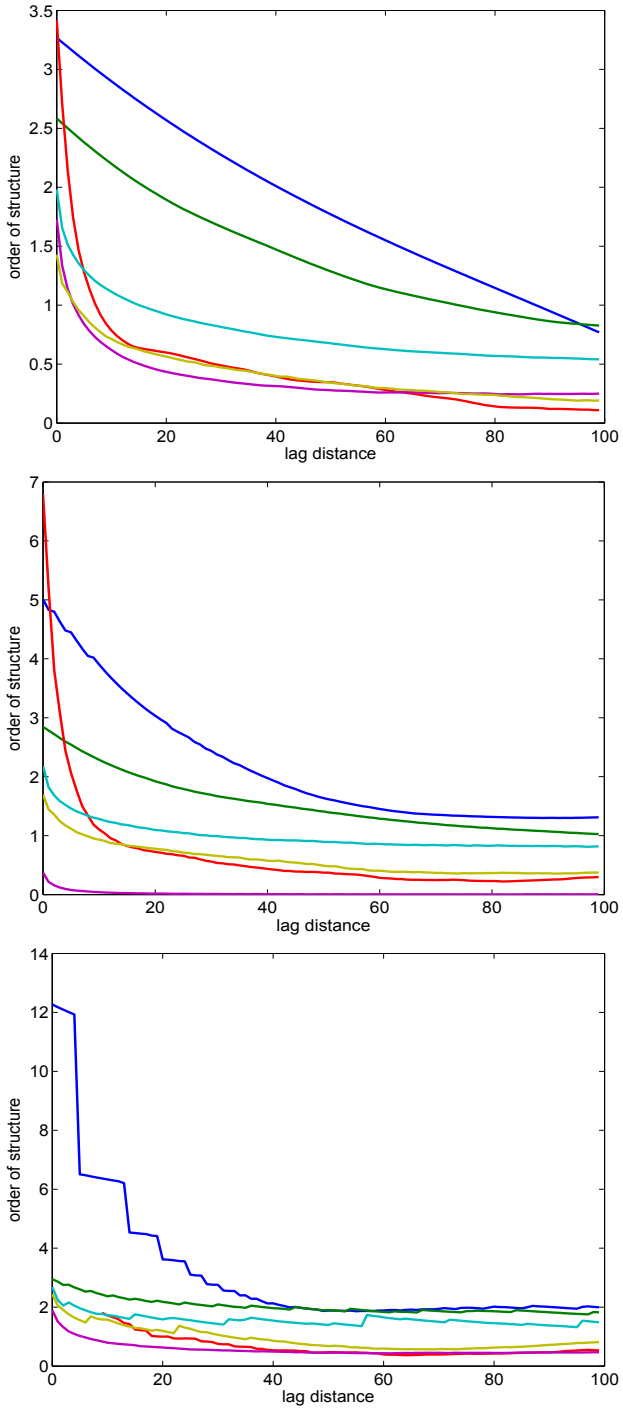

Figure 5.12: The figure at the top represents the summary of order of structure for templates of 2×2 which includes 16 patterns for the six images. The second figure similarly represents the summary of order of structure for templates of 2×3 that includes 64 patterns. And finally, the last figure represents the summary of order of structure for 512 patterns of 3×3 configurations. All configurations contains only two categories.

is why an FOP curve with linear behavior at smaller scale predict more precisely. As can be seen in the corresponding figure, characterization of occurrence of patterns

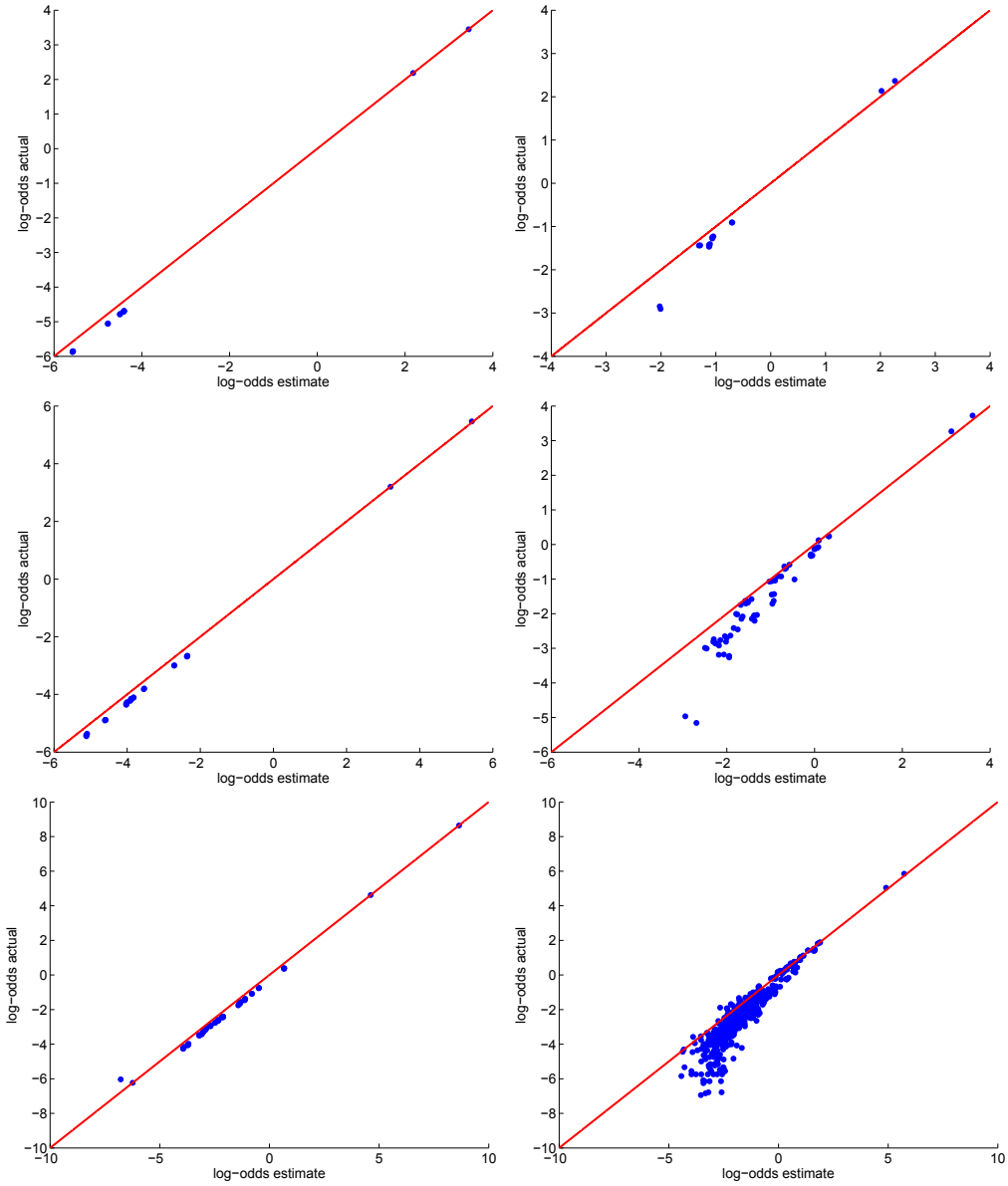

Figure 5.13: These scatter plots represent how the FOP can help with characterizing the short scale variability. The scatter plots on the left belong to the most structured case of the circle shown in Figure 5.7, and the scatter plots at right belong to the case that shows the tree with lots of branches. The two scatter plots at the top represents the predicting log FOP for 16 patterns of 2×2 configuration. The second row is 3×3 configuration and last row is prediction for 9×9 configuration. It can be observed that the estimation becomes less precise as the configuration scheme becomes more complicated. Similarly, when the map has more complex structure, the estimation becomes more complicated.

at smaller scales is more accurate when the selected template is smaller in size and the map is less spatially complex. The bottom right plot represents the FOP predication scatter plot for 3×3 patterns at the map of the complex tree (with too many branches) which is a relatively poor estimation.

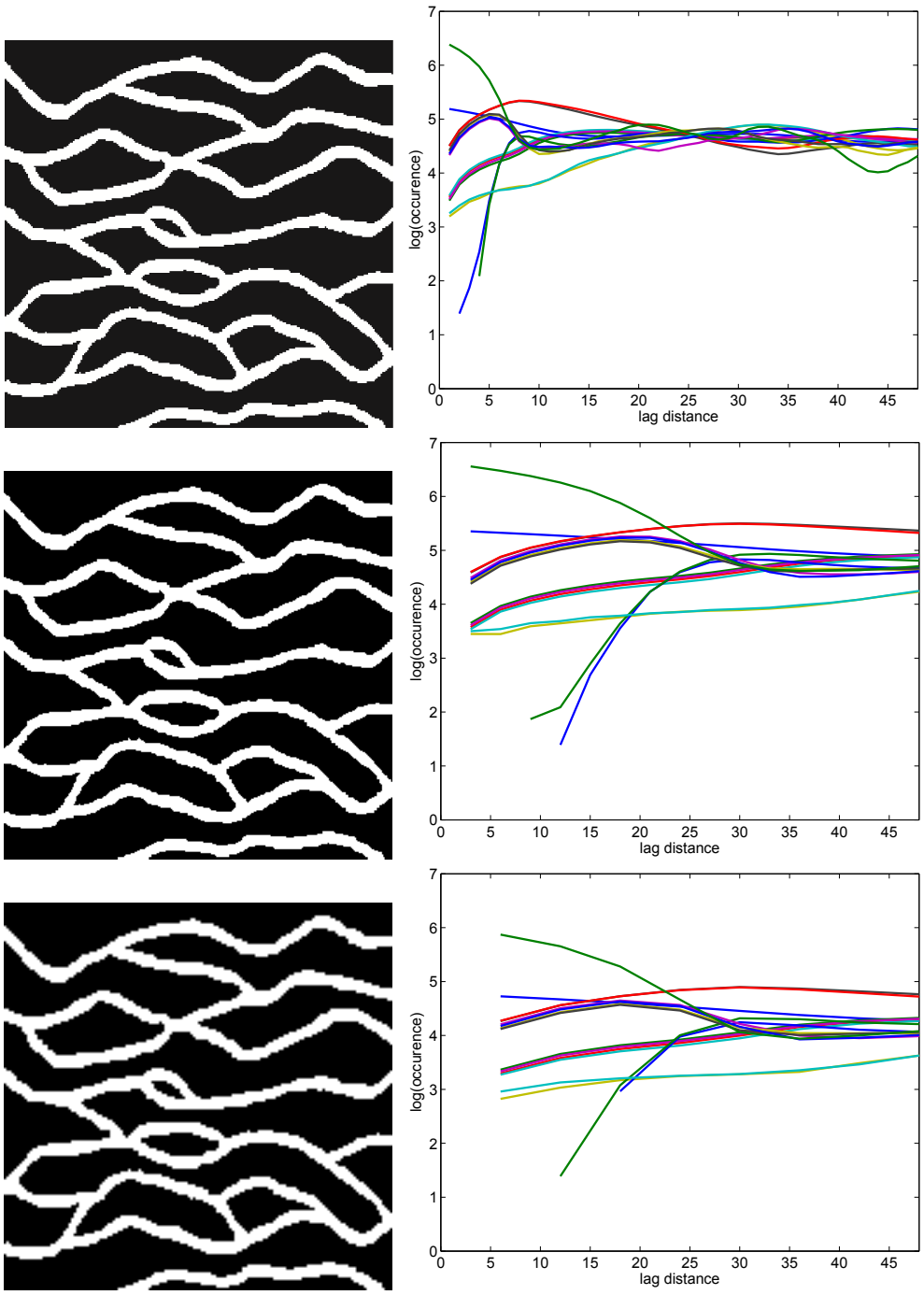

Figure 5.14: Illustration of the occurrence of patterns plot and the corresponding training image. The occurrence of patterns are shown for 16 patterns of a binary 2×2 configuration as a function of lag distance for interval of 0 to 48 m. The first row represents the original map and its corresponding occurrence plot, the second row represents the upscaled map (block of 3×3) and its corresponding occurrence plot, and the last row represents the upscaled map (blocks of 6×6) and its corresponding occurrence plot.

5.2 Challenges in Utilizing FOP

In this section, an exercise is designed to discuss the relationship between the training image, at different resolutions, and their respective FOP profiles. The 16 pat-

terns of 2×2 binary configurations are considered. The preferential patterns are scanned and detected for two different training images depicting petroleum reservoirs. The first training image is the typical channel type petroleum reservoir (Strebelle, 2002; Liu, 2006) that has been considered in three maps of high, medium and low resolution. The high resolution map is identified by utilizing the original training image. The medium and low resolution maps are the result of performing facies upscaling on the original training image in two stages. The facies are upscaled based on assigning the most common facies (Deutsch, 2002); 3×3 grid cells in original training image is translated to 1×1 grid cell in medium resolution map, and 6×6 grid cells in original training image is translated to 1×1 grid cell in low resolution map. The corresponding FOP plots are determined for lag distances changing from 1 to 48 m. The y-axis of FOP represents the occurrence of patterns in logarithmic units. The FOP values for all 16 patterns versus the lag distances are shown in Figure 5.14.

The frequency of every pattern in the corresponding training image is determined as follows: (1) the training image is scanned for a specific lag distance and data is extracted for the template configuration (i.e. 4-points template); (2) the probability of binary facies is evaluated on the extracted data, i.e., P_w and P_b. For example, for the classic training image shown in Figure 5.14 at the top, P_w is approximately 28% and P_b is approximately 72% (these proportions correspond to the lag 0 in original map). Then; (3) the number of occurrence of a pattern is counted in the scanned model; (4) finally, the FOP independent of global proportion is evaluated as in Equation (5.1). If the scale of grid cell in original training image is assumed to represent 1 m, then a 48 m lag distance in FOP covers about 1/5 of the domain in the corresponding 2-D map (250×250). As can be seen in Figure 5.14, the occurrences of 16 patterns somewhat converge after relatively large lag distances. This confirms an earlier claim that the patterns with higher orderness are more probable at smaller lag distances as opposed to the more random patterns. This suggests the models tend to get more random at larger lag distances and therefore the probability of occurrences for all patterns become similar (FOP converges for 16 patterns when lag distance is relatively large).

It can also be concluded that inferring information about high resolution maps from low resolution (upscaled) maps is not trivial; the information regarding small lag distance variability is not preserved in the upscaled process. Thus, to enhance

the resolution of a training image, the information regarding frequency of patterns of a coarse resolution training image would not be sufficient to characterize smaller scale variability. Another observation is that some patterns do not appear until certain lag distances at higher resolution. Extrapolating such patterns from large scale information would be impossible.

For the sake of illustration, the same process is applied to another training image that is shown in Figure 5.15. The first map (top) is the original training image of size 256×256 and its corresponding FOP is determined for up to 50 m lag distance (almost 1/5 of the domain). The second map (middle) is upscaled 5 times so that 5 m lag distance in its corresponding FOP translates to 1 m in high resolution map. The last map (bottom) has 10 times less resolution than the original training image; less continuity could be detected at the edges. The same conclusions are drawn for this training image. Almost after 25 m of lag distance, FOP plot for the high resolution map appears to stabilize for all 16 patterns.

The next section investigates the reproduction of FOP for the maps that their resolution are enhanced differently at some point and upscaled to the original scale. The high resolution maps cannot be reconstructed without making explicit assumption as there is no unique relationship, in this missing region, between fine and coarse scale.

Constructing High Resolution Models

The extrapolation of missing fine scale spatial variability information when coarse training images are considered is discussed. The coarse resolution map (bottom) in Figure 5.15 is considered as a reference to reconstruct the high resolution maps. The reconstruction of a training image at higher resolution is performed using conventional methods. Two high resolution maps are constructed using regridding approach of chapter 4, in which the resolution of first map is increased 5×5 times with zero nugget in spatial continuity and is enhanced 25 times and 40% nugget in variography.

After generating two models at smaller scale, the frequency of pattern plots regarding 2×2 templates are determined for lag distances changing from 1 to 50 m; see Figure 5.16. In the second case that was reconstructed with 40% nugget, the edges are noisy compared to the case with no nugget. As can be observed from their corresponding FOPs (Figure 5.16), the frequency of patterns are different.

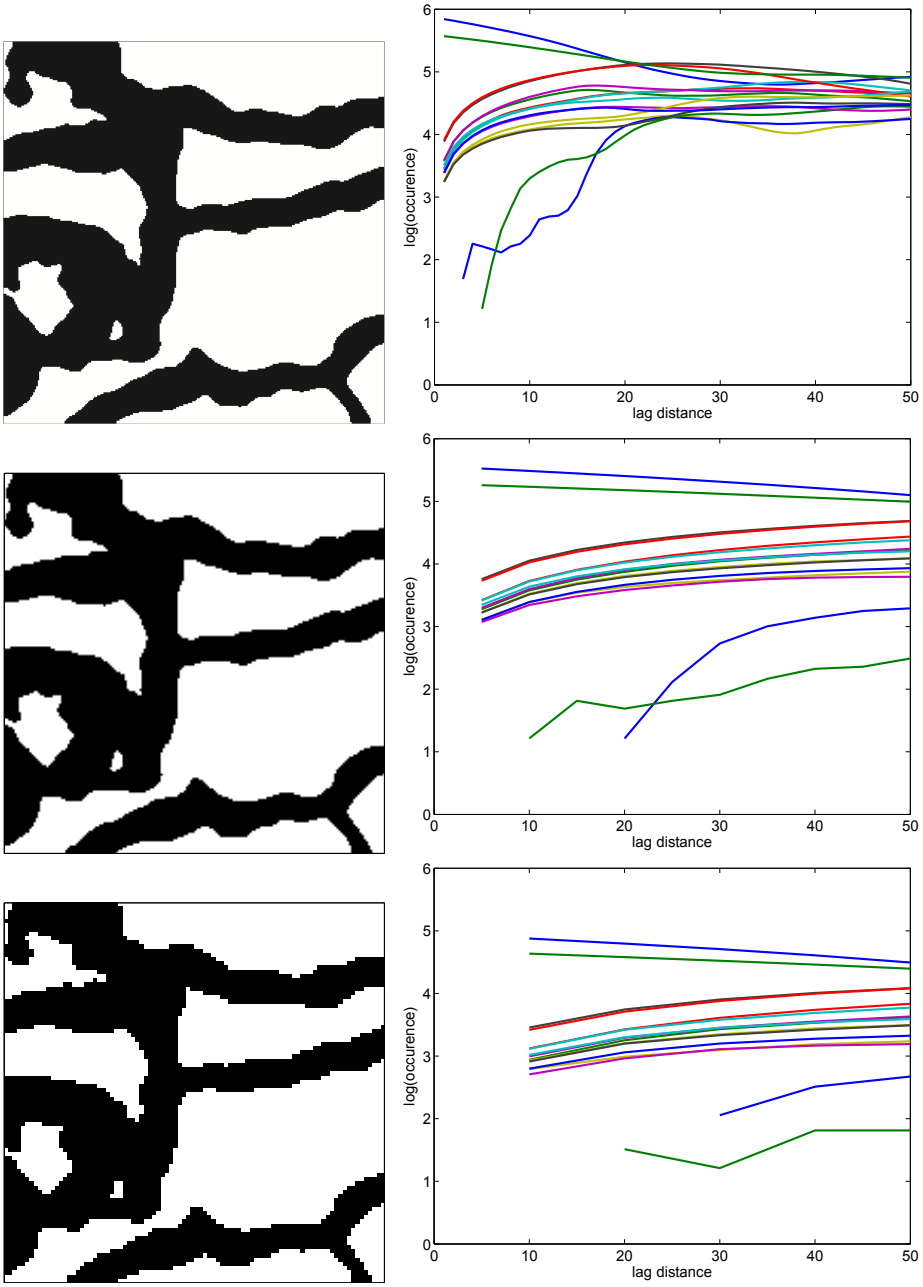

Figure 5.15: Illustration of the occurrence of patterns plot and the corresponding training images. The occurrence of patterns are shown for 16 patterns of a binary 2×2 configuration as a function of lag distance for interval of 0 to 50 m. The first row represents the original map and its corresponding occurrence plot, the second row represents the upscaled map (block of 5×5) and its corresponding occurrence plot, and the last row represents the upscaled map (blocks of 10×10) and its corresponding occurrence plot.

The high resolution maps are then upscaled to the same resolution as the reference map. The upscaled maps and corresponding frequency of pattern plots are shown in Figure 5.17. The first row of the figure corresponds to upscaled model of the case (1) where no nugget considered in reconstruction of the training image, and the second

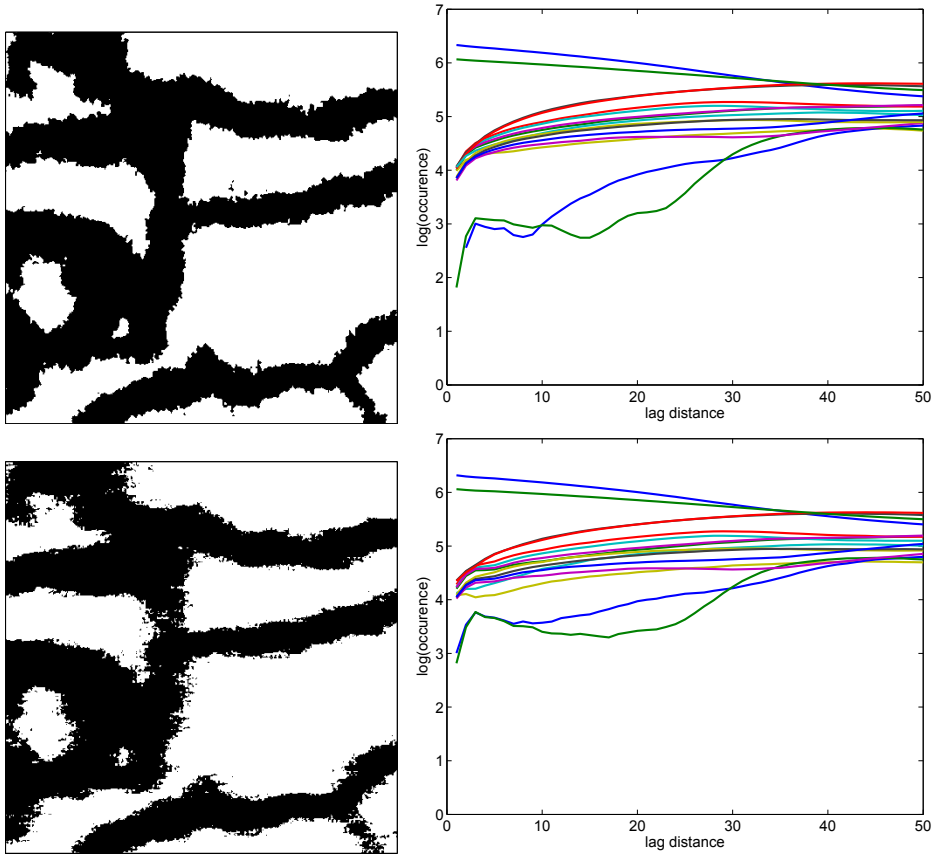

Figure 5.16: Illustration of reconstructed high resolution models and the corresponding occurrence of patterns plot. The first one represents case (1) when no nugget is assumed and the second one is the representation of case (2) when 40% nugget is considered in the simulation process. Note that the reconstruction relies on strong conditioning of coarse resolution training image depicted in previous section. The occurrence of patterns plot is shown for 16 templates of 2×2 for up to 50 m lag distance.

row is the upscaled model of case (2) where 40% nugget effect was considered in the resolution enhancement process. Although the upscaling map of case (2) is not visually appealing, the FOP of both cases seem to be very similar. This is despite of the fact that both high resolution models have different degrees of smoothness on the edges of facies transition. The occurrence of pattern plots for the cases of high resolution with different nugget is more different than that of the corresponding upscaled maps.

The results at this section support the point was made earlier; the information from coarser resolution maps is insufficient to identify the high resolution maps. In other words, reconstruction of high resolution maps using FOP of coarser grid maps is not unique.

The next section discusses the proposed solution in which the resolution of the

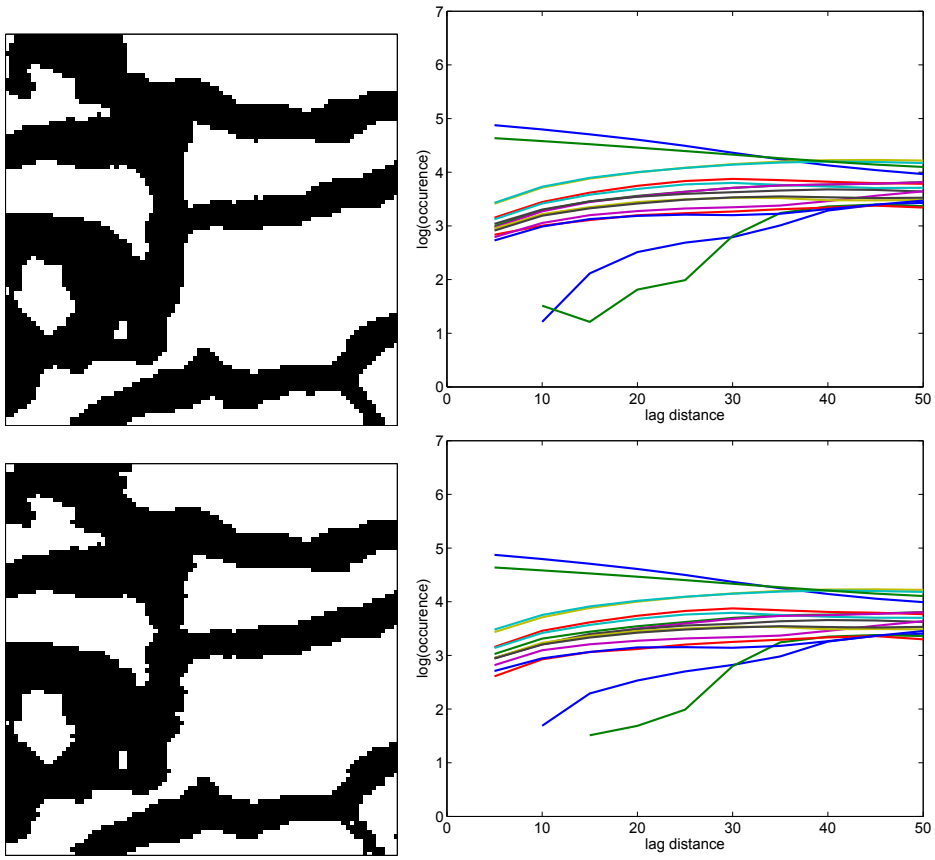

Figure 5.17: Illustration of upscaled models for Figure 5.16 and the corresponding occurrence of patterns plots. The first one represents upscaled map of case (1) when no nugget is assumed and the second one represents upscaled map of case (2) when 40% nugget is considered in the simulation process. Note that the reconstruction relies on strong conditioning of coarse resolution training image depicted in previous section. The transition occurrence plots are determined for 16 templates of 2×2 for up to 50 m lag distance. Note that regardless of their high resolution training images, the corresponding upscaled occurrence of patterns are very similar.

training image is increased directly.

5.3 High Resolution Training Image

The generation of high resolution training images is studied for specific types of deposits with smooth features like channels. Techniques like those in image processing are widely available. Such techniques could be similarly implemented on a training image in order to enhance its resolution. Most image resolution enhancement techniques suffer from undesired smoothness at high frequency regions of the image. The high frequency regions typically attribute to the edges that are essential to people's visual perception. There is a different aspect to edges in geological modeling; features of natural phenomena have rounded and smooth edges. For example, specific

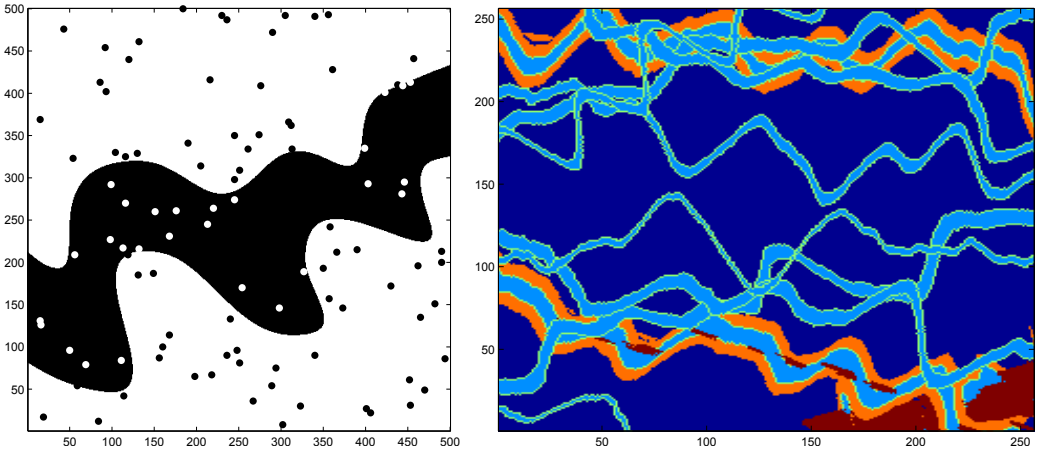

Figure 5.18: The left image is a binary channel depiction of size 500×500 with 100 sampled for conditioning realizations. The right map is a training image of 256×256 and cell size of 8 containing 5 categories of Crevasse like reservoir.

types of fluvial channels, including straight, meandering, and anastomosis present smooth features due to erosion during deposition processes (Nichols, 2009). The smoothing aspect of interpolation techniques could therefore come into advantage in the process of enhancing the resolution of the training image.

Of the most well-known and simplest interpolation techniques are nearest neighbor, bilinear, bicubic and sinc interpolations (bi refers to 2-D image). As discussed in previous chapter, nearest neighbor interpolation simply replicates the pixels to estimate the new grid points which result in blocky edges. Bilinear method employs a 2×2 (4 pixels) neighborhood pixels and average them to define new grid cells. Bicubic interpolation employs 4×4 (16 pixels) surrounding pixels and averages for the new location. The results of averaging methods are typically improved when some form of weighting is considered. The interpolation techniques are discussed considering 2 dimensional maps. The sinc method applies interpolation in the frequency domain. Utilizing more surrounding pixels at the stage of averaging could lead to a better quality high resolution image. The spline interpolation techniques tend to preserve the low frequency content of image and lose the high frequency content (Hou and Andrews, 1978). This could result in artifacts in regions where the map contains more detailed information. Recently, research in image resolution enhancement is directed towards the preservation of high frequency content of data. These methods include nonlinear techniques, interpolation techniques in frequency domain, and techniques that utilize the image geometry.

These interpolation methods along with the signed distance function kriging

of geostatistics are applied to generate high resolution 2-D maps. Two examples are designed to demonstrate the performance of interpolation tools generating high resolution training images. The first one is a binary depiction of a channel which is sampled and simulated at coarse resolution. Interpolation techniques are then utilized to construct the high channel at the original scale from the low resolution. In the second example, a more complex training image containing 5 categories is considerate (see Figure 5.18). The coarse resolution maps—in both examples—are constructed by extracting every forth pixel in both directions uniformly.

Example: Binary Training Image

A binary example illustrates the interpolation process to enhance the resolution of the available training image. An original channel depiction of 500×500 shown on the left side of Figure 5.18 is considered as the initial high resolution training image. 100 samples are selected randomly from the original 2-D map to be considered as the only available data to the simulation process. The realizations are generated utilizing stochastic simulation at 20×20 grid nodes and cell sizes of 25 m × 25 m. This coarse scale realization is considered as the available training image at this point. Different approaches could be taken at this stage to enhance the coarse resolution model to that of the original map. One is to follow geostatistical methods and determine the distance function to be considered in the kriging process and further in the generation of high resolution realizations. The other approaches relate to known interpolation techniques in image processing discussed earlier as shown in Figure 5.19). The resulting estimation at higher resolution for different techniques could be compared visually and further through the comparison of high-order statistics (i.e. FOP) with that of the original training image (see Figure 5.20).

Recall in Chapter 4, the high resolution model of area of interest is supposed to reveal more information regarding the small scale variability that could not be captured or preserved by the large scale model. This was achieved by applying a stochastic process considering a local variogram.

Example: Non-binary Training Image

This example is conducted to investigate complications that arise with more categories. Dealing with more than two categories can easily make the process complex. For the purpose of this exercise a Crevasse sinusoidal training image with 5 cat-

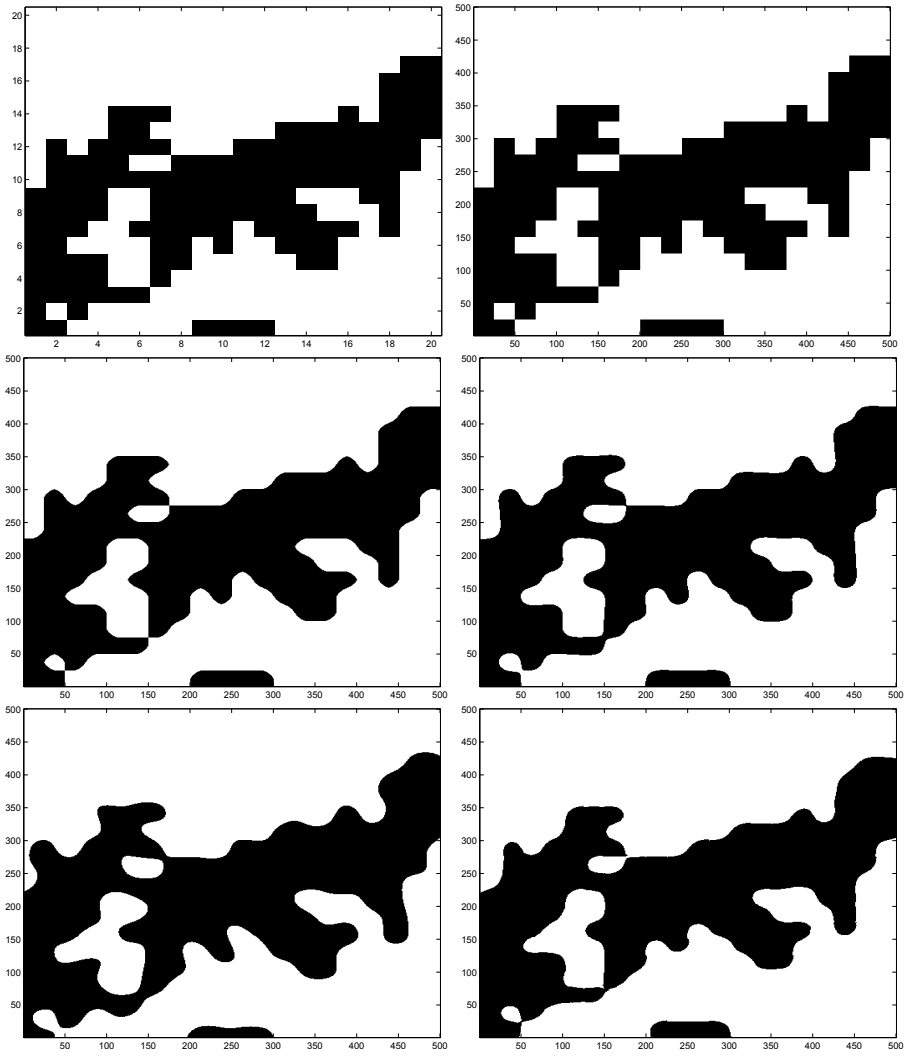

Figure 5.19: The figures should be read from left to right and top to bottom: The coarse map realization that is simulated at the coarse resolution conditioning 100 samples data of binary channel in Figure 5.18, its resolution enhanced once using nearest neighbor interpolation (map in top right), using bilinear interpolation (map in middle left), using bicubic interpolation (map in middle right), using sinc function interpolation (map in bottom right), and using distance function kriging (map in bottom left).

egories is considered. An X-Y slice of the training image, shown in right side of Figure 5.18), is extracted and considered as the training image for this exercise. It can be visually examined that presence of more than two categories in the reservoir results in more abrupt changes from one category to another which makes it harder for the features to be captured.

The training image in this example has 256×256 grid cells with size of 8 m × 8 m. The map is coarsen by extracting every 4 grid cells in both X and Y directions. Notice that, conventional simulation of the sample data in this case does not result

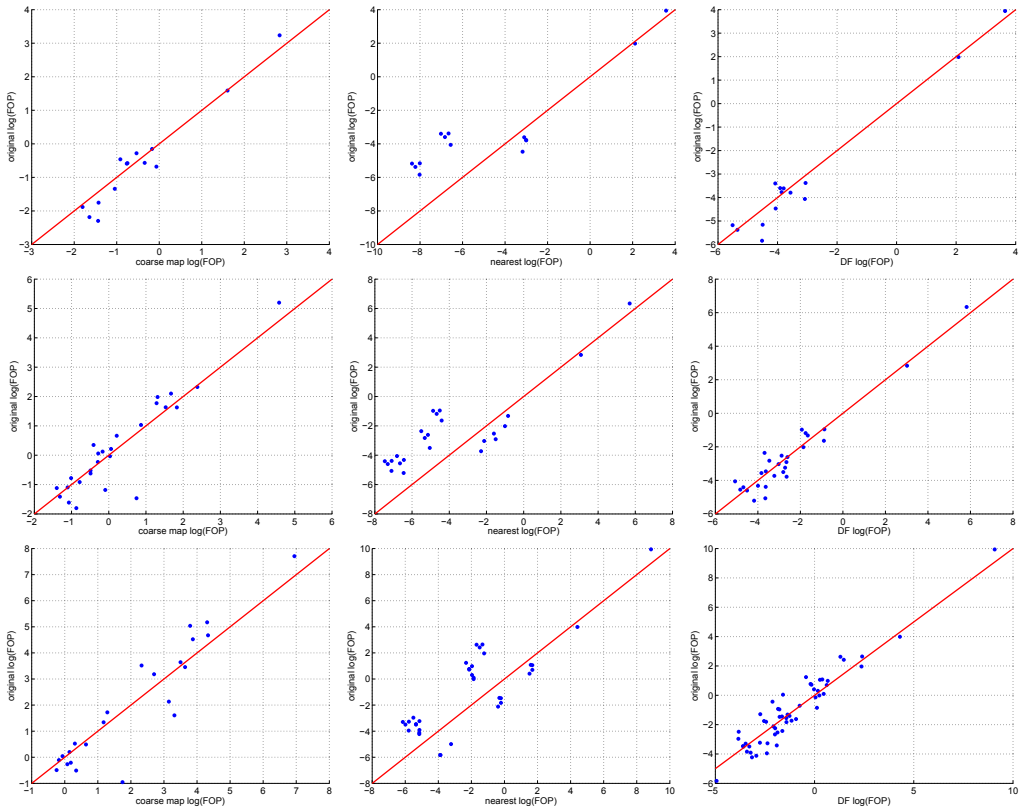

Figure 5.20: These scatterplots illustrate the precision in data statistics at smaller scale based on interpolation of two known statistics at larger scale in logarithmic form of FOP. The first row represents the scatter plot for the 2×2 configuration, second row for 2×3 configuration and last row is 3×3 configuration. The first column represents the relationship of FOP for zero lag of coarse map compared to its associated lag in the original map. The second column represents the relationship of FOP for lag zero of nearest neighbor map compared to its associated lag in the original map. And finally, the third column represents the relationship of FOP for lag zero of distance function kriging map compared to its associated lag in the original map Extrapolation of FOP values to smaller scale for generated high resolution map using nearest neighbor has less accuracy compared to the generated high resolution map using distance function kriging.

in any realistic modeling of the reservoir. The similar interpolation methods as previous example are applied to the coarsen map of 64×64 with cell size of 32 m × 32 m.

5.3.1 Discussion on Methods' Performances

The resulting high resolution maps are shown for nearest neighbor, bilinear, bicubic, sinc and distance function kriging in Figure 5.21. Most interpolation algorithms lead to similar results for the binary image. Whereas, in the second example, the results are more different. It is important at this point to limit the interpolation technique to only one, so that it could be considered regularly for further study. The visual goodness and absence of artifacts are important criteria to consider in the selection

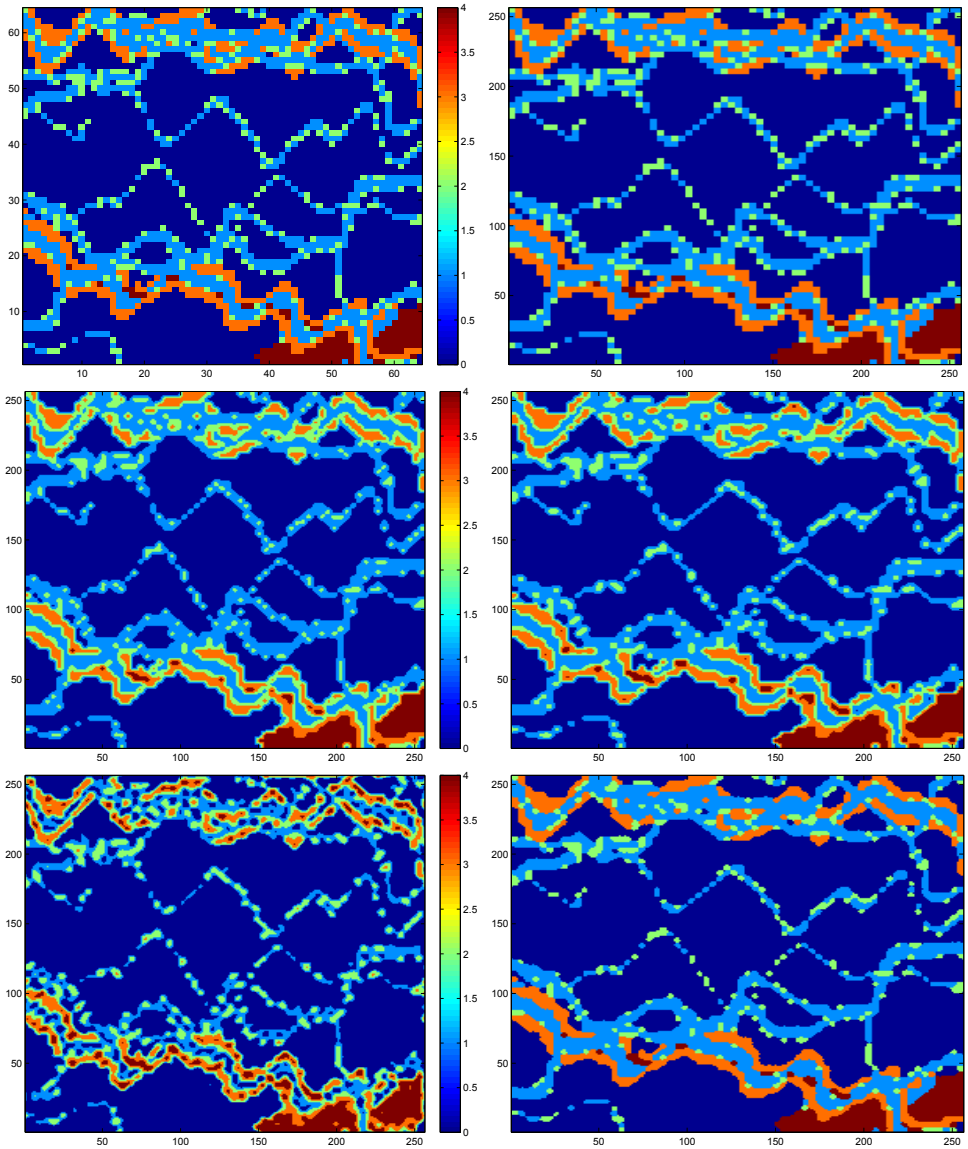

Figure 5.21: Resolution enhancement is applied through interpolation techniques on the Crevasse training image. The plots represent the coarsen map of, nearest neighbor interpolation, bilinear interpolation, bicubic interpolation, sinc function, and distance function kriging from left to right and top to bottom. For three cases of bilinear, bicubic and sinc function, the transition between categories should happen slowly. The green lines in between two facies of orange and dark blue is evident to such an observation. This is not the case for nearest neighbor interpolation and distance function kriging.

of technique. One other criterion is the robustness; a preferred algorithm should be widely applicable to different images. As can be observed from Figure 5.21 that the spline like interpolations are blurry, meaning that transitions happen slowly. For example, the green lines in between the dark blue and orange at the bottom of the map are blurred. This is not the case for the nearest neighbor and distance function kriging. Nearest neighbor, however, leads to blocky edges. Among these techniques,

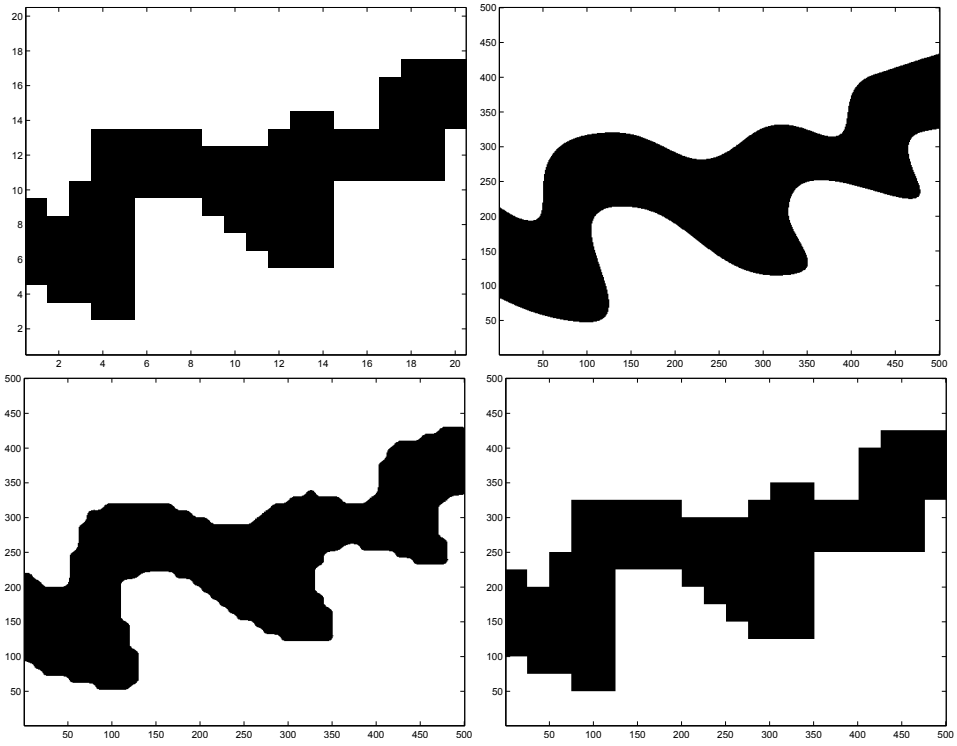

Figure 5.22: The coarse resolution map at the top left represents the training image which is considered to be accessible to this example. The resolution of training image is enhanced to the resolution of interest shown in maps (1) original (right top), (2) using DF kriging interpolation (bottom left), and (3) using nearest neighbor interpolation (bottom right).

distance function kriging interpolation seems to be a good candidate because of its simplicity, stability and visually appealing results. Another advantage of this technique is its flexibility to be manipulated accordingly. For instance, one can specify the variogram specification at the process of kriging, or the distance function could be modified through dilation/erosion to preserve some geological continuity and preferences of its user (see Chapter 6).

The constructed high resolution training image is considered to generate high resolution realizations in the following discussion.

5.3.2 Simulation with Resolution-Enhanced Training Image

This subsection conducts an exercise assuming the available training image (top left in Figure 5.22) does not have the adequate resolution (top right in Figure 5.22). The coarse resolution training image is constructed by extracting the cells regularly from the channel image at 25×25 cells. As can be observed in Figure 5.22, the high resolution image is generated using DF kriging (bottom left), and nearest neighbor interpolation (bottom right). Each of these high resolutions images are considered

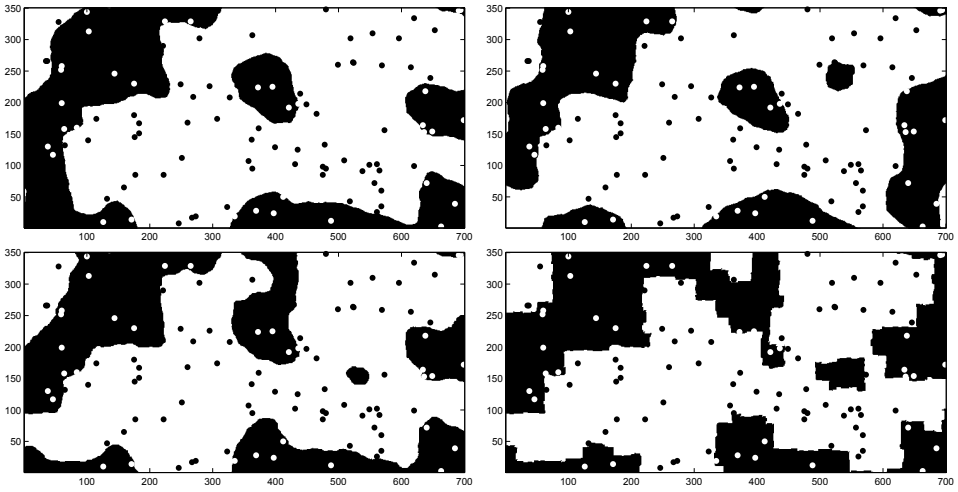

Figure 5.23: The map at the top left is the unconditional realization that has been simulated using MPS and the original training image. The 100 samples are selected randomly (as shown) to condition the further simulation using high resolution training image. The map at top right is the generated realization using MPS simulation, the conditioning data and the enhanced-resolution training image (original one). The realization at bottom left is generated similarly but using DF training image, and the one in the bottom right results from the smaller simulation but enhanced-resolution training image of nearest neighbor interpolation.

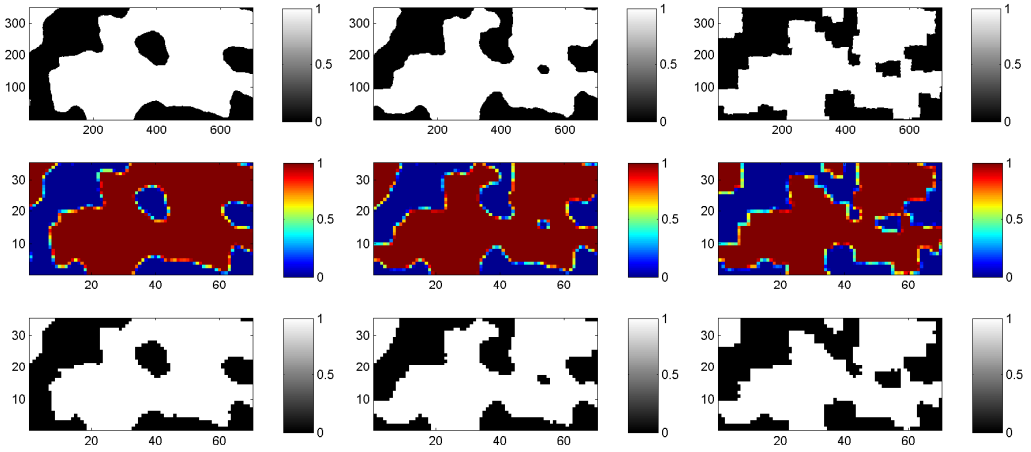

Figure 5.24: The maps at the top represent the high resolution realizations, the ones in the middle are ore proportion in upscaled map and the ones shown in the last row are the final upscaled binary map based on cut off value of 25%. Colored edges indicate the blocks with mixed material of ore and waste. First column refers to upscaling of first scenario, the middle is upscaling of second scenario and the last column refers to third case.

as the training image in three scenarios to construct MPS-based conditional realizations.

To provide conditioning data to this exercise, an unconditional MPS-based realization is generated using SNESIM program (Strebelle, 2000b) with the channel depiction as its training image. Then, 100 samples are regularly extracted from

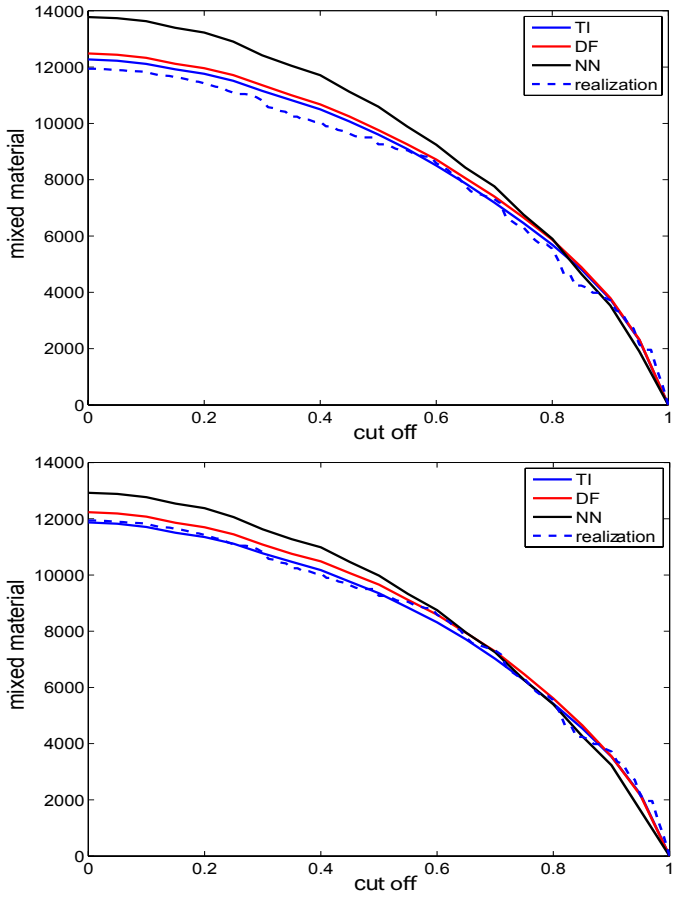

Figure 5.25: Curves for mixed material as a function of cut off values for the three scenarios (upscaled 10×10). The curves are average value of the amount of mixed material for 100 realizations. The curve at top represents the generated high resolution case conditioned to 100 samples; the one at bottom is generated high resolution case conditioned to 300 samples. With strong conditioning DF scenario performs very closely to original training image and reference case.

this realization. This is shown in Figure 5.23 at the top right. This unconditional realization consists of 30% channel. Having 100 samples as conditioning data, the SNESIM considers the three high resolution training image of channel, enhance-resolution based on DF kriging, and enhanced-resolution based on nearest neighbor in three scenario of 1 (baseline), 2 and 3, respectively, in order to simulate 100 realizations. One realization of each scenario is shown at top left, bottom left, and bottom right in Figure 5.23. The performance of the high resolution realizations are now examined through an upscaling problem. The upscaling cell size of 10×10 is considered as the target block size. The small scale features in the high resolution realizations are transferred into block features in the upscaled maps, shown in Figure 5.24. The block assignments of categories are based on exceeding cut off

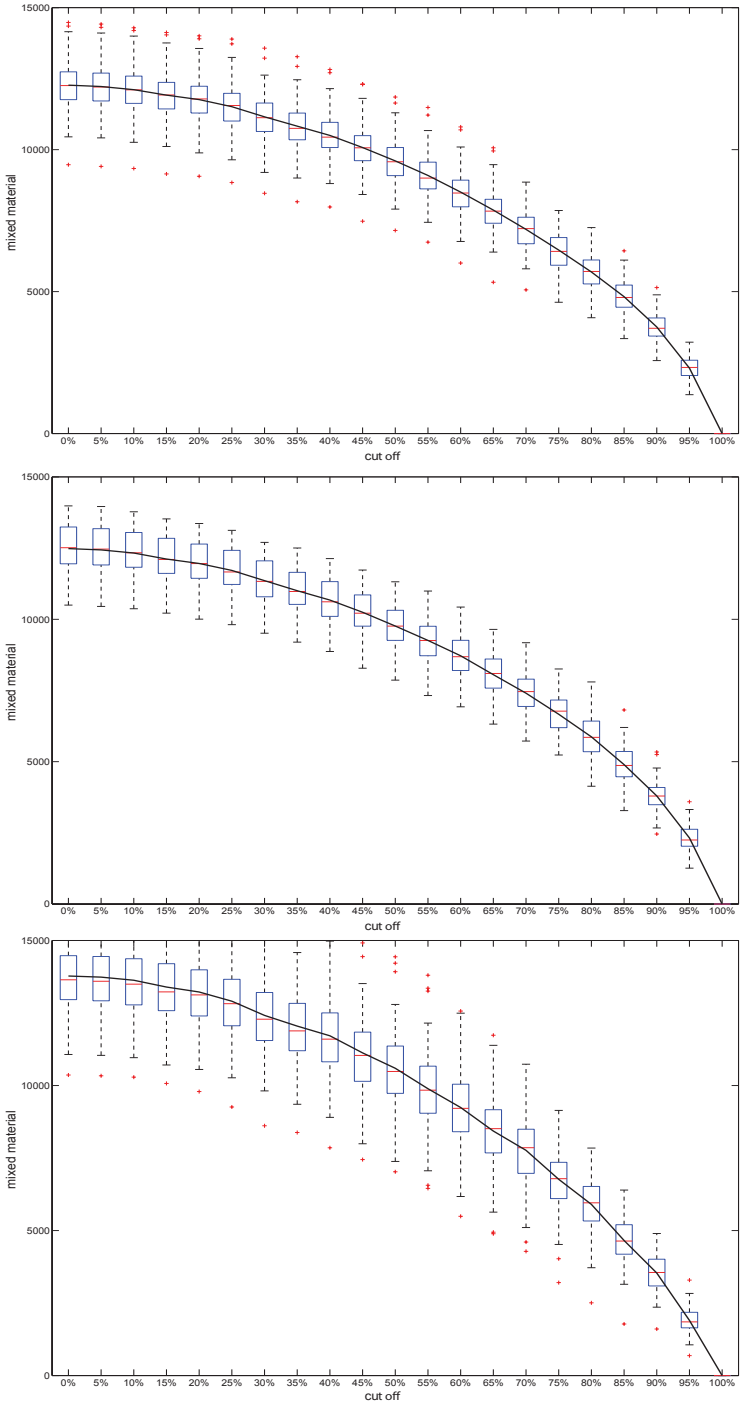

Figure 5.26: Boxplots for amount of mixed material of 100 realizations at every cut off value for all three scenarios. The one at top represents the first scenario with original training image, the one in the middle is the second scenario with enhanced-resolution training image generated using distance function kriging, and the last illustrates the third scenario with enhanced-resolution training image generated using nearest neighbor.

values. This is mostly due to the exclusive assignment of categories into upscaled blocks. This proportion indicates the amount of high quality reserve present in the

block. The performance of three scenarios is compared by measuring the fraction of upscaled blocks that are mixed. Figure 5.25 shows the average amount of mixed material as a function of cut off.

The amount of mixed material for 100 upscaled realizations and the three scenarios are summarized in Figure 5.25. The plot at the top represents the average amount of mixed material for 100 realizations–conditioned to 100 sample–as a function of cut off. As can be seen, the curves for first and second scenarios perform very closely and also close to a realization sample. The black curve belongs to the realizations generated using enhanced resolution training image with nearest neighbor interpolation. The figure at the bottom demonstrates the curve of mixed material for three scenarios and reference case, conditioned to 300 samples. The strong conditioning takes over in this case and curves overlap. The third scenario's performance is slightly poor compares to the rest. Figure 5.26 shows the boxplots for the three scenarios in terms of variability in amount of mixed material. The boxplots illustrate the variability for every 5% cut off values. The boxplot for scenario of nearest neighbor interpolation shows relatively larger variance with slightly larger means which indicate the overestimation. This must be due to blocky edges that results in unrealistic transitions. However, in general, there is no significant impact on the dispersion between the three scenarios. The main influence of using different training images is in the mean.

5.4 Chapter Summary

The smallest scale statistics that can be extracted from a training image is at its native resolution. This makes the generation of high resolution models challenging in the context of MPS. The frequency of patterns (FOP) for specific configurations are utilized to determine data interactions through high-order statistics. The independence of occurrence of patterns is defined relative to a random map with the same global proportions of facies. The FOP is then re-expressed as the natural logarithm of odds ratio and determined as a function of lag distance for lags changing from 0 to some large value. The FOP evaluations are then utilized to demonstrate the challenges in generation of high resolution models. The FOP of the training image at different scales suggest that prediction at smaller scales is not possible.

Later, the resolution of a training image is enhanced directly to account for small scale data interactions. To reach data statistics at scales smaller than that of train-

ing image, spatial resolution enhancement interpolation techniques are considered. Different interpolation techniques generate data in between coarse scale grid cells differently. Kriging signed distance function is advocated as a robust approach.

Chapter 6

Enforcing Connectivity to Categorical Variables

Most realizations generated by cell-based geostatistical simulation techniques present artifacts that are unavoidable. These artifacts often contain noise or unrealistic connectivity/disconnectivity of high or low quality reservoir units. In reservoir geostatistical modeling, understanding the connectivity of net reservoir flow conduits and non-net flow barriers/baffles may be essential for reservoir decision making; unrealistic connectivity of conduits or barriers would lead to biased production performance forecasting. Identifying the disparate facies units and enforcing the realistic connectivity is addressed in this chapter. A robust methodology is proposed on the basis of two mathematical morphology operations: dilation and erosion. This chapter elaborates on the proposed methodology in a 2-D context in the first part, and provides details of 3-D implementations along with examples in the second part.

6.1 Introduction

Model cleaning has been considered in geostatistical model post processing in the past few decades; see (Schnetzler, 1994; Stoyan et al., 1987; Journel and Xu, 1994; Deutsch, 1998a). In geostatistics, most image cleaning algorithms developed to date are focused on removing noise and smoothing facies boundaries. The problem tackled in this chapter, however, is beyond model cleaning; it is to enforce geological connectivity when necessary. The term "connectivity" establishes the fundamental flow setting in the reservoir and is influential in reserve evaluation (Larue and Hovadik, 2006; Hovadik and Larue, 2007; Larue and Hovadik, 2008).

Mathematical morphology has been widely practiced in image processing owing

to its founders Matheron (1975) and Serra (1982, 1988). Similarly, geostatistical post processing techniques have deployed morphological operations to clean models and remove noise (Stoyan et al., 1987; Schnetzler, 1994). The application of such techniques, however, were limited to binary models. More importantly, those techniques did not have explicit control over the global proportions in the model which is quite vital in reservoir assessment. This led to the work of Deutsch (1998a) in which the model cleaning was approached through maximum a-posteriori selection (MAPS). This technique maintains global proportions and visual realism but cannot enforce specific continuity. Later, Pyrcz and Deutsch (2004) facilitated MAPS with homotopic transformation to enforce realistic connectivity while cleaning the model.

This work is explicitly intended on post processing binary and non-binary models to identify unrealistic discontinuities and enforce connectivity on the basis of dilation and erosion. The methodology is established considering two aspects of (1) preserving the objects's geometry and shape (to the greatest extent possible), and (2) maintaining the original proportions. Both of these objectives are to be tackled through the definition of ideal connection: Intuitively, the ideal connection occurs when the objects are (a) expanded along their maximum directions of anisotropy, and (b) eroded orthogonal to the direction of dilation.

Applying dilation and erosion in sequence is known as closing in mathematical morphology (Haralick et al., 1987). In the definition given for ideal connection, dilation is the main operation as it is in closing operation. The distortion that results from dilation of the image is then taken care of by applying the erosion. Erosion and dilation operations are directly related to the shape of the objects and are conventionally applied by structure elements (Haralick et al., 1987). One undesired result of using the structure element scheme is the indiscriminate distortion of all regions in the image. This is in contrast to the purpose of merging objects in a controlled manner. Thus, the ideal connection is proposed to achieve by (1) identifying the disparate objects; (2) evaluating their anisotropy directions; and (3) quantifying the minimum amount of mass added to connect the objects. The implementation of this process is broken down into (1) dilate the targeted objects until merged; and (2) erode the merged unit, using a fast and efficient algorithm.

For simplicity and illustrative purposes, the proposed methodology is described in 2-D context. The development of the methodology in 2-D helps to investigate the robustness, and recognize the control parameters before moving forward to the

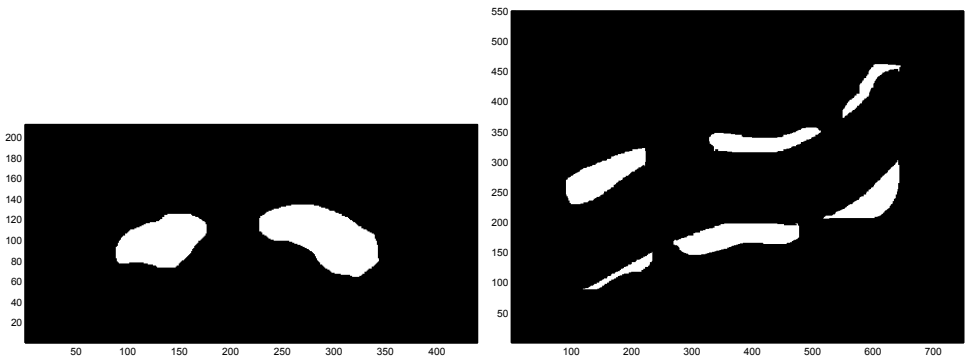

Figure 6.1: The binary map on the left represents two objects that should be unified to one object. The second binary map on the right depicts a levee with broken pieces. The objective of this chapter is to propose a robust method to connect such broken pieces in the model while preserving conditions such as reservoir global proportions.

3-D implementation. Also, it is noted that the terms *connectivity* and *continuity* are used interchangeably in this chapter, while they can have different meanings in other contexts.

6.2 Methodology

The first step in merging objects is to expand them to the point that they touch. This is achieved by applying dilation which results in the increase of the mass of the objects and therefore altering the global proportions. The dilation will be kept as "efficient" as possible; the uncontrolled growth of objects is inadmissible. The term "efficient" implies (1) dilating only along the preferential directions; and (2) eroding back from directions where there is no potential connection. The preferential direction is the direction that will make the object connect to the other object of the same category nearby. To identify the preferential direction, the potential connection need to be first identified. The potential connection depends on several factors such as the objects' relative distances, sizes, and geologic expectations.

In a 2-D implementation, visual inspection helps asses the objects' positions, directions of anisotropy, sizes, and their relative distance. These parameters basically determine how realistic it is to connect the objects. The objects' separation influences whether or not they should be merged. For example, if the objects' lengths must increase by 100%, then connecting them would not be reasonable. Things become more complicated when dealing with objects in 3-D; objects' relative distances cannot be readily detected. Also, in 3-D models, it is difficult to determine if a particular object is enlarged, what other object it would connect to.

Thus, to apply dilation along the preferential direction, the anisotropy of the objects must first be identified. If the objects are grown in their direction of anisotropy, the amount of mass added to the object is mostly along the direction of potential connection. Applying Dilation utilizing a distance map is known to be a more efficient and flexible approach (Laÿ, 1987) compared to the initial use of structure element. The desired dilation can be attained by selecting the appropriate threshold value on the distance map (Ragnemalm, 1992). Then, to dilate in the potential direction, the distance map is proposed to be modified by object's direction of anisotropy. To determine the direction of anisotropy, parameters such as radii, azimuth, dip, and plunge should be determined.

The two binary maps shown in Figure 6.1 will be considered to discuss the proposed workflow and the performance of methodology. The two disconnected objects in the map on the left are supposed to be a unified object and the six disparate objects in the map on the right are supposed to be two parts of a levee so two sets of three objects should be connected.

6.2.1 Dilation Approach

In the proposed dilation operation, the object's expansion is controlled by applying the anisotropy of the object on the distance map. The distance map is evaluated on the binary image by calculating the Euclidean distance of the object of one type to the boundary of the other one. After identifying the rock types, depending on the geologic setting of the deposit, the sequence of the formation of the reservoir, and the properties of the rock types, the process of object connection could be treated sequentially. Thus, for every rock type, it is necessary to identify the disconnected intervals. Also, the most important facies or objects are suggested to be processed last, in case their connections disturb any other previous enforced connectivity.

The identification of the object is equivalent to determining its size, orientation, and position of the object. The non-net intervals are identified by scanning through the realization and calculating connected regions. Connected regions are defined by face-connected voxels (Deutsch, 1998b). Each connected region of non-net interval is defined as a separate non-net geo-object; the geo-obj program of Deutsch (1998b) is used to identify the isolated goe-objects. After identifying the geo-objects, the moment of inertia approach is applied, assuming that all non-net voxels have equal mass, to determine anisotropy and orientation. In the sequence of connecting dis-

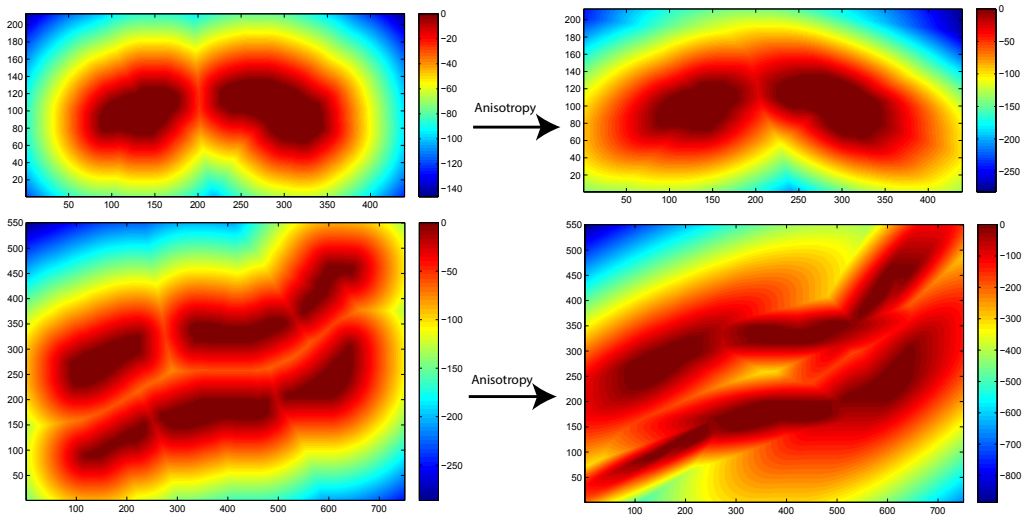

Figure 6.2: The distance maps on the left are determined with no respect to anisotropy of the objects. The ones on the right are calculated considering the anisotropy of the objects.

parate objects of one particular facies, the rest of the facies will be represented by one code while the target facies is identified with another code. The distance map for an object is evaluated from a binary model (the model of target against all others).

Complex geological settings such as fluvial deposits that contain channel features have different continuity in different regions. Thus, the intervals selected will also have different orientations and distributions. To be able to deal with different directions of anisotropy, every object should be studied separately. The distance function of the object is modified with its rotation-anisotropy matrix. This way the points along the direction of anisotropy are represented with lower distances relative to the other points. This approach controls the object's expansion. Figure 6.2 illustrates the influence of considering anisotropy of the objects on the distance map for the two cases of objects and levee.

A dilation parameter D_p is defined to allow the expansion of the object by introducing a threshold to the distance function of the object. Thus, the dilation parameter could be chosen as a function of object's size. As a result of this approach, the object expands honoring the magnitudes of the anisotropic directions. That is to grow faster along the direction of maximum anisotropy, and slower along the direction of minimum anisotropy.

Note that determining the ranges of anisotropy is not straightforward. The geo-object are approximated by a same-size ellipsoid as proposed by (Babak and

Deutsch, 2008; Lajevardi and Deutsch, 2011; Lajevardi et al., 2015) to utilize the ellipsoid's relationship between principal directions and its radii for the range calculations.

6.2.2 Anisotropy of the Object

To characterize the geo-object's anisotropy, the moments of inertia tensor is considered as proposed in Hassanpour and Deutsch (2007, 2008). In this technique, the objects' three principal axis are evaluated by the moment of inertia, also known as mass moment of inertia (or the angular mass of a body). Moment of inertia is the rotational analog of mass; it relates to the distribution of the mass throughout the body. The moment of inertia is the inertia of a rigid rotating body with respect to its rotation:

$$I = \int r^2 dm$$

where m is the mass and r is the perpendicular distance of the point mass to the axis of rotation.

The moment of inertia has two forms: a scalar form that is used when the axis of rotation is known and the tensor form that summarizes all moments of inertia for different axes of rotation. For a rigid body consisting of N point masses m_i, the moment of inertia tensor is defined as (Rana and Joag, 2001):

$$\mathrm{I} = \begin{bmatrix} I_{xx} & I_{xy} & I_{xz} \\ I_{yx} & I_{yy} & I_{yz} \\ I_{zx} & I_{zy} & I_{zz} \end{bmatrix}, \quad \text{with} \tag{6.1}$$

$$I_{xx} = \sum_{i=1}^{N} m_i \ ({y_i}^2 + {z_i}^2); \qquad I_{xy} = I_{yx} = -\sum_{i=1}^{N} m_i \ x_i \ y_i$$

$$I_{yy} = \sum_{i=1}^{N} m_i \ ({x_i}^2 + {z_i}^2); \qquad I_{xz} = I_{zx} = -\sum_{i=1}^{N} m_i \ x_i \ z_i$$

$$I_{zz} = \sum_{i=1}^{N} m_i \ ({x_i}^2 + {y_i}^2); \qquad I_{yz} = I_{zy} = -\sum_{i=1}^{N} m_i \ y_i \ z_i$$

where x_i, y_i and z_i are the distances of point i from the coordinate axes. I_{xx} can be interpreted as the moment of inertia around the x-axis when the objects are rotated around the x-axis and I_{xy} is the moment of inertia around the y-axis when the objects are rotated around the x-axis. Note that the matrix $\mathbf{I}$ is symmetric by definition. This means that its eigenvalues are all real, and its eigenvectors are

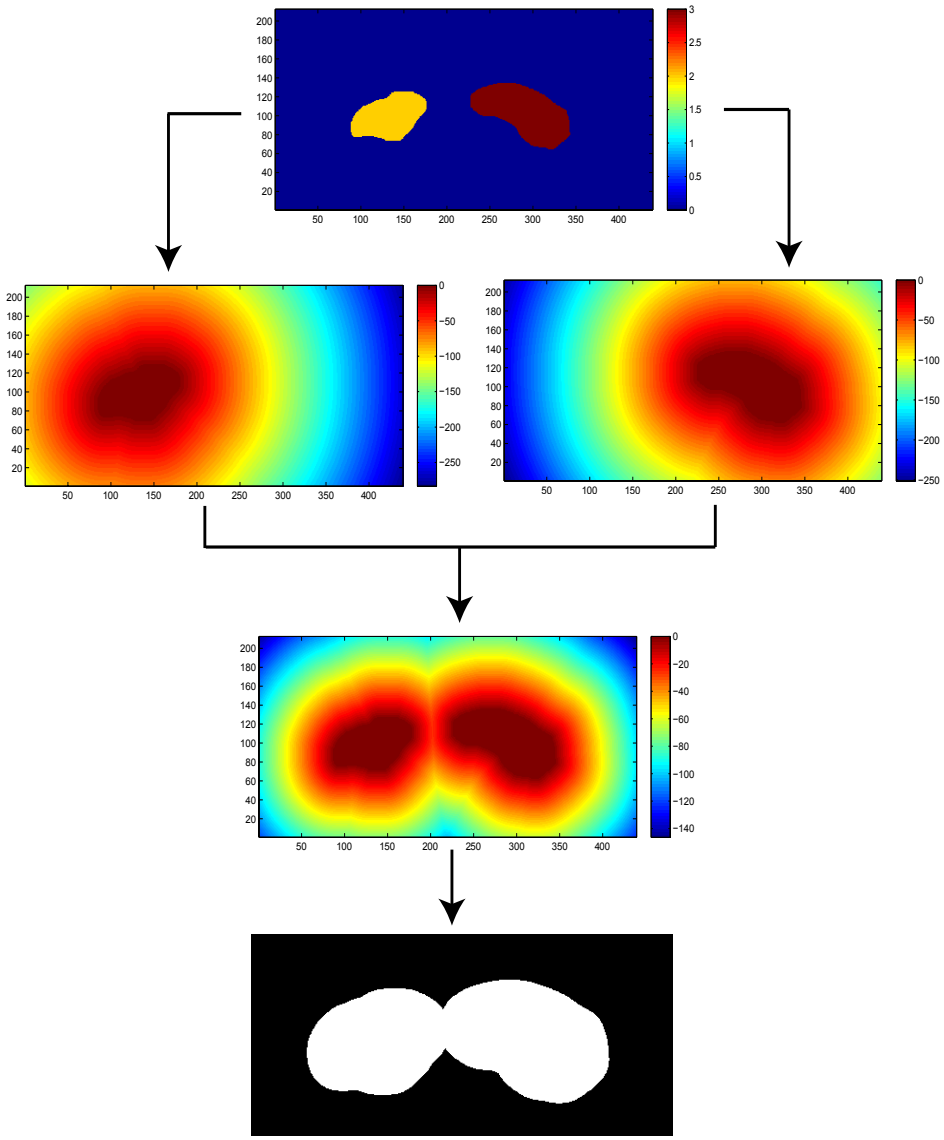

Figure 6.3: Dilation is applied by calculating the distance map of each object separately; note the objects are colored differently. The distance map of the entire model is determined by combining the two distance maps of the two objects. The two objects connect as a result of the growth considering a proper threshold value of -30 on the distance map. The global proportion of the objects increases from the initial fraction of 12% to 31%.

orthogonal to one another. To determine the principal axis of the geo-object, the coordinate system in which the moments of inertia is calculated should align with the principal axis of the object. Therefore, the moments of inertia tensor could be represented as a diagonal matrix in which using the eigenvalue decomposition, the principal values are eigenvalues of the diagonal matrix and the principal directions are its eigenvectors.

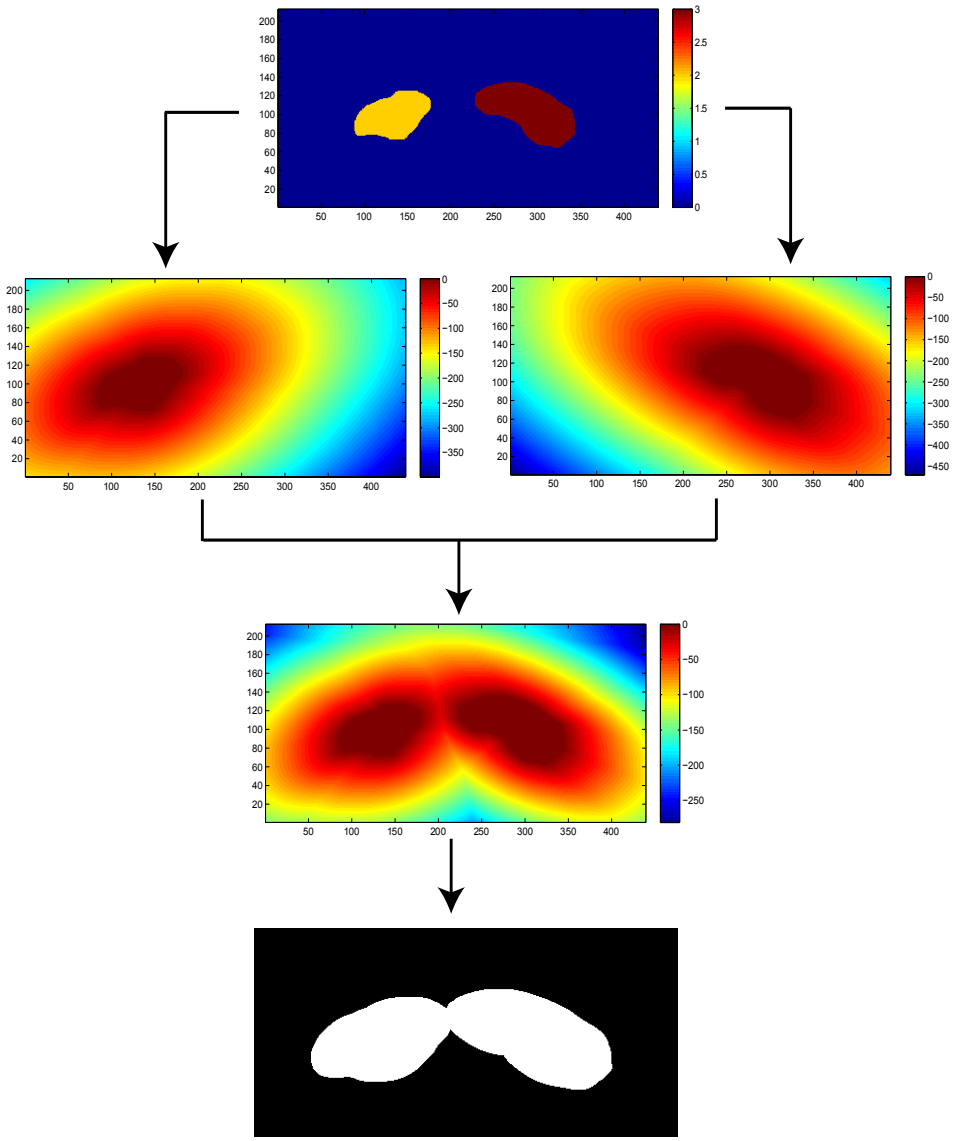

Figure 6.4: The distance function of the two objects are calculated considering the anisotropy of every object. The distance function of the entire map results from combining the two distance maps of the two objects. The two objects connect considering a threshold value of -15 on the distance map shown in dilated figure. The global proportion of the objects is increased from the initial fraction of 12% to 22%. Therefore, the objects are merged with less addition of the mass compared to Figure 6.3.

Distance Function and Rotation-Anisotropy Matrix

The distance function or signed distance function is determined by minimizing the distance between every point on the map to the boundary of the object. The distance of a given point $\mathbf{x}$ from the boundary of a set Ω is mathematically defined by

$$f(x) = \begin{cases} d(\mathbf{x}, \Omega^c) & \text{if } \mathbf{x} \in \Omega \\ -d(\mathbf{x}, \Omega) & \text{if } x \in \Omega^c \end{cases}$$

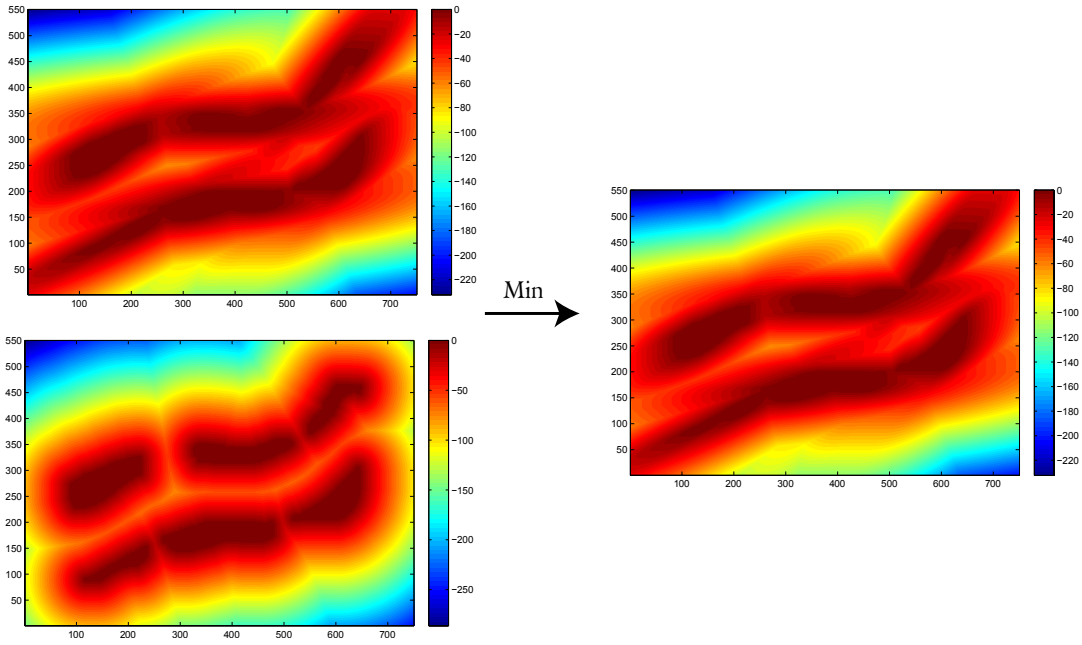

Figure 6.5: The distance map is evaluated for two levees considering the anisotropy of the objects (top), and no anisotropy (bottom). The minimum distance map is the one with anisotropy consideration.

where $d(\mathbf{x}, \Omega) = \inf_{y \in \Omega} d(\mathbf{x}, y)$ and infimum which indicates the greatest lower bound. In Figure 6.3, the distance function for every object is determined differently and the minimum distance of both is the resulting distance function of the map. The dilation map is calculated by applying the threshold to the distance map so the two objects merge.

As proposed, applying the rotation-anisotropy function of the objects into the distance map is to allow an efficient dilation. As shown in Figure 6.4, the distance map of every object is modified by its direction of anisotropy. The two objects are connected by applying the threshold on the distance function map of the two objects. Compare to Figure 6.3, the amount of mass added to merge the objects is smaller. Figure 6.5 shows the distance map of the levee map in which the rotation-anisotropy function of every objects is applied to its distance map at the top. The map at the bottom is the distance function of levee model with no anisotropy consideration. The minimum distance function for every point is distance map which is evaluated considering the anisotropy of objects. This confirms that the minimum distance achieves when the orientation-anisotropy of objects are considered in the distance evaluation.

The mathematical expression to evaluate the rotation-anisotropy matrix is as

follows (Deutsch and Journel, 1998). Angle α is obtained by rotating the original X and Y axes in the horizontal plane about the original z-axis. Similarly, β is the angle rotation around y-axis and θ is the rotation angle around the x-axis.

$$\begin{bmatrix} X_{\text{initial}} \\ Y_{\text{initial}} \\ Z \end{bmatrix} = [R_1] \begin{bmatrix} X \\ Y \\ Z \end{bmatrix} = \begin{bmatrix} cos\alpha & -sin\alpha & 0 \\ sin\alpha & cos\alpha & 0 \\ 0 & 0 & 1 \end{bmatrix} \begin{bmatrix} X \\ Y \\ Z \end{bmatrix}$$

$$\begin{bmatrix} X_{\text{initial}} \\ Y_{\text{rotated}} \\ Z_{\text{initial}} \end{bmatrix} = [R_2] \begin{bmatrix} X_{\text{initial}} \\ Y_{\text{initial}} \\ Z \end{bmatrix} \begin{bmatrix} 1 & 0 & 0 \\ 0 & cos\beta & sin\beta \\ 0 & -sin\beta & cos\beta \end{bmatrix} \begin{bmatrix} X_{\text{initial}} \\ Y_{\text{initial}} \\ Z \end{bmatrix}$$

$$\begin{bmatrix} X_{\text{rotated}} \\ Y_{\text{rotated}} \\ Z_{\text{rotated}} \end{bmatrix} = [R_3] \begin{bmatrix} X_{\text{initial}} \\ Y_{\text{rotated}} \\ Z_{\text{initial}} \end{bmatrix} \begin{bmatrix} cos\theta & 0 & -sin\theta \\ 0 & 1 & 0 \\ sin\theta & 0 & cos\theta \end{bmatrix} \begin{bmatrix} X_{\text{initial}} \\ Y_{\text{rotated}} \\ Z_{\text{initial}} \end{bmatrix}$$

Now, consider that the point dv with components of dx, dy, and dz in XYZ coordinate system should be translated to the coordinates of the anisotropy of the object. The new coordinates are evaluated by:

$$av = \text{anisotropy mtx} \times \text{rotation mtx} \times dv$$

where the rotation matrix is $[R_3] \times [R_2] \times [R_1]$ and the anisotropy matrix is determined by

$$\begin{bmatrix} \frac{\text{range1}}{\text{range2}} & 0 & 0 \\ 0 & \frac{\text{range1}}{\text{range1}} & 0 \\ 0 & 0 & \frac{\text{range1}}{\text{range3}} \end{bmatrix}$$

where range1 is aligned along the y direction, range2 is aligned along the x direction and range3 is aligned the z direction. Recall that the angles α, β, and θ are determined from principal directions calculated in the previous section.

The next section discusses the proposed erosion process to smoothen the dilation and maintain the facies global proportions.

6.3 Erosion: Proportion Map

In the proposed erosion process, the conventional use of structure element is considered since eroding orthogonal to the anisotropy of the merged object is challenging to implement. The structure element is proposed to be applied in an iterative manner through a search template. The search template scans over the dilated map and

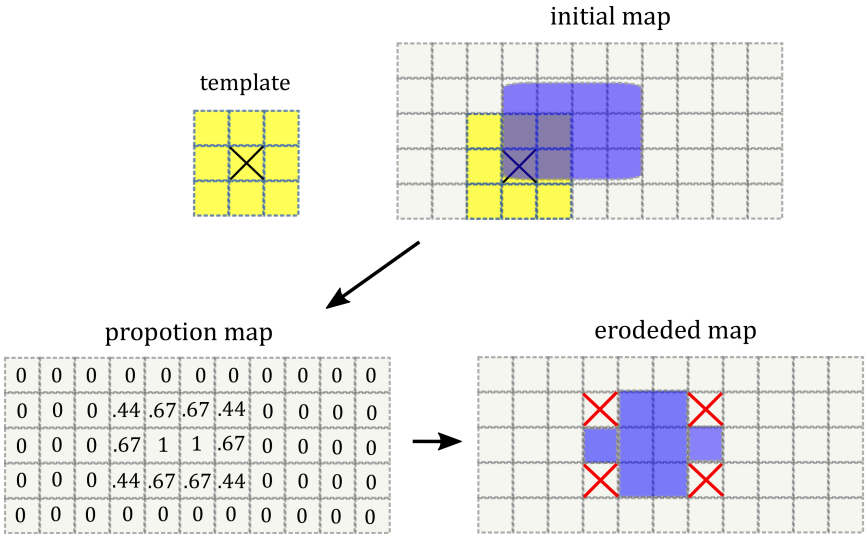

Figure 6.6: A 3×3 template is selected to scan the initial map for erosion. Every grid cell in the proportion map is assigned by the value representing the proportion of template which is inside the object of interest. The erosion is then applied by considering a threshold over the proportion values in proportion map to whether keep or erase the grid cell.

verifies the portion of template that is inside the target object. The result would be a proportion map that represents every grid cell with proportions of the search template being inside the object.

Figure 6.6 demonstrates the generation of the proportion map that results from the scan of the template over the model. As can be observed, the proportion map is sensitive to (i) the size of the search template (ii) the shape of the search template. If the template is very small, a big portion of the target object will be identified by 1 in the proportion map. However, if the template is large, a much smaller portion of the dilated object that is typically closer to the centre of the object will have the proportion value of 1. The utilization of "map" in the proportion map does not limit its usage to 2-D models. Proportion map could be made for 3-D models as well.

In addition to the template's size and shape, a proportion value should be selected on the proportion map to decide on keeping or removing the target grid cell. This proportion value is referred to as "erosion control parameter" in this work. The choice of the control parameter matters on the result of the eroded object. This process is applied iteratively until the global proportion of the dilated model approaches the facies global proportions of the initial model. For instance, a control parameter of 0.9 erodes a big chunk of the object in only one attempt while a control parameter of 0.6 erodes the object more slowly. This is why using a large template

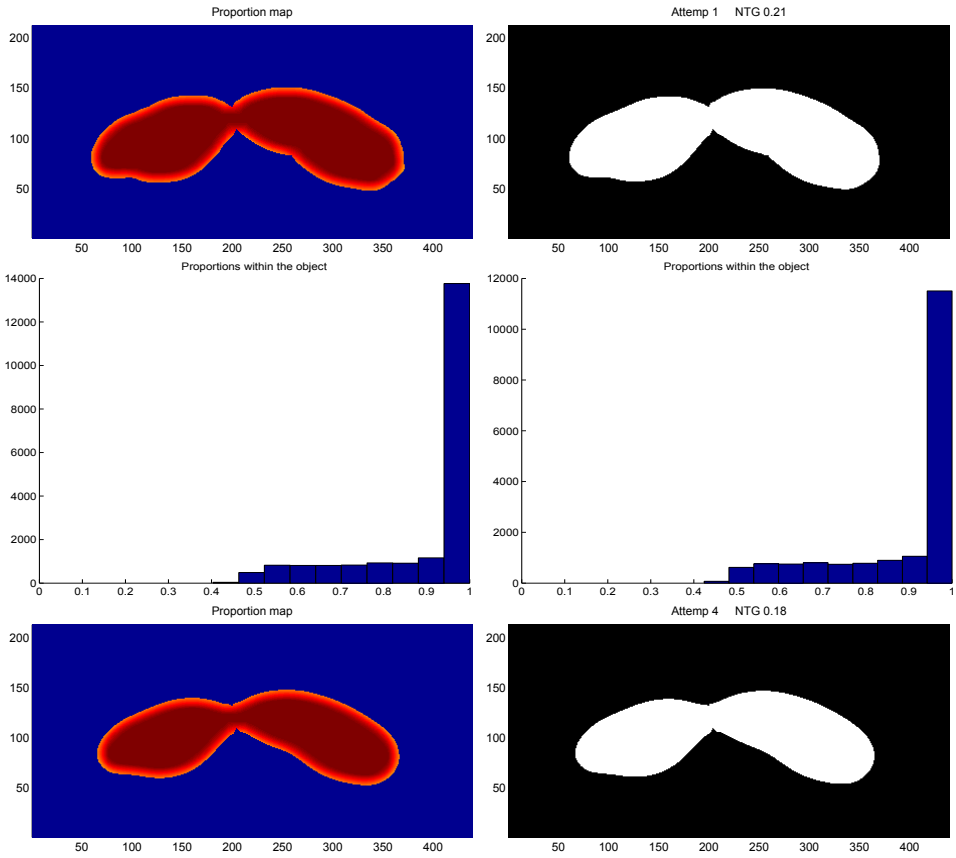

Figure 6.7: The proportion map for the dilated image is shown at the top. The histogram of the proportion map for first iteration is shown on the left, and the one associated to iteration 4 is shown on the right. The resulting dilated map with the NTG of 0.18 is shown at the bottom.

is not recommended since it makes it harder to tune the erosion control parameter to avoid a thick deletion of the object at once.

The erosion is best implemented when the cell deletion preserves the (1) shape of the objects, and (2) the generated connection bond. It is important to see that after connecting the broken objects through dilation, the connection interval cannot be as thick and stable, therefore, any uncontrolled erosion process might result in destroying the connection which is truly undesirable. It is noteworthy to recall that the objective of this work is specifically connecting the disconnected intervals which is attained by the dilation process. The necessity of applying erosion is to maintain the global proportions which is distorted when objects are dilated (although the proposed dilation process limits the global proportion distortion to the creation of the connection bond). In Figures 6.7 and 6.8, the erosion is applied on the dilated map of the connected lobes so that the global proportions is adjusted and the connection stays stable. The global proportion is maintained after 11 iterations

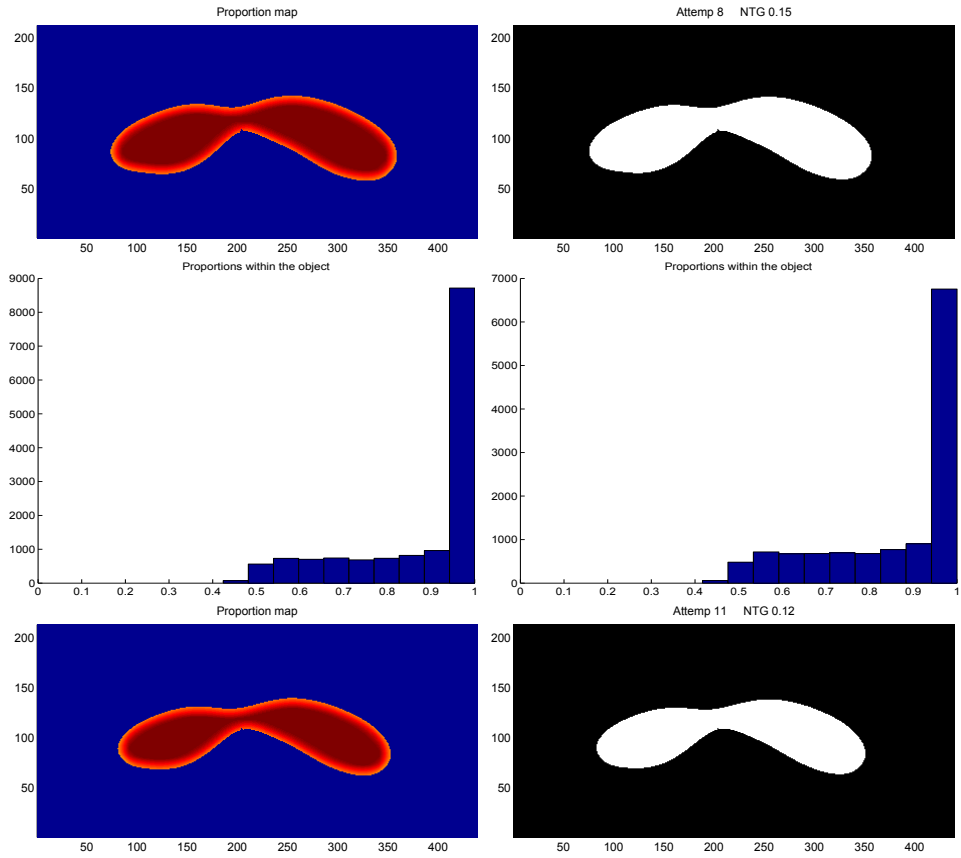

Figure 6.8: The proportion map for the dilated image at iteration 8 is shown at the top. The histogram of the proportion map for iteration 8 is shown on the left, and the one associated to iteration 11 (which is the last iteration to maintain global proportion) is on the right. The resulting dilated map with the NTG of 0.12 is shown at the bottom.

using a small search template. The decrease in the proportion of the object could be observed in four attempts in applying erosion.

For the case of levees shown in Figure 6.9, the initial proportions of geo-objects is 6%. After the dilation process, the facies proportions increases to 21%. This amount of expansion is reasonable since some of the objects are quite further apart. As discussed so far, selecting the (a) search template, (b) the erosion parameter, and (c) the number of iterations are subjective matters. It is important to try different combinations and make sure that the number of geo-objects stay the same after the erosion is applied. In the levee example, the number of objects goes from 6 to 2 when dilation is applied. This means that, the number of objects should remain 2 in the erosion process, while the global proportions is adjusted to its initial fraction.

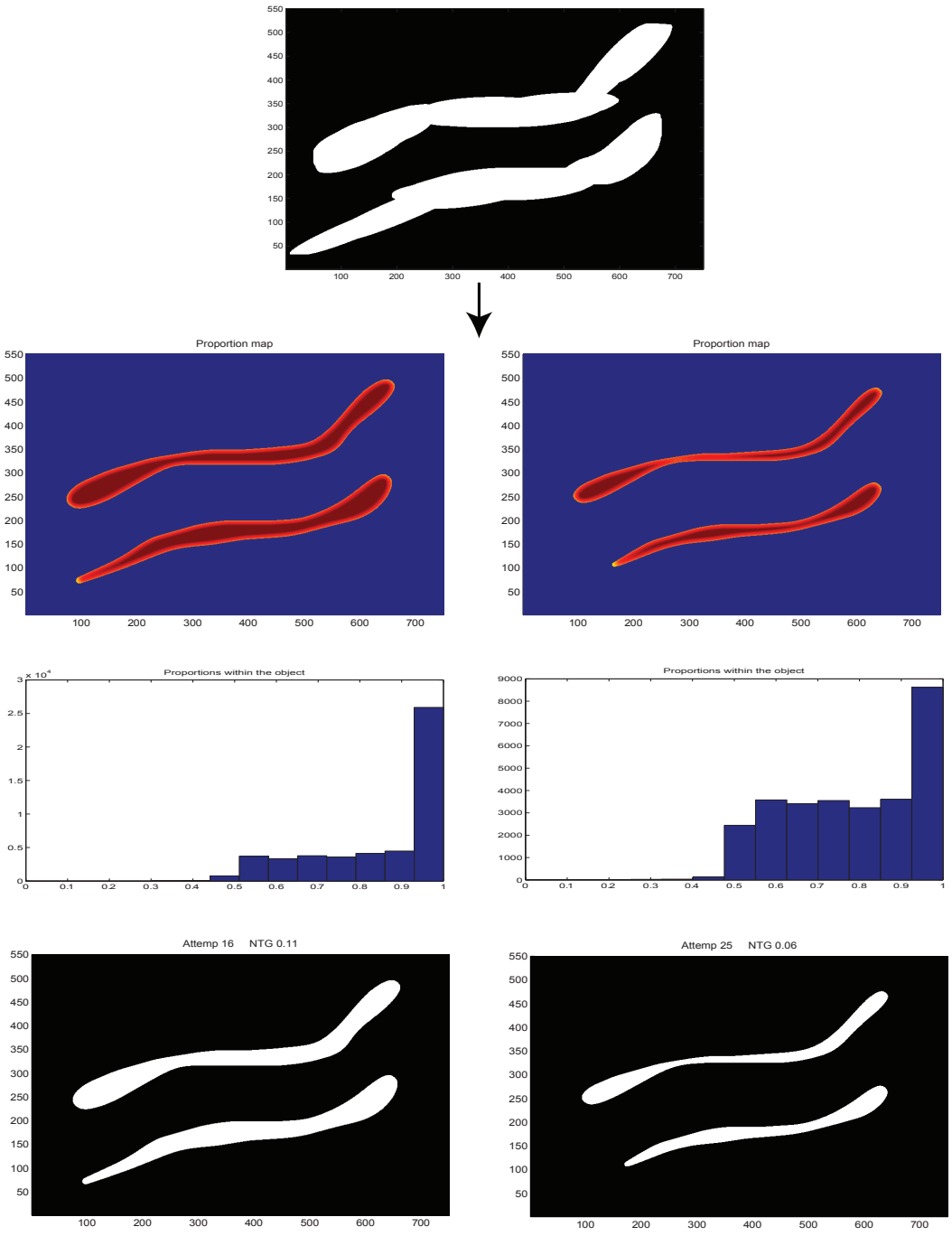

Figure 6.9: The dilation map is generated using a threshold over the minimum distance function. This results in the same rate dilation for all the objects since the threshold value is constant. The proportion map approach is considered for erosion. The global proportions are achieved after 25 iterations of applying erosion.

6.4 Examples and Considerations

Dilation can be performed considering different conditions. For example, in the levee example, disconnected intervals have different sizes, widths and orientations.

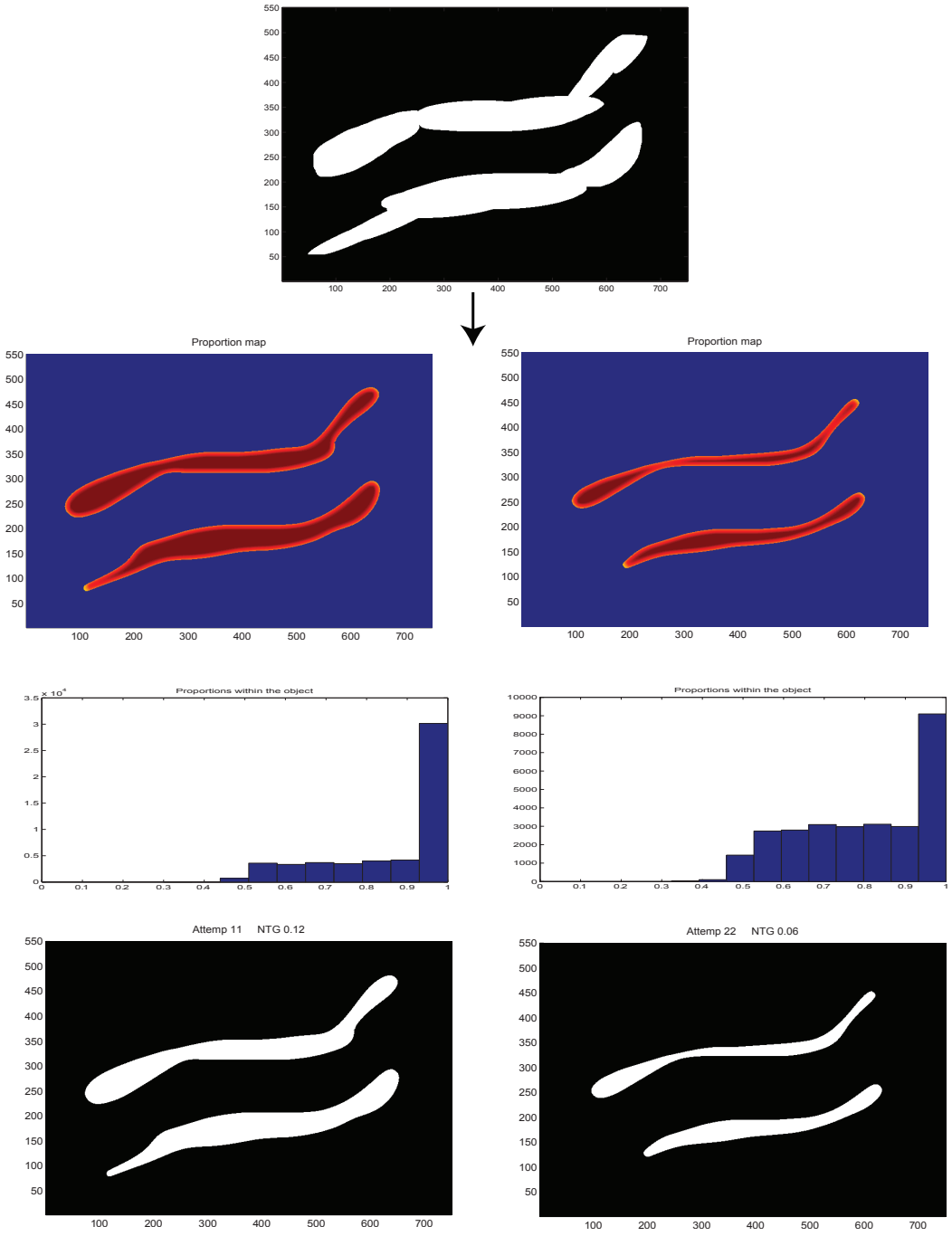

Figure 6.10: The dilation is based on maximum length parameter over every object separately. This results in different rate of growth for every object. The proportion map approach erodes the map as needed. The global proportions are achieved after 22 iterations of applying erosion.

The geological realism requires every three intervals on each side to form an evenly distributed channel levee. The dilation with the same rate on all the objects helps to meet this condition. For all objects to expand with the same rate, a threshold should be applied on the distance map; the relatively small objects have the same chance

of expansion as larger objects. Figure 6.9 represents this case where all objects have grown uniformly. The erosion of the dilated objects is implemented by considering the proportion map approach and applying it iteratively.

Alternatively, the merging could be applied honoring the objects' sizes and lengths in the realization. This could be implemented by defining the threshold on the object's distance function using a ratio factor of its size or maximum range. This form of dilation is applied to the same levee exercise in Figure 6.10. The non-uniform rate of expansion can be observed in this example in which the bigger objects dilate faster than the smaller ones. Subsequently, the erosion process would preserve the shape of the larger objects relatively more than the smaller ones. It can be observed from Figures 6.9 and 6.10 that the resulting eroded maps also differ. Although pursuing different objectives, both approaches connect broken levees in a visually appealing manner and maintain model global proportions.

Lastly, there are cases where the regions of fragments honor the conditioning data and could be removed after implementing erosion. This aspect must be verified during the process; the control parameter can only chose to remove the grid cell if it is not conditional data. Note that the 2-D examples of objects and levees are not considering any conditional data.

The basis of enforcing realistic continuity is dilating along the principal axis of the anisotropy of the objects. Intuitively the erosion is expected to be applied opposite to the direction of dilation. This would be challenging as dilated objects are now connected, and eroding in the orthogonal direction of dilation is different for different parts. Such erosion would not necessarily maintain the global proportions while preserving the connection. Figure 6.11 demonstrates the result of erosion process which is applied on the dilated levee model of Figure 6.9. The distance map is modified by the orthogonal anisotropy matrix of the objects that are connected in the dilated map (The orthogonal anisotropy matrices of objects have been obtained from the original map.) The distance map is eroded by applying a threshold value. The threshold value is tuned so that some amount of added mass is reduced while merged objects are not broken. The resulting map is shown at the bottom right of Figure 6.11. The global proportion of targeted facies at this point is 13% which is more than twice the original proportion. The proposed erosion process is applied further to maintain the target proportion of 6%. The global proportion is reached after 44 iterations shown at the bottom left of the same figure.

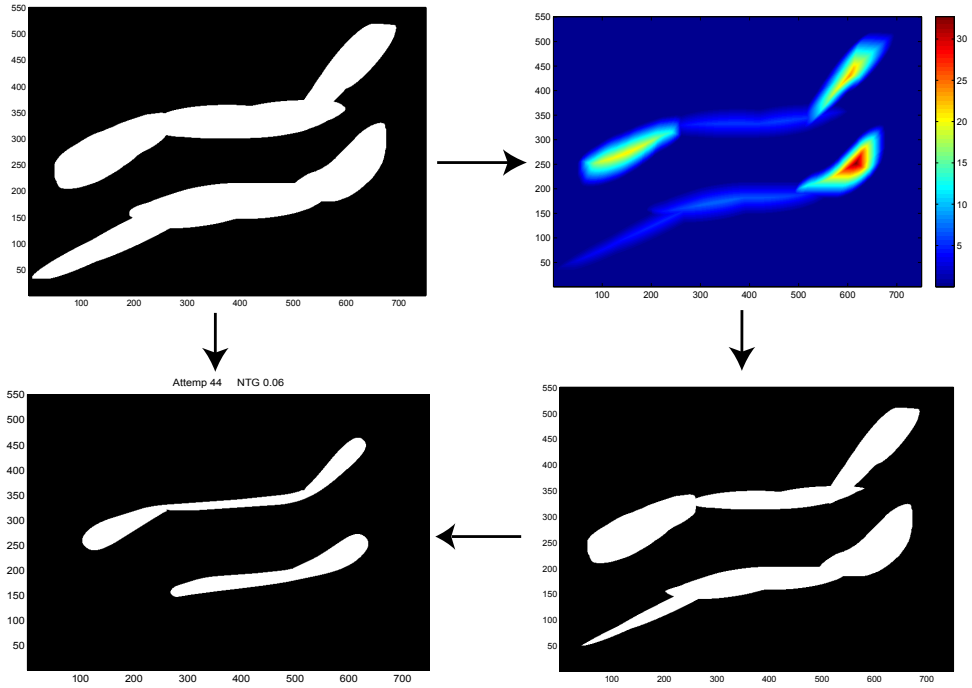

Figure 6.11: The dilation is based on a threshold on the minimum distance map. The orthogonal rotation-anisotropy matrix is used for erosion. The erosion at this point results in global proportion of 0.14. Proportion map is later considered to maintain the initial proportion.

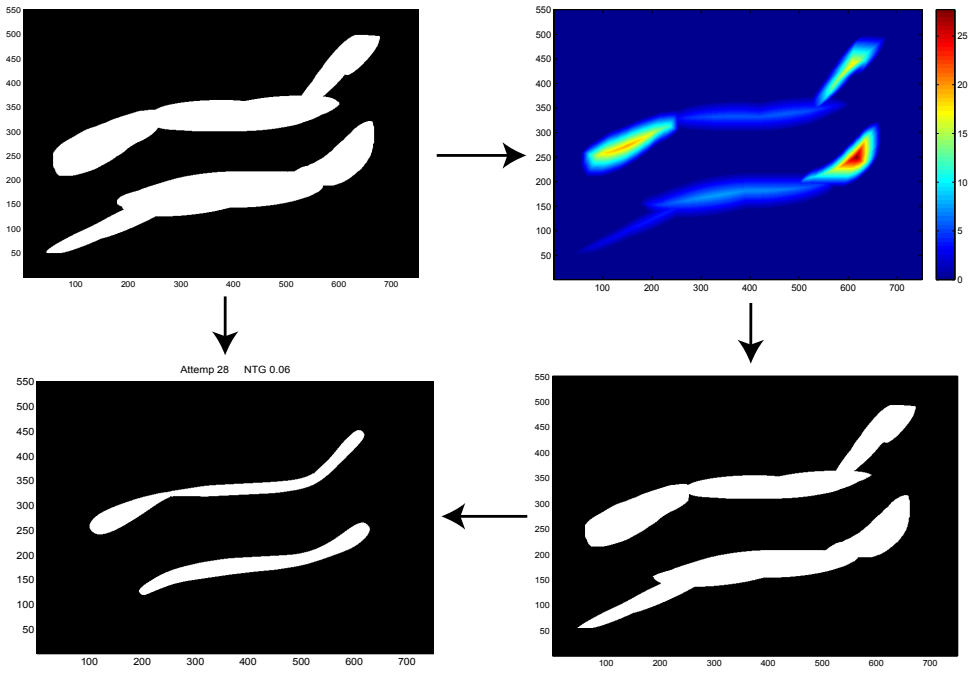

Figure 6.12: The dilation is done considering a ratio of the maximum length with respect to every object separately. The orthogonal rotation-anisotropy matrix is used for erosion which results in global proportion of 0.13. Proportion map technique is used to erode further and maintain global proportion.

Figure 6.12 demonstrates the same procedure applied to the dilated map of example in Figure 6.10 in which the growth of objects is based on their length of continuity or size. Similarly, the proposed erosion map needs to be applied further to maintain global proportion. The global proportion is achieved after 28 iterations. It is interesting to compare the number of erosion iterations in Figure 6.9 which is 25 and Figure 6.11 which is 44. In the latter, the erosion is applied along the opposite direction of dilation. The channels do not look as smooth and realistic when the erosion is applied along the direction opposite to the direction of dilation.

Based on the above results (1) controlling the amount of dilation with the object's size; and (2) applying erosion through the proportion map is considered for the 3-D implementation which comes next.

6.5 3-D Implementation

The proposed methodology is implemented in Fortran for 3-D models. The program accepts 3-D models that are to be considered for connecting disparate objects. The parameter file asks for a dilation parameter that varyies between 0 and 100. This is the parameter applied to distance function of every object to control the expansion by a factor of object's size. The parameter must be tuned until the connections of objects is reasonable. In the implementation context, the most efficient dilation occurs when with largest decrease in the number of objects and the least increase in the facies proportion. The output file `dilated.mod` contains the information regarding the processed dilated model which is generated automatically. This is a subjective process and requires iterative judgment. The dilation parameter should be tuned in order for the connection to happen with small changes in global proportions, but the connection also needs to be stable and moderately insensitive to the erosion process.

One aspect of the proposed dilation is that the expansion of the objects happens only if the connection will be followed. For example, if the dilation parameter is 10%, the objects in the model should be enlarged by 10% of their sizes along their direction of anisotropy. There is no guarantee that the grown objects are going to be connected. If the enlarged object does not touch any other object, it will be return back to its original size. A similar consideration is taken into account in the erosion process. The erosion process aims at maintaining the original global proportion in the model while keeping the connection region intact. Three erosion parameters are

considered in the algorithm: the number of iterations, the threshold factor for the control parameter, and the minimum size of objects. After the dilation process, the program identifies the news objects with new sizes. The minimum size ratio makes sure the unified object does not erode uncontrollably.

Table 6.1: The number of objets, their sizes and model global proportions are listed for every stage.

model	geo-object	size	global proportion
initial	1	708	0.26
	2	682	
	3	493	
	4	464	
dilated	1	1876	0.31
	2	889	
eroded	1	1726	0.26
	2	616	

A small 3-D model of 30×30×10 is considered here. The output file of the program, `geo-obj.sta` shows that the global proportion of targeted facies is 26% with 4 objects. The output file of `geometry.sta` provides mass and direction of anisotropy of the 4 objects. The program utilizes this information to dilate along the anisotropy of the objects as described above. Table 6.1 tabulates the number of objects, their sizes, and global proportions for three models of initial, dilated and eroded models.

3-D Examples

Three examples are shown to demonstrate different aspects of the program, the parameter file, and most importantly the functionality and effectiveness of the proposed methodology. A levee training image is selected from the training image library constructed by Pyrcz et al. (2008). The size of the TI is 256×256×128 grid cells with cell sizes of 16 m × 16 m × 0.156 m with a levee proportion of 20%. Three different parts of this TI have been considered in the following examples. In Figure 6.13, the extracted part has 64×64×40 grid cells.

In the first example, the objective is to connect two objects and not the rest of the objects. Using a dilatation parameter of 15 and applying it to all the objects (option 0) will result in more connections required. The program provides an option

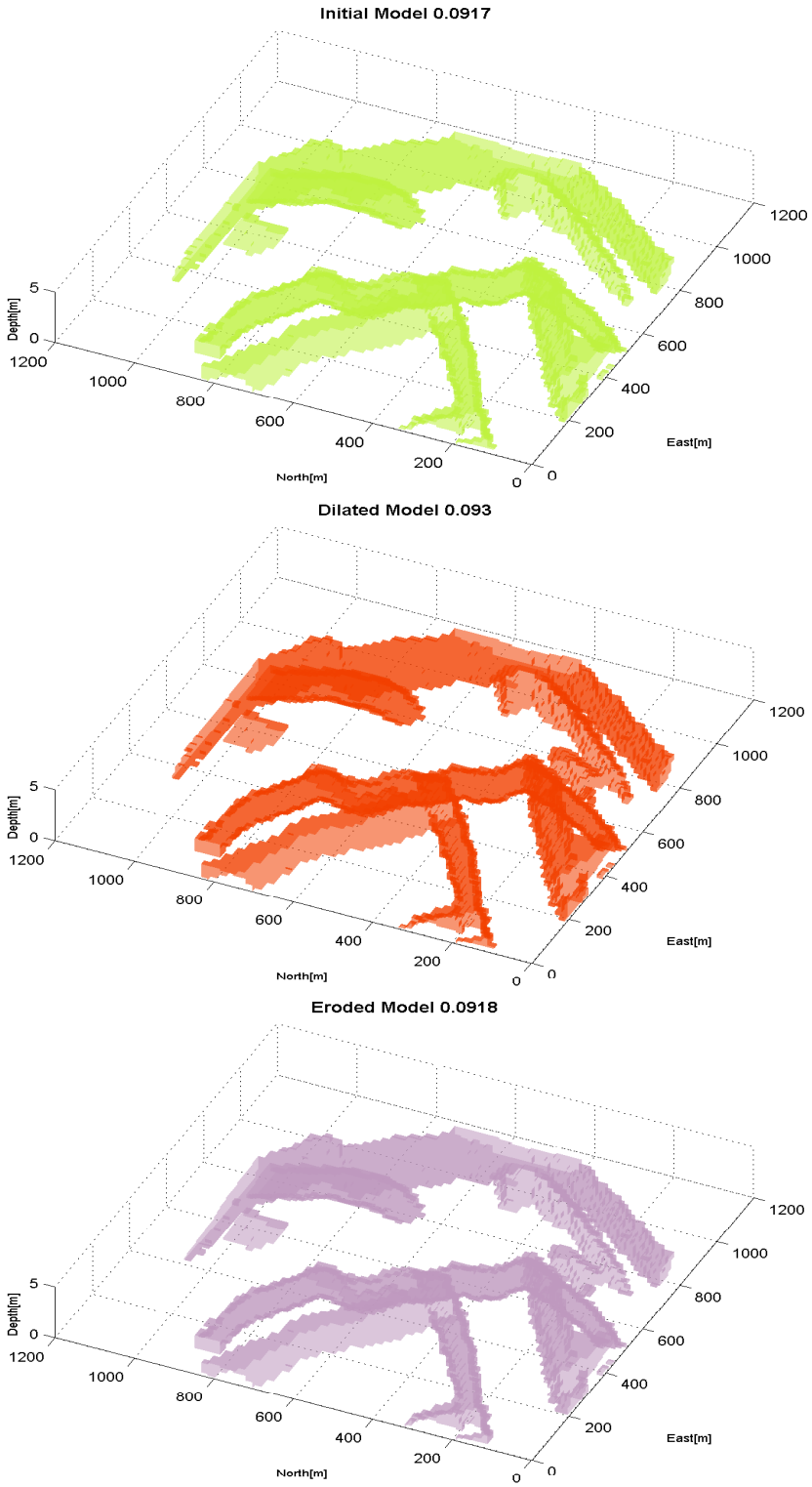

Figure 6.13: This is the first 3-D case explained in the 3-D example section. In this case, the objective is to connect the two objects at the right side of the TI shown at top. The dilation is controlled to be applied to the specific objects rather than the entire model.

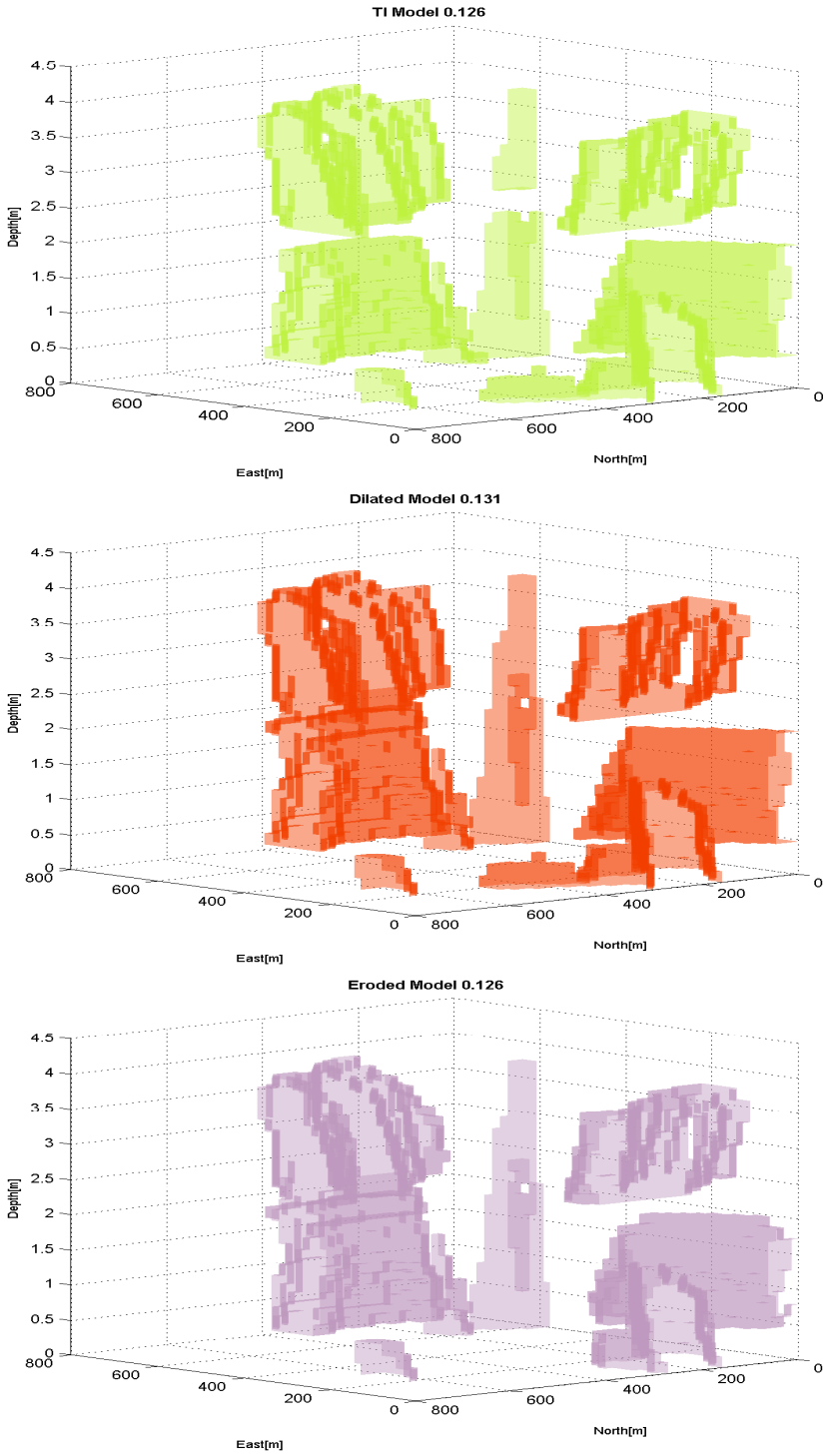

Figure 6.14: This is the second 3-D case explained in the 3-D example section. In this case, the dilation is applied in two processes. In the first dilation process two of the objects connect with smaller dilation parameter, and in the second process, 4 other objects connect with larger dilation parameter. This approach prevents the unnecessary growth of objects that are already connected with smaller dilation parameter.

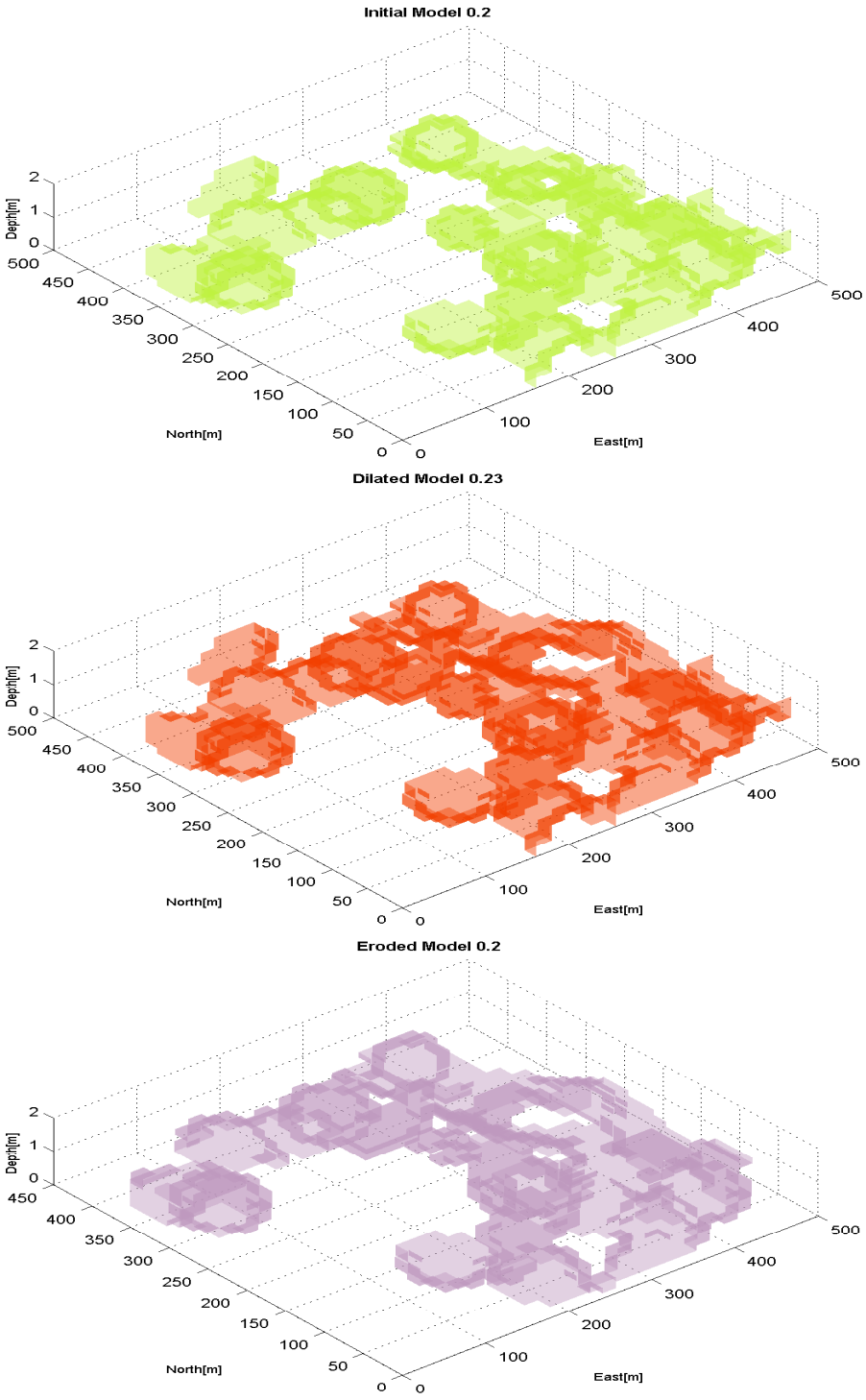

Figure 6.15: This is the third 3-D case explained in the 3-D example section. The selected dilation parameter results in more connection which is not desired. The option of what objects to dilate is considered at this point to control the connectivity.

for the user to specify the objects to dilate. The user can always find out about the objects's number by visualizing the `geo-obj.model` file using different colors, or by

visualizing the growing objects in different iterations. The dilation parameter may have to be changed before any connection occurs. For this specific case, the dilation is only applied to two objects which are identified with number 4 and 6 using a dilation parameter of 15. In this process, the number of objects reduce from 7 to 6 (two objects connect), also the net proportion increases from 9.17% to 9.3%. The change in this example is very small. This always depends on the objects relative distances, their distributions, and the number of objects that connect. The erosion is also applied with a 3×3×1 template. The threshold on proportion map is set to be 17.5% and the restricting size ratio is 1. The erosion is only applied in one iteration. The number of objects after erosion stays the same as the dilated case (= 6 objects), and the facies proportion reduces to the initial of 9.18%.

In the second example shown in Figure 6.14, another approach is taken. A model size of 40×40×30 grid cells has been extracted from the same TI as the previous case. In the first round of dilation, the dilation parameter of 17 is sufficient to connect the two large objects on the left side of the model. A template size of 3×3×2 has been selected to apply the erosion in this case. The threshold for the control parameter on proportion map is 20% and the limiting size ratio set to be 4. The erosion is applied in 4 iterations before the initial global proportions are achieved. Applying the dilation in sequence, in this example, prevents the unnecessary growth of objects that connect faster than the rest. Controling dilation in this aspect helps the erosion to also be applied more efficiently.

The third example, shown in Figure 6.15, is a model of size 30×30×10 filled with different size ellipsoids like barriers with the NTG of 80%. The dilation process is only applied on the first three largest objects with dilation parameter of 22.4. As a result of the dilation process, the number of objects changes from 5 to 3 and NTG decreases to 77%. Erosion is then applied to bring the proportions back to the original one while keeping the number of objects same as the dilated ones (the erosion should not break the connections that dilation has created). The erosion in this case is applied using a template of 2×3×2, and a proportion threshold of 21.75%. The limiting size ratio for erosion is set to be 1 and the erosion process is applied in 5 iterations. The resulting eroded model has 3 objects and NTG of about 80%.

6.6 Chapter Summary

This chapter proposes a methodology using erosion-dilation operations to enforce connectivity of disconnected objects in simulated realizations. Considering the maximum direction of anisotropy in the dilation process is promising in the development of the proposed methodology. Utilizing the proportion map as a tool for erosion purposes and performing it iteratively also works reasonably well; it erodes the objects smoothly and maintains the global proportions. The proposed methodology could be summarized as sequential dilation and erosion. The first step is to make sure the disconnected intervals should be connected. Such intervals are then identified as geo-objects and their size and orientation is evaluated using moments of inertia. The dilation: (a) determines the distance function for objects of the targeted facies; (b) modifies the distance function by object's orientation-anisotropy matrix; (c) calculates the model distance function resulting from the minimum distance of object's distance models; and (d) applies the threshold value on the distance model to dilate. This is a subjective matter and requires judgment for objects to merge with minimal alteration of global proportions.

The erosion steps to maintain the global proportions (a) selects a search template to scan the dilated model; (b) evaluates the proportion map by assigning the fraction of the template being inside the object; (c) keeps or removes the object's boundary based on the selected proportion threshold (histograms could be observed to tune the threshold); and (d) performs erosion iteratively to get to the initial global proportions while preserving the connections created in the dilated model.

Chapter 7

Improvements in Realization Selection Techniques

The "true" reservoir is unknown and the realizations are constructed to understand the space of uncertainty (Deutsch et al., 2002). It is important to realize that realizations are generated by stochastic simulation and no realization is "better" or more probable than another. Processing all realizations is often time-consuming and computationally expensive. Realization selection has been practiced for a few decades. Criteria which are applied to select the realizations are profoundly influential to the final understanding and decision making (Deutsch, 2002). Two ranking enhancements are proposed in this chapter: (1) development of a multiscale ranking approach that considers realizations in different regions and different scales; (2) proposing realization clustering as an alternative to ranking when ranking is inadequate.

7.1 Introduction

There is nearly an infinite number of realizations that reproduce the data equally well yet result in different performances (Haldorsen and Damsleth, 1990; Deutsch and Srinivasan, 1996; Deutsch and Hewett, 1996). Although this might suggest generating as many realizations as possible, processing many realizations through flow simulation is not practical. As such, despite the rapid growth of CPU technology, ranking is still a necessary practice in reservoir modeling. The cost of full flow simulation remains as prohibitive as in the past, as each realization is now represented in much greater detail and with more complete physics. This contradicts the notion that advances in computing power will render the necessity for selecting realizations

obsolete (Deutsch and Srinivasan, 1996). In view of this, it is perhaps advisable to allocate some portion of the new computing power to develop more advanced realization selection techniques, as processing many realizations in the flow simulator may never be the most efficient approach.

Providing detailed information on the relative performance of realizations before applying flow simulation is useful. Ranking is a popular tool in the field of geostatistics to select realizations based on one metric of performance. Ranking provides a probabilistic view to the realization performance by ordering realizations and reducing the dimensionality of input to the flow simulation process. The ranking can be non-unique considering many performance metrics such as original oil-in-place (OOIP), recovery factors, production rates, and different measurements of connectivity of realizations. The selected realizations will then be considered for production evaluation; the realizations' performance provides an estimate for reservoir response distribution (Garb, 1988).

The idea of ranking was processed by Journel and published by Ballin and coauthors in the context of stochastic reservoir modeling (Ballin et al., 1992). Their approach relies on quantile-preserving approximated responses of the flow simulator which is the main method practiced today. Deutsch and Srinivasan (1996) describe ranking as a method that selects the realizations to span the production uncertainty. Ranking considers a simplified transfer function that permits selecting a few realizations for further studies of the reservoir performance as illustrated in Figure 7.1.

In the past few decades, different criteria have been introduced for ranking such as the ones introduced by Hird and Dubrule (1995); Deutsch and Srinivasan (1996); Saad et al. (1996). Two main ranking methods are (1) static ranking, and (2) dynamic ranking. The static type is based on evaluating the volume of high quality reservoir, its connectivity, and tortuosity; whereas the dynamic type estimates the flow simulations using some approximate physical setups such as streamlines or a proxy model. Dynamic ranking is a more complicated procedure that requires more parameters and effort. While Deutsch and McLennan (2005) argue the effect and simplicity of the static method compared to the dynamic one, Yazdi and Jensen (2014) demonstrates the inefficiency of static measures and proposes a form of harmonic average of permeability as a dynamic average that overperforms the realizations selection. An ideal simplified transfer function would lead to a large correlation between the simplified ranking measure and the real production variable

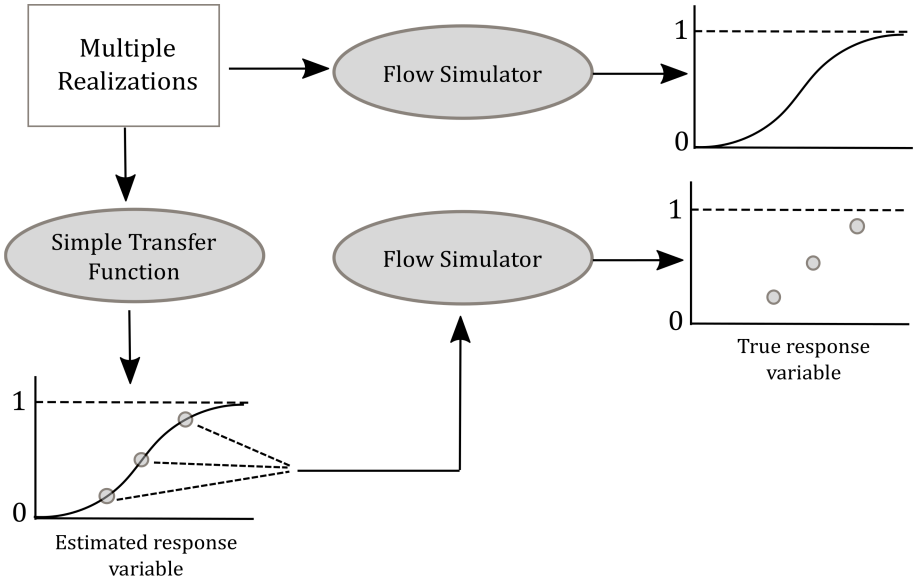

Figure 7.1: A schematic of acquiring the probability distribution of flow performance by applying a full flow simulation (top row) compared to Applying a simple transfer function to approximate response variable distribution through selecting realization to span the uncertainty in the evaluation of production performance.

(see Figure 7.2); it approximately identifies the rank order of every realization based on a quick measurement (Fenik et al., 2009a).

The most reliable measurement in terms of oil productions especially in SAGD recovery is one that evaluates local connectivity of drainage area in terms of flow while considering the net distribution in the reservoir (Deutsch and Hewett, 1996; Deutsch and McLennan, 2005). This implies that the location of the wells is an important aspect for reservoir production (Aziz et al., 1996) and crucial to connectivity measurement. A number of studies have investigated ranking methods considering the connectivity for well placement decisions and the SAGD process (McLennan and Deutsch, 2005b; Fenik et al., 2009a).

The number of realizations, perhaps based on different geological scenarios, should be considered for flow simulations in order to improve the robustness of the decision making process. Detailed studies of decision-making in the presence of uncertainty can be found in da Cruz (2000) and Alshehri (2010).

7.2 Multiscale Ranking

There are many engineering decisions that influence recovery performance, one of which is well placement. Since ranking results in only a few realizations, the ones

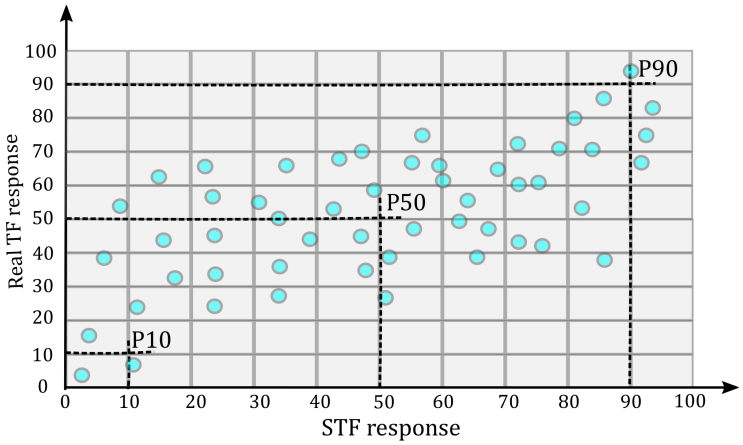

Figure 7.2: A schematic illustration of the correlation between ranking realizations based on their response to comprehensive flow simulation or real transfer function (TF) shown on y-axis with the ranking based on their response to simple transfer function (STF) shown on x-axis. The ranking results of a reliable simple transfer function could show a strong correlation with the ranking quantiles of full flow simulation.

chosen are important for well-placement. Similarly, the connectivity of the high quality reservoir and the low quality barriers are important aspects in the ranking process. The measurements of local connectivity are also influenced by where the injectors and producers are placed. Depending on the recovery plan and geological heterogeneity, the drainage can take place in multiple scales of interest as shown in Figure 7.3; there are multiple well pairs within a drainage area. The shale barrier distribution is never uniform and the evaluated connectivity for different recovery windows could be significantly different. That is why the realization selection for recovery evaluation in SAGD is not as straightforward: it is quite possible that one realization in one drainage setup is ranked high while its response to another recovery scenario is actually low. Then the question is how to integrate the response variables from different scales and recovery settings to select the low, median and high realizations?

A practical methodology is introduced to incorporate multiple recovery setups in evaluating SAGD performance. The proposed ranking uses optimization over all recovery settings of different well placements and scales simultaneously which is referred to as multiscale ranking. Consolidating possible setups and different recovery scales results in considering more scenarios than is typically practiced in reservoir studies. The objective is to establish an optimization approach to select the realization that ranks the closest to the required quantile for all recovery setups. When considering such schemes, the selected P10 model is expected to be a close

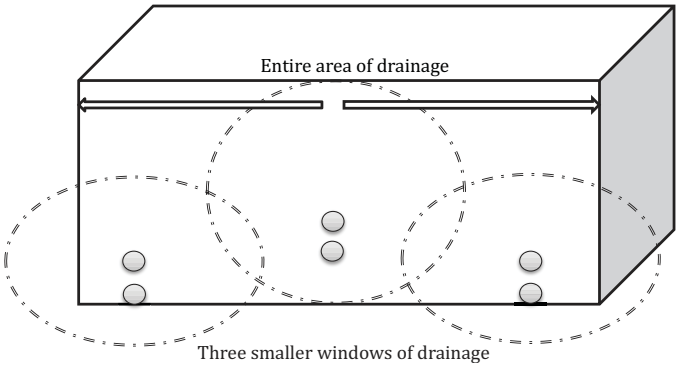

Figure 7.3: Illustration of multiscale well pair drainage within a large drainage region. Assuming that every well pairs is represented by two circles (one on top of another), three well pairs are placed at different locations in the recovery region with different window sizes represented by dashed ellipses around them. Evaluating the realization performance for each of these well pairs and considering their response simultaneously in realization selection is referred to as multiscale ranking.

quantile to P10 for all different areas of recovery drainage.

In conventional ranking techniques, global continuity to well locations may be considered, but not multiple areas simultaneously. In terms of heterogeneous reservoirs, the connectivity of the reservoir determines the ultimate recovery. The multiscale ranking scheme considers this aspect and evaluates recovery for different well-placement configurations with different scales of recovery.

Implementation

To select the specific ranked (quantile-preserved) models, Equation (7.1) is proposed to be considered as an objective function. This function is defined to minimize the distance between the overall drainage rank and the target rank as well as minimizing the difference between realization ranks for different well pairs and the target rank. Every realization represents an actual rank for different drainage well pairs. The realization which its actual rank in all scales is closer to the target quantile will be selected as the representative realization of that quantile. This realization has the least penalty according to the following:

$$O_l = \frac{w_0}{2}\,(r_{l_{\text{overall}}} - r_{\text{target}})^2 + \frac{w_1}{2}\frac{1}{n_{\text{set}}}(r_{l_{\text{set}}} - r_{\text{target}})^2 \tag{7.1}$$

where, l, refers to a quantile, and w indicates a weighting factor. This objective function is minimized when $r_{l_{\text{overall}}}$ and $r_{l_{\text{set}}}$ are as closely possible to the target quantile, r_{target}. Thus, the minimization algorithm considers all the realizations to find the realization that results in the smallest loss when considered by Equation

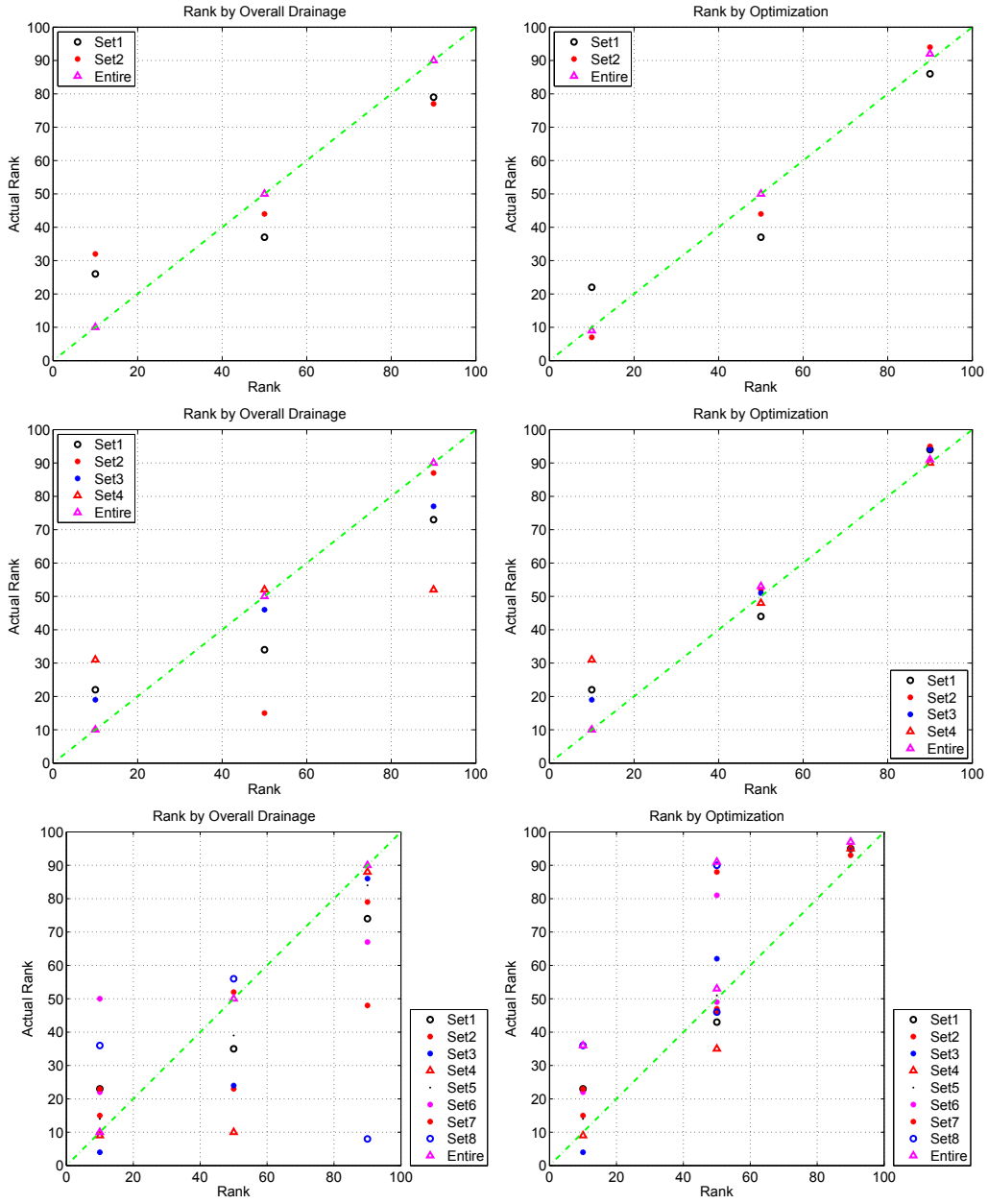

Figure 7.4: Illustration of the advantage of multiscale ranking over the ranking using only one drainage area for the three settings described in the example. The plots on the left show the actual rank of the P10, P50 and P90 realizations (ranked by overall drainage) considering the other well pairs. The similar is illustrated on the plots on the right, except that P10, P50 and P90 realizations are selected based on multiscale ranking approach. First row corresponds to the first setting, second row to the second setting and third row to the third setting.

(7.1).

An example is designed to demonstrate the advantage of multiscale ranking over the widely-use simple ranking. In this example, 100 3-D realizations are considered to be ranked based on their response to CHV value which is evaluated using "CHV"

program (Wilde and Deutsch, 2012). The CHV calculates the connectivity within the specified recovery window size and to the well pairs. Three settings of recovery is considered in this example. Note that all setting include the main well pairs which is located in the middle of the reservoir and its recovery window size covers the entire region. The first setting contains two more well pairs located each at one side of the main well pair and covers almost half a window size as the main well pair. The second setting adds two more well pairs to the first setting by now locating two well pairs at every side of the main well recovery. The window size for each one of the four well pairs is about a quarter of the main well pair. Finally, the third setting includes eight well pairs, with four of them located uniformly at every side of the main well pair (elevation of well pairs are similar).

For all three settings, the representative realizations of P10, P50 and P90 are once selected using the overall drainage assuming no other well pairs is available, and once by proposed multiscale ranking. Figure 7.4 demonstrates how the actual ranks vary for every selected realization. The plots on the left are those selected realizations ranked by overall drainage, and the plots on the right are ranked using optimization approach. The rank on the y-axis, shows the actual rank of the specified well pairs for the selected realization. For example in the first row which represents the first setting, 9 points are shown in three different colors each representing one of the well pairs. Thus every three points belong to one realization which is selected to represent P10, P50, or P90, as shown on x-axis, but its actual rank is different if it was considered as the ranking measure. Since the ranking is based on overall drainage, the triangular points representing the entire drainage are the actual ranks as well.

However, as can be observed from the plots on the right, even the overall drainage does not always have the same rank as the selected realization represents. When considering the performance of all well pairs to perform ranking, the two realizations selected as P10 and P90 differ from the main setting. The CHV performance of the selected realization by optimizations is closer for all three well pairs. The advantage of multiscale ranking is even more clear for the second setting where four well pairs are included with the main well pairs. The selected P50 and P90 by optimization approach, have very similar performance if ranking considered every one of the 5 well pairs. As emphasized by Figure 7.5, realization # 52 which is selected by overall drainage to represent P50 actually represents a significantly low rank in terms of one

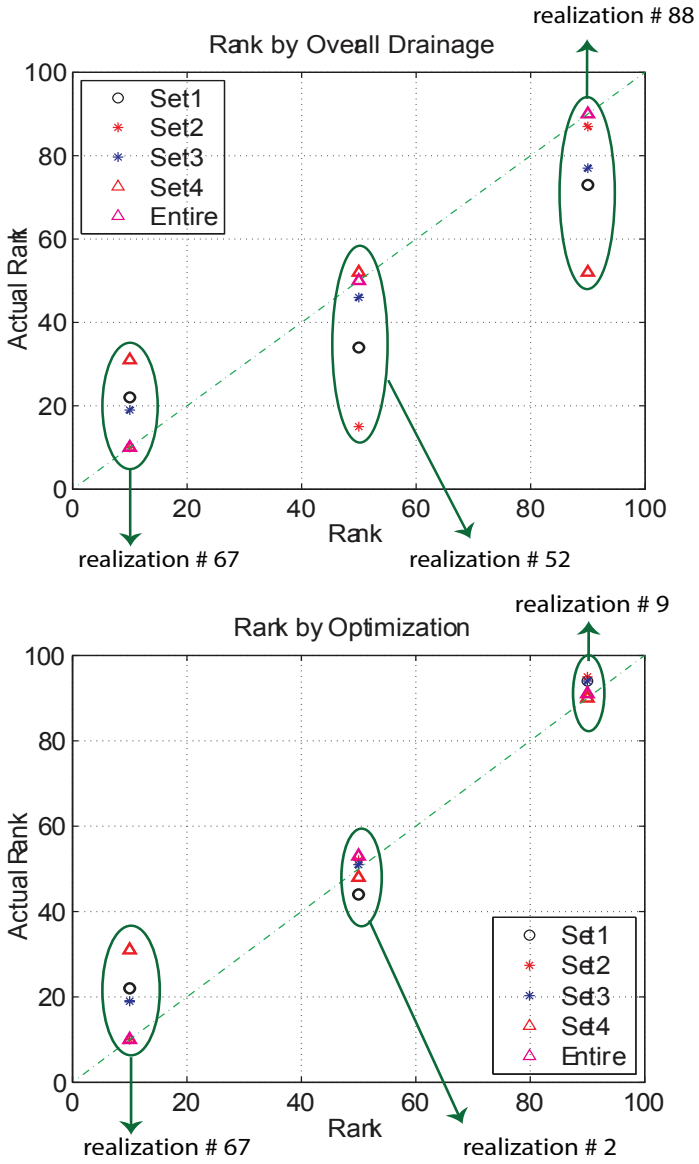

Figure 7.5: Ranking based on only one drainage area could result in the variations in the actual rank of the selected realization if ranked by another well placement. Realization # 52 which is selected as the representative of P50 quantile has a low rank of about 15 in terms of set2. Also, realization # 88 represents P90 quantile while it has the actual rank of about 55 if ranked by set4. Multiscale ranking can effectively reduce the spread of actual ranks for the selected realizations when different well pairs are of interest.

of the well pairs. This could also been observed for realization # 88 that performs P50 if ranked by one other well pairs. The optimization process controls (to some extent) such variations; selected realizations stay within their region of actual ranks for all different well pairs.

The optimization also becomes more challenging as can be observed in the last row of Figure 7.4. For the third setting which includes 8 well pairs in addition to

the main well pairs, the performance of the selected P50 realizations is not exactly different than what has been selected when ranking based on overall drainage. Although the P90 selection still shows a significant advantage over the simple ranking process.

The importance of this study is to make sure that the selected realization would be in the desired ranking position in any kind of drainage plan. As was mentioned before, in every reservoir study three models for P10, P50 and P90 is achieved regardless of the number of well pairs or the scale of recovery setups. In the presence of heterogeneity and non-uniform distribution of barriers, it is possible that a model for the smaller window drainage has a very low recovery while the same model considering bigger window results in a good recovery.

The next section discusses the second proposed approach in improving the realization selection which is clustering realizations.

7.3 Realization Clustering

Ranking does only select the realizations considering one-dimensional reservoir performance; one metric might not fully characterize the reservoir since the recovery performance could be coupled to a number of equally important factors. Clustering of realizations is developed as an alternative to ranking when a simple ranking process is not adequate. Unlike ranking, clustering can consider more than one ranking measure for each realization. Although some features are more/less correlated or important, they could all be simultaneously considered when performing clustering. Also the use of grouping or clustering is in order when choosing arbitrary quantiles is not representative of the character of the realizations—ranking might not lead to a continuous gradation from poor to good performing realizations, instead, they might naturally form clusters.

Clustering is a classical procedure for data description in data mining and data analysis (Jain et al., 1999). The main purpose of clustering is to understand the data by identifying its natural clusters. Clustering algorithms group data whether or not the data have natural clusters. However, if the clusters exist then some algorithms cluster the data better than others (Ghosh and Strehl, 2006). Clustering partitions the realizations into different groups such that the realizations in one group share more similarities (Guha et al., 1998).

There are many algorithms to perform data clustering in literature. An inter-

ested reader is referred to the works of Kogan et al. (2006); Halkidi et al. (2001); Jain et al. (1999) for comprehensive reviews of different clustering techniques, their place of applicability, and comparison of their characteristics. Since evaluating clustering performance is not the main concern in this chapter, the discussion will be focused on a reasonable, simple clustering algorithm to group the realizations. The k-means ensures these mutually exclusive groups are as far as possible unless they are not linearly separable. A transformation of the realizations attributes to higher dimensional domain using kernel functions could be considered in non-linear cases.

The next section demonstrates different cases utilizing several examples. Note that selecting the proper clustering approach and deciding on the number of groups is not trivial (Berkhin, 2006). This chapter proposes to partition data using well-known techniques.

7.3.1 K-means Clustering

K-means (centroid-based) clustering is one of the earliest clustering technique which was introduced by Steinhaus (1957) and popularized as *k-means* clustering by MacQueen (1967). K-means clustering is a simple, effective and widely-used clustering algorithm (Jain et al., 1988; Jain, 2010) which clusters the data into K mutually exclusive groups by maximizing the similarities between the members of a group and minimizing the similarities to the members of other groups (Zhang and Rudnicky, 2002). Every group could then be described by a representative (e.g. centroid). This concept is appropriate for realization clustering proposed in this chapter, as the members of every cluster are expected to perform similarly at the time of recovery. The main verification of this clustering approach is in evaluating the (1) compactness, and (2) separation of groups (Berry and Linoff, 1997), where compactness refers to the closeness of members of every group, and separation refers to the maximum distance to the members of other groups.

The given data set $\chi = x_1, x_2, \cdots, x_N$, is the set of N d-dimensional data to be partitioned into K clusters of $\mathcal{C}_1, \mathcal{C}_2, \cdots, \mathcal{C}_K$, with centroids of $m_1, m_2, \cdots, m_K$. In k-means clustering, when a vector belongs to a cluster, its Euclidean distance to the centre of that cluster should be smaller than to other centroids.

$$E(m_1, \cdots, m_K) = \sum_{n=1}^{N} \sum_{k=1}^{K} I(x_n \in \mathcal{C}_k) \|x_n - m_k\|^2 \tag{7.2}$$

where I indicates the existence of a vector in a specific cluster.

The goal is to minimize the sum of squared error over all clusters which is known to be an NP-hard problem even for small K (Drineas et al., 2004). That is why, in this minimization, k-means tends to trap into a local minima (MacQueen, 1967; Selim and Ismail, 1984). The most common solution is to apply an iterative algorithm that minimizes the sum of distances between objects and their corresponding centroids over all clusters. This algorithm continues moving the objects in between clusters until the sum of distances over all clusters does not drop any further (Davies and Bouldin, 1979). The result is a set of clusters that are as compact and well-separated as possible. The algorithm could be described as follows:

1. Select K realizations randomly and assign them as the centroid of the clusters.
2. Evaluate the distance between every realization and the initial centroids.
3. Assign every realization to the closest centroid.
4. Calculate the new centroid for every cluster: the average position of current members
5. Go back to step 2.
6. Iterate until no realization moves where Equation (7.2) should be a minimum.

Various measurements have been introduced in the literature to quantify the similarities between the data for clustering purposes including conversion from a distance matrix (Euclidean, Manhattan, Minkowsky, etc), cosine measure, pearson correlation and many others (Jain, 2010). Selecting the proper attributes associated with the data and the similarity measures are influential factors in clustering performance that should be considered carefully. The similarity matrix should be selected with respect to the nature of data for the clusters to be meaningful (Jain et al., 1999).

One other consideration in the distance evaluation is the tendency for larger scaled features or the variable ones to dominate the distance function. It is important to normalize the scale of features for all realizations and then perform the distance evaluation (Wilson and Martinez, 1997; Herbrich and Graepel, 2001; Ghosh and Strehl, 2006). The normalization is applied by scaling the feature by its range of variability (Wilson and Martinez, 1997; Graf and Borer, 2001),

$$\tilde{x} = \frac{x}{\|x\|} \in \mathbb{R}^d.$$

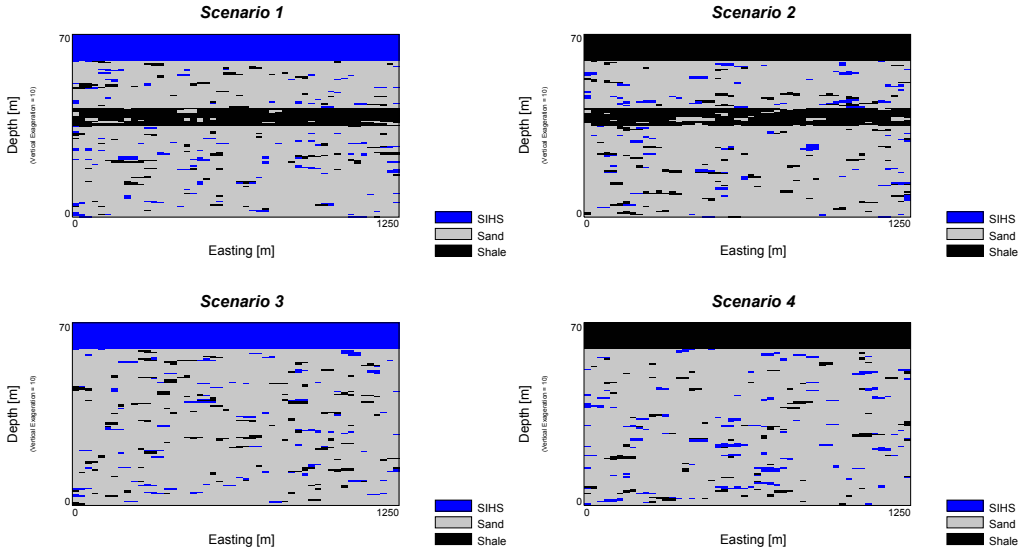

Figure 7.6: Illustration of the X-Z slice of one realization from all four generated scenarios. The lean zone consists of shale (black) in the middle of the first and second scenarios and the thief zone consists of SIHS (blue) at the top of the first and third scenarios are readily detectable.

This becomes even more tricky if one of the features is in categorical form; some algorithms are developed to take care of such situations such as the one by Wilson and Martinez (1997).

In the k-means clustering, or unsupervised clustering algorithms in general, the number of clusters, K, should be determined prior to data clustering (Xiong et al., 2009). There are many works in machine learning literature concentrating on this issue and suggesting global k-means clustering to resolve the initialization problem incrementally (Tzortzis and Likas, 2009). One general solution is to apply k-means for several K values and select the one with the minimum error. The complexity of selecting the number of groups is not considered in this chapter.

The remainder of this chapter investigates cases where clustering could be more beneficial than ranking. The applicability of k-means is also demonstrated where appropriate and compared with a case where kernel function could help with the process.

7.3.2 Scenario Example

An example is conducted to show the applicability of the k-means algorithm to cluster realizations with three specific features to four groups that are visually detectable. An example reservoir is generated with dimensions of 50 grid cells in X-direction, 50 grid cells in Y-direction and 140 grid cells in Z-direction. The cell

Table 7.1: The reservoir types that could be identified in the scenario example.

Reservoir Description	Probability
thin reservoir with a lean zone and a thief zone	35%
thin reservoir with a lean zone	15%
thick reservoir with a thief zone	35%
thick reservoir with no thief zone	15%

size is 25 m × 25 m × 0.5 m. In this example, the reservoir has four scenarios: the first scenario includes a lean zone and a thief zone, the second scenario contains a lean zone and no thief zone. The third scenario includes no lean zone but a thief zone, and the last scenario has neither a lean zone nor a thief zone. There are 100 realizations in total. The first and third scenarios have 35 realizations each, and the second and forth scenarios have 15 realizations each. The lean zone consists of 80% impermeable and 20% permeable facies which if it exists is 7 m thick, and placed at the depth of 28 m from top. The thief zone is made up of a mixed facies, e.g. SIHS, with porosity of 25% and permeability of 500 mD, which if it exists, is placed at the top of the reservoir and is 10 m thick. One slice of every scenario is shown in Figure 7.6.

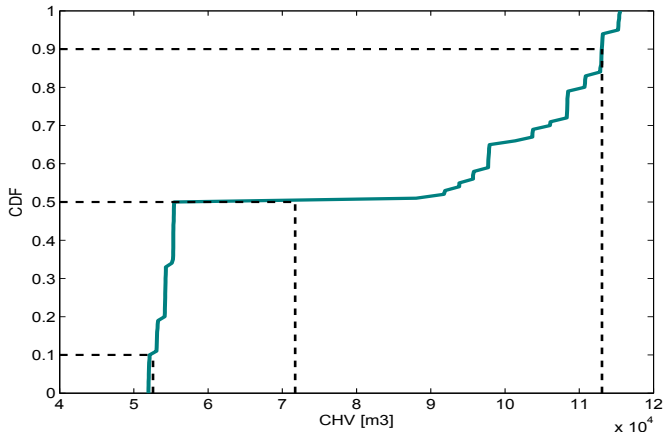

Figure 7.7: CDF illustration of the CHV distribution for 100 simulated realizations. The CHV response is distributed in a few intervals instead of following a continuous increasing plot. The selection of P10, P50 and P90 cannot be representative.

The impact of the thief zone on recovery performance relates to the CSOR as it reduces the efficiency of the process. The presence of a lean zone with lower permeability impedes the flow and reduces efficiency of the process as well. To select the realizations through a common approach of ranking based on CHV value, the CDF in Figure 7.7 will follow. This distribution is not a continuous distribution;

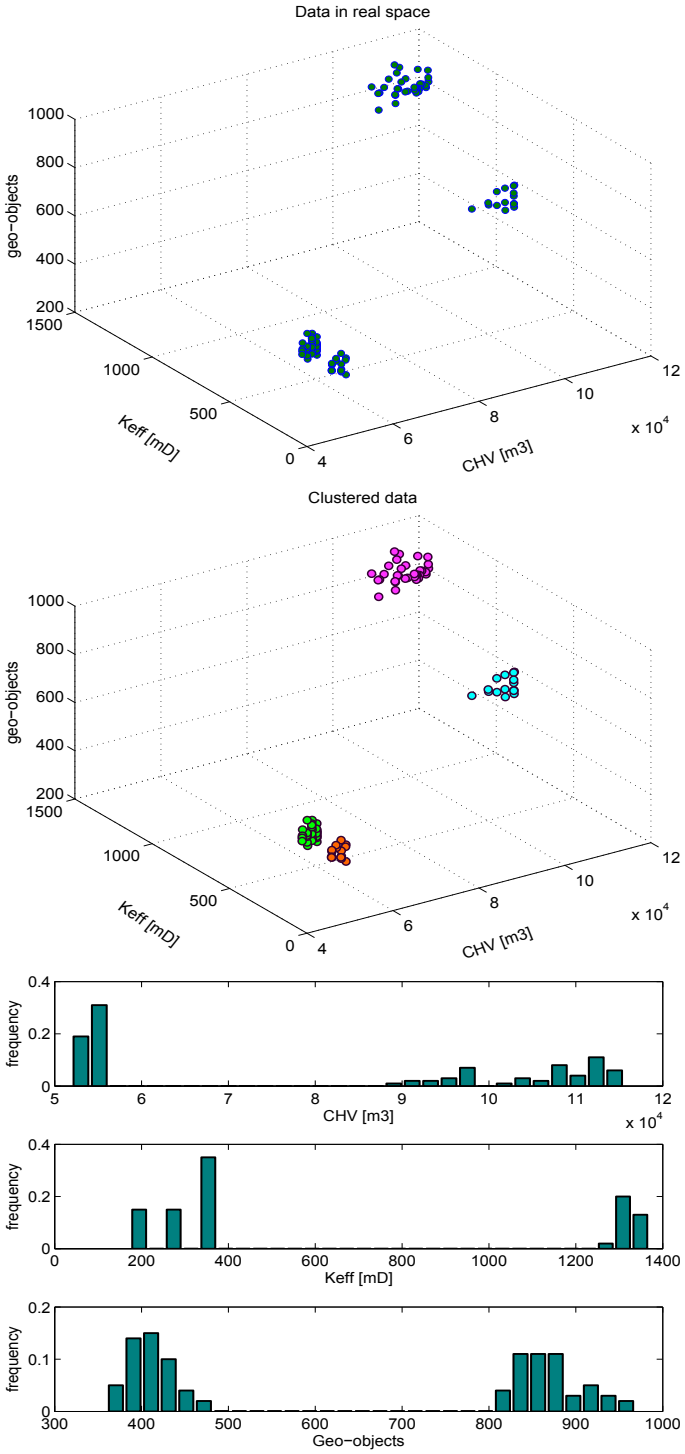

Figure 7.8: Visualization of data distribution, in scenario example, with three dimension of CHV, Keff and geo-objects. Because of the form that data is distributed in the space, k-means is the appropriate algorithm to group the realizations. The histograms (bottom) also show that the distribution of data for all three variables is discrete.

utilizing P10, P50 and P90 realizations would not capture uncertainty.

The three features considered in this example are CHV, Keff, and the amount of geo-objects in a continuous form. The distribution of the 100 realizations is shown in Figure 7.8 where after applying k-means, the four clusters are shown with a different color. The descriptions of the clusters are shown in Table 7.1. As can be observed from this figure, the distribution of data inherits the requirements for suitability of k-means algorithm to perform clustering. For example the realizations are distributed in ellipsoid-like groups which could be separated with linear hyper-planes in the space. The number of groups is visually detectable in this case which enables the utilization of k-means with no sensitivity analysis.

Figure 7.9 presents the distribution of data in 2-D scatterplots colored to their own groups. As can be observed from the first and third scatterplots, the Keff feature has an important role in identifying the fourth cluster; the presence of 4th cluster would have not been appreciated if only the other two dimensions were considered in realizations clustering. This is an interesting aspect of clustering that reveals new dimensionality in the data analysis.

Finally, Figure 7.10 demonstrates realizations of every cluster in one plot. Since the synthetic example here is the generation of an extreme case, every scenario results in one cluster. It is interesting to investigate the variability of attributes for scenarios of different characteristics as summarize in Table 7.1.

Recovery performance compared to Ranking

The purpose here is to investigate the characteristics of the typical P10, P50 and P90 realizations with regards to the clusters. The P10, P50 and P90 for every case would be discussed considering all three ranking conditions. Figure 7.11 ranks the realizations three times, each time with one of the features. The realizations are colored by their clusters. In the plot at the top, the realizations are ranked based on CHV values. As can be seen in this figure, the realizations are increasing in three distinct intervals instead of following a continuous curve. The P10 and P50 quantiles are both selected from the lower part of this distribution which makes ranking in this case not reliable. The second plot is the ranked realizations by Keff values. The realizations are placed in four distinctive intervals. Again, P10 and P50 realizations are selected from the very small interval. In the last plot which the realizations are ordered based on the amount of geo-objects, the population is

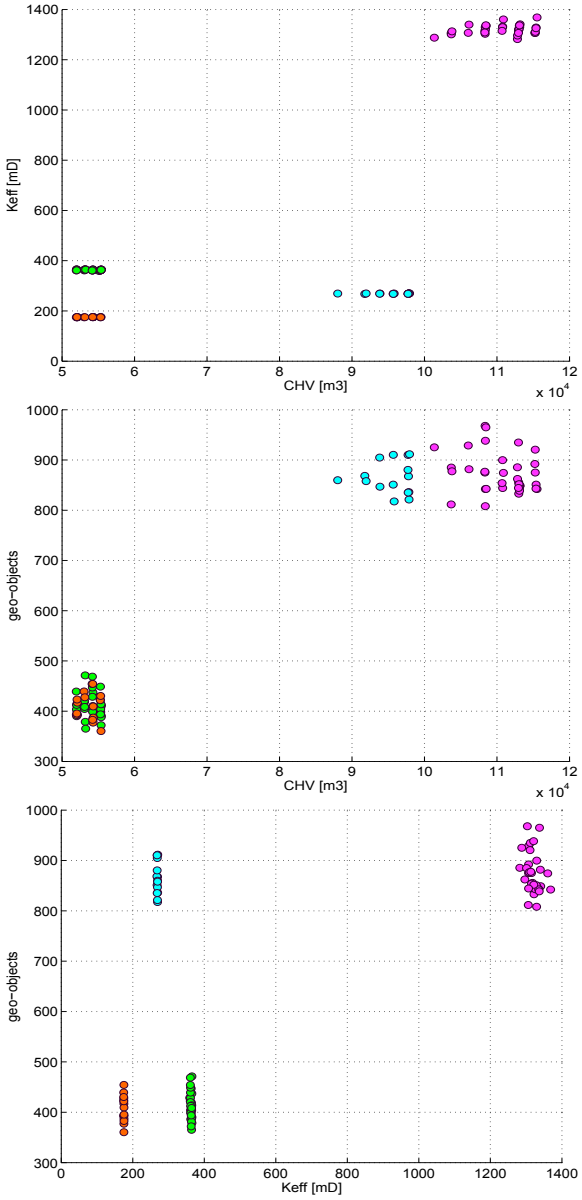

Figure 7.9: The three features of realizations are shown in 2-D scatterplots with points colored to their specific groups. The presence of Keff provides new information regarding data. The fourth cluster can only be detected after the identification of the three clusters by the two features of CHV and geo-objects.

divided into two intervals. Similar to earlier cases, there is a big gap between the P90 quantile and the low- and medium-ranked values.

The selected realizations could also be analyzed from a clustering perspective. It is interesting to see that realizations in red are mostly ranked high in all three ranking results. P90 belongs to the red cluster in the CHV and Keff rankings. The selected P90 realization in geo-object ranking belongs to the blue cluster which is in fact part of the lower-rank realizations. Although the P90 in geo-object ranking

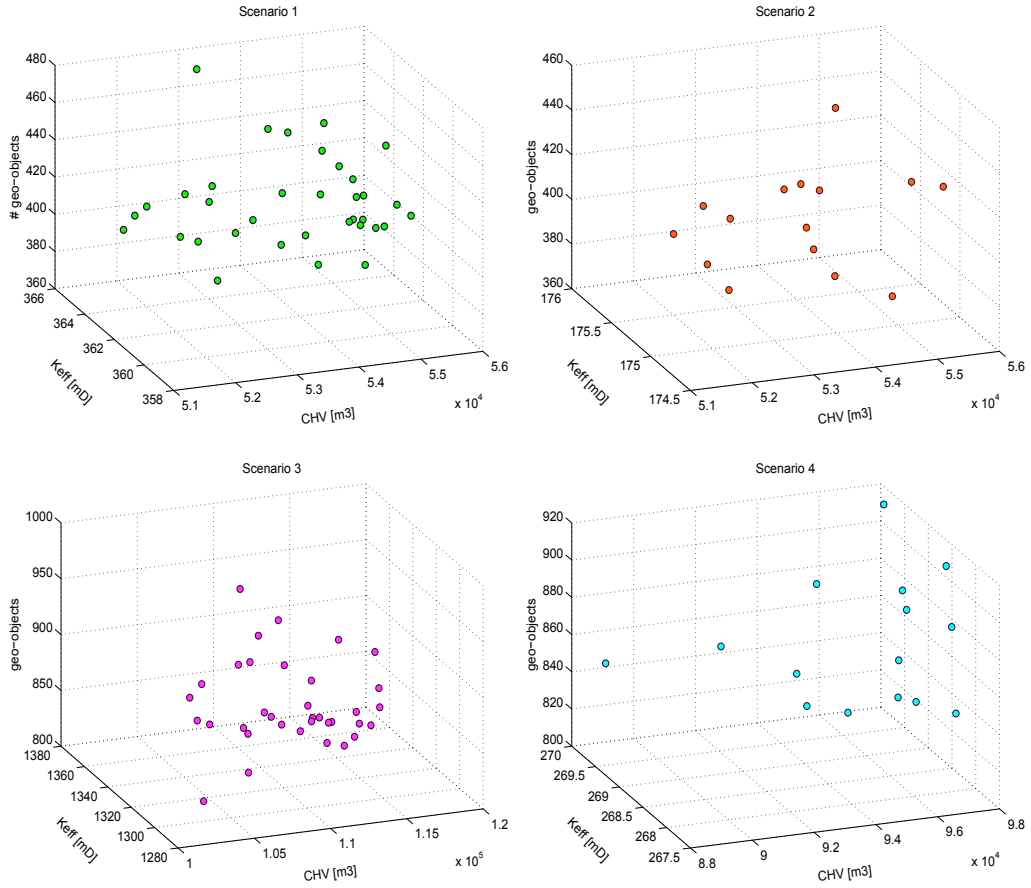

Figure 7.10: Every scenario is shown in its own colored cluster in the 3-D space. The CHV for both scenarios of 1 and 2 that contain a lean zone in the middle of the reservoir are about the same. The CHV for the third and fourth scenarios are also very similar, as expected. The effective permeability seems to be highest for the third scenario (thick reservoir) and the lowest for the second scenario (thin reservoir). The amount of geo-objects also appear to be slightly higher for third and fourth scenarios because of the absence of the lean zone.

is from the blue cluster, the red cluster however, is part of higher-rank range in all three ranking results. It would be reasonable to select the P90 from the red cluster. Interchangeability of the two clusters colored green and orange could be observed in the last plot of Figure 7.9. Enforcing the selection of orange member as the representative of P10 quantile is also a reasonable choice. Such observations are only possible by considering all important features in grouping the realizations as opposed to ranking them by a single metric.

7.3.3 Clustering Index

There are many metrics in the literature to quantify the clustering performance. None of these metrics outperform the others and most of them share the same

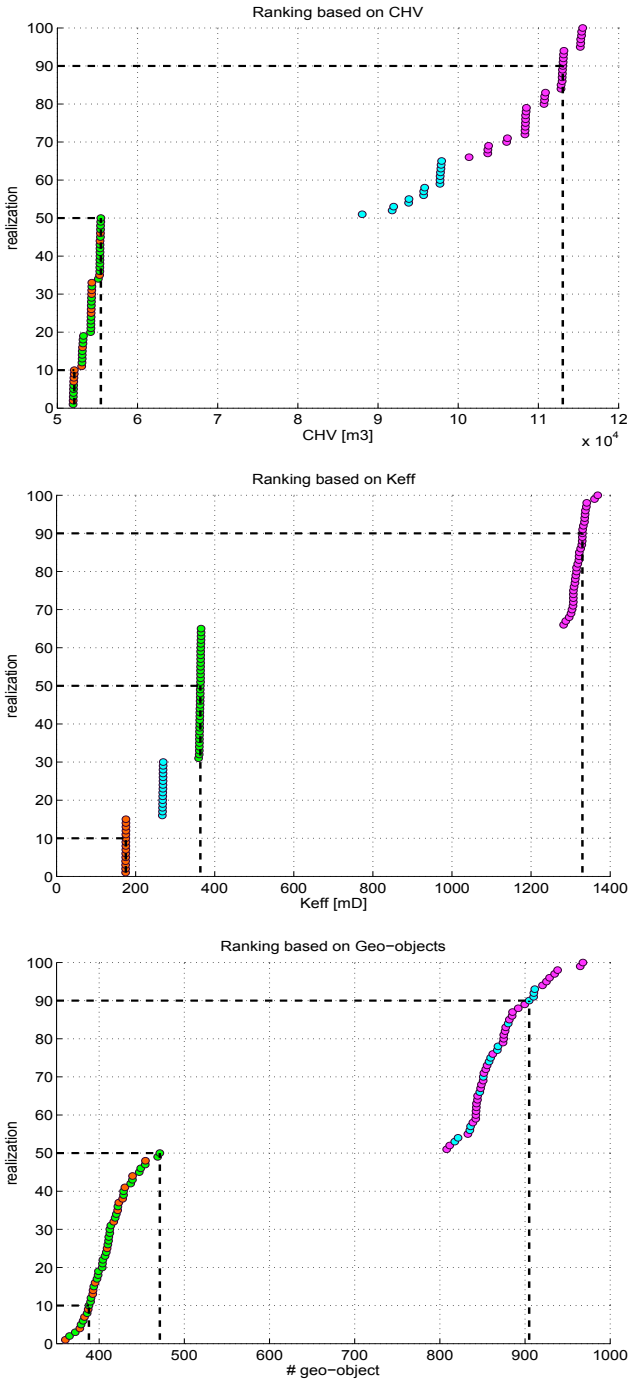

Figure 7.11: All three features are considered to rank the realizations. The top plot is the realizations ranked by CHV and colored by k-means clusters. The one in the middle represents realizations ranked by Keff, and the one at the bottom is ranked by number of geo-objects. The selected P10 based on CHV and Keff ranking happens to be a member of the orange group which differs in the case of geo-objects ranking.

concept. A clustering index is proposed at this point which follows similar concepts from other performance metrics. The k-means clustering performs comparatively

well when the clusters of data are clearly separated from each other and the members of each cluster form an ellipsoidal or spherical shape in the space. This could be thought of in terms of fraction of variance of the cluster's centroids relative to the variance of data and the centroid within each cluster. Or, geometrically, the fraction of the size of the macro cluster (pseudo-cluster of centroids) over the sum of sizes of all other small clusters. Since the size of every cluster can be defined by the average of the distance of members from the centroid, the numerator is the mean distance of c_k and c_M, where c_k is the centroid of cluster k, and c_M is the centroid of all c_k's. Intuitively, the greater the distance between centroids and the macro centroid, the clusters are more stable given that the distance between the members of every cluster to its centroid are relatively small. Thus, the clustering index, C_I could be written as follows:

$$\begin{aligned} C_I &= \frac{\frac{1}{K}\sum_{k=1}^{K}\sqrt{(c_M - c_k)^2}}{\sum_{k=1}^{K}\frac{1}{N_k}\sum_{n=1}^{N_k}\sqrt{(x_n - c_k)^2}} \\ &= \frac{1}{K}\frac{\overline{d(c_k, c_M)}}{\overline{\sum_{n=1}^{N_k} d(x_{nk}, c_k)}} \end{aligned}$$

where nk refers to a member of the group k with population of N_k, and $d(y_1, y_1)$ is the Euclidean distance between two vectors of y_1 and y_2. The clustering index is zero for the case of K=1, since the macro centroid is going to be equal to the centroid. For the maximum number of groups which occurs for $K = N$, the clustering index is undefined.

Figure 7.12 determines the clustering index for the scenario case which described earlier in the chapter. To draw any conclusions from the C_I value, the random distribution of the case should be considered. N data is generated randomly within the example domain in which k-means is applied to cluster data with the same number of K as the case data. The plot at the top shows the C_I value for the data and the histogram for so many number of iterations for the random case. The farther the distance between the random distribution and the C_I value, the more stable and reasonable the resulting clusters are. In the second plot of Figure 7.12, the same procedure is applied for a range of K changing from 1 cluster to 25 clusters. C_I starts with the zero value for $K = 1$ on the plot and diverges for the data case and random case. As the number of clusters grow, the C_I becomes smaller on average; the amount of change in C_I for the random case is very small. The clustering index is at its maximum at $K = 4$. The last plot illustrates the relative C_I of data to

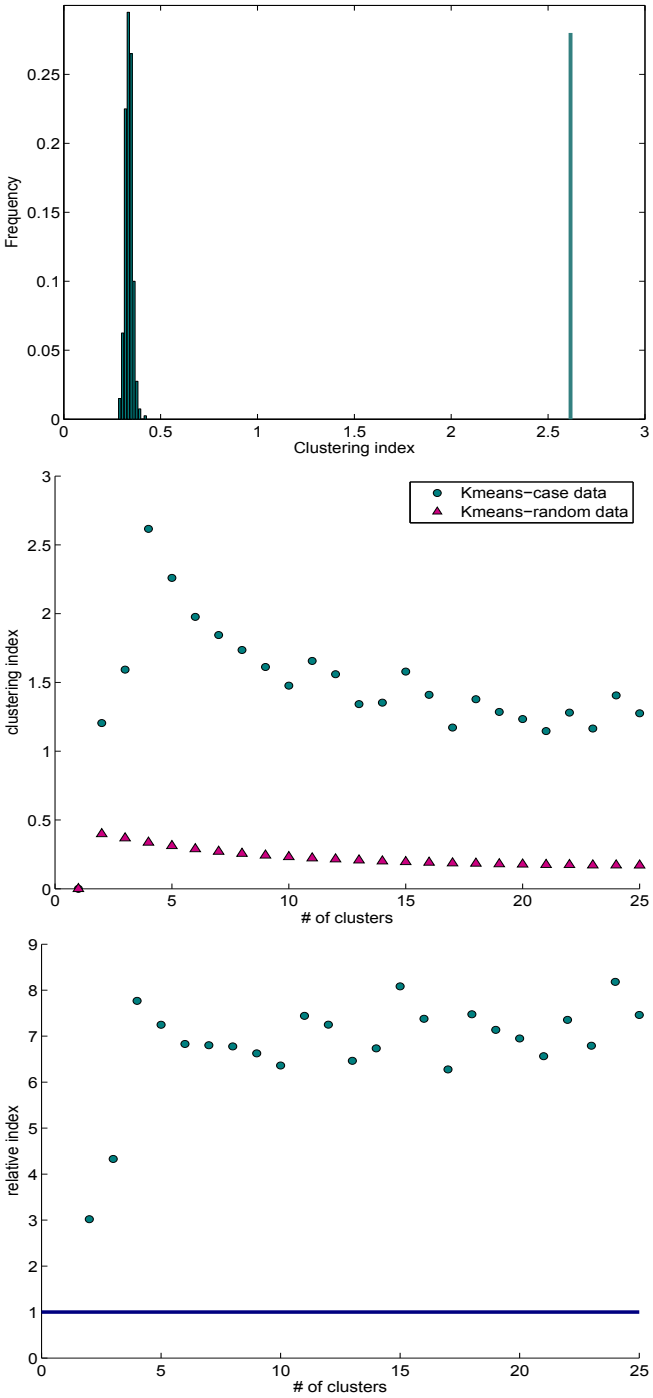

Figure 7.12: The clustering performance is demonstrated by comparing the clustering index to the case of clustering the random data within the same range of data distribution.

its corresponding case of random data. The relative index of 1 indicates the base case in which the clustering performance is equivalent to the case if the data was random.

To transit to the next section, an example is demonstrated in Figure 7.13 in

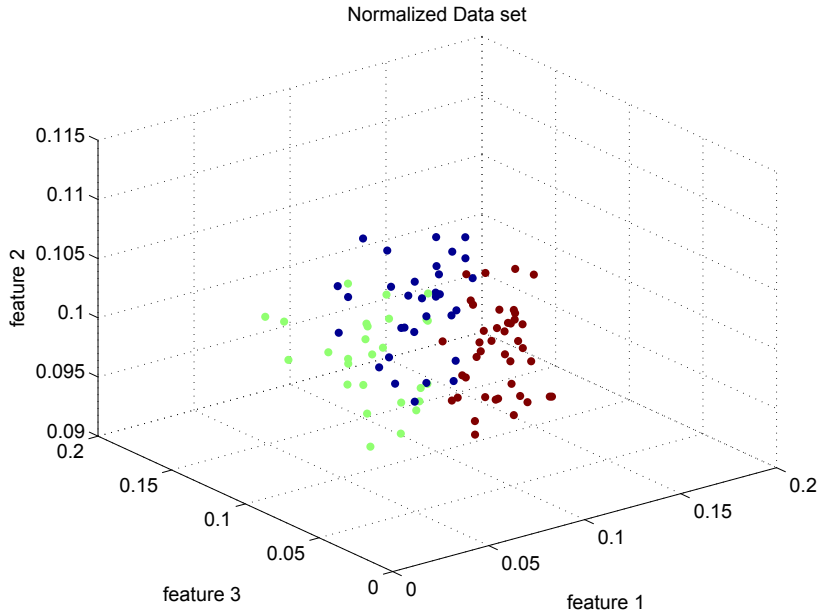

Figure 7.13: Demonstration of realization data in 3-D space in which clustering is not an effective approach.

which clustering is not an effective approach; the data reveals no particular groups of realizations. The clustering index is considered to investigate further and compare the performance of k-means approach with the case of random data as shown in Figure 7.14. The fluctuations of relative C_I around the base 1 indicates realizations inherit no natural clusters.

One important aspect of using geostatistical tools is to apply every technique where it is appropriate. The next section discusses the limitations of k-means algorithms to cluster realizations and propose the use of Kernel function if suitable.

7.4 Kernel k-means

Although k-means clustering is recommended because of its simplicity, it is not always the best partitioning method. There are several characteristics of the data that limit the usage of k-means. One relates to the number of clusters; k-means is not the best option when the number of clusters is not known. Different iterative algorithms have been considered to overcome this limitation and find the appropriate number of clusters based on k-means performance over different number of clustering groups. The shape of data distribution is also very important. K-means performs well when the data is packed in ellipsoidal-shape groups. It functions by separating data linearly; for close unstructured data, linear separation is not always possible.

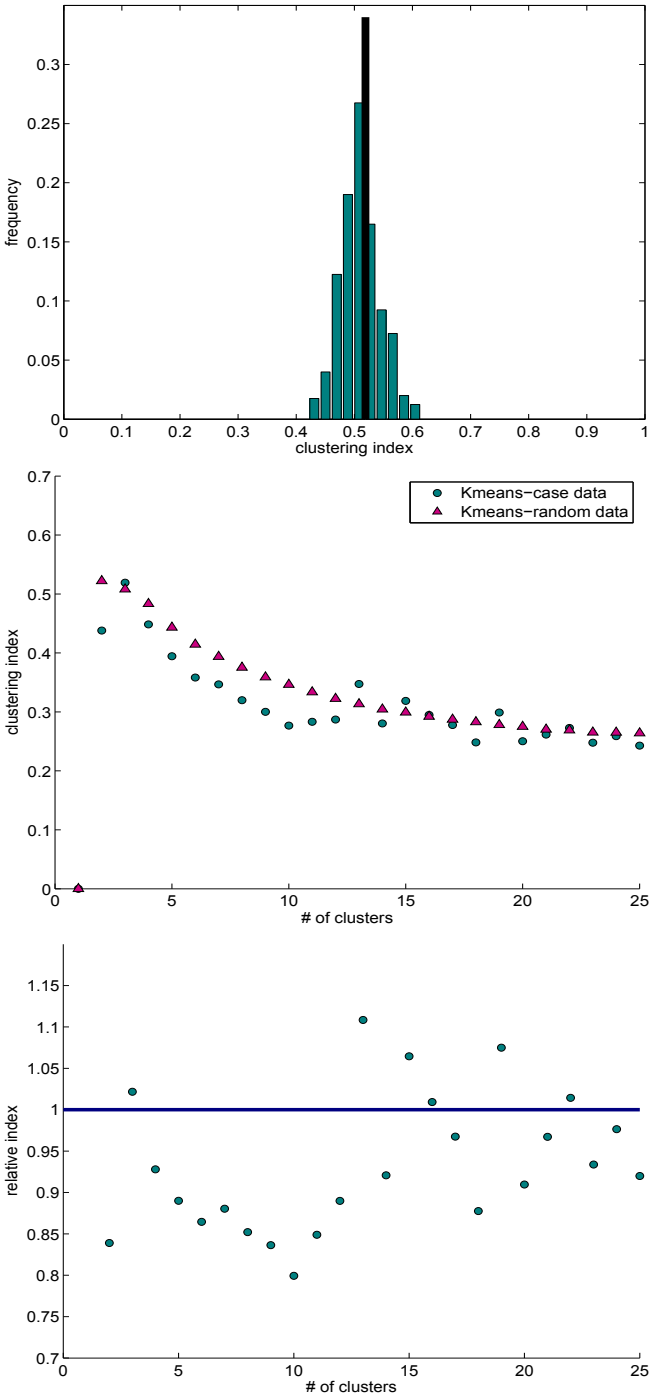

Figure 7.14: Illustration of the case shown in Figure 7.13 where there is no evidence of data being positioned in specific groups in the space. The clustering index for the real data is within the distribution of clustering index for the random data. As shown in the second and third plots, for number of groups changing from 1 to 25, the clustering index for the data is very close to the one from the random case.

A kernel function can account for non-linearity by mapping the data from input space, $\mathbf{R}^{n \times p}$ to the feature space, $\mathcal{F}^{(n \times n)}$, where n indicates number of data, and

p is number of features (dimensions) (see Figure 7.15). There are several different kernel function that transform the data non-linearly such as polynomial kernel (its dot product with order 2), Gaussian kernel, Laplacian kernel, Spline kernel, wavelet kernel, radial basis function (RBF) kernel, and many more. Note that discussing the characteristics of different kernel functions is not considered relevant in this chapter. Kernel function, $K_{ij} = \phi(x_i)^T \phi(x_j)$, directly provides the inner products in feature space. This transformation is nonlinear; it expands the input dimension but captures the structure of the data (Shawe-Taylor and Cristianini, 2004). When data is available at higher dimension, the linear separation becomes possible; the k-means could be applied to group data to non-overlapping clusters.

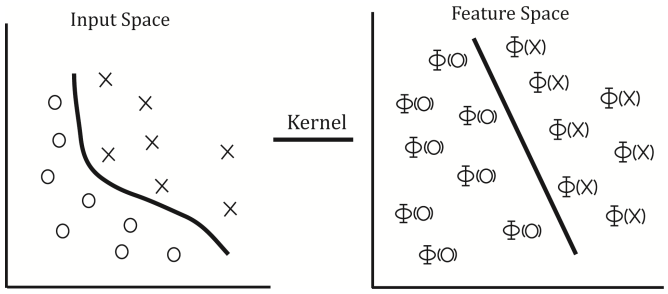

Figure 7.15: Kernel function transfers data from non-linear input space to feature space which data is more linearly separable (Shawe-Taylor and Cristianini, 2004).

The increase of dimensionality, with the use of kernels could suggest the misconception that it contradicts the initial purpose of data compression. Principal component analysis could be considered in case of very large datasets to reduce the dimensionality of the data first and then utilize kernel k-means clustering on the data with reduced dimension. In case of clustering geostatistical realizations however, the increase in dimensionality is not a real concern because the maximum number of realizations is normally in the order of 100s that would result in kernel dimensions of 10,000—still a very low dimension with no computational difficulties.

The first step in kernel k-means clustering is to stabilize the centroids of the clusters. The initial centroids are selected randomly. This requires the algorithm to look for the minimum distance between every kernel data $\phi(X_n)$ and all centroid of clusters $\|\phi(X_n) - m_k\|^2$ where $1 \leq k \leq K$. The cluster which is equivalent to $\arg\min_k(\|\phi(X_n) - m_k\|^2)$ includes $\phi(X_n)$. Recall that data should be normalized prior to clustering: $\tilde{K}(x, y) = \frac{K(x,y)}{\sqrt{K(x,x)K(y,y)}} \in \mathbb{R}$. As in k-means algorithm, the objective of kernel k-means is to minimize the clustering error in feature space

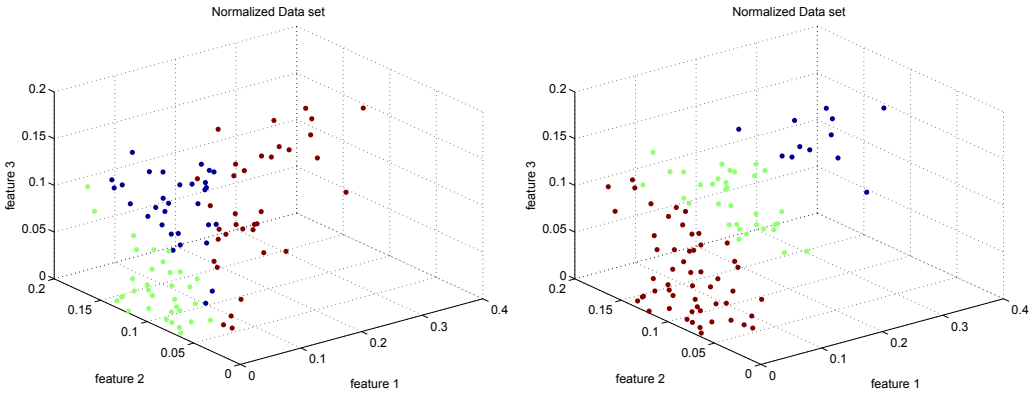

Figure 7.16: Illustration of the clusters in the input space using k-means algorithm (top), and the clusters in real space using kernel k-means on the feature space.

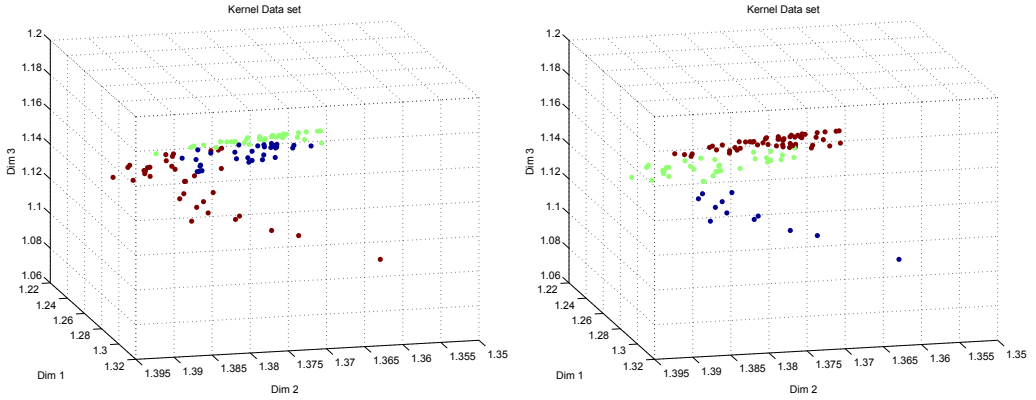

Figure 7.17: Illustration of the clusters in the feature space using k-means algorithm (top), and the clusters in feature space using kernel k-means on the feature space.

where the data vector is replaced by its kernel transform:

$$E(m_1, \cdots, m_K) = \sum_{n=1}^{N} \sum_{k=1}^{K} I(x_n \in \mathcal{C}_k) \|\phi(X_n) - m_k\|^2 \tag{7.3}$$

This algorithm is believed to converge when kernel matrix is positive semidefinite (The kernel matrix generated from the direct use of inner products of data set is always positive semidefinite and suitable for the purpose of realization clustering at this stage). At the end of this procedure, every centroid is equivalent to $m_k = \frac{\sum_{n=1}^{N} I(x_n \in \mathcal{C}_k)\phi(x_n)}{\sum_{n=1}^{N} I(x_n \in \mathcal{C}_k)}$.

Example

A small area of a deposit which contains 100 grid cells in X direction, 20 in Y direction and 100 in Z direction is modeled by 100 realizations. Every realization is described by several attributes such as (1) CHV (2) the amount of geo-objects (3) Keff and (4) the local connectivity. As shown in Figure 7.16, k-means algorithm

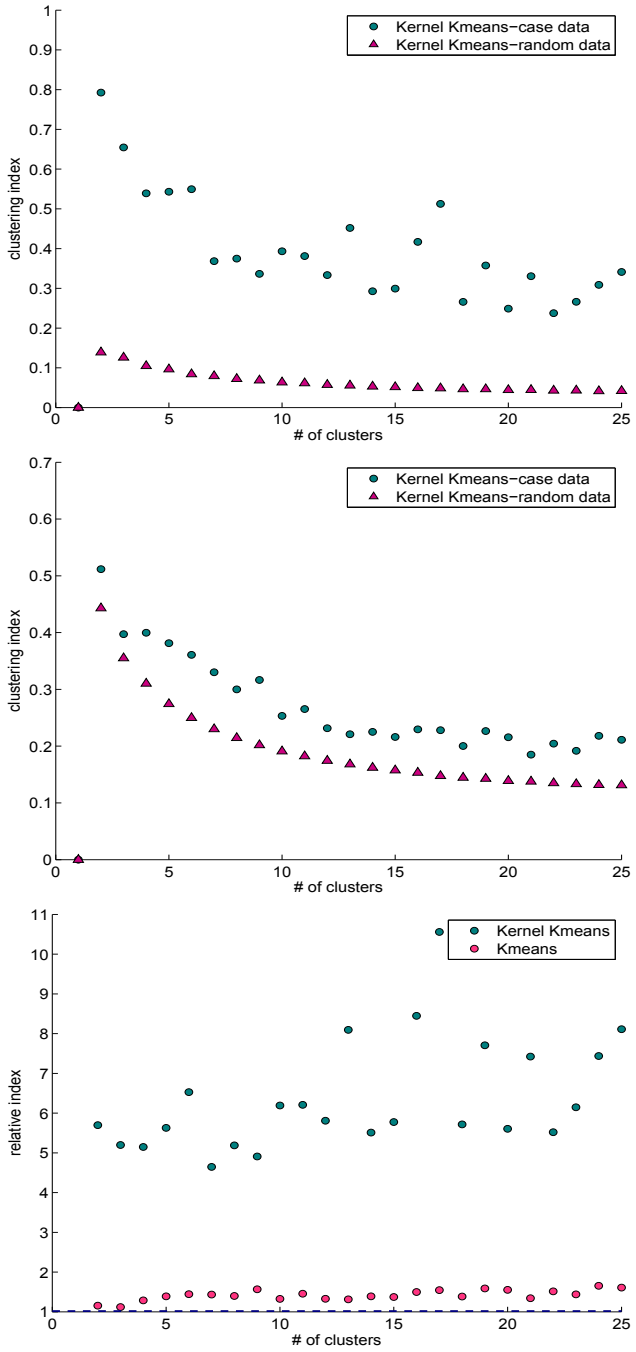

Figure 7.18: Comparing clustering index for both k-means clustering and kernel k-means clustering. Looking at the relative index in the third plot makes it clear that kernel k-means in this case which contains no obvious cluster, is a way better option to group data.

and kernel k-means are both adopted to cluster the realizations. No exact clustering forms is evident in the input space, however, clustering in higher dimension seems to perform much better in grouping data to three similar clusters. Figure 7.17 could be adapted to achieve the separation in higher dimension better than what k-means

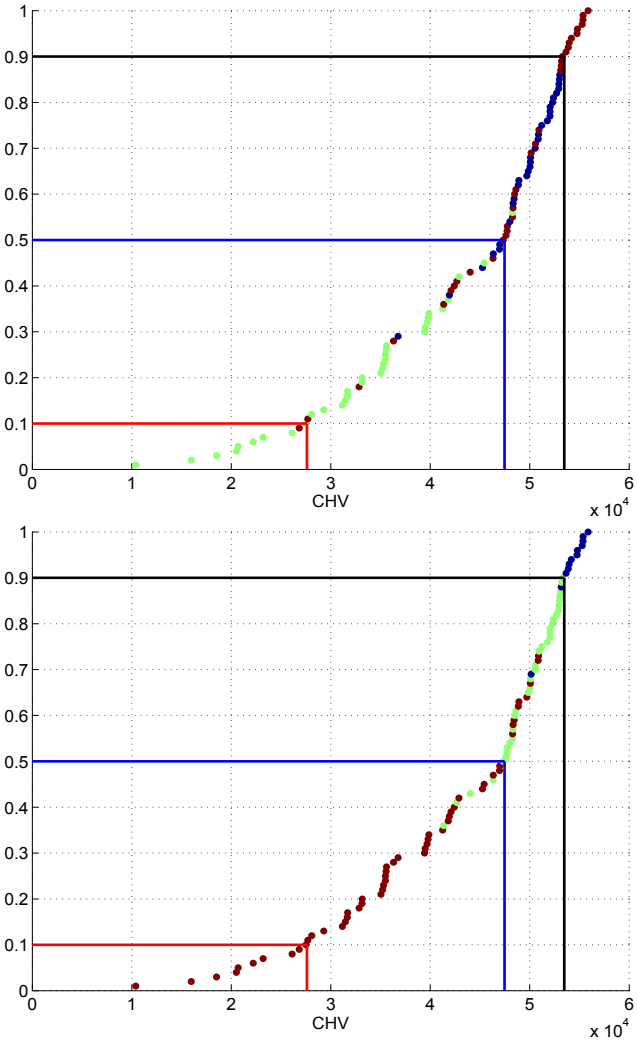

Figure 7.19: Illustration of the realization selection using ranking based on CHV. The order of realization shown in the second plot follow the groups much closer relative to the order of groups in the first plot.

can achieve in input space. Sum of the distances of data from their centroids in the k-means case is 0.45, for the kernel k-means case 0.27 on average.

Clustering index for both cases of k-means and kernel k-means clustering is applied for a range of group numbers changing from 1 to 25 on the realizations. As shown in Figure 7.18, there is a clear improvement in k-means clustering performance when higher dimension is considered using kernel function. The last figure of this chapter, Figure 7.19 demonstrate the order of realizations in terms of CHV colored with their own cluster for both clustering approaches. The CHV features ranking is very close to the order that they are colored.

7.5 Chapter Summary

Ranking is a common practice in reservoir modeling which provides a practical alternative to processing all realizations (typically 100 or more) through flow simulation. Processing the selected realizations provides an understanding of the performance of the set of realizations. The choice of a ranking index varies depending on the application and the complexity of the process. This chapter introduces two techniques to improve the process of realization selection, i.e. multiscale ranking (1) ranking simultaneously with multiple areas, and (2) clustering realizations when ranking is inadequate. SAGD drainage mostly happens at a number of scales and regions while only one model for every quantiles of P10, P50 and P90 is considered to characterize the heterogeneity for multiple well pairs in a single drainage area. Although it is challenging to select the proper model with the similar rank at all settings, the selection of proper model is equivalently crucial to the well-placement and final recovery. Multiscale ranking scheme is introduced to optimize the ranking using a single metric by considering a few recovery settings of different well placements, well pair numbers and scales of recovery.

The second technique developed in this chapter provides practitioners with the information that could not be possibly gained from ranking the realizations using a single metric. A single metric can never represent the entire recovery performance. Clustering is also required when selecting the typical quantiles is not representative. This is mostly the case when distribution of data is not continuous. Overall, applying clustering on the realizations is not as straightforward as ranking. Depending on the reservoir distribution, the spatial correlation of realizations, heterogeneity and the measured variables, the approach and results could be different. Sometimes the realizations are quite homogenous and many variables are too correlated that they are basically redundant in the clustering analysis. Also, sometimes some variables may carry no specific structure that they would be treated as noise in clustering. Such variables may introduce randomness in the clustering.

Chapter 8

Concluding Remarks

Geostatistical tools are widely applied to provide support for uncertainty quantification and reservoir forecasting. This thesis aims at developing tools and techniques to facilitate the use of improved multiple realizations for modern reservoir forecasting, particularly heavy oil reservoirs. The improvements in this thesis are directed towards one of the most important factors in representing reservoir heterogeneity, namely, facies. Unlike most geostatistical studies that improve the facies representation through facies modeling techniques, this thesis enhances facies representation through side operations that support facies modeling. The challenges discussed here are quite common in the practice of geostatistics but they have not been researched intensively. A reasonable geostatistical workflow often requires the practitioners to go out of their way to examine details that are easy to ignore or miss. This thesis helps geostatisticians with some overlooked aspects and subtle issues; practical applicability is a main feature of this thesis. Regardless of the technique utilized to construct 3-D numerical models, the research in this thesis is of potential benefit.

8.1 Thesis Contributions

The contributions of this thesis can be summarized by the following six points (with each point representing a substantial piece of research):

Facies upscaling: Blocking facies information to a constant length prior to 3-D modeling is a necessary process with current 3-D geostatistical modeling techniques. The typically high resolution information from core and well logging must be upscaled. A downside is the inevitable loss of information when the majority facies is assigned to each upscaled interval. A measure of facies mixing (FMM) is proposed in this thesis to account for the loss of information and incorporate it

in the estimating process. Porosity is simulated by facies and collocated to FMM which indirectly helps the facies to be reflected more accurately in the estimation of the porosity. A case study shows that FMM is promising to improve reservoir modeling.

Shale continuity: The second contribution of this thesis is related to the continuity of shale barriers. High net-to-gross reservoirs could contain a significant amount of small shales that act as local barriers for flow. This is particularly important in the McMurray formation. Although these shales could adversely impact the recovery performance, they cannot be efficiently characterized by current practices. An inverse modeling methodology is proposed to infer the lateral continuity of the thin shales. Information from the facies data, well spacing, and well configuration are used with a proposed factor known as total shale connectivity or TSC. The proposed approach characterizes the shale continuity with a probability distribution function of aspect ratio of horizontal to vertical range. Shales with the identified aspect ratio could then be imposed in facies models during pre/post-processing. This technique improves facies modeling by establishing a more realistic shale distribution in the model.

Model regridding: The third contribution addresses the need for high resolution models for heavy oil recovery flow simulation. A coarse resolution model may mask relevant information during reservoir evaluation and decision making. This thesis dismisses the common use of nearest neighbor assignment as regridding approach and advocates the stochastic regridding as the correct way to generate the high resolution models conditioned to coarse scale realizations. The proposed framework of the stochastic regridding utilizes the information of the spatial distribution of facies and/or continuous variables provided by the coarse scale model to reproduce the small scale variability at finer scales by generating multiple realizations that could use local variography of the area. Over/under estimation of small features in the reservoir would be corrected with stochastic regridding whereas such features would cause bias in flow models when regridding is applied using nearest neighbor assignment.

MPS aspect of regridding: The generation of high resolution models with MPS is the next contribution of this thesis. The initial steps in this investigation leads to defining frequency of patterns (FOP) to resemble variogram in two-point statistics which measures variations of geological features at different scales.

The high resolution model is primarily considered through extrapolation of FOP to smaller scale. This is shown to be theoretically and practically intractable. Instead, the problem is reformulated to enhancing the resolution of training image so that the generated models are simulated at the fine resolutions. Distance function kriging is considered to extrapolate data from larger scale of coarse grid cells to smaller scales. The case study suggests that rescaling TI to the desired resolution and considering it for generation of realizations works better than simple nearest neighbor to the coarse scale model.

Unrealistic disconnectivity: The fifth contribution is related to correcting unrealistic discontinuities of facies units. The connectivity is applied while (1) maintaining the global proportions; and (2) preserving the geological realism. Both requirements are implemented carefully, in the methodology that is proposed based on two operations of dilation and erosion. Dilation is performed for the objects to connect through a so-called "efficient dilation", in which the connection is applied at the direction of anisotropy. This is to ensure the least changes in the initial facies proportions. The proposed erosion algorithm utilizes a search template that scans over the dilated model and verifies the fraction outside the object with a threshold parameter. The proper use of erosion technique preserves connectivity while erasing the boundaries.

Realization selection: The last contribution of this thesis relates to selecting realizations for reservoir management. Realization selection is discussed from two perspectives. One is to improve the ranking process through the proposed approach of multiscale ranking which selects realizations by optimizing over different settings of well placement and scales of recovery. The objective function in multiscale ranking scheme is defined so that the distance between the overall drainage ranks and the target ranks for multiple locations are minimized simultaneously. The second aspect is to approach realization selection when there is more than one measurement to evaluate the response variable. Realization clustering is therefore proposed to cluster the realizations into groups that would expect to perform similarly. The clustering methodology is based on K-means technique in which the realizations are grouped to have smallest distance from the members of their group and furthest distance from the members of other groups. As the case study in chapter 7 shows, clustering is proven to be a promising alternative when ranking cannot represent the realization performance adequately, or one single measure is not enough to represent

the recovery performance of the reservoir.

8.2 Limitations and Future Work

Many research directions stem from the research developed in this thesis. Keeping that in mind, future research directions follow:

Facies blocking: Facies blocking is a lossy operation. One way to entirely prevent the loss is to consider facies intervals directly in 3-D modeling. Meaning that instead of simulating fixed size blocks, a certain grid cell parameter can accommodate for the associated intervals of facies at its position. The current geostatistical practices cannot yet support such simulations. Developing a system to be able to take into account this process could introduce significant improvements into the 3-D reservoir modeling framework.

Shale characterization: Acquiring knowledge about the shale continuity utilizing only data and well configuration is challenging. Although the proposed technique in this thesis is novel and promising, it could be inconclusive if the considered factors in the methodology (amount of data, well spacing, etc) are not sufficiently informative relative to each other. With the new method of ground-penetrating radar, new information regarding the shale distributions can be easily extracted from the 3-D images of outcrops. This information if integrated with the proposed method could provide insightful knowledge about the shales.

High resolution models: Although stochastic regridding approach is automated and practical, re-simulation of the coarse-scale realizations could become an extensive work. The entire process of modeling at coarse-scale grid cells might need to be applied to build models at higher resolutions at some occasions. That could become tedious if global variograms are not applicable, and local variograms are determined for large number of facies in the model. Recall that local variography is automated in developed program but the offline checks over the variograms are recommended. Thus, one way to discuss this research, is through a paradigm in which many changes in resolutions or scales are no longer relevant, i.e., the grid free paradigm. If the facies are simulated using the grid-free simulation scheme, then the processes such as facies upscaling for data preparation or model regridding to generate realization at higher resolution would no longer be an issue (Zagayevskiy, 2015).

A similar argument could be discussed in MPS context. The proposed approach

to rescale TI utilizes interpolation techniques which have the feature of smoothing edges. This could limit the application of this technique to smooth domains such as channel like deposits. This is no longer a problem if grid-free scheme is practiced.

Enforcing connectivity: One way to view this is if the disconnectivity could be predicted and expected from its initial source, i.e. simulation. The proposed methodology in this thesis, provides the necessary tool to enforce the connectivity satisfying geostatistical modeling conditions but it does not directly identify the situations that disconnectivity should be treated. This concept could also be perceived from the shale continuity point of view. Most connectivity evaluations are concerned with the presence of stochastic shales. The precise knowledge of shales positions and distributions that is gained previously could be integrated into recognizing the discontinuity of shale units.

Selecting realizations: The limitation comes from the term "selecting". To fully transfer the quantified uncertainty into prediction of production performance, "all realizations" should be considered. Any other way is only an approximation.

Appendix A

Stochastic Model Regridding Program

The regridding process has been automated and developed in two combined forms of *Shell Script* and *FORTAN* programming. All inputs and outputs of this process are practiced in Cartesian grid system. Data are assigned to the center point of every grid block where the grid block sizes are the same in the entire network. The entire process of regridding is assembled in a directory. The directory includes the main script **run-regriddingMaster.bsh**, the parameter file "regridding.par" which is modified by the user, and a folder of all required execution programs (Regridding.exe, nscore-mv.exe, VariogramParameters.exe, gamv2004.exe, varfit.exe, corrmat.exe, sgsim.exe, sisim.exe, mergemod.exe), called "03-Executable". Except for the main program of "Regridding" and "VariogramParameters", which are implemented during the development of regridding program, the rest is borrowed from **GSLIB** (Deutsch and Journel, 1998). The implemented FORTRAN program in this automation of regridding process is responsible for preparing the corresponding parameter files while the scrip takes care of executing each one of them in the proper order.

At first, the input data file should be added to the directory by the user. Data file should be in **GSLIB**-style (the header, the number of variables, the title of variables, and finally the columns of variables). Also, it is required that the user prepares the input with ".dat" extension (the master script will then move it into the right directory). After preparing the input file, the user should modify the main parameter file; "regridding.par" which follows:

Similar to all **GSLIB**-like programs, three lines are reserved for grid specifications (i.e. lines 7–9). It can be specified on line 2 whether the regridding is applied on categorical variable model (i.e. facies), continuous variablae, or a combination of

```
                    Parameters for REGRIDDING
                    **************************
START OF PARAMETERS:
1    ../01-DataFiles/*.dat      -initial simulation data file
2    2                          -categorical(=0), continuous(=1), or combined (=2) model
3    4   2                      -number of variables for regridding, TO MODEL
4    1   2   5                  -facies column, variable columns
5    4                          -secondary variable column
6    100                        -number of initial realizations
7    100   12.0   24.0          -nx,xmn,xsiz
8    150   12.0   24.0          -ny,ymn,ysiz
9    50   0.5   1.0             -nz,zmn,zsiz
10   RLZ                        -which realizations?
11   20   20                    -new origin in X, new origin in Y
12   20                         -rotation angle (in degrees clockwise)
13   30   80                    -length for data extraction in X and Y direction
14   50   50                    -zmin, zmax for depth of data extraction
15   1.0   1.0                  -size of refined grids in X and Y
16   10                         -number of realizations per re-simulation
17   5                          -number of variogram directions 0° to 90° (3,5,7,..)
18   2                          -number of nested structure (2 is recommended)
```

both. If regridding is applied for more than one continuous variable, the columns could be specified on line 4. Most information in parameter file relates to the specifications of data extraction and geometry of the area of interest, length of area of interest in the X direction, length of area of interest in the Y direction, the rotation angle (defined as positive if clockwise, starting at origin), the depth of elevation by determining the minimum and maximum levels at Z, and how many realizations per initial realization to be generated (i.e. lines 11–16). The target refined grid size can be specified on line 15. The only part which should stay untouched is where it asks for *which realization* on line 10. This should remain as **RLZ** variable. Note that regridding is not considered in Z direction since data in the vertical direction is typically available at reasonably high resolution.

Regridding is applied one at a time for every realization (at coarser grid size) in this program. The user will be prompted to enter the range of the realizations that he wishes to simulate the model at finer grids. For example, if 5 number of re-simulated realizations are required to be conditioned to coarse scale realization ranging from 20 to 50, then 5 is entered on line 16, and 20, space, 50 are entered as soon as the master script runs. The script then sends the realization number to the variable **RLZ** so that in the data extraction, the right realization is selected. From then on, everything will be automated and at the end the simulated realizations are collected in directory "04-SimResults". Every file in this folder is named as

"string+number+Realization+number". The first number refers to the corresponding primary (to model) variable and the second refers to the coarse scale realization. For a case where two variables of permeability and water saturations are to be regridded (assuming type 2), the "merg1Realization13" contains the simulated values for permeability with higher resolution in 5 realizations. The regridding has been applied to the initial realization number 13, which belongs to the original simulated results. This is considered a good practice as it enables the user to exploit the variability of uncertainty of the finer realizations within and between the original coarse realizations.

After the program is given its parameter file, it begins with finding the required realization and grid specifications and rotation on the input data file. It then extracts the grid nodes information and save them in a data file called "dataExtracted.out". Remember that all these output files are created for the user's record or sanity check and there is absolutely no need for the user to be concerned about them. Another file called, "coordinates.out" records the extracted data with all the coordinate specifications, realization number and coordinates in the user's specified Cartesian domain (see Figure 4.6). Now that the area of interest and all its specifications have been determined, the program decides on which procedure to take for re-simulation. This will be decided based on the type of the data input that the user specifies on line 2 where categorical data is indicated by 0, continuous by 1, and the most common case of combined (facies+primary+secondary) is indicated by 2. For the case of categorical data file, before the program creates the necessary parameter file, it has to determine some data statistics regarding stationary domain of rock types. The program divides the extracted data file into the available categories (stationary domain) and determines the proportions of facies and saves them in a non-**GSLIB**-style file of `proportions.data`. This process is also required to be applied for the data type of 2 (combined). For the case in which the available variables are continuous, the entire domain of interest is assumed stationary since no facies distribution is available.

At this point, the continuity of data should be determined. To have this stage as part of the automatic process, the variogram is been automatically calculated for number of directions. In the parameter file, the user is asked to enter an odd number, which would represent the number of directions of variogram calculations in the range of 0° to 90°. For example, specifying 5 means that gamv2004 will calculate

the variogram of the required variable in 9 directions in the range of 0° to 180°. The developed program "VariogramParameters" evaluates azimuth (its tolerance and bandwidth), dip (its tolerance and bandwidth), as well as the number of lags and lag separations and the tolerance on the horizontal plane based on the geometry specifications that the user specifies at the main parameter file. These parameters are used by gamve2004 to evaluate the variogram at the specified directions for every considered variable in the area of interest. Note that data for variogram determination should be in normal score since simulations is done in the Gaussian domain. Thus, "nscore-mv" should be applied on extracted data beforehand. The transformed data is recorded in the output file called `DataNS.dat` in the directory *01-DataFiles*. In case of combined model, the generated normal score data file is as many as the number of facies available in the area of interest. For example, if three categories of 2, 4 and 5 exist in the area of interest, there will be three data files of `DataC1NS.dat`, `DataC2NS.dat` and `DataC3NS.dat`. The file `DataNS.dat` would be generated regardless of input data file, to keep all normal score transformation of extracted data. This is because the shortage of pairs to determine variogram is possible; if the simulation process does not find the required variogram, it uses the so-called back up.

All necessary parameter files for the regridding process are collected in the directory *02-BashFiles* to enable sanity check. The program applies the entire process of regridding on every realization for all the involved variables at once. In case secondary variables exist, a different bash file **variogramSec.bsh** includes the necessary parameter files to calculate the variogram for the secondary variables. The fitting of all variables is possible using a previously developed **GSLIB** program called "varfit" which can fit the variogram in several directions simultaneously. The varift program includes the principal (e.g., number of variograms, number of structures, number of directions, and minimum number of points) options and more advanced ones such as fixing structure type, fixing nugget effect, fixing the sill, etc. The preference of the regridding program is to keep these options limited. Yet, `regridding.par` has this option for the user to specify the number of structures; however, 2 number of structures with spherical type (type is fixed) is strongly recommended as it reliably captures the short range and long range variograms. For the same reason, the nugget effect is fixed to zero to avoid discontinuity at short ranges.

In the presence of secondary variables, collocated cokriging is the preferred method of simulation in this program. Throughout the regridding process, strong conditioning of data at regular grid points is a good reason to rely on screening approach. This, however, requires the program to find out about the correlation coefficient of the primary and secondary variables. This program only considers one secondary variable; strong conditioning justifies this simplification. For example, in case there are two variables of interest and one secondary variable available at coarse grids, `correlationSecVar1.bsh` and `correlationSecVar2.bsh` provide the correlation coefficient for the first variable and secondary data and second variable and secondary data. The "corrmat" program uses these parameter files to generate the correlation coefficient. Although, "corrmat" is able to determine the correlation coefficient matrix for as many variables, separation of the files eases the following process of capturing the corresponding coefficient and input them to the sequential Gaussian simulation. Note that the entire previous process is applied to "DataNS.dat", which contains all the extracted variables in one file regardless of the associated category type. All previous variogram specifications apply to the secondary data as well.

The last part of regridding process is devoted to simulation. The simulation is done on the new grid specification that the program figures out based on length of area of interest and the resolution of new simulation. The regridding program prepares the appropriate parameters for simulating the regridded realizations. For the categorical data in both cases of type 1 or 2 input file, **BlockSIS.bsh** is created to generate realizations as many as user's option (specified in regridding.par file) for the facies modeling. The number of categories, the categories and their proportions are all extracted from `proportions.data` file. The information regarding columns for X, Y, Z, and variables are also gained from `coordinates.dat` Maximum search radii for all types of simulation is kept to 4 times the original coarse grid size. This choice is justifiable considering how kriging works. The input data is available through realizations which are aligned in Cartesian system and when kriging is applied, it assigns higher weights to the closer grid nodes and much smaller weights or even negative weights to the further ones. In other words, having bigger search radii does not change the simulation results as the closest grid nodes are the most influential in the kriging system; this is also known as the screening effect in geostatistics.

The associated variogram models for all the categories in the area of interest are

attached to the simulation parameter file. The file "run-VarIndicator" is the corresponding parameter file to determine the variogram for every category in several directions and fit them automatically. The minimum pairs of variogram calculations is been fixed to 40. In case the variogram model is not created, the process of simulation captures the total variogram model (back up). For the case of continuous variables, however, SGSIM simulation should be applied. This requires the program to create the corresponding parameter file which best suits the specific variable and sequential Gaussian simulation in **GSLIB**. These files could be found in the directory "02-BashFiles". For example, the bash file `run-SGSIM3-var2.bsh` corresponds to simulation of the second variable of interest associated with the third facies in the area of interest. The corresponding columns for X, Y, Z and the variable are all detected from extracted data files (`DataC3.dat` for **run-SGSIM3-var2.bsh**).

In sequential Gaussian simulation also, the lower and upper tails of variable should be known. The regridding program at the beginning records the maximum and minimum data associate with every variable. Therefore, considering the extracted variable in the simulation rather than the normal scored ones allows the program to not have to determine the minimum and maximum of data values in the Gaussian domain. Fortunately, the "sgsim" program in **GSLIB** is capable of doing the transformation inside. This option is fixed on in the developed regridding process. The associated debugging and output files are all named in a way to be easily distinguishable from each other. In case there is a secondary variable, the "run-sgsim" bash file includes the corresponding parameter file to apply simulation for the secondary variable on the re-simulation data grid. The secondary data should be simulated differently for different facies as they fill up different grid nodes. After the simulation is over, if the input type is 2, the process is not finished until merging is applied. Separate simulation of variables corresponding to different facies should come together to fill up the domain. Merging parameter file is attached to the end of **BlockSIS.bsh** (if the regridding type is 2). The final merged models at this point are the ones which will be transferred to the final destination directory "04-SimResults". The user can always choose to plot the generated realizations to compare with the coarse realizations.

Appendix B

Enforce Realistic Connectivity Program

The fundamentals of approach taken to establish connectivity over disparate units is discussed in Chapter 6. The developed program is called "ED-SE" standing for *Efficient Dilation - Smart Erosion*. ED-SE is designed to generate many auxiliary files associated with the original model, dilated model, and the eroded one. These files are generated to help with understanding parameters, entailing visualization and providing further checks. Three *stat* files are generated for all three models. Each one of these *stat* files lists the number of objects identified in the model from largest to smallest with its corresponding size. `Geo-obj.model` is the initial data file identifying the target object cells with object's number and the rest with 0. This file is helpful to visualize the distribution of the objects in the model and their relative distances. Note that if there are a number of facies having broken objects, the dilation process is applied hierarchically in which the model become a binary one recognizing the target facies.

The parameter file of "ED-SE" program is shown below. The option to specify objects to connect is on line 7. In case, the growth of all objects does not result in undesired connection, option 0 can be set. Since the dilated cells are eroded back when no connection occurs, option 0 can be applied safely. This feature stabilizes the dilation process in addition to dilation along the direction of anisotropy. Two generated files associated with dilation are `potential-dilate.out` and `added-cells.out`. `Potential-dilate.out` contains as many columns as twice the number of objects in the model. Every two columns are same except for the added cells after dilation is applied which would be indicated as 1. If the added cells confront the same cells in other columns, it means the corresponding object is connected with the other

object. Otherwise, the added-cells will get back to zero. `added-cells.out` contains the finalized changes in the model.

```
                    Parameters for ED-SE
                    ********************
START OF PARAMETERS:
1    ../model.out              - input rock type model
2    ../data.dat               - conditioning data file with coordinates
3    30   30   10   1         - nx, ny, nz, num realizations
4    1.0  1.0  1.0            - xsiz, ysiz, zsiz
5    1 0                       - number of net facies, code facies to connect
6    ../dilated.out            - dilated model
7    4 1 4 5 8                 - how many, objects to connect (0 for all)
8    ../eroded.out             - eroded model
9    15                        - dilation parameter
10   3    3    1               - offset template size for erosion: x, y, z
11   10   0.3  4               - erosion parameter:
                                  iteration, control threshold, size ratio
```

Dilation parameter can be specified on line 9. Parameter value of 50 will grow the object twice as big. The file `threshold.out` contains the threshold values that have been used for every object on its distance function model to grow; `dist-obj.out` also contains all the distance value and a column listing the closest object to the cell. The file `proportionMap.out` records the proportion of template inside the object while scanning the model. The file has as many columns as the dilated objects. The template size can be specified along X, Y, and Z directions on line 10. The template can only form to a box but with varying size. The three erosion parameters of number of iterations, threshold on the distance map (changing between 0 and 1), and size ratio are specified on line 11. The parameter of size ratio is implemented in the program to control the reduction in object's size. For example, the value 4 ensures the erosion stops over the object which the size of the objects reaches its quarter.

Bibliography

Image five. (Accessed: May, 2013). https://goo.gl/BKqe4B.

Image four. (Accessed: May, 2013). https://goo.gl/LJ1goy.

Image six. (Accessed: May, 2013). https://goo.gl/6GCss6.

Image three. (Accessed: May, 2013). https://goo.gl/K0BaMx.

Image two. (Accessed: May, 2013). https://goo.gl/6klOR0.

Alshehri, N. S. (2010). *Quantification of Reservoir Uncertainty for Optimal Decision Making*. PhD thesis, University of Alberta, Edmonton, AB.

Armstrong, M., Galli, A. G., Beucher, H., Le Loc'h, G., Renard, D., Doligez, B., Eschard, R., and Geffroy, F. (2003). *Plurigaussian Simulations in Geosciences*. Springer, 1st edition.

Aziz, K. (1993). Reservoir simulation grids: opportunities and problems. *Journal of Petroleum Technology*, 45(07):658–663.

Aziz, K., Arbabi, S., and Deutsch, C. V. (1996). Why it is so difficult to predict the performance of non-conventional wells? *SPE Paper Number 37048*.

Aziz, K. and Settari, A. (1979). *Petroleum Reservoir Simulation*. Elsevier Applied Science, New York.

Azom, P. N. (2013). *Improved Modeling of the Steam-Assisted Gravity Drainage (SAGD) Process*. PhD thesis, University of Texas, Austin, TX.

Azom, P. N. and Srinivasan, S. (2011). Modeling the effect of permeability anisotropy on the steam-assisted gravity drainage (SAGD) process. In *Canadian Unconventional Resources Conference*. Society of Petroleum Engineers.

Babak, O. and Deutsch, C. V. (2008). Nonnet size determination with mass moments of inertia. Technical report, Center for Computational Geostatistics, University of Alberta, Edmonton, Alberta.

Babak, O., Manchuk, J. G., and Deutsch, C. V. (2013). Accounting for non-exclusivity in sequential indicator simulation of categorical variables. *Computers & Geosciences*, 51:118–128.

Ballin, P. R., Journel, A. G., and Aziz, K. A. (1992). Prediction of uncertainty in reservoir performance forecasting. *Journal of Canadian Petroleum Technology*, 31(4).

Barnett, R. M. (2015). *Managing Complex Multivariate Relations in the Presence of Incomplete Spatial Data*. PhD thesis, University of Alberta, Edmonton, AB.

Begg, S. H. and Chang, D. M. (1985). A simple statistical method for calculating the effective vertical permeability of a reservoir containing discontinuous shales. In *SPE Annual Technical Conference and Exhibition*. Society of Petroleum Engineers.

Belgrave, J. D. M. and Bora, R. (1996). On the performance of horizontal wells

in reservoirs containing discontinuous shales. *Journal of Canadian Petroleum Technology*, 35(05):38–44.

Berkhin, P. (2006). A survey of clustering data mining techniques. In *Grouping multidimensional data*, pages 25–71. Springer.

Berry, M. J. and Linoff, G. (1997). *Data mining techniques: for marketing, sales, and customer support*. John Wiley & Sons, Inc.

Bland, J. M. and Altman, D. G. (2000). Statistics notes: the odds ratio. *BMJ: British Medical Journal*, 320(7247):1468.

Boisvert, J. B., Pyrcz, M. J., and Deutsch, C. V. (2007). Multiple-point statistics for training image selection. *Natural Resources Research*, 16(4):313–321.

Boschan, A. and Nœtinger, B. (2012). Scale dependence of effective hydraulic conductivity distributions in 3d heterogeneous media: a numerical study. *Transport in porous media*, 94(1):101–121.

Boucher, A. (2009). Sub-pixel mapping of coarse satellite remote sensing images with stochastic simulations from training images. *Mathematical geosciences*, 41(3):265–290.

Burns, E. R., Bentley, L. R., Therrien, R., and Deutsch, C. V. (2010). Upscaling facies models to preserve connectivity of designated facies. *Hydrogeology journal*, 18(6):1357–1373.

Burton, R. C., Chin, L. Y., Davis, E. R., Enderlin, M., Fuh, G., Hodge, R., Ramos, G. G., VanDeVerg, P., Werner, M., Mathews, W. L., and Petersen, S. D. (2005). North slope heavy oil sand control strategy: Detailed case study of sand production predictions and field measurements for Alaskan heavy oil-multi-lateral field developments. *paper SPE*, 97279:9–12.

Butler, R. M. (1991). *Thermal recovery of oil and bitumen*. Prentice Hall, Englewood Cliffs, New Jersey.

Butler, R. M. (1998). SAGD comes of age. *Journal of Canadian Petroleum Technology*, 37(7):9–12.

Butler, R. M., McNab, G. S., and Lo, H. Y. (1981). Theoretical studies on the gravity drainage of heavy oil during steam heating. *Canadian Journal of Chemical Engineering*, 59(4):455–460.

Butler, R. M. and Stephens, D. J. (1981). The gravity drainage of steam-heated heavy oil to parallel horizontal wells. *Journal of Canadian Petroleum Technology*, 20(2).

Butler, R. M. and Yee, C. T. (2002). Progress in the in situ recovery of heavy oils and bitumen. *Journal of Canadian Petroleum Technology*, 41:31–40.

Carrigy, M. A. (1959). Geology of the mcmurray formation, part iii, general geology of the mcmurray area. *Alberta Research Council, Memoir 1*. 130 p.

Chen, Q., Gerritsen, M. G., and Kovscek, A. R. (2008). Effects of reservoir heterogeneities on the steam-assisted gravity-drainage process. *SPE Reservoir Evaluation & Engineering*, 11(5):921–932.

Christie, M. A. (1996). Upscaling for reservoir simulation. *Journal of Petroleum Technology*, 48(11):1–004.

Christie, M. A. and Blunt, M. J. (2001). Tenth spe comparative solution project: A comparison of upscaling techniques. *SPE Reservoir Evaluation & Engineering*, 4(04):308–317.

Chu, L., Schatzinger, R. A., and Tham, M. K. (1998). Application of wavelet analysis to upscaling of rock properties. *SPE Reservoir Evaluation & Engineering*, 1(01):75–81.

Chugunova, T. L. and Hu, L. Y. (2008). Multiple-point simulations constrained by continuous auxiliary data. *Mathematical Geosciences*, 40:133–146.

Clemensten, R., Hurst, A. R., Knarud, R., and Omre, H. (1990). A computer program for evaluation of fluvial reservoirs. In Buller, A. T., editor, *North Sea Oil and Gas Reservoirs II*. Graham and Trotman, London.

Cody, J., Youn, S., Riddy, A., and Gittins, S. (2001). Implications of reservoir "compartments" on the design and execution of the christina lake thermal recovery project.

Cross, T. A. and Homewood, P. W. (1997). Amanz gressly's role in founding modern stratigraphy. *Geological Society of America Bulletin*, 109(12):1617–1630.

da Cruz, P. S. (2000). *Reservoir Management Decision-Making in the Presence of Geological Uncertainty*. PhD thesis, Stanford University, Stanford, CA.

Dalrymple, R. W. and Choi, K. (2007). Morphologic and facies trends through the fluvial–marine transition in tide-dominated depositional systems: a schematic framework for environmental and sequence-stratigraphic interpretation. *Earth-Science Reviews*, 81(3):135–174.

Davies, D. L. and Bouldin, D. W. (1979). A cluster separation measure. *Pattern Analysis and Machine Intelligence, IEEE Transactions on*, (2):224–227.

Demaison, G. J. (1977). Tar sands and supergiant oil fields. *AAPG Bulletin*, 61(11):1950–1961.

Deutsch, C. V. (1987). A probabilistic approach to estimate effective absolute permeability. Master's thesis, Stanford University, Standfor, CA.

Deutsch, C. V. (1998a). Cleaning categorical variable (lithofacies) realizations with maximum a-posteriori selection. *Computers & Geosciences*, 24(6):551–562.

Deutsch, C. V. (1998b). Fortran programs for calculating connectivity of three-dimensional numerical models and for ranking multiple realizations. *Computers & Geosciences*, 24(1):69–76.

Deutsch, C. V. (2002). *Geostatistical Reservoir Modeling*. Applied Geostatistics Series. Oxford University Press, New York, 1 edition.

Deutsch, C. V. (2006). What in the reservoir is geostatistics good for? *Journal of Canadian Petroleum Technology*, 45(4):14.

Deutsch, C. V. (2010). Estimation of vertical permeability in the mcmurray formation. *JCPT*, 49(12).

Deutsch, C. V., Dembicki, E., and Yeung, K. (2002). Geostatistical determination of production uncertainty: Application to Firebag project. *Center for Computational Geostatistics (CCG), University of Alberta, Edmonton, Alberta, Canada*.

Deutsch, C. V. and Hewett, T. A. (1996). Challenges in reservoir forecasting. *Mathematical geology*, 28(7):829–842.

Deutsch, C. V. and Journel, A. G. (1998). *GSLIB: geostat istical Software Library and User's Guide*. Oxford University Press, New York, 2nd edition.

Deutsch, C. V. and McLennan, J. A. (2005). Guide to SAGD reservoir characterization using geostatistics. In *Guidebook Series*, volume 3, page 121, University of Alberta. Centre for Computational Geostatistics (CCG).

Deutsch, C. V. and Srinivasan, S. (1996). Improved reservoir management through ranking stochastic reservoir models. In *SPE/DOE Tenth Symposium on Improved Oil Recovery, Tulsa, OK*, pages 105–113, Washington, DC. Society of Petroleum Engineers. SPE Paper Number 35411.

Ding, D. Y. (1996). Scaling-up in the vicinity of wells in heterogeneous field. In

13th SPE Symposium on Reservoir Simulation, pages 441–451, San Antonio, TX. Society of Petroleum Engineers. SPE Paper # 29137.

Ding, D. Y. (2004). Near-well upscaling for reservoir simulations. *Oil & Gas Science and Technology*, 59(2):157–165.

Drineas, P., Frieze, A., Kannan, R., Vempala, S., and Vinay, V. (2004). Clustering large graphs via the singular value decomposition. *Machine learning*, 56(1-3):9–33.

Dunbar, C. O. and Rodgers, J. (1957). Principles of stratigraphy.

Durlofsky, L. J. (2003). Upscaling of geocellular models for reservoir flow simulation: a review of recent progress. In *7th International Forum on Reservoir Simulation Bühl/Baden-Baden, Germany*, pages 23–27. Citeseer.

Durlofsky, L. J. (2005). Upscaling and gridding of fine scale geological models for flow simulation. In *Paper presented at the 8th International Forum on Reservoir Simulation*, pages 441–451, Iles Borromees, Stresa, Italy. Society of Petroleum Engineers. SPE Paper # 29137.

Durlofsky, L. J., Jones, R. C., and Milliken, W. J. (1997). A nonuniform coarsening approach for the scale-up of displacement processes in heterogeneous porous media. *Advances in Water Resources*, 20(5):335–347.

Durlofsky, L. J., Milliken, W. J., and Bernath, A. (2000). Scale-up in the near-well region. *Journal of Petroleum Technology*, 5(07):658–663.

Edmunds, N. (1993). Effective application of steam assisted gravity drainage of bitumen to long horizontal well pairs. *Journal of Canadian Petroleum Technology*, 32.

Edmunds, N. R., Kovalsky, J. A., Gittins, S. D., and Pennacchioli, E. D. (1994). Review of phase A Steam-Assisted Gravity-Drainage test. *SPE Reservoir Engineering*, 9(02):119–124.

Eidsvik, J. (2015). Pyrcz and deutsch: Geostatistical reservoir modeling. *Mathematical Geosciences*, 47(4):497–499.

Emery, X. (2007). Simulation of geological domains using the plurigaussian model: new developments and computer programs. *Computers & geosciences*, 33(9):1189–1201.

Englund, E. J. (1993). Spatial simulation: environmental applications. *Environmental Modeling with GIS*, pages 432–437.

ERCB (2013). STB98-2013: Alberta's energy reserved 2012 supply/demand outlook 2013-2022.

Farmer, C. L. (2002). Upscaling: a review. *International Journal for Numerical Methods in Fluids*, 40(1-2):63–78.

Fenik, D. R., Nouri, A., and Deutsch, C. V. (2009a). Criteria for ranking realizations in the investigation of SAGD reservoir performance. In *Canadian International Petroleum Conference*, Calgary, AB. Society of Petroleum Engineers.

Fenik, D. R., Nouri, A., and Deutsch, C. V. (2009b). Ranking realizations for sagd performance predictions. Technical Report 204, CCG Annual Report 11, Edmonton, AB.

Flach, P. D. (1984). *Oil sands geology: Athabasca deposit north.* Geological Survey Department, Alberta Research Council.

Flach, P. D. and Mossop, G. D. (1985). Depositional environments of lower cretaceous mcmurray formation, athabasca oil sands, alberta. *AAPG Bulletin*, 69(8):1195–1207.

Frykman, P. and Deutsch, C. V. (1999). Geostatistical scaling laws applied to core

and log data. *SPE Annual Technical Conference and Exhibition*.

Fustic, M. (2007). Stratigraphic dip analysis–a novel application for detailed geological modeling of point bars, and predicting bitumen grade, mcmurray formation, muskeg river mine, northeast alberta. *Natural Resources Research*, 16(1):31–43.

Fustic, M., Bennett, B., Adams, J., Huang, H., MacFarlane, B., Leckie, D. A., and Larter, S. (2011). Bitumen and heavy oil geochemistry: a tool for distinguishing barriers from baffles in oil sands reservoirs. *Bulletin of Canadian Petroleum Geology*, 59(4):295–316.

Galloway, W. E. and Hobday, D. K. (1996). *Terrigenouus Clastic Depositional Systems: applications to fossil fuel and groundwater resources*. Springer, New York.

Garb, F. A. (1988). Assessing risk in estimating hydrocarbon reserves and in evaluating hydrocarbon-producing properties. *Journal of Petroleum Technology*, 40(6).

Ghosh, J. and Strehl, A. (2006). Similarity-based text clustering: a comparative study. In *Grouping Multidimensional Data*, pages 73–97. Springer.

Giger, F. M., Reiss, L. H., and Jourdan, A. P. (1984). The reservoir engineering aspects of horizontal drilling. In *Paper presented at the 8th International Forum on Reservoir Simulation*, Houston, TX. Society of Petroleum Engineers. SPE Paper # 13024.

Gonzalez, R. C., Woods, R. E., and Eddins, S. L. (2009). *Digital image processing using MATLAB*, volume 2. Gatesmark Publishing Knoxville.

Goovaerts, P. (1997). *Geostatistics for Natural Resources Evaluation*. Oxford University Press, New York.

Graf, A. B. A. and Borer, S. (2001). Normalization in support vector machines. In *Pattern Recognition*, pages 277–282. Springer.

Grimes, D. A. and Schulz, K. F. (2008). Making sense of odds and odds ratios. *Obstetrics & Gynecology*, 111(2, Part 1):423–426.

Guardiano, F. and Srivastava, R. M. (1993). Multivariate geostatistics: beyond bivariate moments. In Soares, A., editor, *Geostatistics Troia 1992*, volume 1, pages 133–144. Kluwer.

Guha, S., Rastogi, R., and Shim, K. (1998). Cure: an efficient clustering algorithm for large databases. In *ACM SIGMOD Record*, volume 27, pages 73–84. ACM.

Haldorsen, H. and Lake, L. (1984). A new approach to shale management in field-scale models. *Old SPE Journal*, 24(4):447–457.

Haldorsen, H. H. (1989). On the modeling of vertical permeability barriers in single-well simulation models. *SPE Formation Evaluation*, 4(03):349–358.

Haldorsen, H. H., Brand, P. J., and Macdonald, C. J. (1988). Review of the stochastic nature of reservoirs. In Edwards, S. and King, P. R., editors, *Mathematics in Oil Production*, pages 109–209. Clarendon Press, Oxford.

Haldorsen, H. H. and Damsleth, E. (1990). Stochastic modeling. *Journal of Petroleum Technology*, pages 404–412.

Haldorsen, H. H. and Damsleth, E. (1993). Challenges in reservoir characterization. *Bulliten of the American Association of Petroleum Geologists*, 77(4):541–551.

Halkidi, M., Batistakis, Y., and Vazirgiannis, M. (2001). On clustering validation techniques. *Journal of Intelligent Information Systems*, 17(2-3):107–145.

Haralick, R. M., Sternberg, S. R., and Zhuang, X. (1987). Image analysis using mathematical morphology. *Pattern Analysis and Machine Intelligence, IEEE Transactions on*, (4):532–550.

Hassanpour, R. M. and Deutsch, C. V. (2007). Determination of locally varying direction through mass moment of inertia tensor. *CCG Paper 2007*, (112).

Hassanpour, R. M. and Deutsch, C. V. (2008). Fitting local anisotropy with mass moments of inertia. *CCG Paper 2008*, (403).

Hatløy, A. S. (1995). Numerical facies modeling combining deterministic and stochastic method. In Yarus, J. M. and Chambers, R. L., editors, *Stochastic Modeling and Geostatistics: principles, Methods, and Case Studies*, pages 109–120. AAPG Computer Applications in Geology, No. 3.

Hein, F. J., Cotterill, D. K., and Berhane, H. (2000). An atlas of lithofacies of the mcmurray formation, athabasca oil sands deposit, northeastern alberta: surface and subsurface. *Earth Sciences Report*, 7.

Henriquez, A., Tyler, K., and Hurst, A. (1990). Characterization of fluvial sedimentology for reservoir simulation modeling. *SPE Formation Evaluation*, 5(3):211–216.

Herbrich, R. and Graepel, T. (2001). A PAC-Bayesian margin bound for linear classifiers: Why SVMs work. In *Advances in Neural Information Processing Systems 13: Proceedings of the 2000 Conference*, volume 13, page 224. MIT Press.

Hewett, T. A. (1993). Modelling reservoir heterogeneity with fractals. In *Geostatistics Tróia92*, pages 455–466. Springer.

Hird, K. B. and Dubrule, O. (1995). Quantification of reservoir connectivity for reservoir description applications. In *1995 SPE Annual Technical Conference and Exhibition Formation Evaluation and Reservoir Geology*, pages 415–424, Dallas, TX. Society of Petroleum Engineers. SPE Paper # 30571.

Hongfu, F., Yongjian, L., Liying, Z., and Xiaofei, Z. (2002). The study on composition changes of heavy oils during steam stimulation processes. *Fuel*, 81(13):1733–1738.

Hosseini, A. H., Leuangthong, O., and Deutsch, C. V. (2008). An integrated approach to permeability modeling using micro-models. In *International Thermal Operations and Heavy Oil Symposium*.

Hou, H. and Andrews, H. (1978). Cubic splines for image interpolation and digital filtering. *Acoustics, Speech and Signal Processing, IEEE Transactions on*, 26(6):508–517.

Hovadik, J. and Larue, D. K. (2007). Static characterizations of reservoirs: Refining the concepts of connectivity and continuity. *Petroleum Geoscience*, 13(4):195–211.

Hove, K., Olsen, G., Nilsson, S., Tonnesen, M., and Hatløy, A. (1992). From stochastic geological description to production forecasting in heterogeneous layered reservoirs. In *SPE Annual Conference and Exhibition, Washington, DC, Society of Petroleum Engineers Paper*, number 24890, pages 311–325.

Ichaso, A. A. and Dalrymple, R. W. (2009). Tide-and wave-generated fluid mud deposits in the tilje formation (jurassic), offshore norway. *Geology*, 37(6):539–542.

Isaaks, E. H. (1990). *The Application of Monte Carlo Methods to the Analysis of Spatially Correlated Data*. PhD thesis, Stanford University, Stanford, CA.

Isaaks, E. H. and Srivastava, R. M. (1988). Spatial continuity measures for probabilistic and deterministic geostatistics. *Mathematical Geology*, 20(4):313–341.

Jain, A. K. (2010). Data clustering: 50 years beyond k-means. *Pattern recognition letters*, 31(8):651–666.

Jain, A. K., Dubes, R. C., et al. (1988). *Algorithms for clustering data*, volume 6. Prentice hall Englewood Cliffs.

Jain, A. K., Murty, M. N., and Flynn, P. J. (1999). Data clustering: a review. *ACM*

computing surveys (CSUR), 31(3):264–323.

Jha, S. K., Mariethoz, G., Evans, J. P., and McCabe, M. F. (2013). Demonstration of a geostatistical approach to physically consistent downscaling of climate modeling simulations. *Water Resources Research*.

Jimenez, J. (2008). The field performance of SAGD projects in canada. In *International Petroleum Technology Conference*, pages 3–5, Kualalampur, Malaysia.

Johnson, S. M. and Dashtgard, S. E. (2012). The nature of inclined heterolithic stratification in a mixed tidal-fluvial setting, Fraser River. In *AAPG Annual Convention and Exhibition*, Long Beach, California. AAPG Search and Discovery Article # 50657 ©2012.

Joshi, S. D. (1988). Augmentation of well productivity with slant and horizontal wells (includes associated papers 24547 and 25308). *Journal of Petroleum Technology*, 40(06):729–739.

Journel, A. G. (1983). Non-parametric estimation of spatial distributions. *Mathematical Geology*, 15(3):445–468.

Journel, A. G. (1989). *Fundamentals of Geostatistics in Five Lessons*. Volume 8 Short Course in Geology. American Geophysical Union, Washington, DC.

Journel, A. G. and Alabert, F. G. (1990). New method for reservoir mapping. *Journal of Petroleum Technology*, pages 212–218.

Journel, A. G. and Huijbregts, C. J. (1978). *Mining Geostatistics*. Academic Press, New York.

Journel, A. G. and Xu, W. (1994). Posterior identification of histograms conditional to local data. *Mathematical Geology*, 26:323–359.

Kamath, V. A., Sinha, S., and Hatzignatiou, D. G. (1993). Simulation study of steam-assisted gravity drainage process in ugnu tar sand reservoir. *SPE paper 26075*.

Kaviani, D. and Jensen, J. L. (2010). Reliable connectivity evaluation in conventional and heavy oil reservoirs: A case study from senlac heavy oil pool, western saskatchewan. In *Canadian Unconventional Resources and International Petroleum Conference*. Society of Petroleum Engineers.

Kaviani, D. and Valkó, P. P. (2010). Inferring interwell connectivity using multiwell productivity index (mpi). *Journal of Petroleum Science and Engineering*, 73(1):48–58.

Khan, D. (2014). Personal communications.

Kogan, J., Nicholas, C., Teboulle, M., et al. (2006). *Grouping multidimensional data*. Springer.

Komery, D. P., Luhning, R. W., and ORourke, J. C. (1995). New era for oil sands development: SAGD project. In *In 6th UNITAR International Conference on Heavy Crude and Oil Sands*, New York, NY (United States).

Kupfersberger, H., Deutsch, C. V., and Journel, A. G. (1998). Deriving constraints on small-scale variograms due to variograms of large-scale data. *Mathematical geology*, 30(7):837–852.

Labrecque, P. A., Hubbard, S. M., Jensen, J. L., and Nielsen, H. (2011). Sedimentology and stratigraphic architecture of a point bar deposit, lower cretaceous mcmurray formation, alberta, canada. *Bulletin of Canadian Petroleum Geology*, 59(2):147–171.

Lajevardi, S., Babak, O., and Deutsch, C. V. (2015). On barrier size determination and optimal well placement. *Journal of Petroleum and Geosciences*.

Lajevardi, S. and Deutsch, C. V. (2011). Characterization of geoobjects continuity using moments of inertia. Technical Report 128, CCG Annual Report 13, Edmonton, AB.

Lajevardi, S. and Deutsch, Clayton, V. (2015). Stochastic regridding of geological models for flow simulation. *Bulletin of Canadian Petroleum Geology*. In production.

Lake, L. W. and Srinivasan, S. (2004). Statistical scale-up of reservoir properties: concepts and applications. *Journal of Petroleum Science and Engineering*, 44(1):27–39.

Larue, D. K. and Hovadik, J. (2006). Connectivity of channelized reservoirs: a modelling approach. *Petroleum Geoscience*, 12(4):291–308.

Larue, D. K. and Hovadik, J. (2008). Why is reservoir architecture an insignificant uncertainty in many appraisal and development studies of clastic channelized reservoirs? *Journal of Petroleum Geology*, 31(4):337–366.

Laÿ, B. (1987). Recursive algorithm in mathematical morphology. In *Acta Stereologica, Proc. 7th Int. Congress for Stereology*, volume 6/III, pages 691–699, Caen, France.

Le Blanc, R. J. (1977). Distribution and continuity of sandstone reservoirs. *Journal of Petroleum Technology*, 29(7):776–792.

Le Ravalec, M., Morlot, C., Marmier, R., and D., F. (2009a). Heterogeneity impact on SAGD process performance in mobile heavy oil reservoirs. *Oil & Gas Science and Technology-Revue de l'IFP*, 64(4):469–476.

Le Ravalec, M., Morlot, C., Marmier, R., and Foulon, D. (2009b). Heterogeneity impact on SAGD process performance in mobile heavy oil reservoirs. *Oil & Gas Science and Technology-Revue de l'IFP*, 64(4):469–476.

Lettley, C. D. and Pemberton, S. G. (2004). Speciation of mcmurray formation inclined heterolithic strata: Varying depositional character along a riverine estuary system. In *Canadian Society of Petroleum Geologists, Annual Meeting, Calgary.*

Li, D., Cullick, A., and Lake, L. (1995). Global scale-up of reservoir model permeability with local grid refinement. *Journal of Petroleum Science and Engineering*, 14(1):1–13.

Li, W., Jensen, J. L., Ayers, W. B., Hubbard, S. M., and Heidari, M. R. (2009). Comparison of interwell connectivity predictions using percolation, geometrical, and monte carlo models. *Journal of Petroleum Science and Engineering*, 68(3):180–186.

Lien, S. C., Haldorsen, H. H., and Manner, M. (1992). Horizontal wells: still appealing in formations with discontinuous vertical permeability barriers? *JPT Journal of petroleum technology*, 44(12):1364–1370.

Liu, Y. (2006). Using the SNESIM program for multiple-point statistical simulation. *Computers & geosciences*, 32(10):1544–1563.

Luster, G. R. (1985). *Raw materials for Portland cement: applications of conditional simulations of coregionalizations.* PhD thesis, Stanford University, Stanford, CA.

Lyster, S. J. (2009). *Simulation of Geologic Phenomena Using Multiple-Point Statistics in a Gibbs Sampler Algorithm.* PhD thesis, University of Alberta, Edmonton, AB.

MacQueen, J. (1967). Some methods for classification and analysis of multivariate observations. In *Proceedings of the fifth Berkeley symposium on mathematical statistics and probability*, volume 1, pages 281–297. Oakland, CA, USA.

Manchuk, J. G. (2010). *Geostatistical Modeling of Unstructured Grids for Flow Simulation.* PhD thesis, University of Alberta, Edmonton, AB.

Marren, P. M., McCarthy, T. S., Tooth, S., Brandt, D., Stacey, G. G., Leong, A., and Spottiswoode, B. (2006). A comparison of mud-and sand-dominated meanders in a downstream c oarsening reach of the mixed bedrock-alluvial Klip River, eastern free state, South Africa. *Sedimentary Geology*, 190(1):213–226.

Matheron, G. (1962). *Traité de géostatistique appliquée*, volume 14. Editions Technip, Paris.

Matheron, G. (1971). La théorie des variables régionalisées et ses applications. Fasc. 5, École Nat. Sup. des Mines, Paris.

Matheron, G. (1975). *Random Sets and Integral Geometry*. Wiley, New York.

Matheron, G., Beucher, H., de Fouquet, H., Galli, A., Guerillot, D., and Ravenne, C. (1987). Conditional simulation of the geometry of fluvio-deltaic reservoirs. SPE Paper # 16753.

McLennan, J. A. (2005). Scaling and gridding geology for SAGD flow simulation. Technical Report 210, CCG Annual Report 7, University of Alberta, Edmonton, AB.

McLennan, J. A. and Deutsch, C. V. (2005a). Local ranking of geostatisical realizations for flow simulation. Technical Report 114, CCG Annual Report 7, University of Alberta, Edmonton, AB.

McLennan, J. A. and Deutsch, C. V. (2005b). Ranking geostatistical realizations by measures of connectivity. In *SPE/PS-CIM/CHOA International Thermal Operations and Heavy Oil Symposium, Calgary, AB, Canada*, Calgary, AB. Society of Petroleum Engineers. SPE Paper Number 98168.

McLennan, J. A. and Deutsch, C. V. (2006). Permeability modeling for the SAGD process using minimodels. In *SPE Annual Technical Conference and Exhibition*, San Antonio. Society of Petroleum Engineers.

Miall, A. D. (1996). *The Geology of Fluvial Deposits*. Springer-Verlag, New York.

Michel, J., Boulvain, F., Philippo, S., and Da Silva, A.-C. (2010). Palaeoenvironmental study and small scale correlations using facies analysis and magnetic susceptibility of the mid-emsian (himmelbaach quarry, luxembourg). *Geologica Belgica*, 13(4).

Mikes, D. and Geel, C. (2006). Standard facies models to incorporate all heterogeneity levels in a reservoir model. *Marine and petroleum geology*, 23(9):943–959.

Mossop, G. D. and Flach, P. D. (1983). Deep channel sedimentation in the lower cretaceous mcmurray formation, athabasca oil sands, alberta. *Sedimentology*, 30(4):493–509.

Nichols, G. (2009). *Sedimentology and Statigraphy*. Wiley-Blackwell, 2 edition.

Nœtinger, B., Artus, V., and Zargar, G. (2005). The future of stochastic and upscaling methods in hydrogeology. *Hydrogeology Journal*, 13(1):184–201.

Nœtinger, B. and Zargar, G. (2004). Multiscale description and upscaling of fluid flow in subsurface reservoirs. *Oil & Gas Science and Technology*, 59(2):119–139.

Norrena, K. P. and Deutsch, C. V. (2002). Automatic determination of well placement subject to geostatistical and economic constraints. In *SPE International Thermal Operations and Heavy Oil Symposium and International Horizontal Well Technology Conference*.

Nzekwu, B. (1997). Drilling and completion for Steam-Assisted Gravity Drainage (SAGD) operations. *Journal of Canadian Petroleum Technology*, 36.

Peaceman, D. W. (1993). Representation of a horizontal well in numerical reservoir simulation. *SPE Advanced Technology Series*, 1(5).

Pooladi-Darvish, M. and Mattar, L. (2002). SAGD operations in the presence of overlying gas cap and water layer-effect of shale layers. *Journal of Canadian Petroleum Technology*, 41(6).

Pryor, W. and Fulton, K. (1978). Geometry of reservoir-type sandbodies in the holocene rio grande delta and comparison with ancient reservoir analogs. In *SPE Symposium on Improved Methods of Oil Recovery*.

Pyrcz, M. J. (2004). *Integration of Geologic Information into Geostatistical Models*. PhD thesis, University of Alberta, Edmonton, AB.

Pyrcz, M. J., Boisvert, J. B., and Deutsch, C. V. (2008). A library of training images for fluvial and deepwater reservoirs and associated code. *Computers & Geosciences*, 34(5):542–560.

Pyrcz, M. J. and Deutsch, C. V. (2004). maximum a posteriori selection with homotopic constraint. Technical Report 203, CCG Annual Report 6, Edmonton, AB.

Pyrcz, M. J. and Deutsch, C. V. (2014). *Geostatistical Reservoir Modeling*. Applied Geostatistics Series. Oxford University Press, New York, 2 edition.

Pyrcz, M. J., McHargue, T., Clark, J., Sullivan, M., and Strebelle, S. (2012). Event-based geostatistical modeling: description and applications. In Abrahamsen, P., Hauge, R., and Kolbjørnsen, O., editors, *Geostatistics Oslo 2012*, volume 17 of *Quantitative Geology and Geostatistics*, pages 27–38. Springer Netherlands.

Ragnemalm, I. (1992). Fast erosion and dilation by contour processing and thresholding of distance maps. *Pattern recognition letters*, 13(3):161–166.

Rana, N. C. and Joag, P. S. (2001). *Classical Mechanics*. Tata McGraw-Hill, New Delhi.

Ranger, M. J. (1994). *A Basin Study of the Southern Athabasca Oil Sands Deposit*. PhD thesis, University of Alberta, Edmonton, AB.

Ranger, M. J. and Gingras, M. (2006). Geology of the Athabasca oilsands: Field guide and overview. *Canadian Society of Petroleum Geologists*. 120 p.

Ranger, M. J. and Gingras, M. K. (2003). Geology of the athabasca oilsands: Field guide and overview. In *Ranger, Michael J and Gingras, Murray K.*

Ranger, M. J., Gingras, M. K., and Pemberton, S. G. (2008). The role of ichnology in the stratigraphic interpretation of the athabasca oil sands. In *2007 Hedberg Conference, Heavy Oil and Bitumen on Foreland Basins-From Processes to Products*, volume 30.

Reading, H. G. (2001). Clastic facies models, a personal perspective. *Bull Geol Soc Denmark*, 48:101–115.

Ren, W. and Deutsch, C. V. (2005). Exact downscaling in geostatistical modeling. Technical Report 101, CCG Annual Report 7, Edmonton, AB.

Richardson, J. G., Harris, D. G., and Rossen, R. H. (1978). The effect of small, discontinuous shales on oil recovery. *Journal of Petroleum Technology*, 30(11):1531–1537.

Rose, P. R. (1987). Dealing with risk and uncertainty in exploration: How can we improve? *AAPG Bulletin*, 71(1):1–16.

Rossi, R. E., Borth, P. W., and Tollefson, J. J. (1993). Stochastic simulation for characterizing ecological spatial patternsf and appraising risk. *Ecological Applications*, pages 719–735.

Saad, N., Maroongroge, V., and Kalkomey, C. T. (1996). Ranking geostatistical models using tracer production data. In *European 3-D Reservoir Modeling Conference*, Stavanger, Norway. Society of Petroleum Engineers. SPE Paper # 35494.

Salomão, M. C. and Grell, A. P. (2001). Uncertainty in production profiles on the basis of geostatistics characaterization and flow simulation. In *SPE Latin American and Caribbean Petroleum Engineering Conference*. Society of Petroleum Engineers. SPE Paper # 69477.

Schaaf, T., Mezghani, M., and Chavent, G. (2002). Direct conditioning of fine-scale facies models to dynamic data by combining gradual deformation and numerical upscaling techniques. In *8th European Conference on the Mathematics of Oil Recovery*.

Schnetzler, E. (1994). Visualization and cleaning of pixel-based images. Master's thesis, Stanford University, Stanford, CA.

Selim, S. Z. and Ismail, M. A. (1984). K-means-type algorithms: a generalized convergence theorem and characterization of local optimality. *Pattern Analysis and Machine Intelligence, IEEE Transactions on*, (1):81–87.

Serra, J. (1982). *Image Analysis and Mathematical Morphology*. Academy Press, London.

Serra, J. e., editor (1988). *Image Analysis and Mathematical Morphology Vol. II, Theoretical Advances*. Academy Press, London.

Shannon, C. E. (1948). The mathematical theory of communication. *Bell Syst, Tech J.*, 27(2):379–423.

Sharma, B. C., Khataniar, S., Patil, S. L., Kamath, V. A., and Dandekar, A. Y. (2002). A simulation study of novel thermal recovery methods in the ugnu tar sand reservoir, North Slope, Alaska. In *SPE Western Regional/AAPG Pacific Section Joint Meeting*. Society of Petroleum Engineers.

Shawe-Taylor, J. and Cristianini, N. (2004). *Kernel methods for pattern analysis*. Cambridge University Press Cambridge.

Sneider, R. M., Tinker, C. N., and Meckel, L. D. (1978). Deltaic environment reservoir types and their characteristics. *Journal of Petroleum Technology*, 30(11):1538–1546.

Srivastava, R. M. (1994). An overview of stochastic methods for reservoir characterization. In *Stochastic Modeling and Geostatistics: principles, Methods, and Case Studies*. AAPG.

Stanley, K. O., Jorde, K., Raestad, N., and Stockbridge, C. P. (1990). Stochastic modeling of reservoir sand bodies for input to reservoir simulation, Snorre Field, Northern North Sea. In Buller, A. T., editor, *North Sea Oil and Gas Reservoirs II*. Graham and Trotman, London.

Steinhaus, H. (1957). The problem of estimation. *The Annals of Mathematical Statistics*, pages 633–648.

Stoyan, D., Kendall, W. S., and Mecke, J. (1987). *Stochastic Geometry and its Applications*. John Wiley & Sons, New York.

Straubhaar, J., Renard, P., Mariethoz, G., Froidevaux, R., and Besson, O. (2010). An improved parallel multiple-point algorithm using a list approach. *Mathematical Geosciences*, 43(3):305–328.

Strebelle, S. (2000a). *Sequential Simulation: drawing Structures from Training Images*. PhD thesis, Stanford University, Stanford, CA.

Strebelle, S. (2000b). *Sequential Simulation: drawing Structures from Training Images*. PhD thesis, Stanford University, Stanford, CA.

Strebelle, S. (2002). Conditional simulation of complex geological structures using multiple-point statistics. *Mathematical Geology*, 34(1):1–21.

Thomas, R. G., Smith, D. G., Wood, J. M., Visser, J., Calverley-Range, E. A., and

Koster, E. H. (1987). Inclined heterolithic stratificationterminology, description, interpretation and significance. *Sedimentary Geology*, 53(1):123–179.

Tyler, K., Henriquez, A., MacDonald, A., Svanes, T., and Hektoen, A. L. (1992). MOHERES - a collection of stochastic models for describing heterogeneities in clastic reservoirs. In *3rd International Conference on North Sea Oil and Gas Reservoirs III*, pages 213–221.

Tzortzis, G. F. and Likas, A. C. (2009). The global kernel-means algorithm for clustering in feature space. *IEEE transactions on neural networks*, 20(7):1181.

Verrien, J. P., Couraud, G. P., and Montadert, L. P. (1967). Applications of production geology methods to reservoir characteristics analysis from outcrops observations. In *7th World Petroleum Congress*.

Walker, R. G. (1984). General introduction: facies, facies sequences and facies models. In *SPE Annual Conference and Exhibition, Washington, DC, Society of Petroleum Engineers Paper*, number 24890, pages 1–9.

Webb, A. C., Schroder-Adams, C. J., and Pedersen, P. K. (2005). Regional subsurface correlations of albian sequences north of the Peace River in NE British Columbia: northward extent of sandstones of the Falher and Notikewin members along the eastern flank of the foredeep. *Bulletin of canadian petroleum geology*, 53(2):165–188.

Wightman, D. M. and Pemberton, S. G. (1997). The lower cretaceous (aptian) mcmurray formation: an overview of the fort mcmurray area, northeastern, alberta.

Wilde, B. and Deutsch, C. V. (2012). Calculating an improved connected hydrocarbon volume with line-of-sight for ranking by SAGD performance. Technical Report 205, CCG Annual Report 14, University of Alberta, Edmonton, AB.

Wilson, D. R. and Martinez, T. R. (1997). Improved heterogeneous distance functions. *Journal of artificial intelligence research*, pages 1–34.

Wong, R. C. K., Samieh, A. M., and Kuhlemeyer, R. L. (1994). Oil sand strength parameters at low effective stress - its effects on sand production. *Journal of Canadian Petroleum Technology*, 33:44–49.

Xiong, H., Wu, J., and Chen, J. (2009). K-means clustering versus validation measures: a data-distribution perspective. *Systems, Man, and Cybernetics, Part B: Cybernetics, IEEE Transactions on*, 39(2):318–331.

Yang, G. and Butler, R. M. (1992). Effects of reservoir heterogeneities on heavy oil recovery by steam assisted gravity drainage. *Journal of Canadian Petroleum Technology*, 31:8–37.

Yazdi, M. M. and Jensen, J. L. (2014). Fast screening of geostatistical realizations for sagd reservoir simulation. *Journal of Petroleum Science and Engineering*, 124:264–274.

Zagayevskiy (2015). *Multivariate Geostatistical Grid-Free Simulation of Natural Phenomena*. PhD thesis, University of Alberta, Edmonton, AB.

Zeito, G. (1965). Interbedding of shale breaks and reservoir heterogeneities. *Journal of Petroleum Technology*, 17(10):1223–1228.

Zhang, R. and Rudnicky, A. I. (2002). A large scale clustering scheme for kernel k-means. In *Pattern Recognition, 2002. Proceedings. 16th International Conference on*, volume 4, pages 289–292. IEEE.

Zhang, W., Youn, S., and Doan, Q. T. (2007). Understanding reservoir architectures and steam-chamber growth at christina lake alberta by using 4d seismic and crosswell seismic imaging. *SPE Reservoir Evaluation & Engineering*, 10(05):446–452.